DOE/BC/14994-10
OSTI ID: 9322

SUPRI HEAVY OIL RESEARCH PROGRAM
TWENTY-FIRST ANNUAL REPORT

AUGUST 26, 1997 -- AUGUST 25, 1998

SUPRI TR 111

By
William E. Brigham
Anthony R. Kovscek
Louis M. Castanier

May 1998

Work Performed Under Contract No. DE-FG22-96BC14994

Stanford University
Stanford, California

National Petroleum Technology Office
U. S. DEPARTMENT OF ENERGY
Tulsa, Oklahoma

DISCLAIMER

Portions of this document may be illegible in electronic image products. Images are produced from the best available original document.

DOE/BC/14994-10
Distribution Category UC-122

Supri Heavy Oil Research Program Twenty-First Annual Report

August 26, 1997 -- August 25, 1998

SUPRI TR 111

By
William E. Brigham
Anthony R. Kovscek
Louis M. Castanier

May 1998

Work Performed Under Contract DE-FG22-96BC14994

Prepared for
U.S. Department of Energy
Assistant Secretary for Fossil Energy

Thomas Reid, Project Manager
National Petroleum Technology Office
P.O. Box 3628
Tulsa, OK 74101

Prepared by
Stanford University
Petroleum Engineering Department
65 Green Earth Sciences Bldg.
Stanford, CA 94305

TABLE OF CONTENTS

TABLE OF TABLES

TABLE OF FIGURES

PROJECT 1: FLOW PROPERTIES STUDY

ACKNOWLEDGEMENTS

This work was supported by the United States Department of Energy, under contract no. DE-FG22-96BC14994 to Stanford University. Present industrial affiliate members are: Arco Exploration and Production, Chevron Petroleum Technology Co., Elf Exploration Production, Exxon, Intevep, Mobil, Texaco, and Total Exploration Production USA, Inc.

SUMMARY

The goal of the Stanford University Petroleum Research Institute is to conduct research directed toward increasing the recovery of heavy oils. Present, SUPRI is working in five main directions:

1. FLOW PROPERTIES STUDIES - To assess the influence of different reservoir conditions (temperature and pressure) on the absolute and relative permeability to oil and water and on capillary pressure.

2. IN-SITU COMBUSTION - To evaluate the effect of different reservoir parameters on the in-situ combustion process. This project includes the study of the kinetics of the reactions.

3. STEAM WITH ADDITIVES - To develop and understand the mechanisms of the process using commercially available surfactants for reduction of gravity override and channeling of steam.

4. FORMATION EVALUATION - To develop and improve techniques of formation evaluation such as tracer tests and pressure transient tests.

5. FIELD SUPPORT SERVICES - To provide technical support for design and monitoring of DOE sponsored or industry initiated field projects.

PROJECT 1: FLOW PROPERTY STUDIES

To assess the influence of different reservoir conditions (temperature and pressure) on the absolute and relative permeability to oil and water and on capillary pressure.

1.1 EFFECTS OF TEMPERATURE ON MULTIPHASE RELATIVE PERMEABILITY

(S. Akin)

1.1.1 INTRODUCTION

Production of oil from petroleum reservoirs usually involves simultaneous flow of two or more immiscible fluids through a porous rock. Multiphase flow in porous media is a complex process that depends on a number of factors including the absolute permeability, pressure drop, capillary pressure, fluid viscosities, and relative permeabilities of each phase. Of these, the relative permeability is probably the most important parameter determining reservoir performance. For modeling thermal recovery processes for heavy oil recovery, one needs to know not only the relative permeabilities at the original reservoir temperature, but also the changes expected at higher temperatures. Over the past three decades, a number of experimental studies have reported contradictory temperature effects on two phase relative permeabilities in porous media. Most experiments were performed on consolidated rocks, and only a few studies used reservoir cores and crude oils.

The reasons for divergence among experimental multiphase relative permeability data may be summarized as follows:

1. Errors in saturation measurements.
2. Errors caused by neglect of capillary pressure end effects.
3. Wettability variations with differing oils and brines.
4. Assumptions made to develop experimental procedures or calculations.
5. Inadequacy of mathematical models to represent multiphase flow conditions.

It is clear that unless the above problems can be overcome, a better understanding of the effects of temperature on relative permeabilities will not be achieved. Therefore careful, unsteady state, relative permeability experiments at differing temperatures were

conducted and reported here. Two phase saturation profiles along an unconsolidated core were measured using computerized tomography (CT) which is a reliable and accurate means of measuring local saturations. A black oil simulator, coupled with a global optimization code was then used to estimate two-phase relative permeabilities. Experimental saturation profiles, differential pressure and recovery data were used in a least squares manner in the numerical model. Heterogeneity effects were considered in the simulations by using CT calculated porosity values along the core.

1.1.2 LITERATURE REVIEW

Relative permeability is the basis used to predict multiphase flow through porous media. It is an empirical concept which allows Darcy's Law to be generalized for multiple phases (Honarpour, 1986). This is done by assuming that the absolute permeability, used in Darcy's Law, may be replaced by a term which contains both the absolute permeability and a "relative permeability" which is a function of the fluid saturation. For a two phase system (oil and water), the flow equations are given as:

$$u_o = -\frac{kk_{or}}{\mu_o}\left(\nabla p_o - \rho_o \, g/g_c\right) \tag{1}$$

$$u_w = -\frac{kk_{wr}}{\mu_w}\left(\nabla p_w - \rho_w \, g/g_c\right) \tag{2}$$

where u_i is the flow velocity, k is the absolute permeability, $k\,r_i$ is the relative permeability, μ_i is the dynamic viscosity, ∇p_i is the gradient of the pressure, ρ_i is the density. In these equations, i represents oil or water, g is the gravitational acceleration, and g_c is the universal constant in Newton's Law. Three differing absolute (base) permeabilities are commonly used: the absolute air permeability, the absolute water permeability, and the permeability to oil at reservoir connate water saturation. Throughout this report water permeability will be used.

Although the concept of relative permeability is simple, the measurement and interpretation of relative permeability versus saturation is not. For example, there is evidence that relative permeability may be a function of many more parameters than fluid saturation (Honarpour, 1986). Temperature, flow velocity, saturation history, wettability changes and the mechanical and chemical behavior of the matrix material may all play roles in changing the functional dependence of relative permeabilities on saturation. The best defined of these dependencies is the variation of relative permeability with saturation history; relative permeability curves show hysteresis between drainage (wetting phase decreasing) and imbibition (wetting phase increasing).

A common use of relative permeability data is in numerical simulators. These data are fundamental parameters necessary in all simulations. However, numerical simulation of thermal recovery processes also requires knowledge of its temperature dependence. Often, relative permeabilities measured at ambient conditions are used to predict performance at higher temperatures, which in turn, may lead to erroneous results.

Over the last three decades, a number of laboratory studies have appeared in the literature on the effects of temperature on relative permeability and residual oil saturation as well as irreducible water saturation. Edmondson (1965) found a reduction in residual oil saturation in Berea cores as the temperature increased. Using refined oils and an unsteady state experimental technique, he noted that the relative permeability ratio of oil to water shifted toward a higher water saturation as the temperature increased.

Poston *et al.* (1970) investigated the effects of temperature on unconsolidated sand using refined oils. They reported that irreducible water saturation increased, and the residual oil saturation decreased with increasing temperature. Moreover, they concluded that relative permeabilities to both oil and water increased with increasing temperature.

Contradicting previous researchers, two studies (Sufi *et al.,* 1982 and Miller and Ramey, 1985) conducted at Stanford University reported temperature independent relative permeability data obtained from unsteady state experiments in unconsolidated and Berea cores using refined oils. Miller and Ramey (1985) noted various artifacts such as; material balance errors, viscous instability, clay migration, wettability alteration by

miscible cleaning methods, and capillary pressure end effects, that may have affected former conclusions on the effect of temperature on relative permeability data.

Closmann *et al.* (1985) used the steady state technique to measure altered, unaltered and deasphalted tar and brine relative permeabilities at elevated temperature using frozen Peace River cores. They concluded that at higher temperatures tar and water relative permeability curves shifted toward lower water saturations.

Maini and Batcyky (1985) conducted unsteady state experiments at temperatures ranging from room temperature to 522°F using a frozen core from a heavy-oil reservoir, and stock tank oil and formation brine from the same reservoir. They measured the absolute permeability to formation water using a transient pressure decay test, and used history matching calculations to obtain relative permeabilities. They concluded that, irreducible water saturation increased and residual oil saturation decreased with increasing temperature until an optimum temperature. Moreover, they reported that relative permeability to oil decreased and the relative permeability to water remained unchanged with increasing temperature.

Polikar *et al.* (1986) used the steady state technique to measure the relative permeability of Athabasca bitumen using unconsolidated Ottawa sand as the porous medium. Their results showed no significant effect of temperature on relative permeability and saturation data up to 392°F.

Maini and Okazawa (1987) analyzed unsteady state experiments conducted on an unconsolidated silica sand using Bodo stock tank oil and deionized water. They history matched production and differential pressure data to obtain relative permeability curves. They concluded that the most reliable data they obtained was at residual oil saturation after 3 pore volumes of fluid injected. They observed increasing relative permeability to water with increasing temperature.

Unlike the previous researchers, Watson and Ertekin (1988) studied the effect of temperature gradient on relative permeability measurements using the steady state technique. They found that different temperature gradients caused differences in both the irreducible water saturation and residual oil saturations. This suggested that the fired Berea cores became increasingly water-wet, and unfired cores became increasingly oil

wet, during imbibition and drainage. Moreover, they concluded that relative permeabilities to both oil and water decreased with increasing temperature. They also observed that the absolute water permeabilities of fired Berea sandstone cores were unaffected by temperature.

Polikar *et al.* (1990) conducted both steady-state and unsteady-state relative permeability experiments to find out the effects of temperature on relative permeability. Using Athabasca bitumen and deionized water, they used the JBN technique to analyze their results. They observed no significant temperature effects on relative permeability of either phase, nor in the residual oil and irreducible water saturations. They attributed the small changes seen to the heterogeneity effect. Moreover, they reported that steady-state and unsteady-state techniques resulted in similar relative permeability curves with little differences.

More recently, Muqeem *et al.* (1993) conducted steady state two phase and three phase relative permeability experiments at 75°C and 125°C using an unconsolidated silica sand with refined oil, brine and nitrogen gas. The measured relative permeabilities showed no significant temperature effect.

Kumar and Inouye (1994) used the JBN technique to analyze unsteady state relative permeability experiments conducted at differing temperatures. They tried to obtain low temperature analogues to high temperature relative permeability data. They concluded that relative permeability data obtained at ambient conditions can be used for high temperatures as long as the viscosity ratios and the wettabilities are similar. They also reported that residual oil saturation and irreducible water saturation are independent of temperature and are a function of viscosity ratio.

The results obtained from the aforementioned studies are summarized in Table 1. It can be observed that, because of the experimental duration and convenience, most of the researchers preferred to use unsteady-state experiments. The relative permeability data were obtained by interpreting such experiments either with the JBN technique or by one dimensional finite difference computer history matching. Moreover, most experiments were performed on consolidated rocks, and only a few studies used reservoir cores and crude oils.

Table 1. A Summary of the Recent Experimental Investigations of Temperature Effects on Relative Permeability.

Reference	Experimental Technique	Fluids	Core	Temperature Range	Saturation Measurement	End Point Saturation	Relative Permeability
Edmondson, 1965	Unsteady State (Welge)	Refined Oils (No 5 & 15)	Berea (1382°F)	room-500°F	graduated cylinders	$S_{or}\downarrow$ T↑	shifted
Sufi et al., 1982	Unsteady State (JBN)	Refined Oil	Unconsolidated Ottawa (170-200)	room-250°F	photo cell + frequency counter	independent	independent
Miller & Ramey, 1985	Unsteady State (JBN)	Refined Oil (Blandol)	Unconsolidated Ottawa (100-200) + Berea (932°F)	room-300°F	separator + graduated cylinders	independent	independent
Closmann et al., 1985	Steady State	Altered-unaltered-deasphalted tar	Frozen Peace River Cores	385°F	electrical resistance	np	k_{rw} shifted to lower S_w
Maini & Batcyky, 1985	Unsteady State (History Matching)	Stock Tank Oil	Frozen Core from a Hvy Oil Res	room-522°F	separator + fractional collector	$S_{wir}\uparrow$ T↑ $S_{or}\downarrow$ T↑ (until T_{opt} transverse)	$k_{ro}\downarrow$ T↑ $k_{rw}\rightarrow$ T↑
Polikar et al., 1986	Steady State	Athabasca Bitumen	Unconsolidated Ottawa (~200)	room-482°F	material balance	independent	independent below 392°F
Maini & Okazawa, 1987	Unsteady State (History Matching)	Bodo Stock Tank Oil+3.5% ether	Unconsolidated Silica Sand (140-170)	room-392°F	separator + fractional collector	np	$k_{rw}\uparrow$ T↑ $k_{ro}\downarrow\uparrow$ T↑
Watson & Ertekin, 1988	Steady State	Refined Oil (Soltrol 170)	Berea (1832°F) + unfired	room-300°F	material balance	$S_{wir}\uparrow$ T↑	k_{ro}, $k_{rw}\downarrow$ T↑
Polikar et al., 1990	Steady & Unsteady State (JBN)	Athabasca Bitumen	Unconsolidated Silica Sand (170-230)	212°F-482°F	material balance	independent	independent
Muqeem et al. 1993	Steady State	Refined Oil+N2	Unconsolidated Silica Sand (140-200)	167°F&257°F	separator	np	independent
Kumar & Inouye, 1994	Unsteady State (JBN)	Refined Oil-Drakeol 19-G.E. Silicon Oil-San Joaquin Valley Hvy Oil-	Unconsolidated preserved cores + Berea (925°F)	room-300°F	graduated cylinders	independent	shifted

The reasons for divergence of experimental multiphase relative permeability data may be summarized as follows:

1. Errors in saturation measurements.
2. Errors caused by neglect of capillary pressure end effects.
3. Wettability variations with differing oils, and brines.
4. Assumptions made to develop experimental procedures or calculations.
5. Inadequacy of mathematical models to represent multiphase flow conditions.

It is clear that, unless the problems stated above are overcome, a better understanding of the effects of temperature on relative permeabilities will not be achieved.

1.1.3 APPLICATION OF THE UNSTEADY-STATE RELATIVE PERMEABILITY ESTIMATION TECHNIQUE TO HEAVY OIL SYSTEMS

The principal objective of this section is to examine whether or not a Buckley-Leverett type displacement model could be used describe the megascopic behavior of unstable displacements (and to see if it is possible to do so by adjusting the relative permeability curves to account for viscous instabilities). To achieve this goal, several unstable immiscible displacements were simulated. These were conducted to analyze a possible effect of temperature on relative permeabilitiy curves reported by Sufi *et al.* (1982). It should be noted that the selection is based solely on the availability and the quality of the data. The level of instability in those experiments were quantified by a dimensionless stability number, N_{is} proposed by Peters and Flock (1981).

$$N_{is} = \frac{(M-1)(V-V_c)\mu_w d^2}{N_w k_{wor} \sigma} \tag{3}$$

In this equation M refers to end point mobility ratio, V is superficial velocity (m/s or ft/s), V_c is characteristic velocity (m/s or ft/s), μ_w is oil viscosity (m Pa s or cp), d is core diameter (m or ft), N_w is dimensionless wettability number, k_{wor} is the permeability to water at residual oil saturation (m^2 or darcy), and σ is interfacial tension (mN/m or dyne/cm). According to Peters and Flock (1981), a core flood will be stable (no viscous fingering) if the dimensionless stability number is less than 13.56. The stability numbers and the properties of the porous medium and the fluids used in the experiments reported by Sufi *et al.* (1982) are presented in Tables 2 and 3. It can be observed that even at a high temperatures the core floods have high instability numbers. Therefore all the core floods reported should have suffered from significant viscous fingering. However, capillary end effects were found to be minimum as the scaling coefficient proposed by Rapoport and Leas (1953) were higher than the critical (i.e. $Lu\mu_w$,ft-ft/s-cp is greater than 3.5) for all experiments.

Table 2. Properties of Porous Medium and Fluids Used by Sufi *et al* (1982).

Porous Medium	**Fluid Properties**
Ottawa Sand (mesh 170-	Oil used is Kaydol (equivalent to Chevron
Permeability, k = 5.3	Viscosity at °70 F = 220 cp
Porosity, ϕ = 0.394	Density at °70 F = 0.878 gm/cc
Length, L = 17.8 cm	Water used is distilled and de-mineralized
Diameter, d = 2.54 cm	Viscosity at °70 F = 0.97 cp
	Density at °70 F = 1.00 gm/cc

A black oil simulator, ECLIPSE 100, was used to simulate the experimental conditions given in Table 2. Three dimensional, radial geometry was used to simulate the experiments as shown in Fig 1. To account for viscous fingers center grids have smaller diameter compared to the outer ones* . The first and last grid planes in the z

*This type of grid was selected to compare CT images during the experiments which will be seen in the following sections.

direction had higher transmissibility compared to other grids to reproduce the experimental inlet and outlet lines together with spider-web shaped end plates .

Table 3. Stability Numbers for Different Experiments with No Initial Water Saturation as Reported by Sufi *et al.* (1982)

Experiment	1	2	3
Temperature, °F	70	122	150
Stability Number$_s$	40167	6650	3174

Buckley-Leverett type relative permeability estimation techniques use production and pressure differential history across the core collected during displacements in linear core floods. Unsteady-state relative permeability data is then computed by applying the JBN technique (Johnson *et al.*, 1959) or the graphical equivalent proposed by Jones and Roszelle (1978). The JBN technique is based on the solution of the three equations given below:

$$f_o = \frac{1}{1+\frac{k_{rw}\mu_o}{k_{ro}\mu_w}} = \frac{dN_p}{dW_i} \tag{4}$$

$$S_{w2} = S_{wi} + N_p - W_i f_o \tag{5}$$

$$\frac{f_o}{k_{ro}} = \frac{d\left(\frac{1}{W_i I_r}\right)}{d\left(\frac{1}{W_i}\right)} \tag{6}$$

In these equations f is the fractional flow, k_{ro} and k_{rw} are the relative permeabilities to oil and water, S_w is saturation of brine, N_p and W_i are the oil produced and brine injected in terms of pore volumes, and I_r is the relative injectivity. The data required are pressure drop across the core and produced volumes of fluids as functions of volume injected.

Figure 2 gives the comparison of the saturation distributions at 0.193PV of water injected obtained from simulations of three different temperatures (70, 122, and 150°F) at four different locations along the core with a zero initial water saturation. It can be observed that the front is not stable, and moreover, the fingering pattern is visible in the center of the core. It should be noted that the same set of relative permeability curves were used to generate these data.

The relative permeability curves obtained using the JBN analysis are compared to the input curves in Fig 3. It can be observed that although the same relative permeability curves were used to simulate at different temperatures, different apparent relative permeability curves were obtained using the JBN technique. Interestingly, the resulting relative permeability curves show a false temperature dependence. That is to say, there is a considerable increase in relative permeability to oil and a decrease in relative permeability to water at a constant saturation as temperature increases. This false temperature dependence agrees with the general trend that oil and water relative permeability curves shift to the right as reported in studies by Sinnokrot (1969), Weinbrandt et al. (1975), and others. Moreover, these false findings agree with the concept of decreased residual oil saturation with a temperature increase.

Three more hypothetical experiments were simulated to see the effect of initial water saturation. The stability numbers were much smaller compared to the no initial water saturation case, as observed in Table 4. In these cases, the calculated relative permeability curves did not show a false temperature effect, but failed to find the input relative permeability curves as shown in Fig 4. Similar to the previous case, the calculated residual oil saturation decreased with a temperature increase.

The findings on the next page clearly show that JBN, and like techniques, can not be used to determine heavy oil - water relative permeability curves, and can lead to erroneous results. It seems that the viscous instability effects get smaller if the core is initially saturated with water. Another important finding is that the JBN technique also leads to a false temperature effect.

Table 4. Stability Numbers for Different Experiments with 10% Initial Water Saturation as Reported by Sufi *et al.* (1982)

Experiment	1	2	3
Temperature, °F	70	122	150
N_{is}	582.3	96.4	46.0

Another common technique used to estimate relative permeability curves is one dimensional history matching. To estimate relative permeability curves with the history matching or parameter estimation approach, an objective function is constructed as a weighted sum of squared differences between the measured data and calculations from a one dimensional mathematical model of the experiment. For a typical displacement experiment, the measured data might consist of the pressure drops across the core, the recoveries of the displaced phase, and the internal saturation profiles. Then, the objective function, J, can be expressed as:

$$J = \sum_{i=1}^{N} W_{pi}\left(\Delta P_i^{obs} - \Delta P_i^{cal}\right)^2 + \sum_{i=1}^{N} W_{qi}\left(Q_{ti}^{obs} - Q_{ti}^{cal}\right)^2 + \sum_{k=1}^{M}\sum_{i=1}^{N} W_{si}\left(S_{i,k}^{obs} - S_{i,k}^{cal}\right)^2 \quad (7)$$

In the above equation, P is pressure, Q is cumulative production, S is saturation, and the W_i's are the inverses of the variances of the experimental measurement errors which will give the maximum-likelihood (minimum-variance) estimates of the

parameters (Akin, 1997). A single set of data (i.e., pressure profiles) or more than one set of data (pressure, production, saturation profiles) may be used in a history matching procedure.

To see the effects of viscous instability we also used this technique to analyze the hypothetical data generated before. In this study, the numerical reservoir simulator used is the well known black oil simulation code ECLIPSE 100 by Geoquest (1995), and the optimization code is a version of the simulated annealing process developed by Goffe *et al.* (1994). The computer code requires an input data file, and an output data file for execution. The input data file is basically divided into two parts: initialization and recurrent data sections. The initialization data consists of model grid dimensions and geometry, distribution of porosity and permeability, PVT data, and initial pressure and saturation distributions, as well as the solution method and various run parameters. The recurrent data include well data and the time step control information. In this study, the input data file is modified such that relative permeability and capillary pressure data are controlled within the optimization code as unknowns to be found. One other change with the simulator is the usage of extra output files that produce time dependent pressure and production data as well as saturation profiles. These data files are then used by the optimization code so that Eq. 7 can be used.

By using a one-dimensional radial grid definition, the same hypothetical, aforementioned data were used to generate relative permeability curves by matching the pressure and production response at ambient temperature. Figure 5 compares the estimated relative permeability curves with the input data. Note that the water relative permeability curve agrees with the input curve at low to moderate water saturations but becomes higher at higher water saturations. This is probably due to short duration of the hypothetical experiment, where water saturations never exceeded 0.6. However, the computed oil relative permeability curve is lower then the input curve. Therefore, it can be concluded that one dimensional history matching is not producing correct relative permeability curves when viscous fingering is present. Another history matching was carried out using a two dimensional radial grid to find out whether there would be any improvement. The water relative permeability curve did not change much, but the oil

curve seemed to improve as seen in Fig 5. Therefore it was concluded that two dimensional history matching produced better results then the one dimensional history match.

1.1.4 EXPERIMENTAL APPARATUS AND PROCEDURE

High temperature relative permeability experiments require core holders and sleeves that can be used at high temperature and pressure. The SUPRI CT laboratory now has a high temperature and high pressure core holder shown in Fig 6. It consists of an aluminum outer shell with internal adjustable centralizers which hold and centralize a high temperature and pressure, 1 3/4 in ID, and 16 in long aluminum core sleeve. The core sleeve can operate safely up to 482°F and 1000 psi. With its current design the core holder is suitable for CT monitored high temperature experiments using a heating circulator.

Two successful experiments were conducted and analyzed, using South Belridge sand and oil. Table 5 gives the average reservoir properties of the South Belridge field. Oil viscosities, brine viscosities and oil-water viscosity ratios are given in Figs 7 through 9 as functions of temperature.

Table 5. Properties of South Belridge Sand and Fluids Used in the Experiments.

Porous Medium	South Belridge sand Reservoir Temperature ~ 30°C 0.5-10Darcies 30-35% porosity
Oil	South Belridge oil 13 - 15 °API 0.96 - 0.98 gm/cc
Water	De-ionized water + 8%KBr

The same experimental procedure was used in all experiments. After packing the core holder, it is placed on the positioning system and vacuumed to less than 200 mtorr. Following that, a total of 18 reference dry scans were taken using 1 in spacing between slices. The sand pack is then flooded with several pore volumes of South Belridge oil ensuring 100% oil saturation. Reference oil saturated images were taken at the same locations and porosity of the sand pack was calculated. Figure 10 gives a three dimensional reconstruction of the porosity images in Run 1. The average porosity of this sand pack was about 31%. Brine was then injected at a fixed rate of 2ml/min, which was high enough to minimize capillary end effects, as the Rapoport and Leas number was greater than 3.5 CT scans at prescribed locations were taken at different times and these were used to calculate saturation distributions along the sand pack. After a run is finished at ambient temperature, temperature is increased to 122°F and CT scans are again taken at different times. This part of the experiment was continued until oil production ceased. After that, temperature was increased to 150°F and the above procedure is repeated.

1.1.5 METHOD OF SOLUTION

The pressure, saturation and production data collected during the ambient part of the experiment are used to calculate heavy oil - water relative permeability curves using the aforementioned two dimensional history matching procedure. Then, using these relative permeability curves, the rest of the experiment was simulated for the higher temperature data.

There are two possible outcomes of this procedure:

1. Both parts of the data (i.e. cold and hot) are matched by using only one set of relative permeability curves, which would indicate that the flow functions do not depend on temperature.
2. The algorithm fails to represent both parts of the experimental data (i.e. cold and hot) using a single set of relative permeability curves, which would indicate that the flow functions depend on temperature.

A hypothetical heavy oil - water relative permeability run is simulated using the above procedure. A single set of relative permeability curves was used to generate "no temperature effect" pressure, production and saturation profiles. Then, the optimizer-simulator is used to obtain relative permeability curves using the cold part of this hypothetical experiment. Figures 11 - 13 give the pressure, production and saturation profile fits to both cold and hot parts of the hypothetical experiment. Although there are some minor differences between the input and fitted data, a general agreement is observed. There is also good agreement with the input relative permeability curves, as observed in Fig 14. This hypothetical example shows that the proposed technique can be used to find the effect of temperature on flow functions.

1.1.6 RESULTS AND DISCUSSION

The results of two experiments (one with zero initial water saturation, the other with 30% initial water saturation) will be presented in this section. Figure 15 gives saturation images obtained for the experiment with an initial water saturation of 30%. The injection port is on the right and the production port is on the left of these images. There is a 2 cm spacing between successive images. The top two lines correspond to images taken during the ambient part of the experiment whereas the third and fourth line corresponds to images taken at 122°F and 150°F. Viscous fingers are clearly visible as small circular sections. Figure 16 gives the reconstruction of these saturation images on the x-plane. It can be observed that brine is initially flowing at the bottom of the sand pack for the cold part of the experiment. But as time goes by and the temperature of the system is increased, there is a general brine saturation increase throughout the sand pack. However, brine is still flowing in its own finger structures.

Figures 17 and 18 give the pressure fit and the relative permeability curves used to fit the data using the numerical model. Although the pressure curve is rather noisy a general agreement with the model of the experiment is observed at ambient and at 122°F. Initially, the fit seems to be rather poor. This can be explained with the sensitivity of the

least squares minimization process. An alternative may be the use of "the least absolute value" technique which is not sensitive to data outliers. Another interesting point is that, the pressure curve is slightly different for the 150°F part of the experiment. The pressure fit does not seem to be reproducing the experimental trend especially at late time. We do not have an explanation for this problem. So returning to the original hypothesis that states "if both parts of the experimental data (i.e. cold and hot) are matched using only one set of relative permeability curves then the flow functions do not depend on temperature", we can conclude that relative permeability is not a function of temperature for the temperature range studied. However, it is clear that more experiments are needed to clarify this phenomenon accurately.

Another experiment was conducted to see the effect of temperature on heavy oil - water relative permeability curves. Unfortunately, this experiment failed, because of a tubing and core holder failure. In this case, there was no initial water saturation. Probably, the heavy oil plugged the outlet tubing and eventually pressure increased to a level above the burst pressure of the tubing. Figure 19 gives the CT calculated saturation distribution along the core just before the failure. This saturation data is completely different than the previous experiment. Fingering is also present. However, the fingers are larger than the previous experiment. The inlet end seems to be totally swept and the length of the swept area is rather short. There is a main finger structure that continuously decrease in diameter (width) from inlet to the outlet of the sand pack.

1.1.7 NOMENCLATURE

Roman

f	:	Fractional flow
g	:	Gravitational acceleration
k	:	Relative permeability
u	:	Darcy velocity
I	:	Relative injectivity

J	:	Objective function
M	:	Number of grids
N	:	Production or number of data points
Q	:	volume of displaced phase recovered
Δp	:	Pressure differential across the core
∇p	:	Pressure gradient
S	:	Wetting phase saturation, fraction
W	:	Pore volumes injected or weighing factor

Greek

μ : Viscosity

ρ : Density

Subscripts and superscripts

cal	:	Calculated
exper	:	Experimental
i, j, k	:	Indices
iter	:	Iteration
model	:	Model
o	:	Oil
obs	:	Observed
p	:	Produced
scale	:	Scale
w	:	Water
w2	:	End point

1.1.8 REFERENCES

1. Akin, S. : "Application of Computerized Tomography to the Determination of Three Phase Relative Permeabilities," Phd dissertation, Middle East Technical University, Ankara, Turkey, Jan 1997.
2. Closmann, P. J., Waxman, M. H., and Deeds, C. T.: "Steady-State Tar/Water Relative Permeabilities in Peace River Cores at Elevated Temperature," paper SPE 14227 presented at 60th Annual Technical Conference and Exhibition of Society of Petroleum Engineers held in Las Vegas, USA, Sept. 22-25, 1985.
3. Edmondson, T. A.: "Effect of Temperature on Waterflooding," J. Cdn. Pet. Tech. (Oct. - Dec. 1965) 236-42.
4. Goffe, Ferrier and Rogers : "Global Optimization of Statistical Functions with Simulated Annealing," Journal of Econometrics, vol. 60, no. 1/2, Jan./Feb. 1994, 65-100.
5. Honarpour, M., Koederitz, L., and Harvey, A. H .: "Relative Permeability of Petroleum Reservoirs," CRC Press, Boca Raton , Florida, 1986.
6. Johnson, E.F., Bossler, D. P., and Naumann, V. O. : "Calculation of Relative Permeability From Displacement Experiments," Trans. AIME (1959) 216, 61-63.
7. Kumar, M., and Inouye, T. A.: "Low-Temperature Analogs of High-Temperature Water/Oil Relative Permeabilities," paper SPE 28616 presented at 69th Annual Technical Conference and Exhibition of Society of Petroleum Engineers held in New Orleans, USA, Sept. 25-28, 1994.
8. Maini, B. B., and Batycky, J. P.: "Effect of Temperature on Heavy-Oil/Water Relative Permeabilities and Vertically Drilled Core Plugs," JPT (Aug. 1985) 1500-1510.
9. Maini, B. B., and Okazawa, T.: "Effect of Temperature on Heavy Oil-Water Relative Permeability of Sand," J. Cdn. Pet. Tech. (May - June 1987) 33-41.

10. Miller, M. A., and Ramey, H. J. Jr.: "Effect of Temperature on Oil/Water Relative Permeabilities of Unconsolidated and Consolidated Sands," JPT (Dec. 1985) 945-953.
11. Muqeem, M., Bentsen, R., and Maini, B.: "Effect of Temperature on Three-Phase Water-Oil-Gas Relative Permeabilities of Unconsolidated Sands," paper 5593-03 presented at the 5th Petroleum Conference of the South Saskatchewan Section, the Petroleum Society of CIM, held in Regina, Canada, Oct. 18-20, 1993.
12. Peters, E.J. and Flock, D.L.: "The Onset of Instability During Two-Phase Immiscible Displacement in Porous Media" Soc. Pet. Eng. J.(April, 1981) 249-258.
13. Polikar, M., Ali, F. S. M., and Puttagunta, V. R.: "High Temperature Relative Permeabilities for Athabasca Oil Sands," SPE Res. Eng. (Feb. 1990) 25-32.
14. Polikar, M., Ferracuti, F., Decastro, V., Puttagunta, V. R., and Ali, F. S. M.: "Effect of Temperature on Bitumen-Water End Point Relative Permeabilities and Saturations," J. Cdn. Pet. Tech. (Sep. - Oct. 1986) 44-50.
15. Poston, S. W., Israel, S., Hossain, A. K. M. S., Montgomery III, E. F. and Ramey, H. J. Jr.: "The Effect of Temperature on Irreducible Water Saturation and Relative Permeability of Unconsolidated Sands," Soc. Pet. Eng. J. (June, 1970) 171-180.
16. Rapoport, L. A., and Leas, W. J.: "Properties of Linear Waterfloods," J. Pet. Tech. (May 1953) 139-48.
17. Sinnokrot, A.A., Ramey, H.J.Jr., and Marsden, S.S,Jr. :"Effect of Temperature Level upon Capillary Pressure Curves," Soc. Pet. Eng. J. (March 1971) 13-22.
18. Sufi A. H., Ramey, H. J. Jr., and Brigham, W. E.: "Temperature Effects on Relative Permeabilities of Oil-Water," paper SPE 11071 presented at 57th Annual Fall Technical Conference and Exhibition of Society of Petroleum Engineers held in New Orleans, USA, Sept. 26-29, 1982.
19. Watson, R. W., and Ertekin, T.: "The Effect of Steep Temperature Gradient on Relative Permeability Measurements," paper SPE 17505 presented at the SPE Rocky Mountain Regional Meeting held in Casper, WY, USA, May 11-13, 1988.
20. Weinbrandt, R.M., Ramey, H.J.Jr., and Casse, F.J. : "The Effect of Temperature on Relative and Absolute Permeability of Sandstones," Soc. Pet. Eng. J. (Oct. 1975) 376-84.

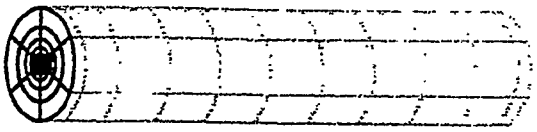

Figure 1. Grid System Used for Simulating Experiments by Sufi et al. (1982).

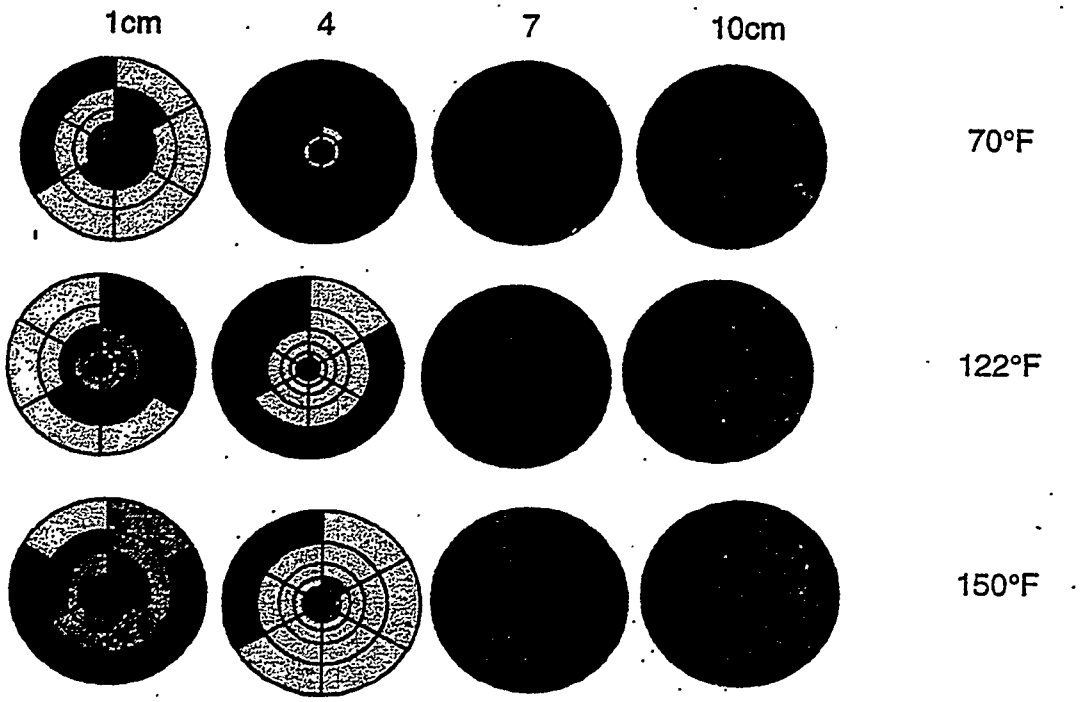

Figure 2.Comparison of Saturation Distributions at Different Temperatures.

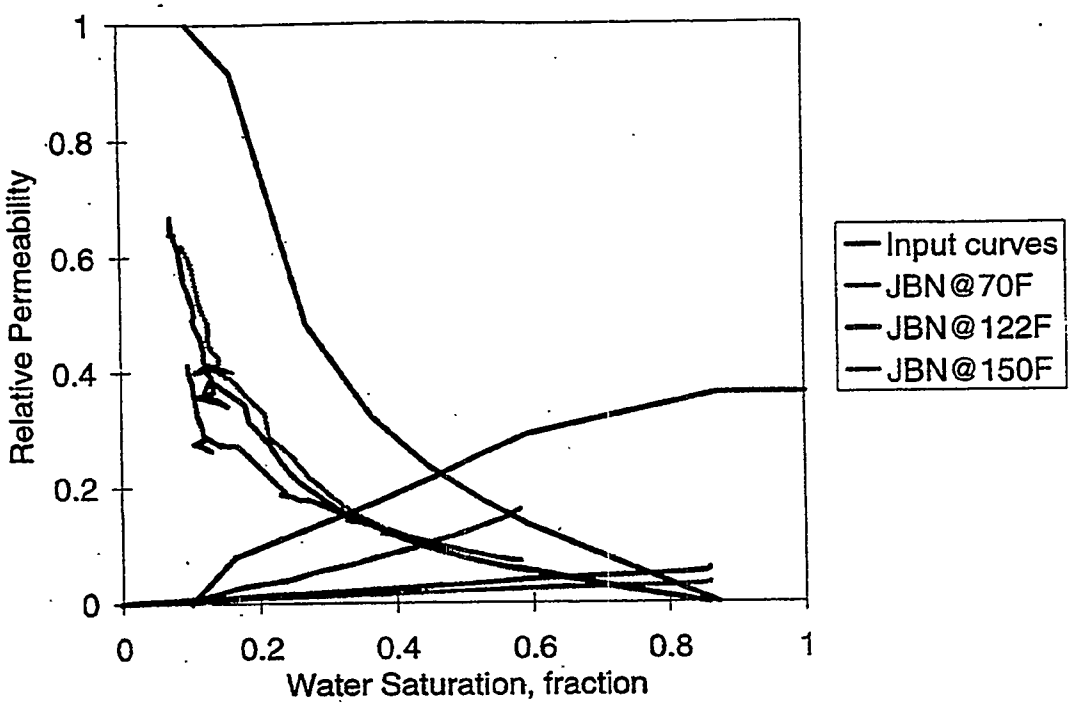

Figure 3. Comparison of JBN Relative Permeability Curves to Input Relative Permeability Data (No Initial Water Saturation).

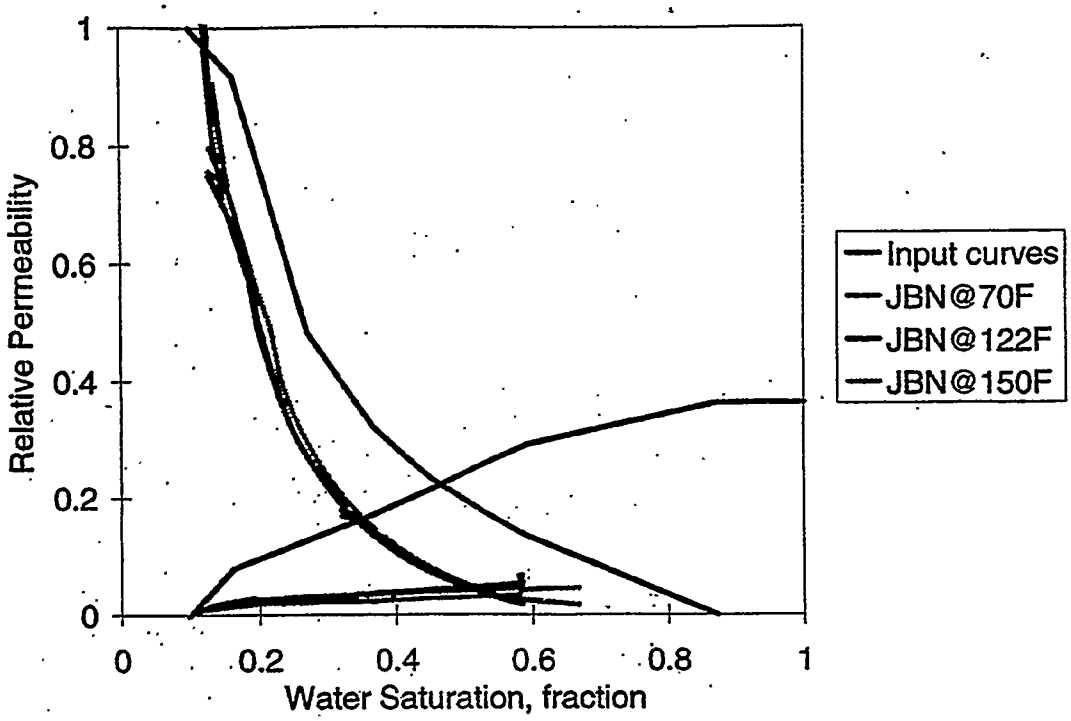

Figure 4. Comparison of JBN Relative Permeability Curves to Input Relative Permeability Data (Initial Water Saturation is 10%).

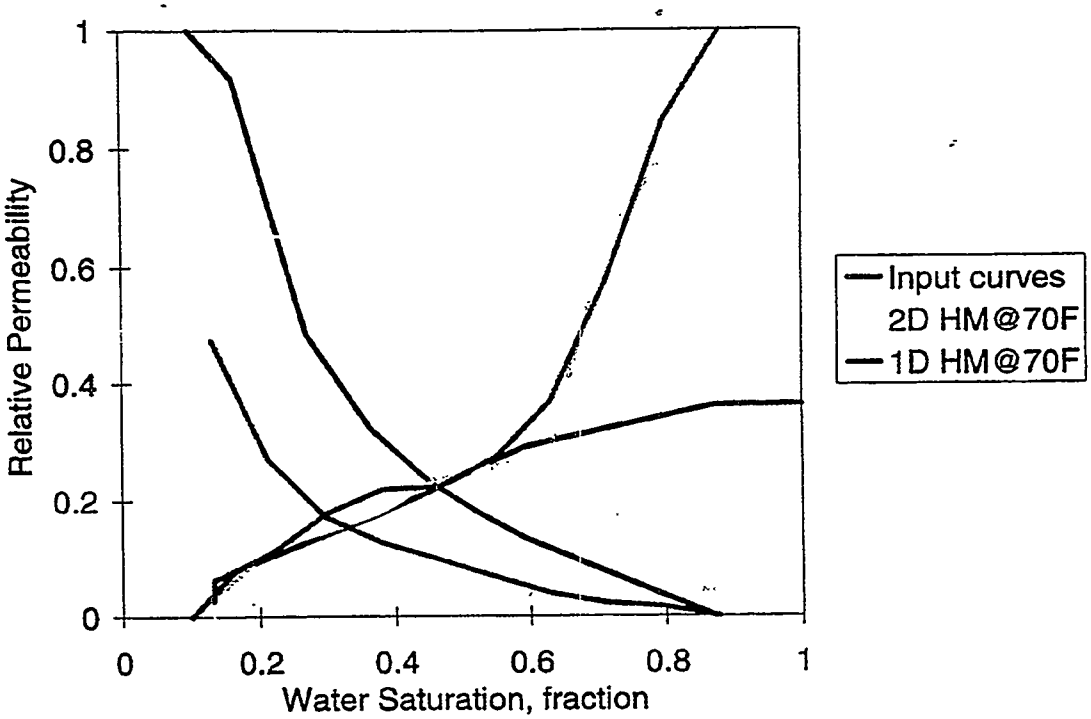

Figure 5. Comparison of 1D and 2D History Matched Relative Permeability Curves to Input Relative Permeability Data (No Initial Water Saturation).

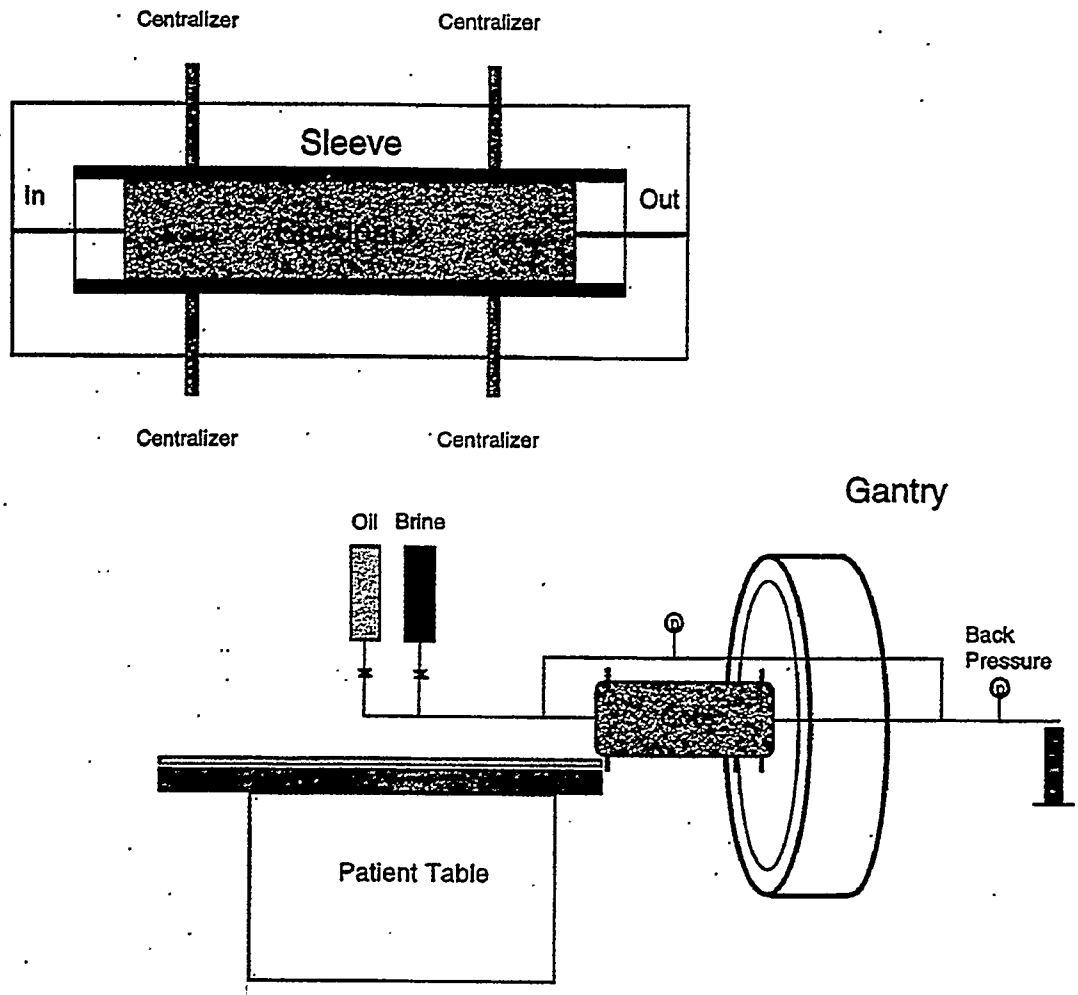

Figure 6. Schematic Diagram of the Experimental Setup.

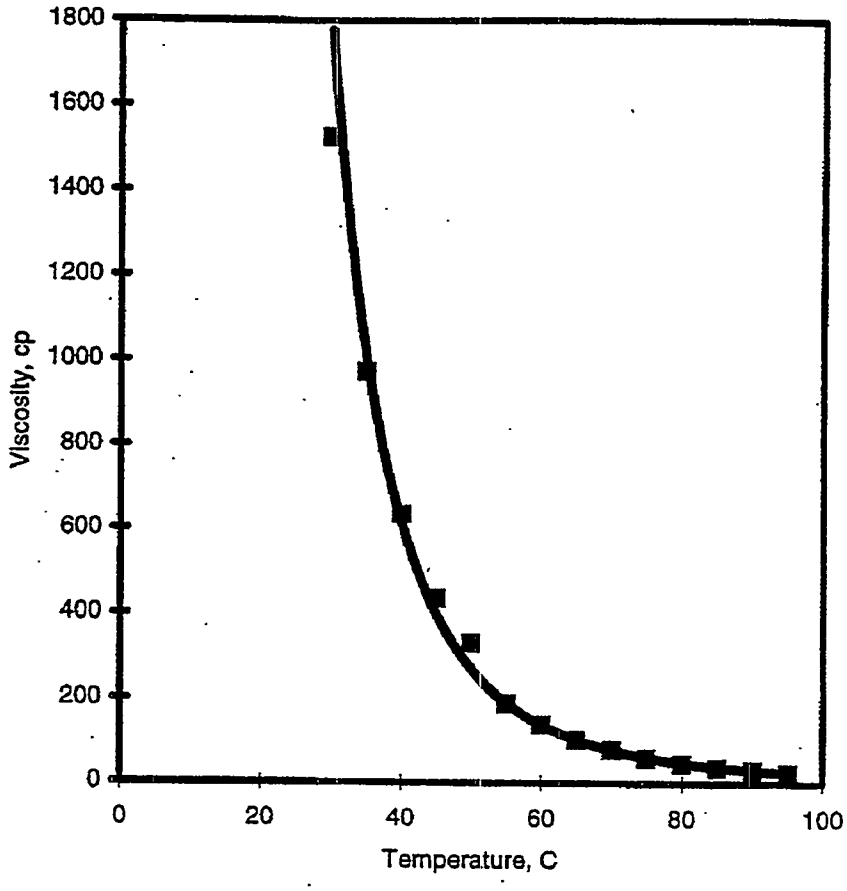

Figure 7. South Belridge Heavy Oil Viscosity Versus Temperature.

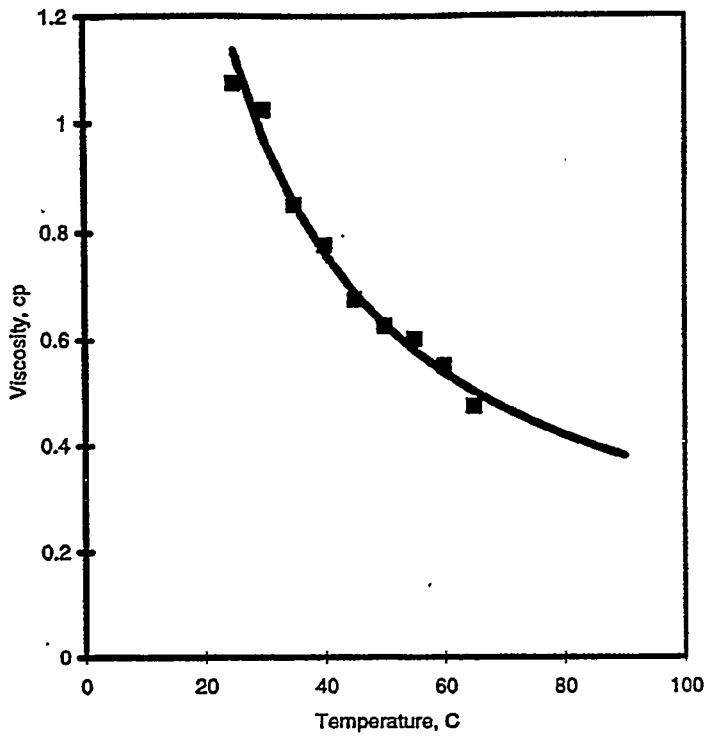

Figure 8. 8% Sodium Bromide Water Viscosity Versus Temperature.

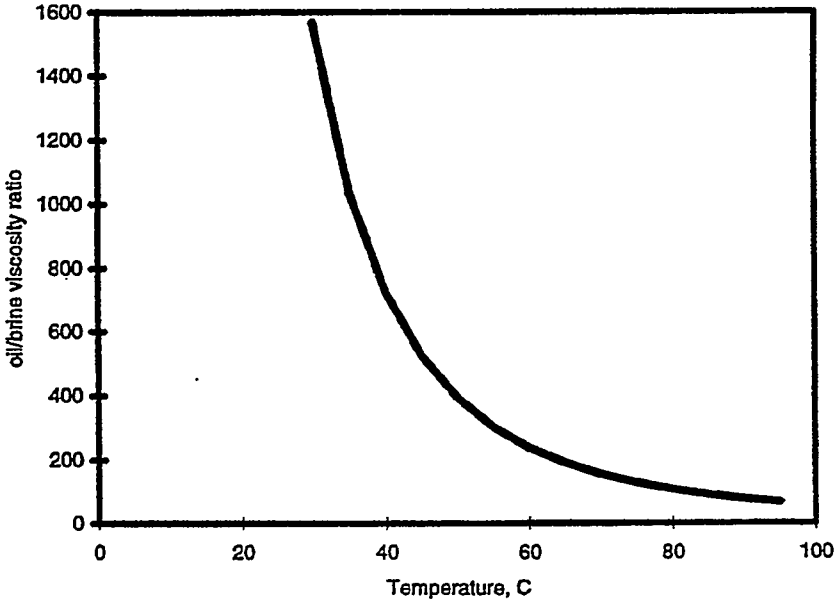

Figure 9. South Belridge Oil - Brine Viscosity Ratio Versus Temperature.

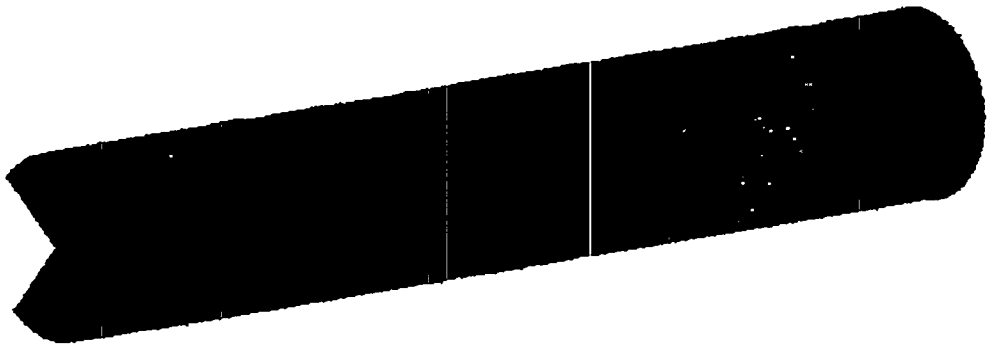

Figure 10. Three Dimensional Reconstruction of Porosity Images in Run 1.

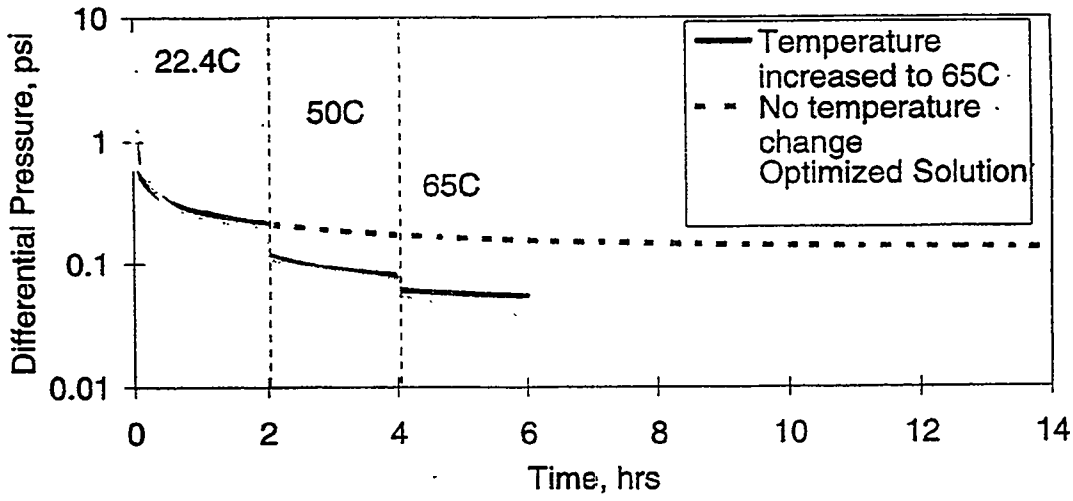

Figure 11. Differential Pressure Fit to Hypothetical "No Temperature Effect" Run.

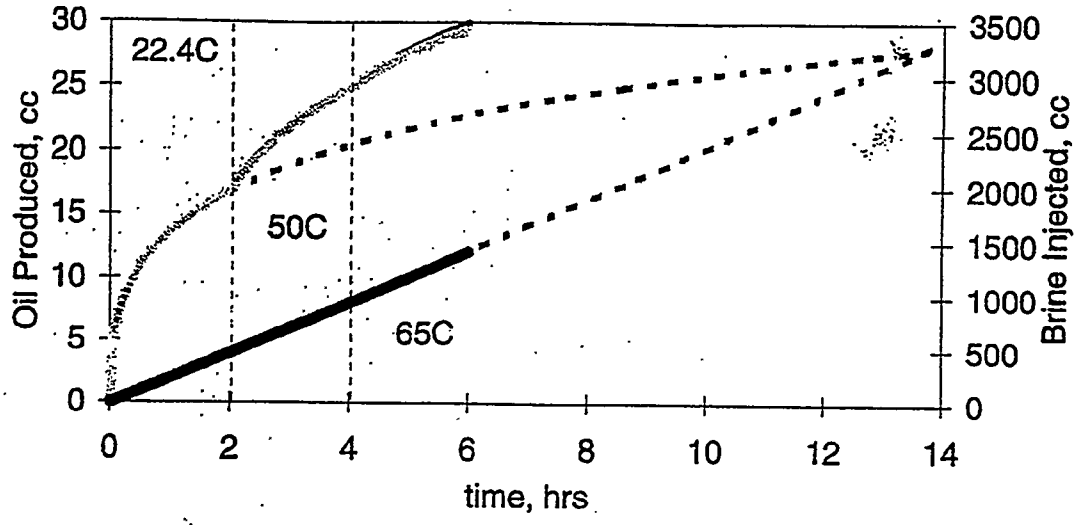

Figure 12. Production Fit to Hypothetical "No Temperature Effect" Run.

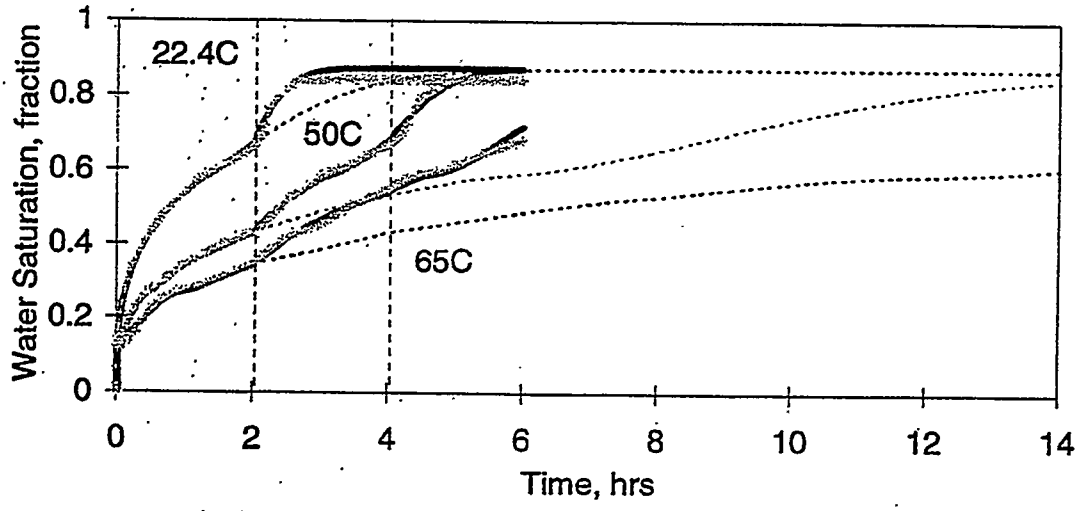

Figure 13. Saturation Fit to Hypothetical "No Temperature Effect" Run.

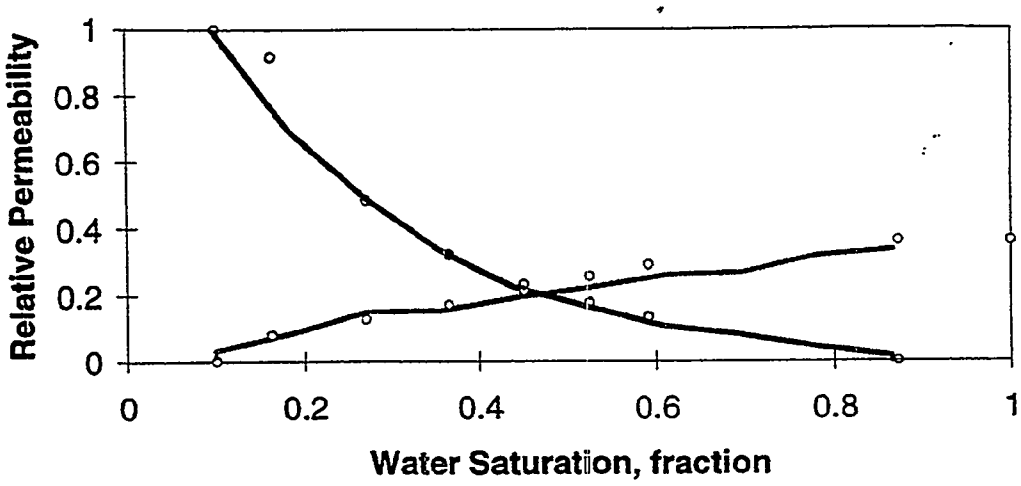

Figure 14. Relative Permeability Fit to Hypothetical "No Temperature Effect" Run.

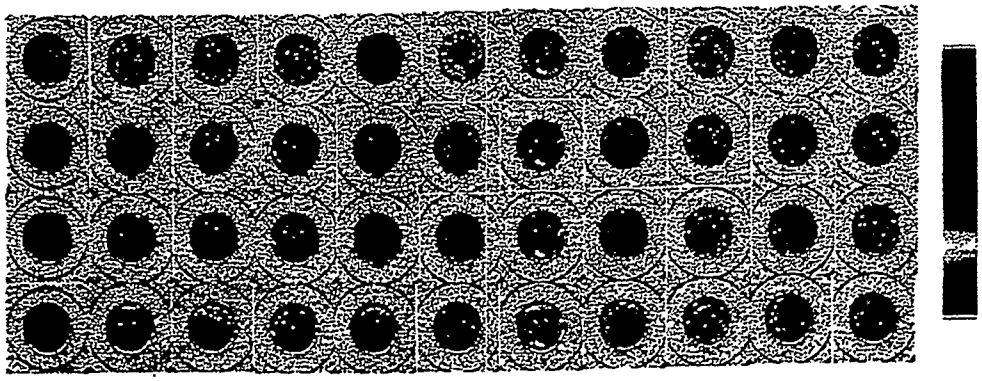

Figure 15. Water Saturation Images in Run 1.

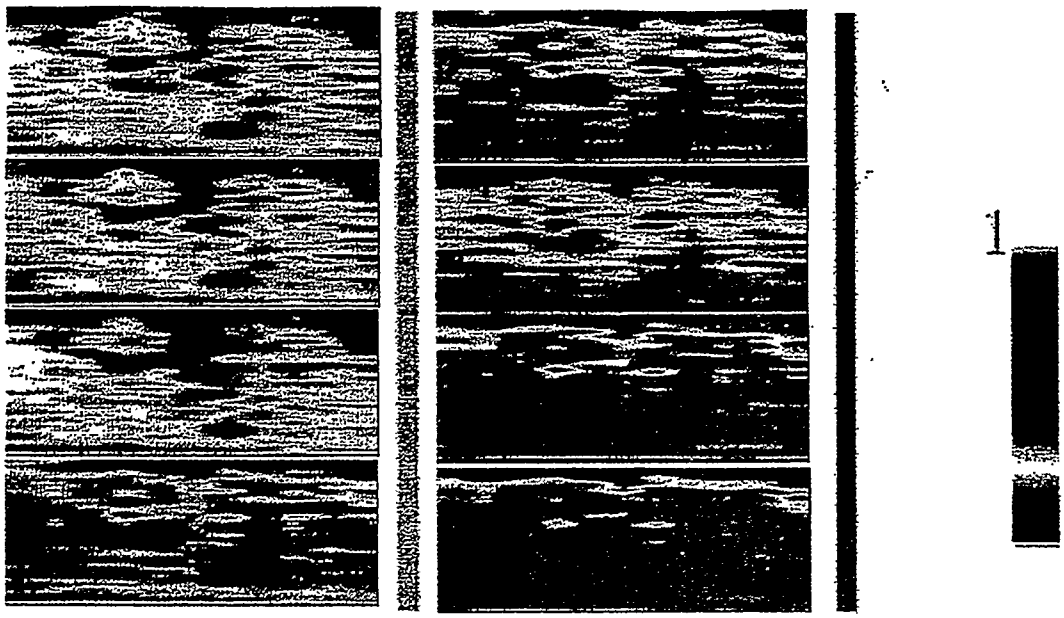

Figure 16. Three Dimensional Water Saturation Images in Run 1.

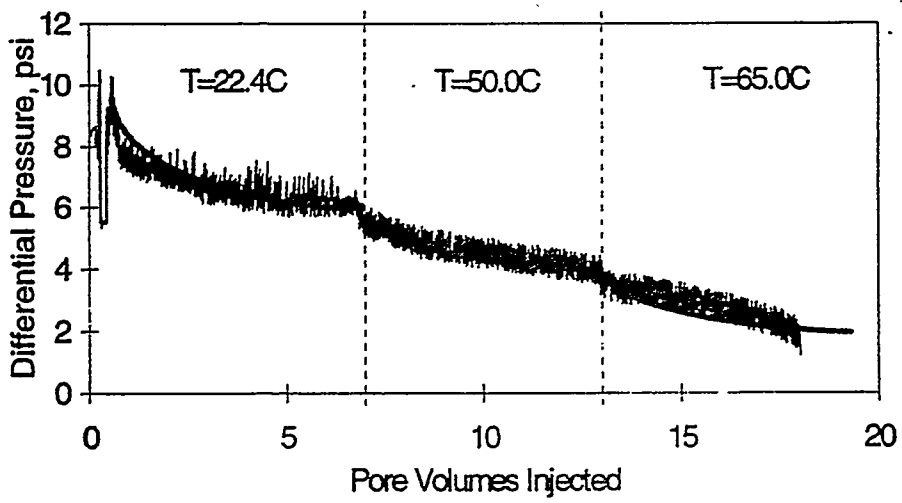

Figure 17. Pressure Fit For Run 1.

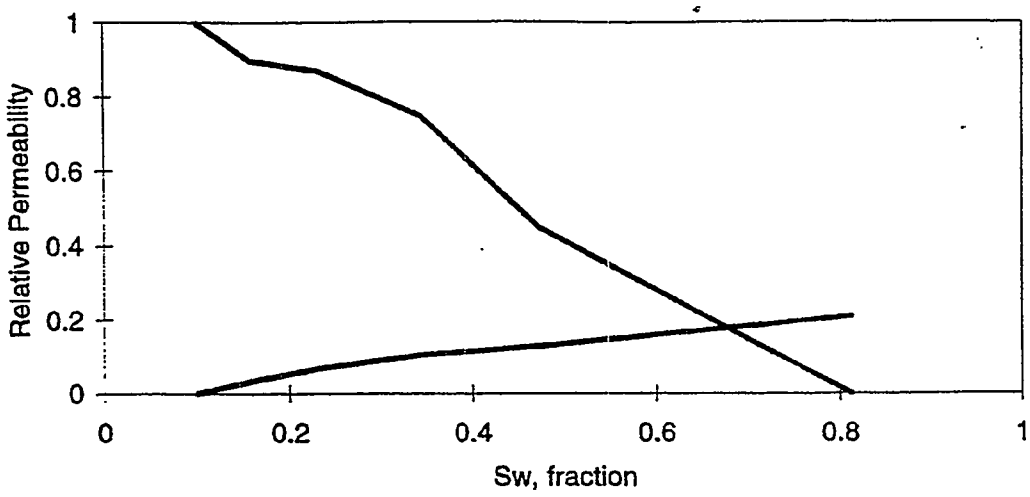

Figure 18. Relative Permeability Curves For Run 1.

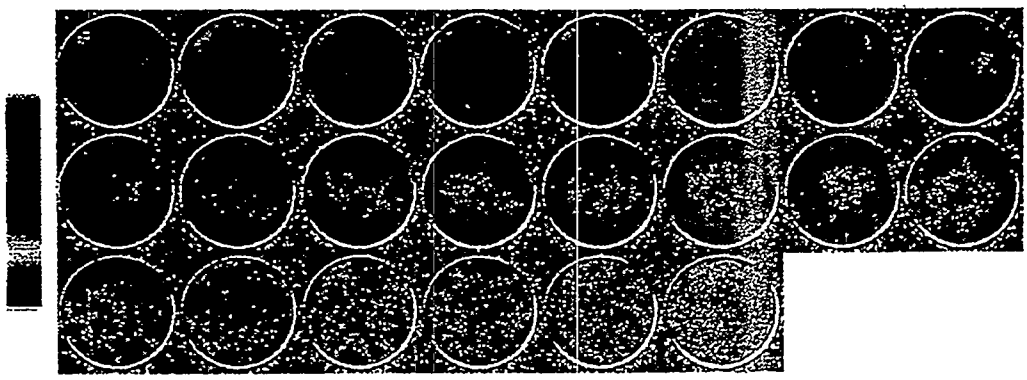

Figure 19. Water Saturation Images in Run 2.

1.2 TWO-PHASE FLOW EXPERIMENTS IN FRACTURED POROUS MEDIA USING CT SCANNER

(E. Rangel-German)

1.2.1 ABSTRACT

The fluid transfer parameters between rock matrix and fracture are not well known. Consequently, simulation of fractured reservoirs uses, in general, very crude and unproved hypotheses such as zero capillary pressure in the fracture and/or relative permeability linear with saturation. In order to improve the understanding of flow in fractured media, an experimental study was conducted and numerical simulation of the experiments were made.

A laboratory flow apparatus was built to obtain data on water-air imbibition and oil-water drainage displacements in horizontal single-fractured block systems. For this purpose, two configurations have been used: a two-block system with a 1mm spacer between the blocks, and a two-block system with no spacer. During the experiments, porosity and saturation measurements along the cores have been made utilizing an X-ray Computerized Tomography (CT) scanner. Saturation images were reconstructed in 3-D to observe how matrix-fracture interactions occurred. Differences on fluid saturations and relative permeabilities caused by changes on fracture width have also been analyzed.

In the case of water-air imbibition, the thin fracture system showed a more stable front and faster breakthrough than the wide fracture system. However, the final water saturation was higher in the blocks near the wide fracture, thus showing that capillary pressure in the narrow fracture has more effect. During oil-water drainage, oil saturations were higher in the blocks near the thin fracture, again showing the effect of fracture capillary pressure. Oil fingering was observed in the wide fracture. Fine grid simulations of the experiments using a commercial reservoir simulator have been started. Relative

permeability and capillary pressure curves will be obtained by history matching the experiments. The preliminary results showed that the assumption of fracture relative permeability equal to phase saturation is incorrect. We found that the processes are both capillary and viscous dominated. The matrix capillary pressure obtained by matching an experiment showed lower values than reported in the literature. However, we have yet to complete the simulation study to be sure of these preliminary conclusions.

1.2.2 INTRODUCTION

Fractured porous media are usually divided into two systems: a matrix system that contains most of the fluid storage, and a fracture system where fluids can flow more easily. Under this assumption, flow equations are written considering that recovery is dominated by the transfer of fluid from the matrix to the high conductivity fractures which are also often entirely responsible for flow between blocks and flow to wells. The purpose of this study is to investigate this problem both experimentally and by numerical simulation.

The flow through fractured media depends on some mechanisms (e.g., imbibition, drainage, snap-off, piston like flow) that can be studied by means of both numerical analysis and experimental work. Although some people have already worked on the problem, no one knows exactly which mechanisms occur and how strongly they affect results. We know that a better understanding of the physical mechanisms and the parameters that influence flow through fractured porous media leads to more accurate results from simulator calculations.

To obtain more data on parameters such as capillary pressure, fracture relative permeabilities and/or saturation distributions, we need further experimental work. Most of the first experimental studies tried to represent single block reservoirs with artificial fractured models where the actual fracture distribution was known.

Detailed measurements of pressure, rate and saturation distribution, as the test were being performed, were recorded and attempts to measure phase distribution inside the fracture were also made using a computerized tomography (CT Scanner). This research resulted in a much better handle on the physical processes that occur when two and three phases flow in a fractured system, compared to previous studies such as Guzman and Aziz (1993) or Hughes (1995).

Our first step was reconstructing an apparatus capable of emulating the functions done by that built by Hughes (1995). Thus, we ran similar experiments using two of the coreholders used by him in order to verify that this new experiment gives proper results. Once the apparatus was tested, we ran multiphase flow experiments using an 8% NaBr brine solution as the wetting phase and decane as the nonwetting. Three stages in each experiment were completed: study of water imbibing into a dry core, decane displacing water in a water saturated core; and, water displacing oil.

1.2.3 LITERATURE REVIEW

Most of the early studies focused on the representation of reservoirs by means of single reservoir blocks. Most of the time these studies have relied on the sparse experimental data in the literature (Mattax and Kyte, 1962; Kleppe and Morse, 1974; Kazemi and Merrill, 1979) to verify their models; however those experiments provided rough approximations of the recovery obtained in the actual reservoirs. Later on, experimental work was focused on understanding of mechanisms that control the flow of fluids in porous media (Horie *et al.* 1988; Firoozabadi and Hauge, 1990; Labastie, 1990; Firoozabadi and Markeset, 1992). Hughes (1995) discusses these experiments in detail. From the most recent experiments, we can see that most of them lack an explicit saturation distribution, since its accurate measurement has been one of the biggest difficulties in these kinds of studies. Some of the experimental studies focused on the mechanisms dominant in gravity drainage situations and in small block imbibition

displacements, whereas others have emphasized understanding flow through a single fracture with no transfer from the matrix.

In general, several authors (Kazemi and Merrill, 1979), Beckner (1990), Gilman *et al.*, 1994) have assumed that fracture capillary pressures are negligible. Other have shown experimentally capillary continuity becomes important when gravity provides a driving force (Horie *et al.*, 1988; Firoozabadi and Hauge, 1990; Labastie, 1990; Firoozabadi and Markeset, 1992a, 1992b). Kazemi (1990) states his belief that capillary continuity is prevalent in the vertical direction and has suggested that, to reduce the number of equations to solve, fractured reservoir simulations should use the dual permeability formulation for the z direction and the dual porosity formulation for the x and y directions.

1.2.4 REVIEW OF PREVIOUS STANFORD RESULTS

Two of the previous studies are worth mentioning. The first one was a study initiated by Guzman and Aziz (1993), in which an experiment was designed that intended to measure saturation distribution in two cores of identical material, with the final objective of measuring fracture relative permeabilities. Saturations would be measured by means of a CT scanner. Fine grid simulations were performed to help in the design of the experimental procedure. The experiment was built, but problems at the very beginning did not allow them to obtain results. The second one was developed by Hughes (1995). He redesigned Guzman and Azizís experimental set-up, improving most of their experiment by building a new apparatus and obtaining some results on water imbibition into a dry system of two fractured blocks. Three core configurations were constructed. The configurations were a compact core, a two-block system with a 1mm spacer between the blocks, and a two-block system with no spacer. The blocks were sealed in epoxy so that saturation measurements could be made throughout the displacement experiments using a CT Scanner. Hughes presented results from a water/air experiment; however, he only presented CT images. These results

suggest that it is incorrect to assume negligible capillary continuity between matrix blocks as is often done.

Hughes (1995) evaluated how water imbibed into an unsaturated core. Migration of the water was monitored with the CT scanner. Despite the fact that water was being injected only into the bottom block, capillary imbibition pulled the water across the discontinuity and through the top block such that water from the top block actually broke through before the bottom block.

Three rectangular blocks of Boise sandstone were prepared for this work. The first is a compact (solid) core measuring 3-1/8 x 3-1/16 x 11 inches. The second and third cores consist of two 2-15/16 x 1-1/2 x 11 inch blocks. The second core system has a 1 mm thick spacer fastened in place with Epoxy 907 to provide a separation between the blocks that simulates a fracture. The third core system is constructed similarly but has no spacer between the blocks. The original design of Hughes had two pressure taps on the top and two on the bottom. In addition, a Plexiglas plate that was epoxied to the top surface of the core was removed in the new design. The plate was found to be unnecessary and a potential source for leaks.

1.2.5 EXPERIMENTAL DESIGN

Due to the rectangular shape and the desire to measure in-situ saturations through the use of the CT scanner, conventional core holders could not be used. A core holder similar to the original designed by Guzman and Aziz (1993) was developed for each of the cores used in Hughesí experiments. It consists of an epoxy resin surrounding the core. Plexiglas end plates were constructed for the core holders with a piece of 3/8 inch Viton acting as a gasket between the core and the Plexiglas end plates. The Viton gaskets were held in place with automotive gasket material and Plexiglas rods. In Hughesí experiments (1995), the Viton was cut for each end face of the core holder, cutting a hole in the Viton so that the core face would be exposed; however following this procedure caused problems in those experiments. The water injected first dribbled down in the space

in between the Plexiglas end plate and the rock (the hole previously cut in the Viton.) To avoid this problem, some material that could fill this space and could guarantee that the injected fluids were in contact with the whole surface at the same time as well was needed. Thus, four sheets of filter paper having all together the same thickness as the Viton, were used. The same automotive gasket material was then used to glue the Viton to the epoxy and the Viton to the Plexiglas end plates as shown in Fig. 1.

Two pumps were calibrated and used. Each calibration curve for these pumps are given in Figs. 2 and 3. Each pump could deliver 0.01 to 9.99 cm^3/min in 0.01 increments. Plumbing downstream of the pumps allows mixing of the fluids being discharged by each pump. This setup allows injection pressure to be monitored with a test gauge and recirculation to measure pump output rates.

All tubing used for the experiment was Paraflex 1/8 inch diameter, with 500 psi working pressure plastic tubing connected with stainless steel Swagelok fittings. This system allows fluids to be directed to any port or combination of ports in the experiment such that, (1) It can be directed to test the calibration of the pressure transducers, (2) inject from one end and produce from the opposite end, (3) inject into one or more if the ports on the top and bottom of the core holder, or (4) to bypass the core holder completely. Figure 4 shows the flow system utilized for this work.

The production measurement system is an adaptation of a design first proposed by engineers at Conoco, Inc that was built by Ameri and Wang (1985) and modified by Qadeer (1994). Figure 5 shows this system.

The tubing labeled with 'from Core outlet' in Fig. 5 carries oil and water from the core. The oil is separated due to density differences and held inside a confining cap in an inner vessel which is suspended from an electronic balance. Water over flows through siphon and is collected in a container (e.g., a beaker) which is on other balance.

The electronic balance attached to the inner vessel measures the bouyant weight of the vessel. The change on the weight corresponds to the variation of total oil accumulated inside the inner vessel. These changes on the cumulative production of oil and water are the oil and water production rates. These rates should be equal to the injection rates when steady state conditions are reached.

The electronic balances are connected to a serial communication ports of a personal computer (PC) that recorded all the signals coming from their measurements.

1.2.6 EXPERIMENTAL PROCEDURE

The first core used had a fracture with no space in between the blocks. Due to the length of this core (11 inches), and despite the stainless steel fittings that were used for the ports on the top and the bottom of the coreholder, it was decided to choose a regular sequence of scan locations. This was because even when the fitting ports could be avoided it was found that both the previous and the next slices had some artifacts because of the stainless steel fittings, so it was better to find a distribution in which we could scan exactly at those locations and reduce the effects on the previous and next slices as well.

Thus, it was decided to fix the scan location every 2 cm starting from the first two centimeters from the inlet face since any location at less distance could have either effects from the injection stainless steel fitting port or scan the Viton gasket and filter paper.

The total travel distance of the positioning system was then 25.5 cm, resulting in 13 slices including those two located at the fitting ports (fourth and eleventh, for the first experiment; and fourth and tenth, for the second one.) Figure 6 shows the CT scan locations.

To assure the same locations for the next stages of the experiment, the patient table of the CT Scanner was fixed at a proper location, so the positioning system (accuracy $\pm$ 0.01mm) would do the rest of the locating process. This provided more accurate results for the porosity and saturation calculations. This was a major improvement compared to Hughes (1995) experiments, since he was using the patient table whose accuracy is $\pm$ 1 mm .

The field of view used for this experiment was 24 cm, the image matrix, resolution, voltage, amperage, filter used, and more scanner settings are shown in Table

1. The first step of this experiment was to scan the dry core. This step was very important to verify that the apparatus and all the set-up was working properly. For instance, we could notice some problems with the coreholder in a first trial for the dry scan. We could not keep its position horizontal, because it was quite heavy and held only by one of the sides. Moreover, the gasket makes it harder to hold since it was not rigid. In order to solve this problem, two C clamps were used to strengthen the attachment to positioning system to keep the coreholder in the same position (horizontal) during the experiment. After these improvements, the dry scans were done successfully.

Table 1. CT Scanner Settings

Parameter	Setting
Field of View	24 cm
Image Matrix	512 x 512
Sampling	1024
Scan Speed	3 sec
Slice Thickness	10 mm
Resolution	High
kV	140
mA	65
x-ray filter	3
MAS	341 per slice
Exposure	5.09 sec/slice
Pilot	0.00 sec

The second step was to evaluate how water imbibed into an unsaturated core. This part of the experiment gave us results that can be compared with the ones obtained by Hughes (1995), and eventually used to evaluate how well the new experiment worked. Starting with a flow rate of 2 cm^3/min, CT images of the core were taken every 5 minutes until the first 20 minutes of water injection; after this, images were taken at 30 min, 45 min, 1 hr., 1hr 30 min, 2 hr, 3 hr, and 4 hours after water injection started. Following that the top and bottom ports were opened since we wanted to fill up the core to the maximum water saturation (Sw = 1). Common to all time steps, we tried to take images up to one location ahead of the possible water front.

After 5 hours of water injection, the flow rate was changed to 0.5 cm^3/min in order to inject water for 14 more hours to reach higher possible water saturations. After 19 hours, a new set of slices were taken. Then, at 19 hours and 45 min the water rate was changed back to 2 cm^3/min, and the top and bottom ports were closed. At 21 hours a final set of slices was taken to find a possible change in CT numbers. Negligible changes in CT numbers were observed. At 23 hours of water injection, the third step of the experiment started.

The third step of the experiment involved injecting Decane at 2 cm^3/min. The scanning frequency was intended to be the same as the water injection process. Thus, images of the core were taken every five minutes until the first 20 minutes of oil injection; after that, more images were taken at 30 min, 45 min, 1 hr., 1hr 30 min, 2 hr 30 min, and 3 hr 45 min. after oil injection started. Then, the top and bottom ports were opened at 4 hours of starting oil injection since we wanted to fill the core up to the maximum possible point. At 4 hr 30 min of oil injection, one more set of images was taken. After 5 hours of oil injection, the flow rate was changed to 1 cm^3/min for 16 hours to reach higher possible oil saturations (S_{wc}). After 21 hours of oil injection, a new set of slices was taken, and the ports were closed. Then, at 21 hours and 39 min the oil injection was stopped, and water injection at the maximum pump rate (9.99 cm^3/min) was started.

The fourth step of the experiment was the water displacing oil stage. Injecting 9.99 cm^3/min of water, images were taken at 5 min, 15 min, and 30 min. At 1hr 10 min, water injection was stopped, the inlet and outlet lateral ports were also closed, leaving all

of the coreholders' ports closed. One more set of images was taken after two days of closing the coreholder to observe if capillary equilibrium had been reached. Table 2 summarizes the flow rates used and the timing of each of them.

The second experiment was done using the coreholder that contained a system with two blocks with a 1 mm thick fracture in between. The same experimental procedure was followed. Essentially, we wanted to obtain CT images, and then saturation values for equivalent times, so we could eventually compare the differences between the two systems. The rates and timing for the case of two blocks with a wider fracture are shown in Table 3.

1.2.7 METHOD OF SOLUTION

The most common way to calculate porosity from CT Scanner images is the following expression (Withjack, 1988):

$$\phi = \frac{CT_{cw} - CT_{cd}}{CT_w - CT_a} \tag{1}$$

where CT_{cw} is the CT number for a water saturated core at a matrix location, CT_{cd} is the CT number for a dry core at a matrix location, CT_w is the CT number for water, and CT_a is the CT number for air. The CT number for water (8%NaBr solution, for this work) is around 360, while the CT number for air is -1000.

We found that the average value for porosity calculated from the scans was 15% which matches with the average value 14.35% reported by Hughes (1995); however, this value differs from the average porosity measurements of 25.4% obtained by Guzman and Aziz (1993) and 29.3% obtained by Sumnu (1995). All of these previous studies have also shown areas in the rocks which have lower permeability.

Table 2. Rates and Timing for the Coré with Thin Fracture

Fluid Injected	Time [hr.]	Flow Rate [cm^3/min]	Ports
Water	0.0 - 4.0	2.0	Top and bottom closed, lateral open.
Water	4.0 - 5.0	2.0	Top and bottom open, lateral closed.
Water	5.0 - 19.8	0.5	Top and bottom open, lateral closed.
Water	19.8 - 23.0	2.0	Top and bottom closed, lateral open..
Decane	23.0 - 27.0	2.0	Top and bottom closed, lateral open.
Decane	27.0 - 28.0	2.0	Top and bottom open, lateral closed.
Decane	28.0 - 44.7	1.0	Top and bottom open, lateral closed.
Water	44.7 - 46.0	9.99	Top and bottom closed, lateral open.
	46		Shut down everything

Table 3. Rates and Timing for the Core with Wider Fracture

Fluid Injected	Time [hr.]	Flow Rate [cm^3/min]	Ports
Water	0.0 - 5.0	2.0	Top and bottom closed, lateral open.
	5.0 - 21.0	0.0	Top and bottom closed, lateral closed.
Water	21.0 - 22.5	2.0	Top and bottom open, lateral closed.
Water	22.5 - 25.6	2.0	Top open, bottom closed, and lateral closed..
	25.6 - 45.0	0.0	Top and bottom closed, lateral closed.
Decane	45.0 - 48.0	2.0	Top and bottom closed, lateral open.
Decane	48.0 - 49.2	4.0	Top and bottom closed, lateral open.
Decane	49.2 - 51.0	4.0	Top and bottom open, lateral closed.
	51.0 - 52.0	0.0	Top and bottom closed, lateral closed.
Water	52.0 - 54.3	4.0	Top and bottom closed, lateral open.
Water	54.3 - 68.8	0.5	Top and bottom closed, lateral open.
Water	68.8 - 71.0	4.0	Top and bottom open, lateral closed.
	71		Shut down everything

The water and oil saturations were also calculated from the CT images. The following equations show the way to evaluate water saturation for the air displacing air case, and for the case oil displacing water or water displacing oil.

$$Sw = \frac{CT_{aw} - CT_{cd}}{CT_{cw} - CT_{cd}} \tag{2}$$

where CT_{aw} is the CT number for a water and air saturated core at a matrix location. Similarly, for the case of oil-water systems

$$Sw = \frac{CT_{ow} - CT_{cw}}{\phi\,(CT_o - CT_w)} \tag{3}$$

where CT_{ow} is the CT number for a water and oil saturated core at a matrix location, and CT_o is the CT number for oil. The CT number for oil (decane, for this work) is around -272.

All the saturation values are shown in the following section, as well as the way to read them in the corresponding figures.

1.2.8 RESULTS

Guzman and Aziz (1993) presented a CT image from which it can be seen that CT numbers can indicate differences in fluid saturations Later on, Hughes (1995) presented images showing how water imbibes into an unsaturated core. As we stated previously, his coreholder contained a gap between the core and the Plexiglas plate, so the CT images show the water going down, filling first the gap and then imbibing the core. It can be easily concluded, that his results showed the water imbibing first the bottom block. After some time water filled the gap, but it was late because the water had imbibed a good portion of the bottom block, and finally much time had passed before water reach the fracture level. Hughesí (1995) results are good in the sense that he

conducted a reasonably controlled experiment, he showed that CT images for different times could be obtained, and that his shortcuts could be improved. Thus, his results started the motivation for this work; considering the development of more sophisticated software as well as better computers, we thought experiments like those presented in this work could be done. Improving previous designs, following carefully the procedure planned and trying to obtain the data as accurately as possible, we would be able to complete a multiphase flow experiment in fractured porous media. We also could obtain images of theporosity distribution, as well as the saturation images.

The following sections present a set of images, each square shows a scan location, with the distribution shown in Fig. 6. First of all, we computed the values of porosity at each location, so we could obtain the best approximation of the porosity distribution of the two systems. The different porosity images for both systems are shown in Fig. 7, the values below each square correspond to the mean and the standard deviation respectively of the porosity values obtained from CT numbers. This step was essential for both experiments because from these images and their corresponding values we could differentiate the regions with higher or lower porosity. Thus, in those images, the range of values are shown in the color bar in the right hand side in Fig. 7. There, we can also see that the system with the thin fracture has a little higher porosity than the system with the wide fracture, specially in the top block, where values up to 0.13 were observed.

1.2.8.1 Results for the Thin Fracture System

Following the procedure explained above, and the flow rates, times and injection/production conditions shown in Table 1, we ran the first experiment. Figures 8, 9 and 10 show the sets of images corresponding to 1 hour, 1.5 hours, and 2 hours of water injection. Similarly as the porosity images, each square correspond to one location, but now the water saturation distributions are shown. The pairs of values presented below each square correspond to the mean and standard deviation (separated by commas) of the

top, bottom and both blocks respectively. Colors for each saturation value were also assigned. The color bar on the right hand side show the range of values and their corresponding lightness or darkness. In all the images shown in Figs. 8-10, darker shades indicate lower water saturation. For instance, black means zero water saturation, and white means water saturation equal to 1. Those figures also include plots of the water saturation profiles. The left hand side ones correspond to the average values (the last mean of each square); and the right hand side ones, correspond to the values of the top and bottom blocks (first and second means of each square respectively). Different profiles, corresponding to different pore volumes of water injected are shown in Fig. 11. There we can see that the profiles are stable and they appear to follow Buckley-Leveret theory.

Similar images were obtained for the second stage of the first experiment (oil injection). Figures 12 and 13 show sets of images corresponding to 2.5 hours and 3.75 hours of oil injection. Here, the pairs of values below each square indicate the mean and the standard deviation of oil saturations, respectively. Colors were also assigned to the oil saturation values; thus, the color bar on the right hand side show the range of values and their corresponding lightness or darkness. In all the images shown in Figs. 12 and 13, darker shades indicate lower oil saturation. For instance, black means zero oil saturation. Figure 14 shows oil saturation profiles for different times. There, one can see some special behavior up to 3.75 hours; however, we could not follow it because we opened the lateral ports of the coreholder at 4 hours in order to fill up the core at the maximum possible point (Sw =1.)

Images for the third stage of the experiment (water displacing oil) were also obtained; however, due to problems with one of the pumps, we could not analyze properly the rest of the data.

1.2.8.2 Results for the Wide Fracture System

Following the procedure explained above, and the flow rates, times and injection/production conditions shown in Table 2, we ran the second experiment.

Figures 15-17 show the sets of images corresponding to 1 hour, 1.5 hours, and 2 hours of water injection for the wider fracture system. Similarly as the images obtained in the case for thin fracture system, each square corresponds to one location, and also the water saturation distributions are shown. The pairs of values presented below each square also correspond to the mean and standard deviation (separated by commas) of the top, bottom and both blocks respectively. In all the images shown in Figs. 15-17 darker shades indicate lower water saturation. For instance, black means zero water saturation, and white means water saturation equal to 1. Different profiles, corresponding to different pore volumes injected are shown in Fig. 18. There we can see that the profiles are less stable than those for the thin fracture system.

Figures 19 and 20 show sets of images corresponding to 2.5 hours and 3.75 hours of the second stage of the second experiment (oil injection). Similar to the sets of images of oil injection of the first experiment, the pairs of values below each square indicate the mean and the standard deviation of oil saturations, respectively. Colors were also assigned to the oil saturation values. In all the images shown in Figs. 19 and 20 darker shades indicate lower oil saturation. For instance, black means zero oil saturation. Figure 21 shows the profiles for different times. Nothing special can be seen due to some leaks during this stage. Although, we could observe very low saturation values in zones far from the leaking point.

Images for the third stage of the second experiment (water displacing oil) were also obtained. The most interesting sets are shown in Figs. 22 and 23, where one can see how the displacement of oil is completed almost perfectly. Some oil is in the core at 16 hours, and after 17 hours of water injection the oil is totally swept from the core. See the differences between Figs. 22 and 23.

1.2.8.3 Comparison of the Results for Both Systems

Due to the fact that the experiments ended in different ways, we were able to compare the results up to the second stage of both experiment. This section show graphically how they can be compared.

Three-dimensional (3-D) reconstructions of the sets of images were done. These 3-D images show more clearly how the fluids actually flow through fractured porous media. This work was intended to show the differences in the flow patterns for different fractures thicknesses. The reconstructed images are shown in Figs. 24- 27. Each image corresponds to a specific time; thus, the first image of Fig. 24 is compared to the first one of Fig. 26, the second image of Fig. 24 was done for the same time as the second image on Fig. 26, and so on. There, we can see how the water front for the wider fracture system goes almost at the same speed as the water front for the thinner fracture system does for the same time. For instance, one can see that after 1.5 hours of water injection, the water front of the thin fracture system seems to be ahead of the front for the wide fracture system; however, after two hours of water injection water has filled up both systems.

Similarly, 3-D reconstructions for the second stage (oil injection) were done. Since the oil saturations were low for both cases, it is a bit harder to see the differences; however, it is possible to see that the thinner fracture system had higher oil saturation close to the fracture. This is shown in Figs. 28 and 29. One can see that the thin fracture system had lighter colors close to the injection surface. We can also see that for the case of a wide fracture system, the oil do not penetrate; furthermore, it flows almost completely through the fracture; this is shown in Fig. 29 by the almost white horizontal line, which correspond to the fracture. Remember that for the case of oil injection stages, darker means lower oil saturation.

1.2.9 PRELIMINARY CONCLUSIONS

The results of the experiments we made in this work showed that:

a. Using this apparatus as well as the procedure explained here, one can identify areas with lower permeability and porosity.
b. Thin fracture systems show more stable fronts and faster breakthrough than wide fracture systems.

c. Capillary pressure has more effect in thin fractures.

d. Multiphase flow through the fracture was observed.

e. Larger recoveries can be obtained when the fracture are wider.

1.2.10 FUTURE WORK

Fine grid simulations of the experiments using a commercial reservoir simulator have been started. Relative permeabilities and capillary pressure curves will obtained by history matching the experiments.

After the simulation work is done we will try to obtain complete conclusions on mutiphase flow in fractured porous media. This will allow us to establish a procedure for looking at both the transmissibilities and the transfer terms that appear on the flow equations for any reservoir simulator.

1.2.11 REFERENCES

1. Beckner, B.L.: "Improved Modeling of Imbibition Matrix/Fracture Fluid Transfer in Double Porosity Simulators," PhD dissertation, Stanford University (July 1990).
2. Firoozabadi, A. and Hauge, J.: "Capillary Pressure in Fractured Porous Media," *JPT* (June 1990) 784-791.
3. Firoozabadi, A. and Markeset, T.: "An Experimental Study of Capillary and Gravity Crossflow in Fractured Porous Media," SPE 24918, presented at the 67th SPE Annual Technical Conference and Exhibition, Washington, D.C. (October 4-7, 1992).
4. Firoozabadi, A. and Markeset, T.: "An Experimental Study of Gas-Liquid Transmissibility in Fractured Porous Media," SPE 24919, presented at th 67th SPE Annual Technical Conference and Exhibition, Washington, D.C. (October 4-7, 1992).

5. Gilman, J.R., Bowzer, J.L. and Rothkopf, B.W.: "Application of Short-Radius Horizontal Boreholes in the Naturally Fractured Yates Field," SPE 28568, presented at the 69th SPE Annual Technical Conference and Exhibition, New Orleans, LA (September 25-28, 1994).
6. Guzman, R.E. and Aziz, K.: "Design and Construction of an Experiment For Two-Phase Flow in Fracuted Porous Media," SUPRI TR-95, Stanford Petroleum Research Institute, Stanford, CA (June 1993).
7. Horie, T., Firoozabadi, A. and Ishimoto, K.: "Capillary Continuity in Fractured Reservoirs," SPE 18282, presented at the 63rd SPE Annual Technical Conference and Exhibition, Houston, TX (October 2-5, 1988).
8. Hughes, R.G.: "CT Measurements of Two-Phase Flow in Fractured Porous Media," Masters Report, Stanford University (December 1995).
9. Kazemi, H. and Merrill, L.S.: "Numerical Simulation of Water Imbition in Fractured Cores," *SPEJ* (June 1979) 175-182.
10. Kazemi, H.: "Naturally Fractured Reservoirs," Third International Forum on Reservoir Simulation, Baden, Austria (1990).
11. Kleppe, J. and Morse, R.A.: "Oil Production from Fractured Reservoirs by Water Displacement," SPE 5084 presented at the 49th Annual Meeting of the Society of Petroleum Engineers, Houston, TX (October 6-9, 1974).
12. Labastie, A.: "Imbibition Oil Recovery from Fractured, Water-Drive Reservoir," *SPEJ* (June 1962), 177-184.
14. Operator's Guide, Synerview 600s/1200SX, C85:f, REV1, Picker International (January 1983).
15. Qadeer, S.: "Techniques to Handle Limitations in Dynamic Relative Permeability Measurements," PhD dissertation, Stanford University (to be completed).
16. Withjack, E.M: "Computed Tomography for Rock-Property Determination and Fluid-Flow Visualization," *SPEFE* (December, 1988) 696-704.

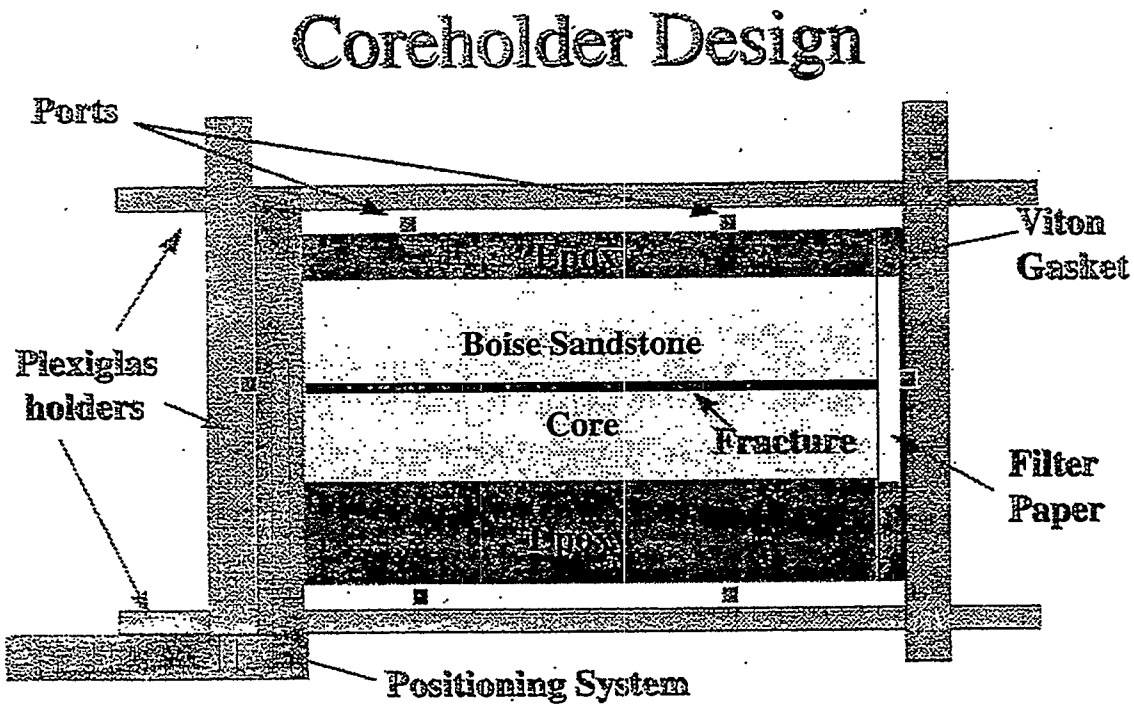

Figure 1. The core holder.

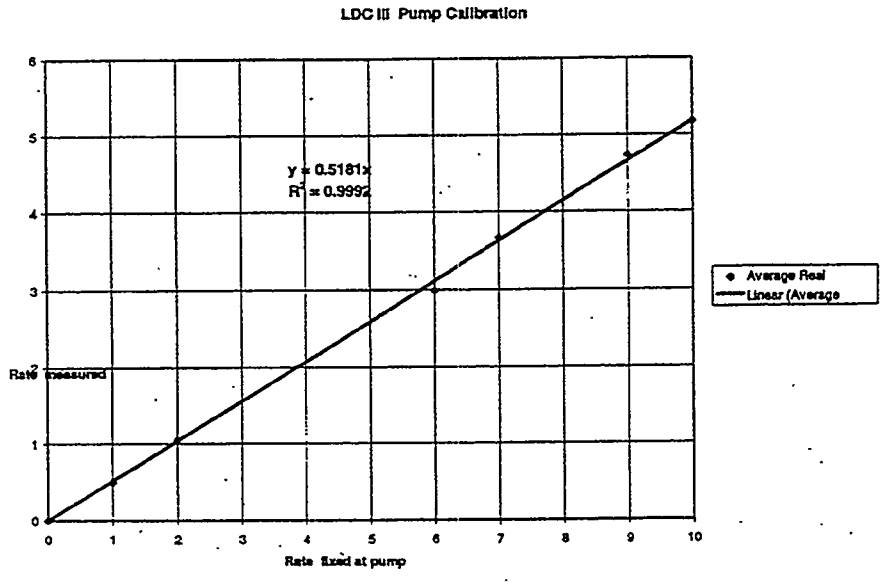

Figure 2. LDC III Pump Calibration Curve.

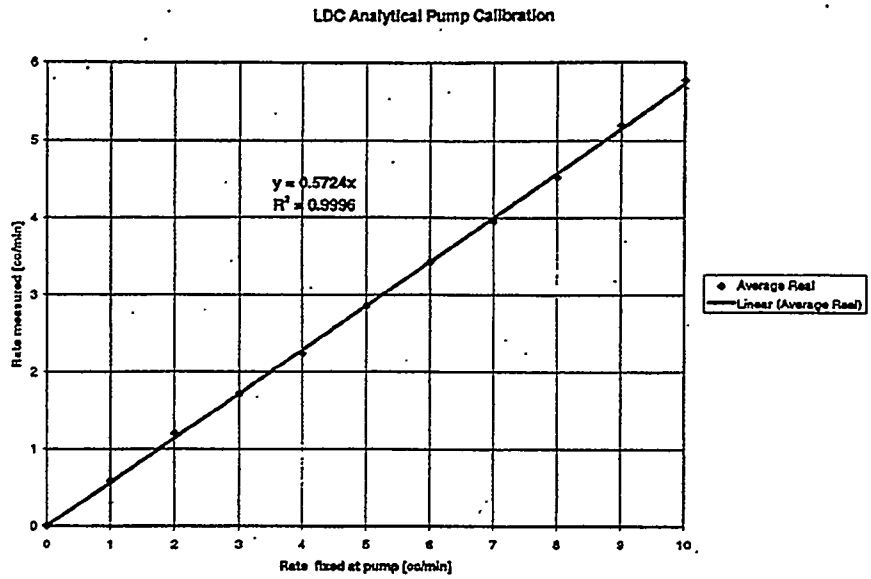

Figure 3. LDC Analytical Pump Calibration Curve.

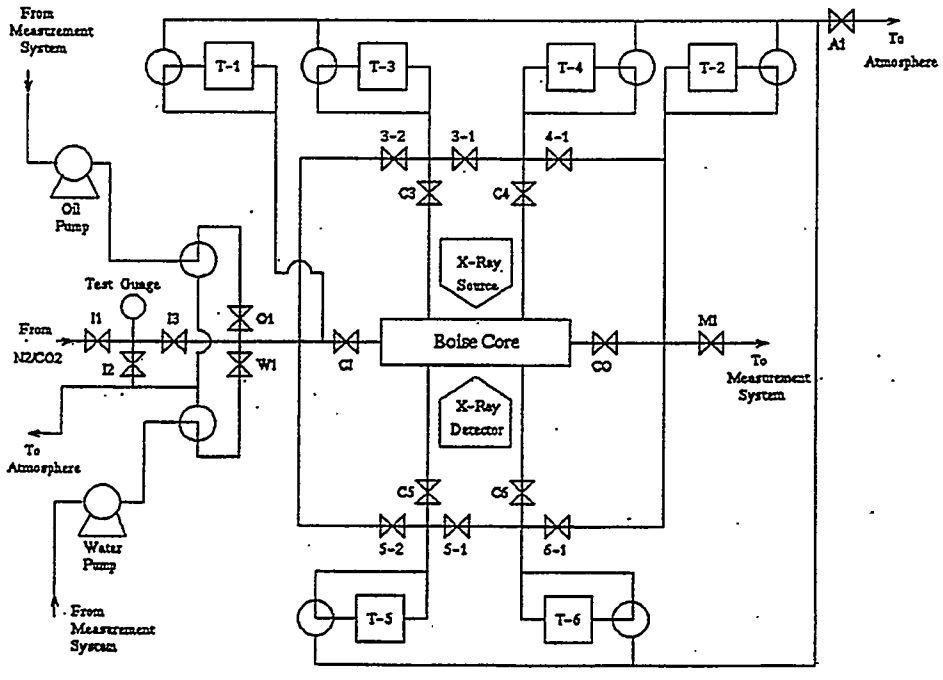

Figure 4. Flow System (Hughes, 1995.)

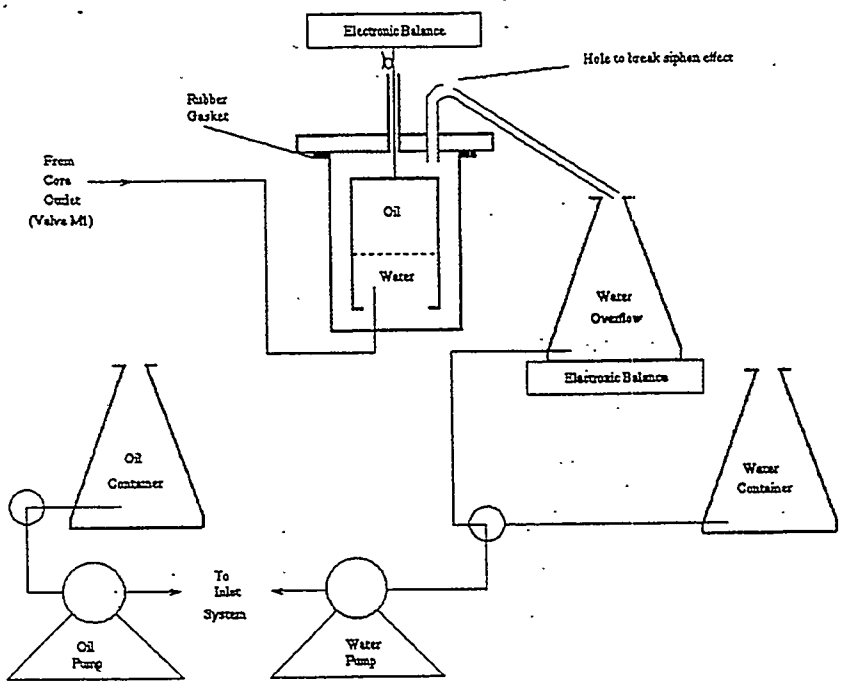

Figure 5. Production System (After Hughes, 1995)

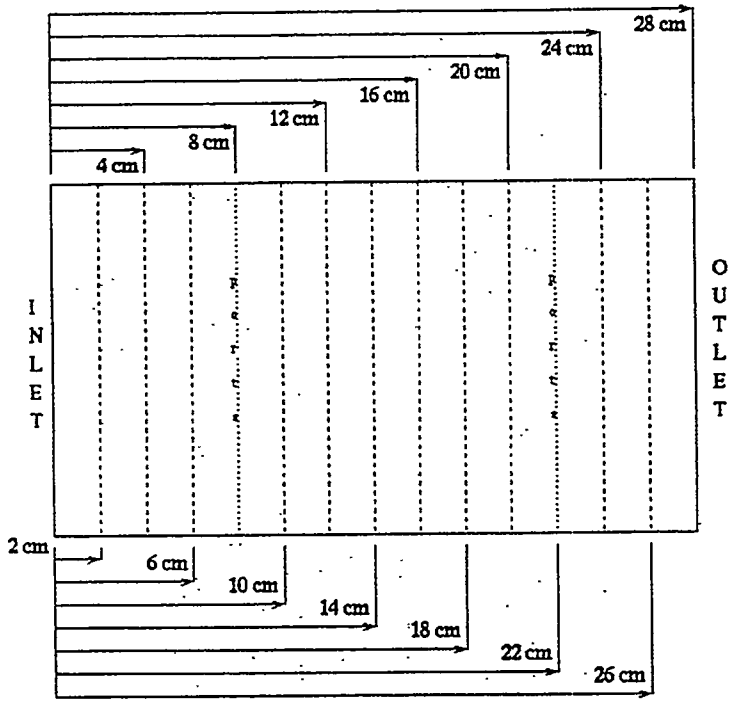

Figure 6. CT Scan Locations.

Porosity Distribution

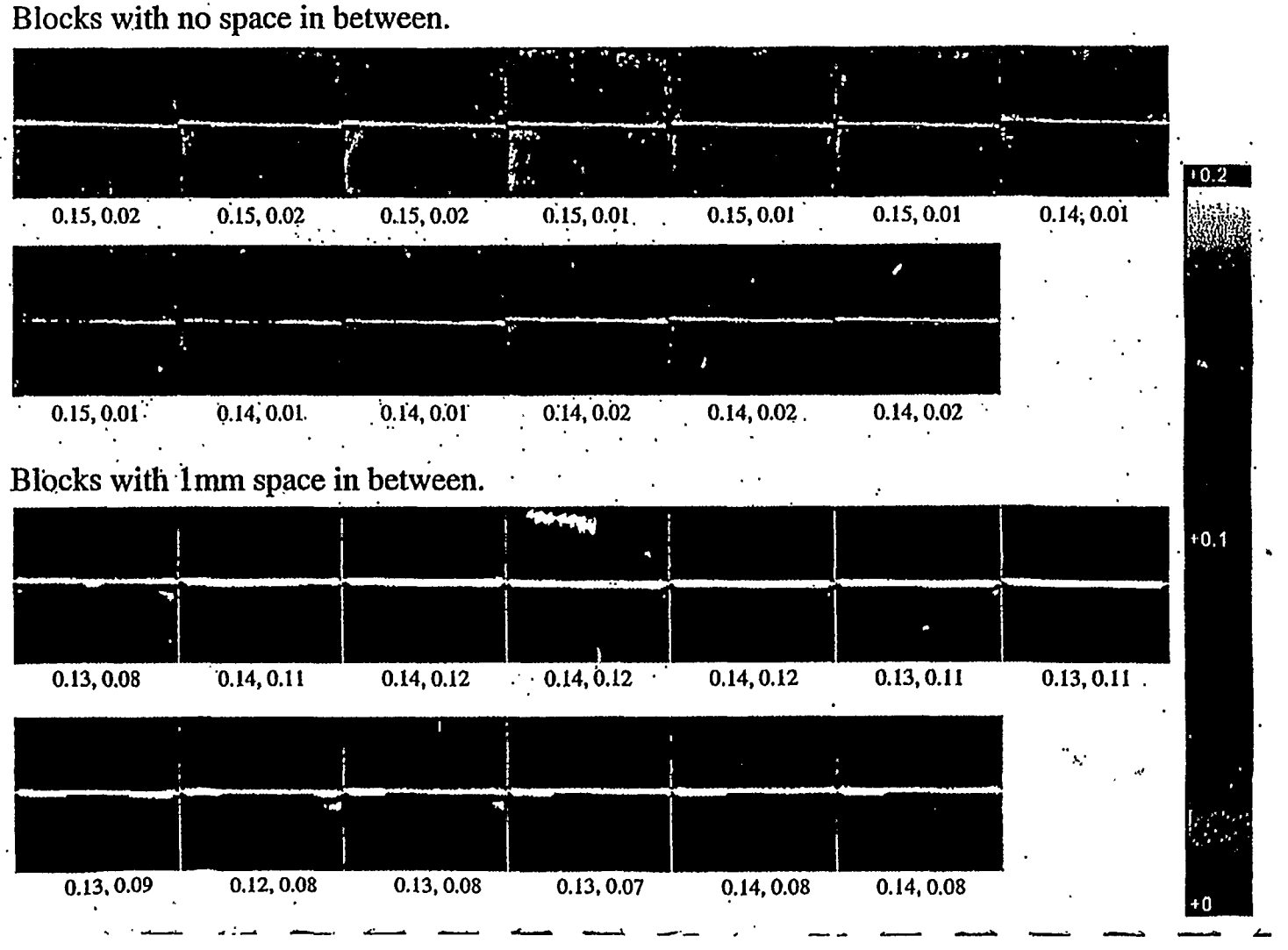

Figure 7. Porosity Distribution for the experimental system

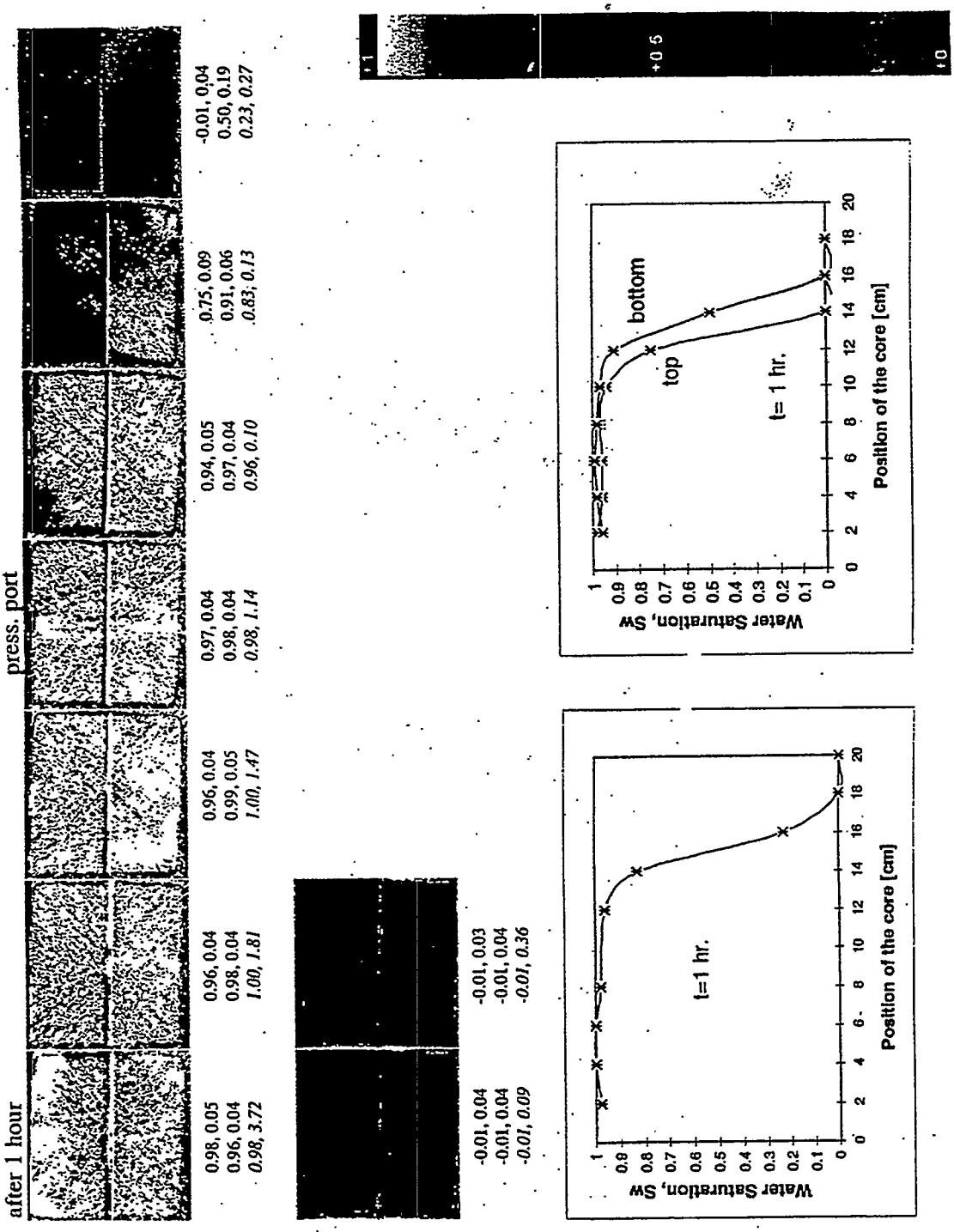

Figure 8. CT Saturation images for the Thin Fracture System after 1 hr of Water injection (0.45 PV)

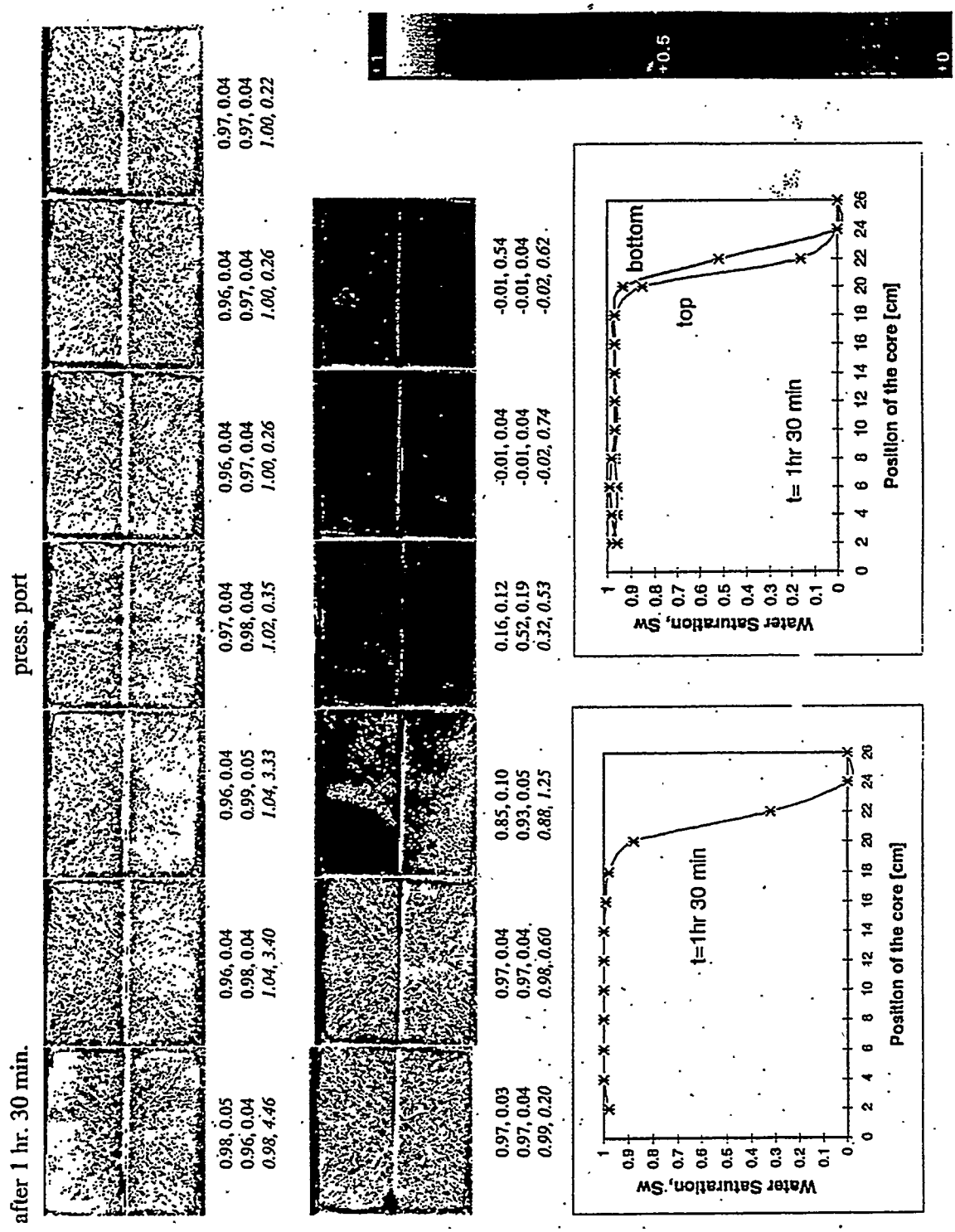

Figure 9. CT Saturation images for the Thin Fracture System after 1 hr 30 min of Water injection (0.67 PV)

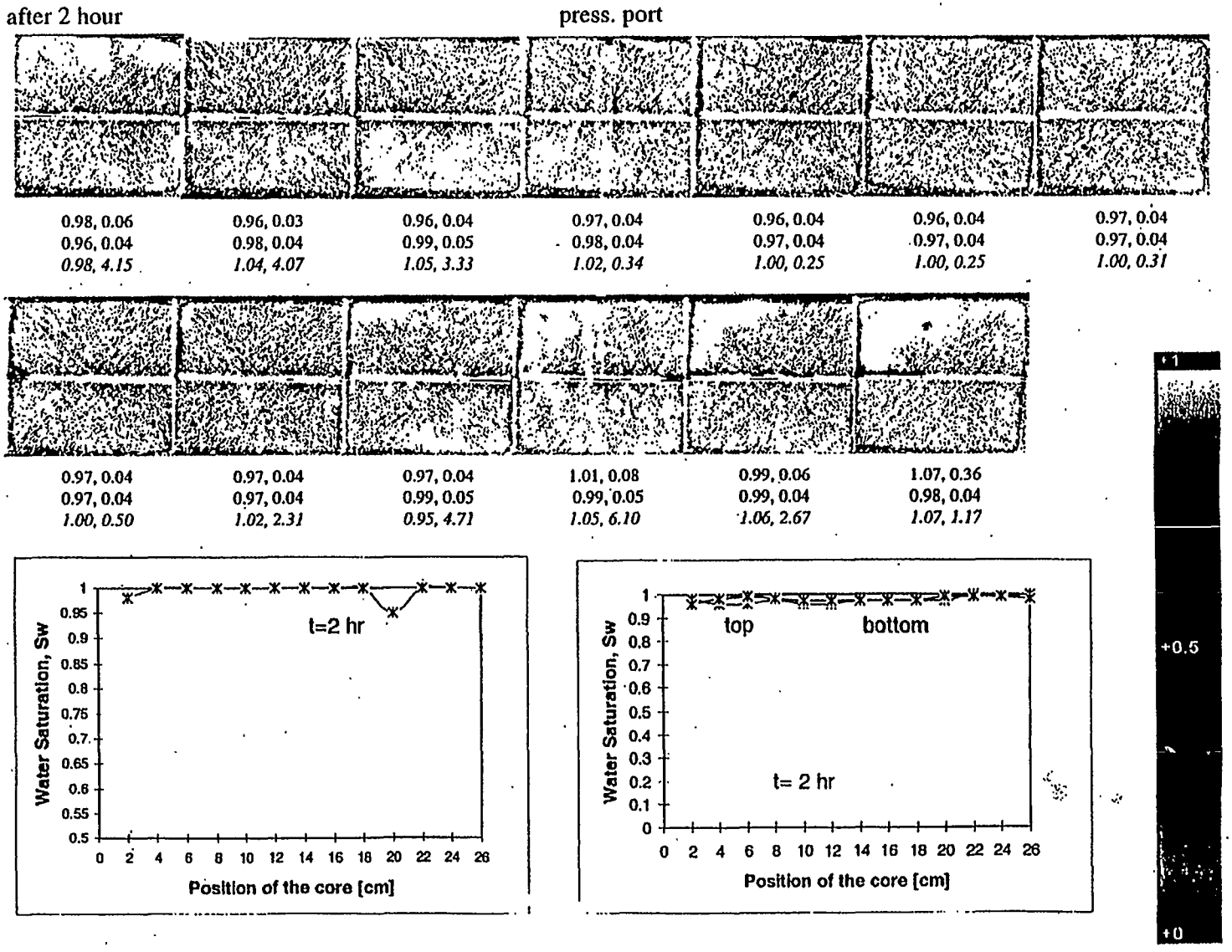

Figure 10. CT Saturation images for the Thin Fracture System after 2 hr of Water injection (0.89 PV)

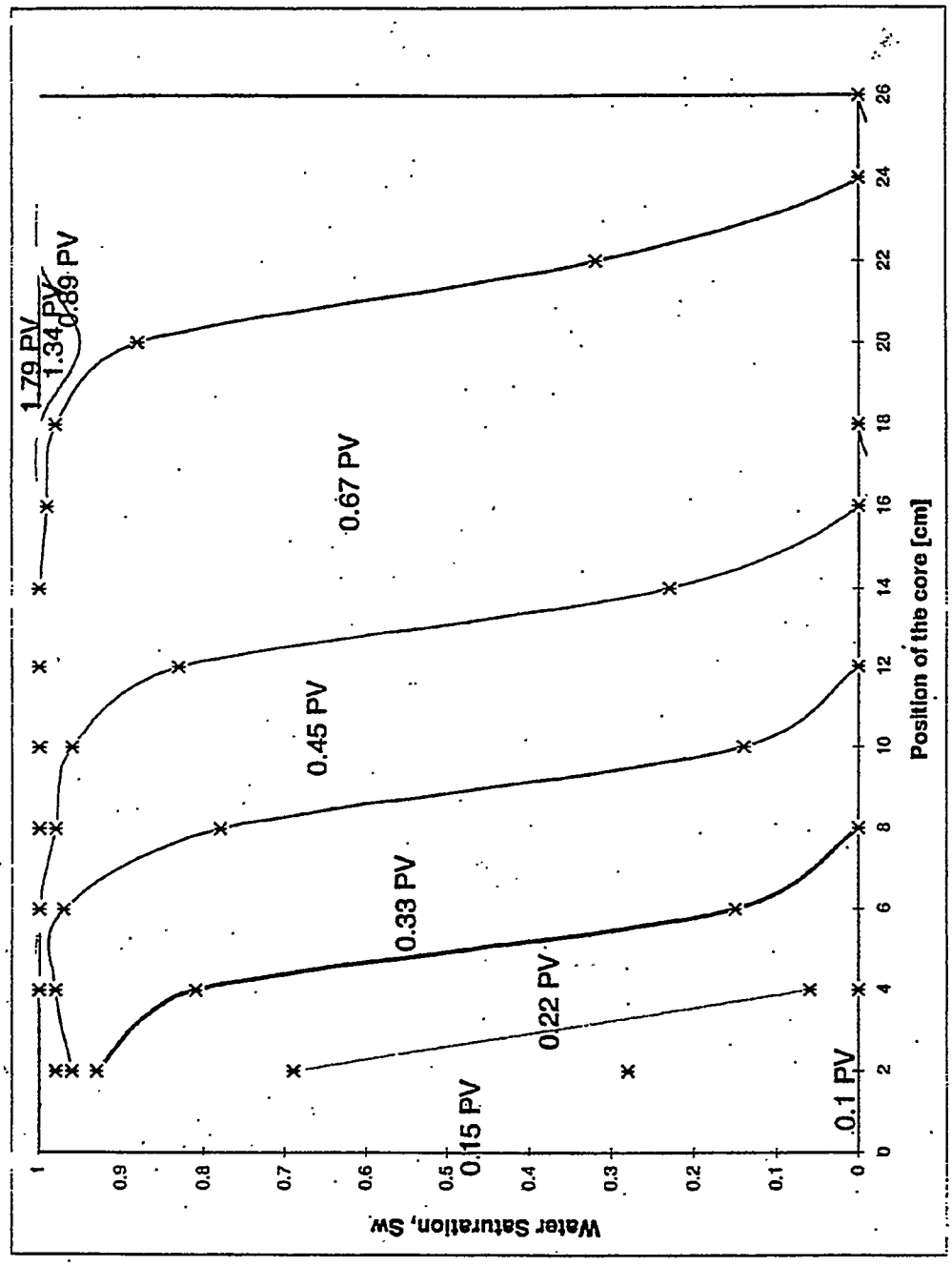

Figure 11. Water Saturation Profiles for Thin Fracture sytem for different PV of Water injection

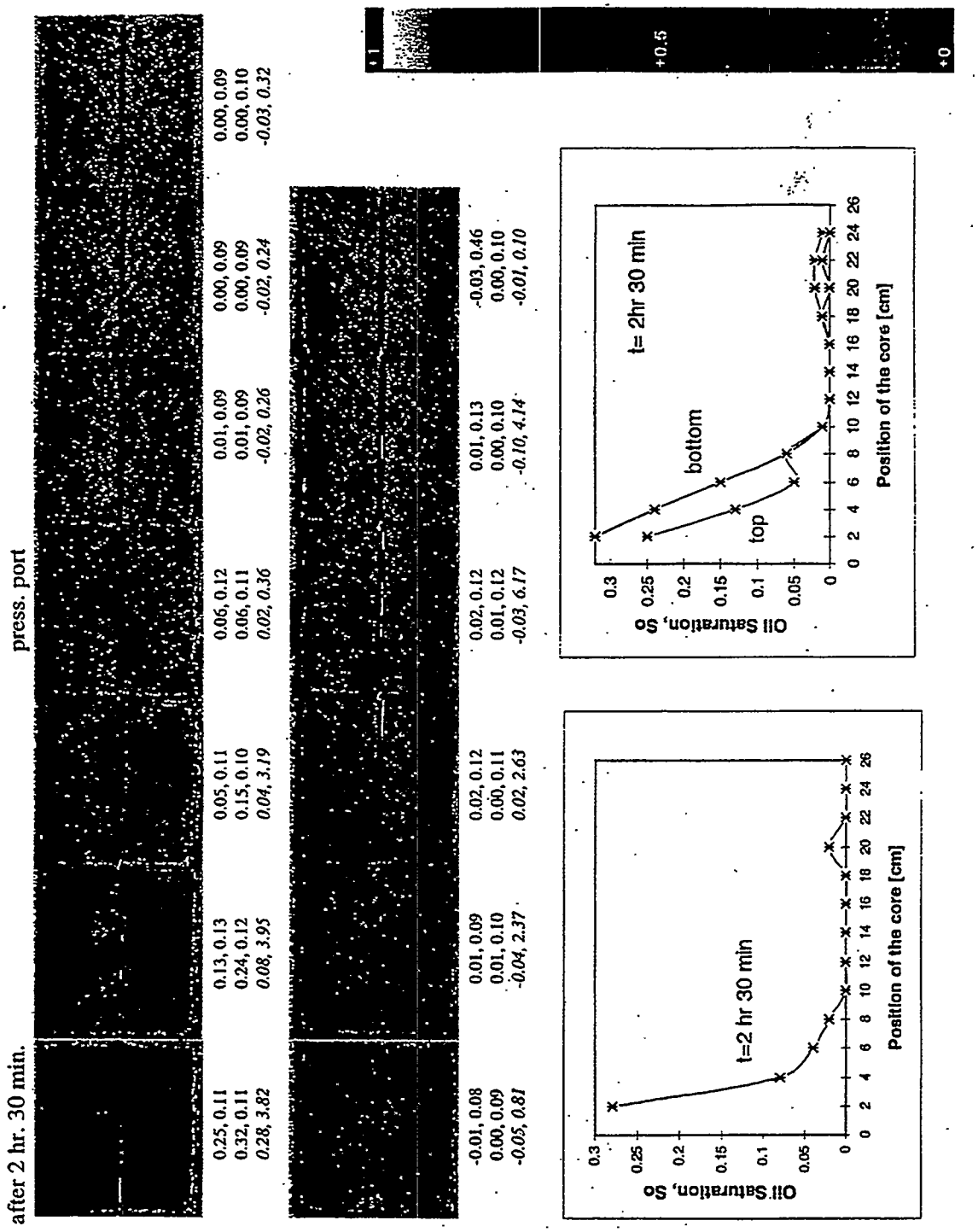

Figure 12. CT Saturation images for the Thin Fracture System after 2 hr 30 min of Oil injection (1.11 PV)

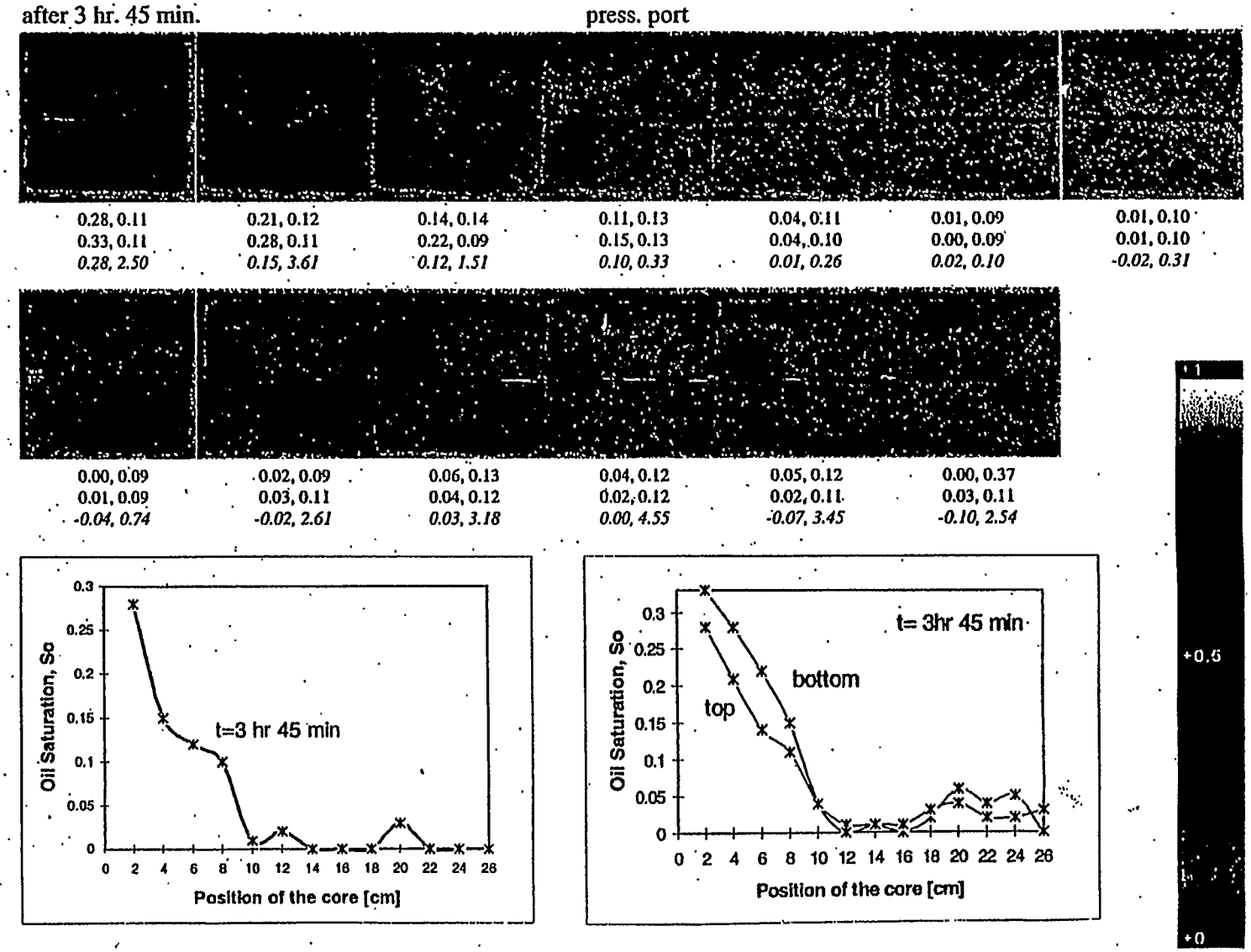

Figure 13. CT Saturation images for the Thin Fracture System after 3 hr 45 min of Oil injection (1.67 PV)

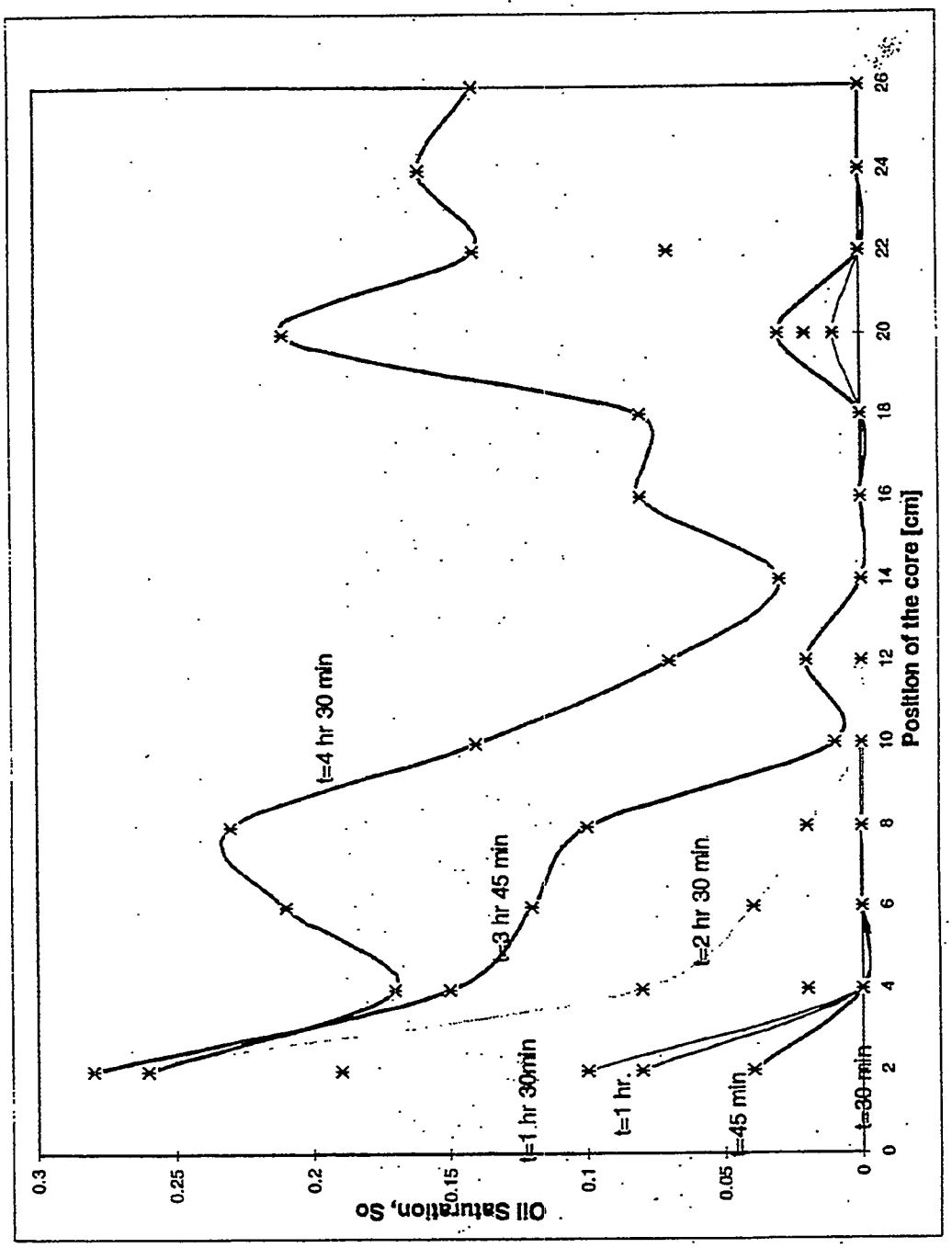

Figure 14. Oil Saturation Profiles for Thin Fracture sytem for diferent time of Oil injection

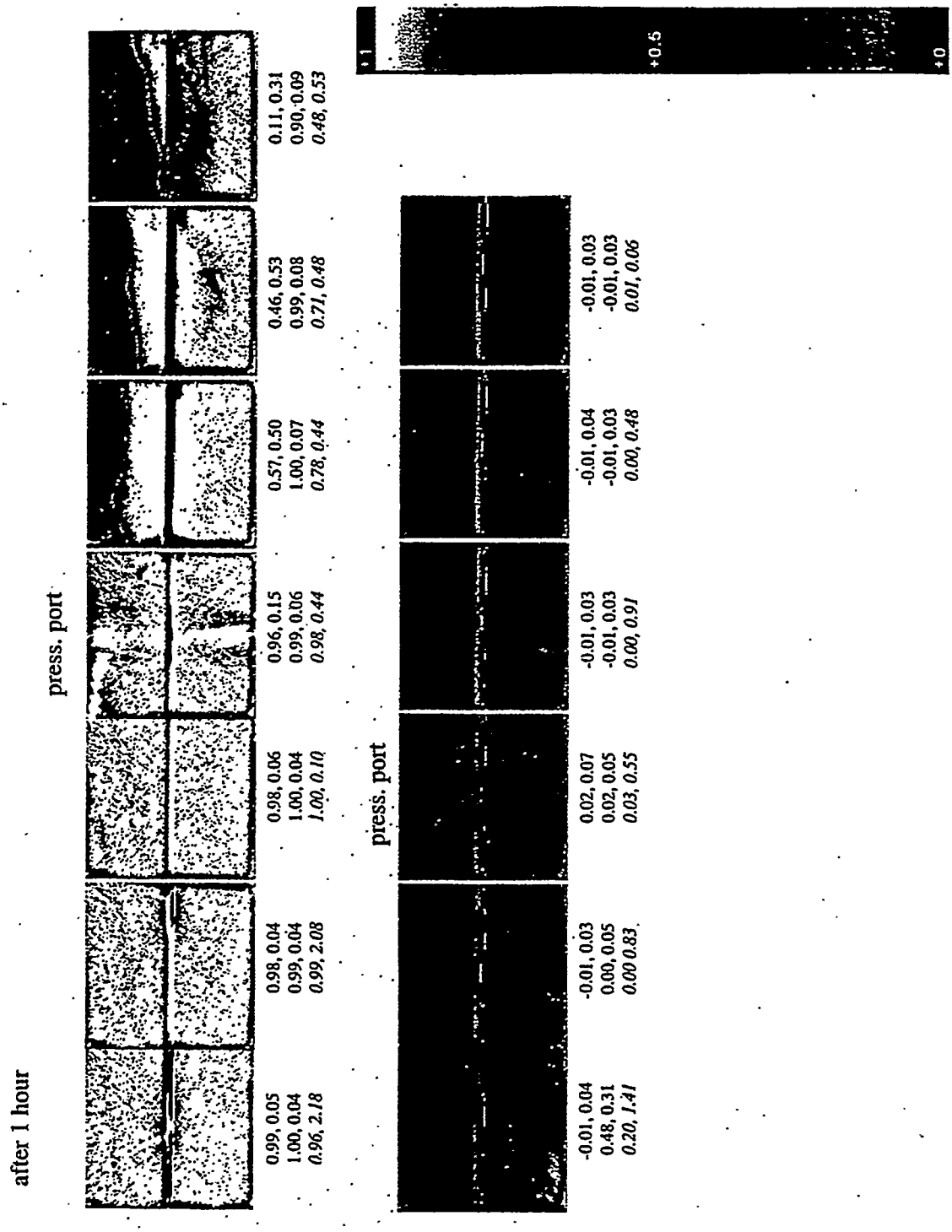

Figure 15. CT Saturation images for the Wide Fracture System after 1 hr of Water injection (0.45 PV)

Figure 16. CT Saturation images for the Wide Fracture System after 1 hr 30 m of Water injection (0.67 PV)

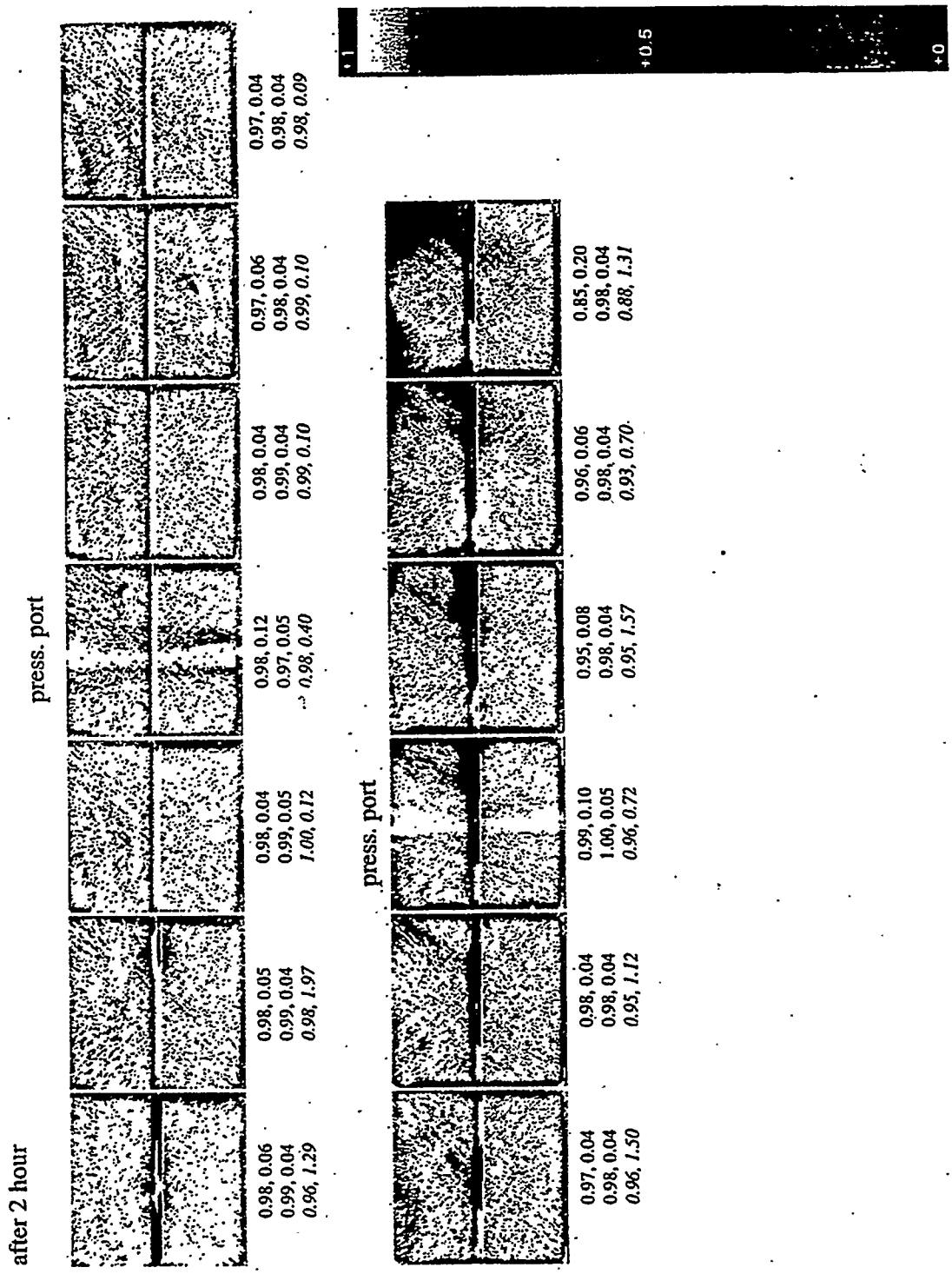

Figure 17. CT Saturation images for the Wide Fracture System after 2 hr of Water injection (0.89 PV)

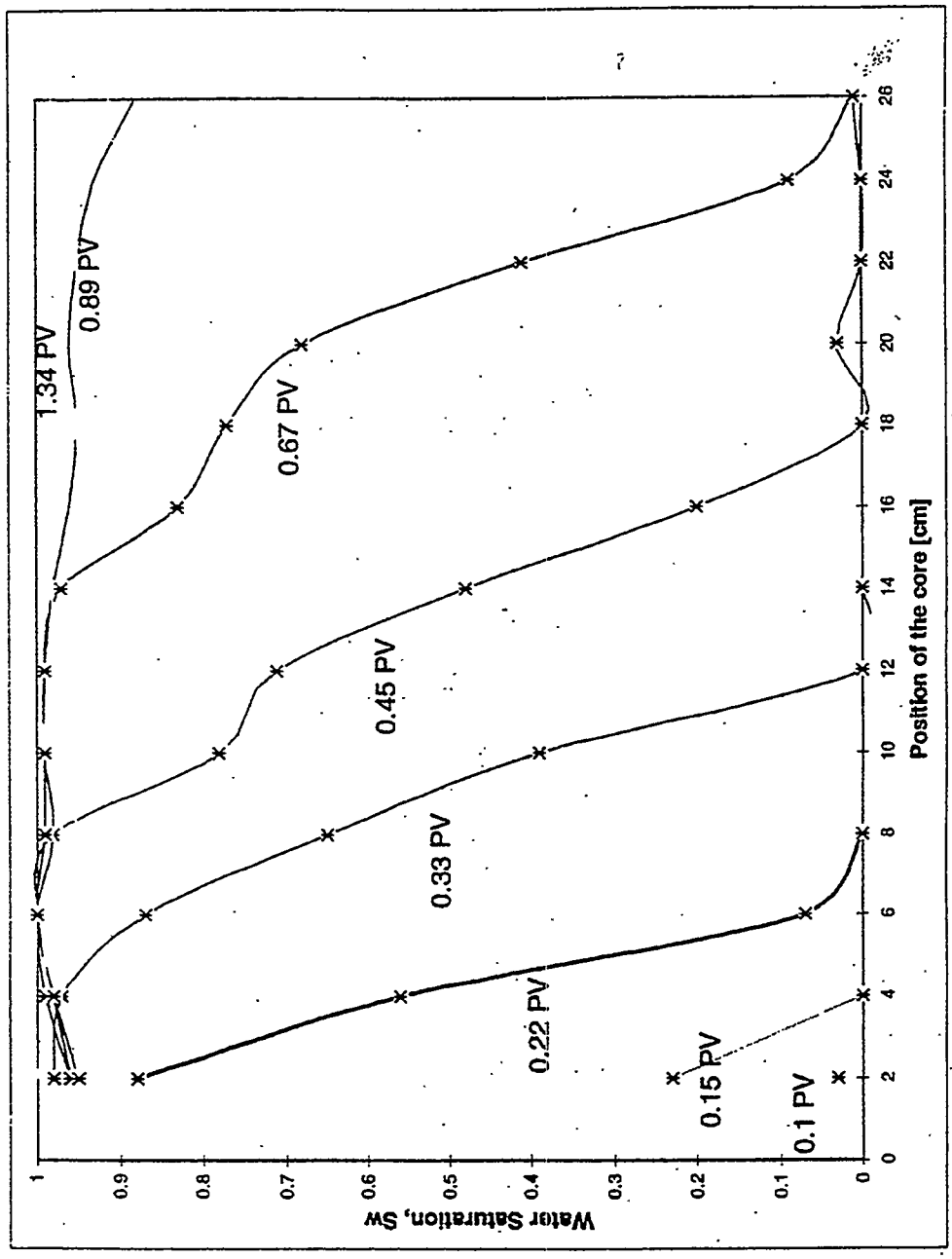

Figure 18. Water Saturation Profiles for Wide Fracture sytem for different PV of Water injection

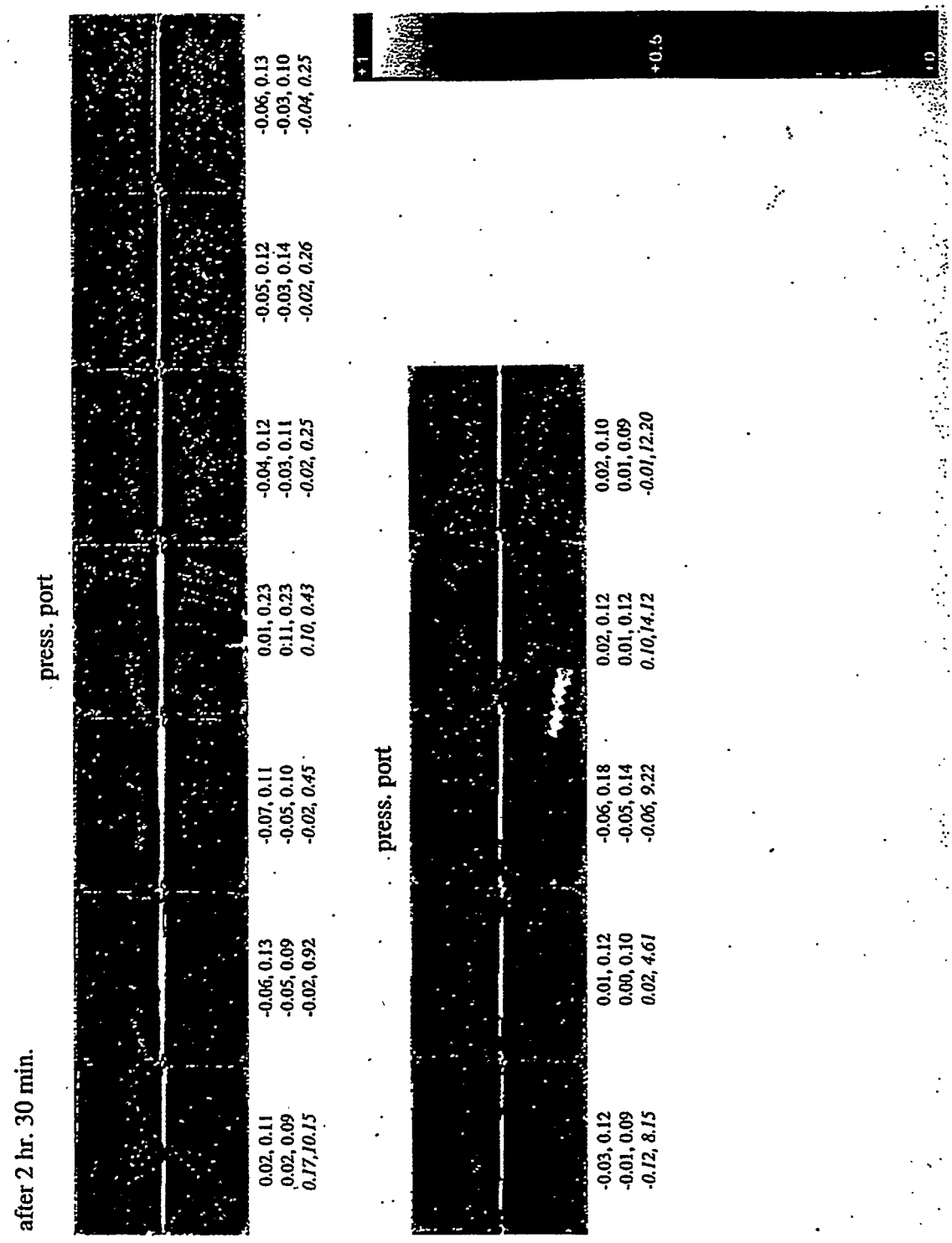

Figure 19. CT Saturation images for the Wide Fracture System after 2 hr 30 m of Oil injection (1.11 PV)

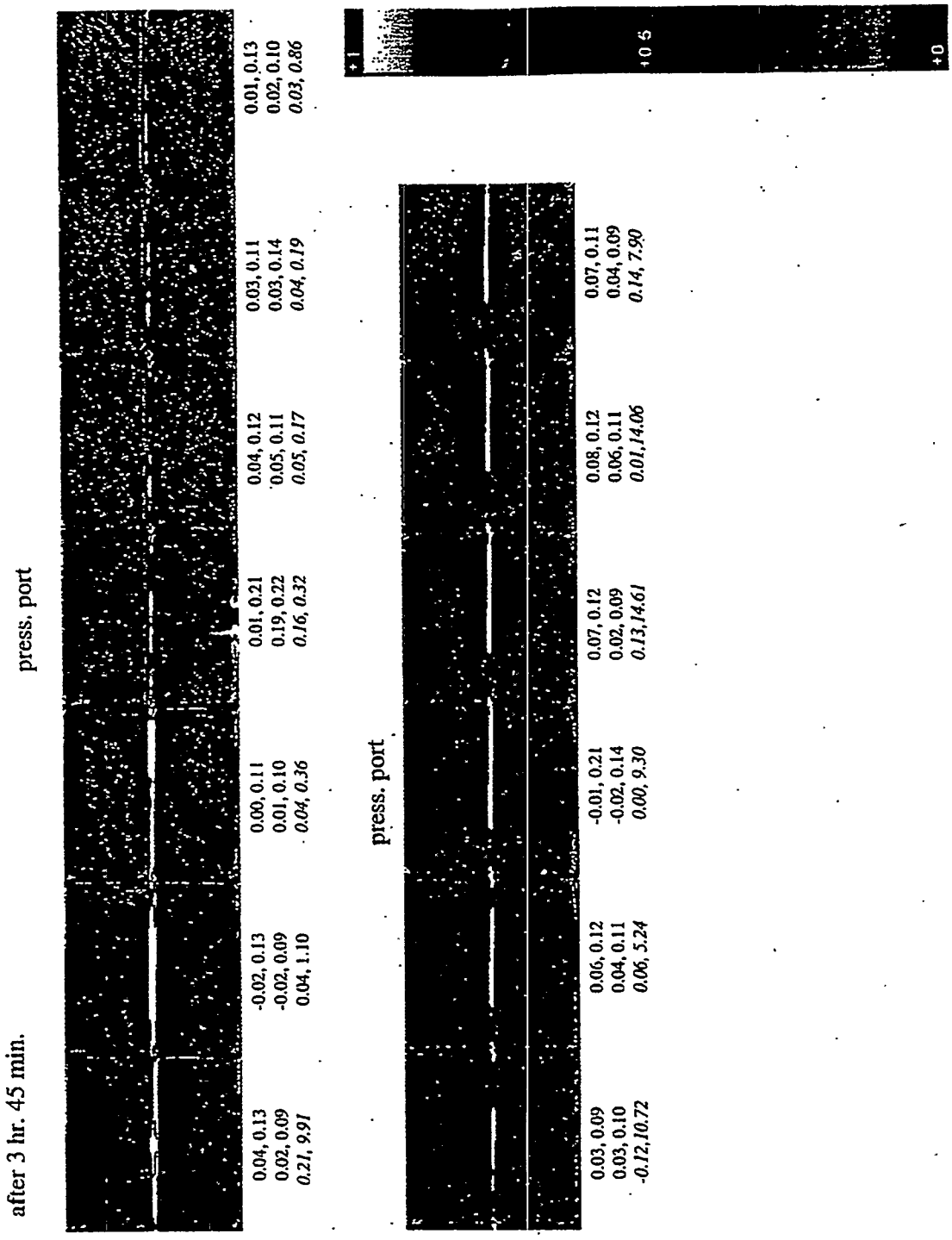

Figure 20. CT Saturation images for the Wide Fracture System after 3 hr 45 m of Oil injection (1.67 PV)

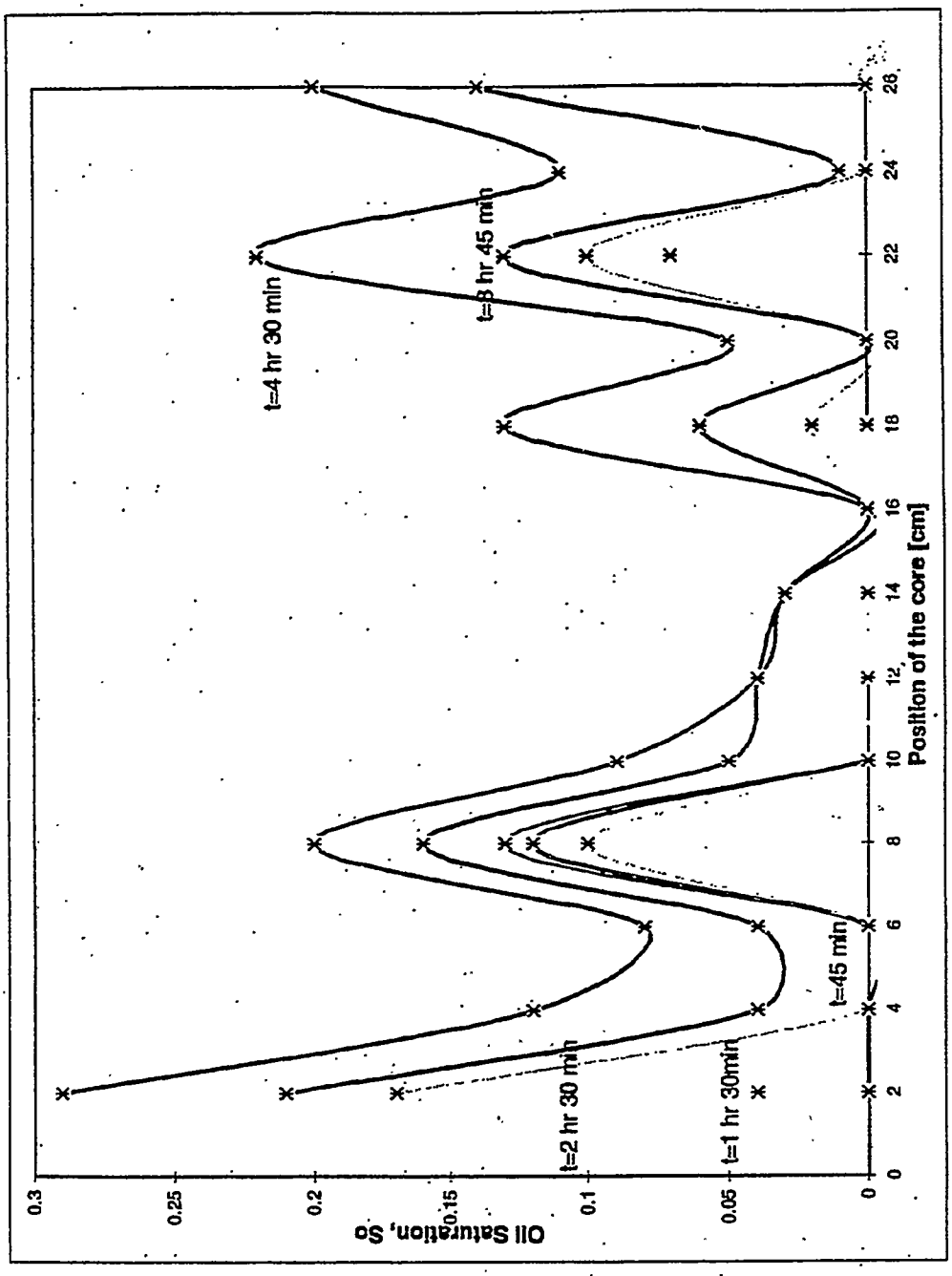

Figure 21. Oil Saturation Profiles for Wide Fracture sytem for diferent time of Oil injection

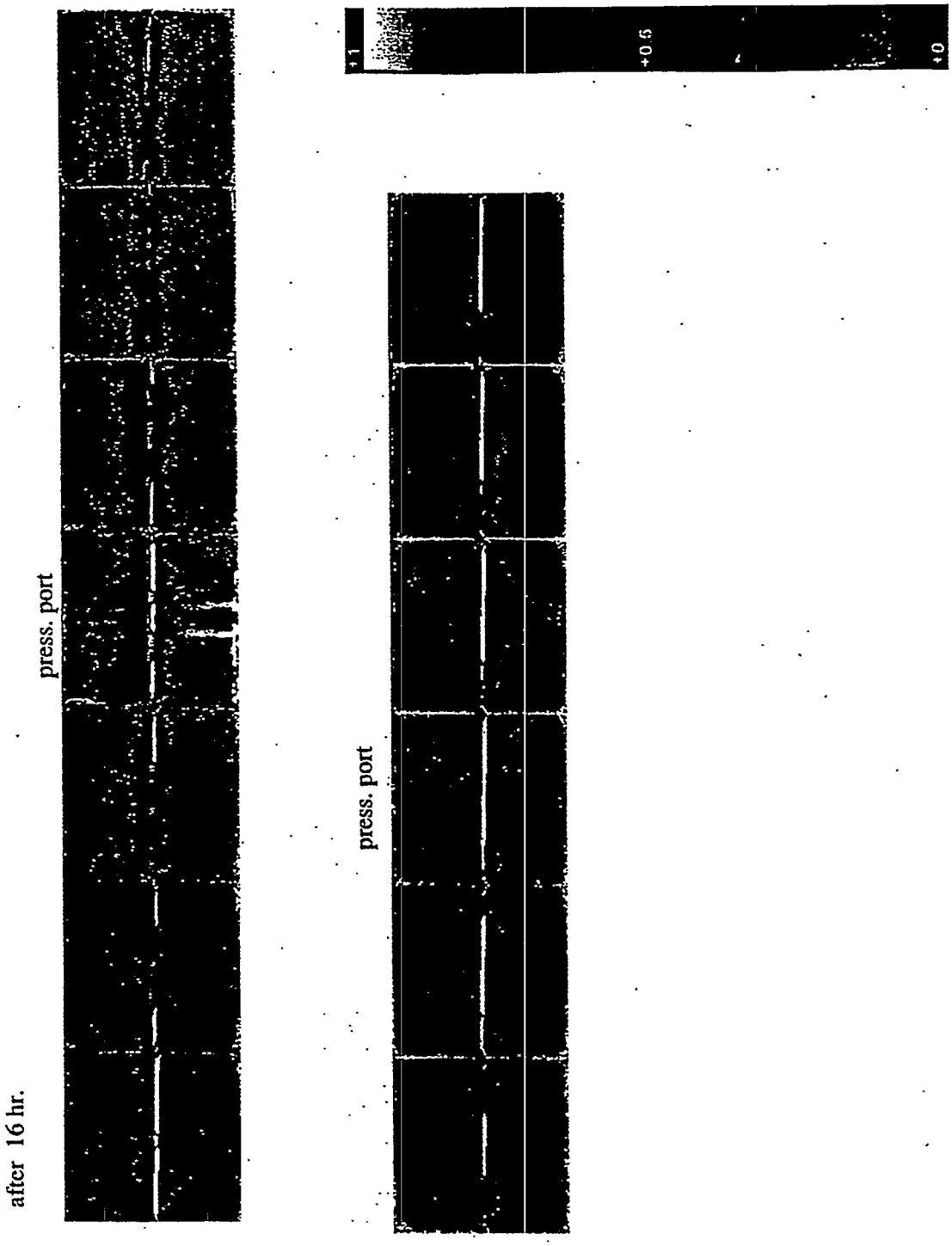

Figure 22. CT Saturation images for the Wide Fracture System after 16 hr of Water injection (7.11 PV)

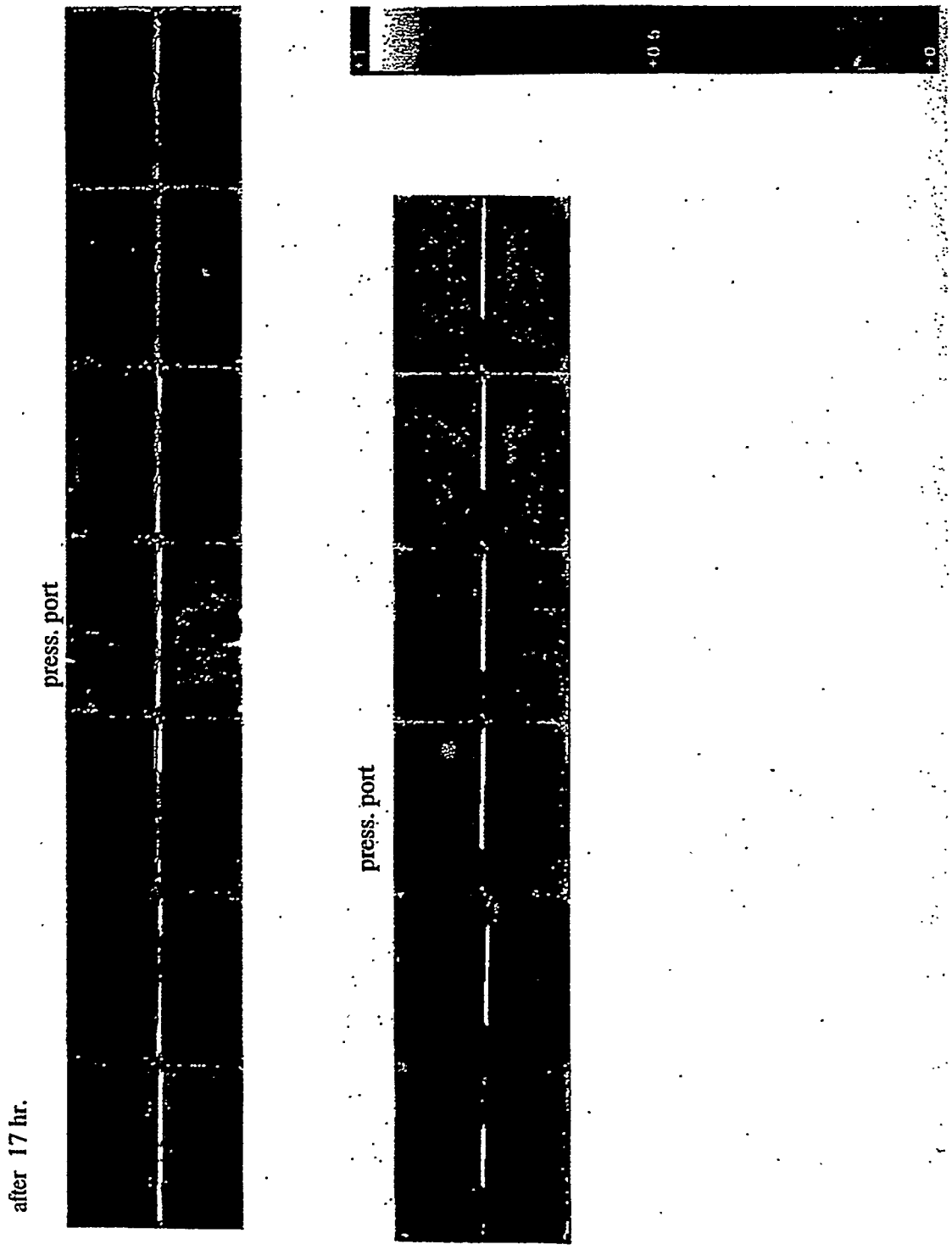

Figure 23. CT Saturation images for the Wide Fracture System after 17 hr of Water injection (7.56 PV)

Water Injection (thinner fracture)

0.22 PV (30 min)

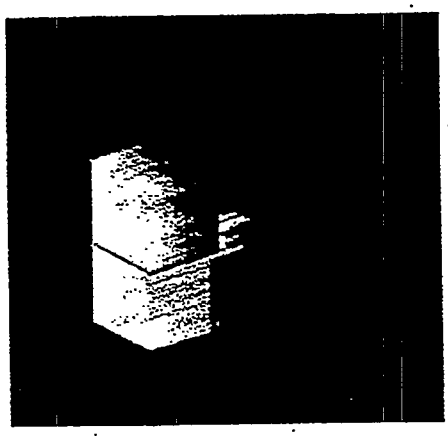

0.33 PV (45 min)

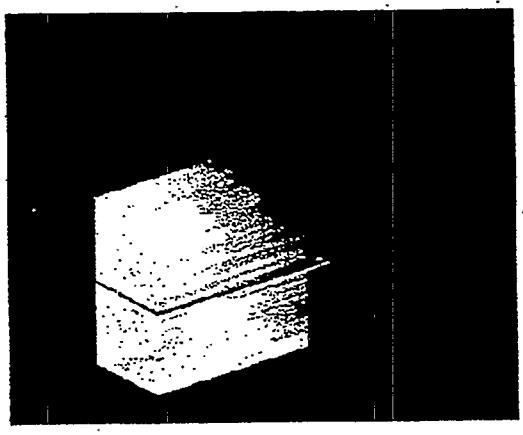

Figure 24. 3-D Reconstructions for the Thin Fracture system

0.45 PV (1hr.)

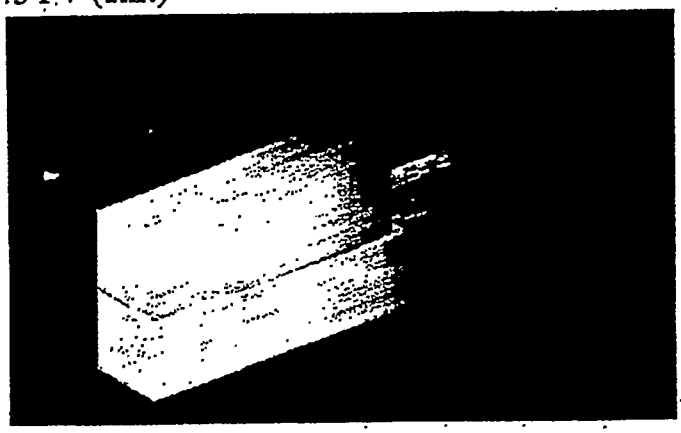

0.67 PV (1hr. 30 min)

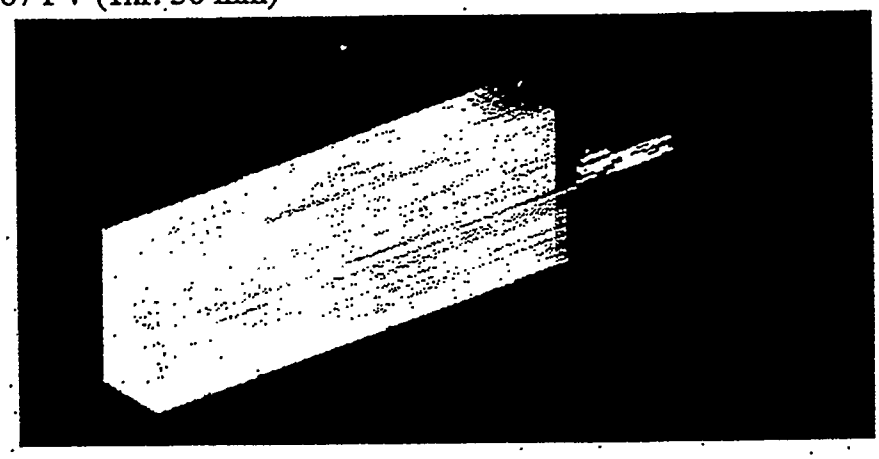

0.89 PV (2 hr.)

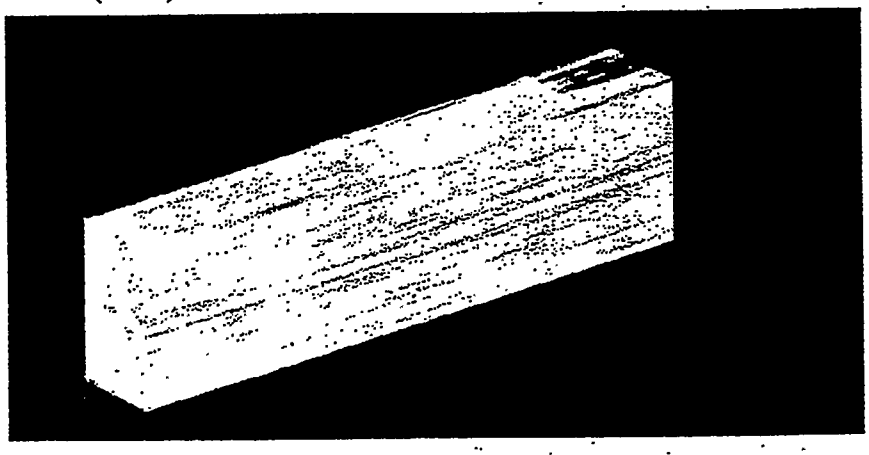

Figure 25. 3-D Reconstructions for the Thin Fracture system

Water Injection (wider fracture)

0.22 PV (30 min)

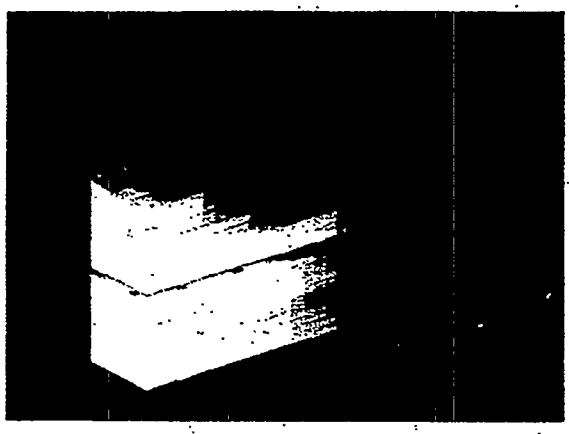

0.33 PV (45 min)

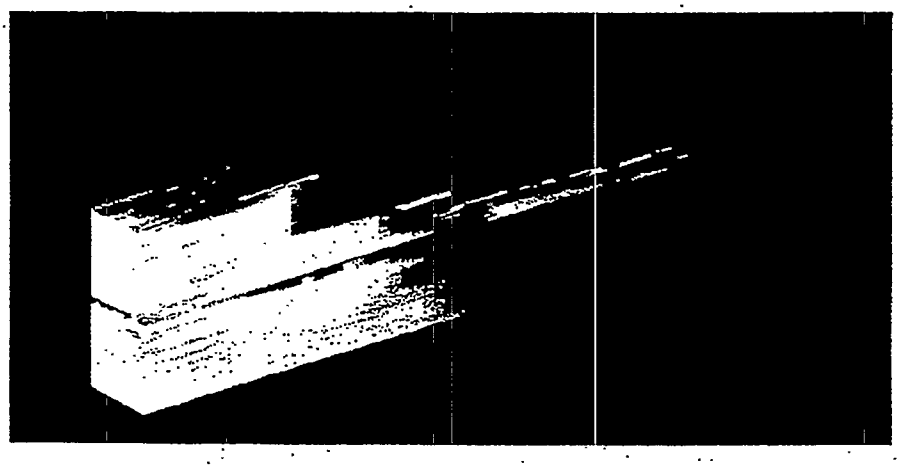

Figure 26. 3-D Reconstructions for the Wide Fracture system

0.45 PV (1hr.)

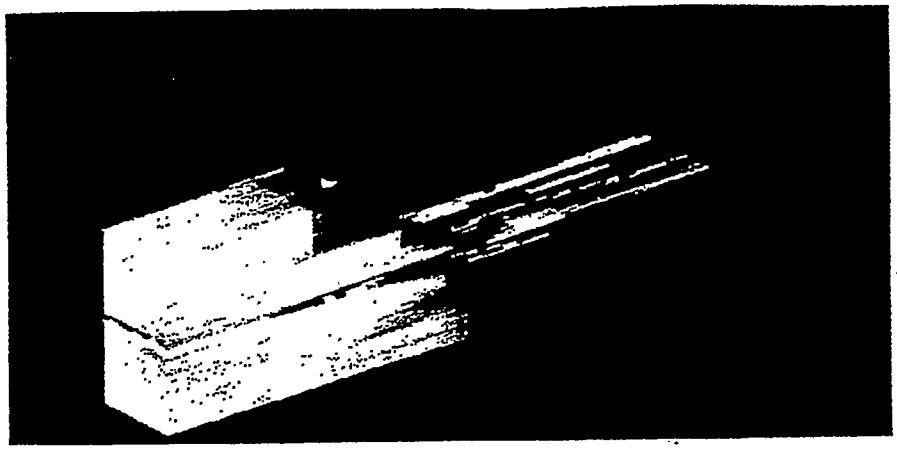

0.67 PV (1hr. 30 min)

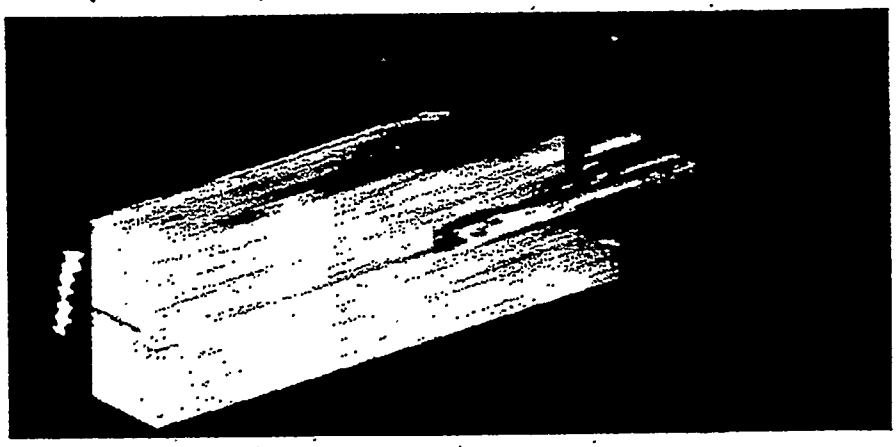

0.89 PV (2 hr.)

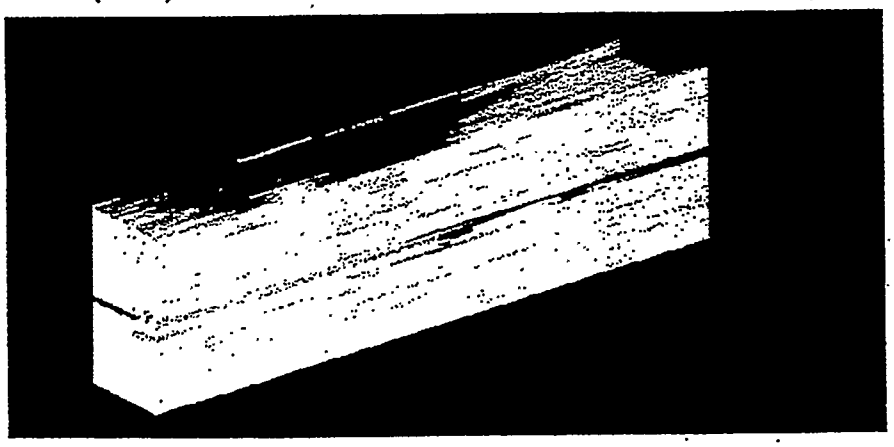

Figure 27. 3-D Reconstructions for the Wide Fracture system

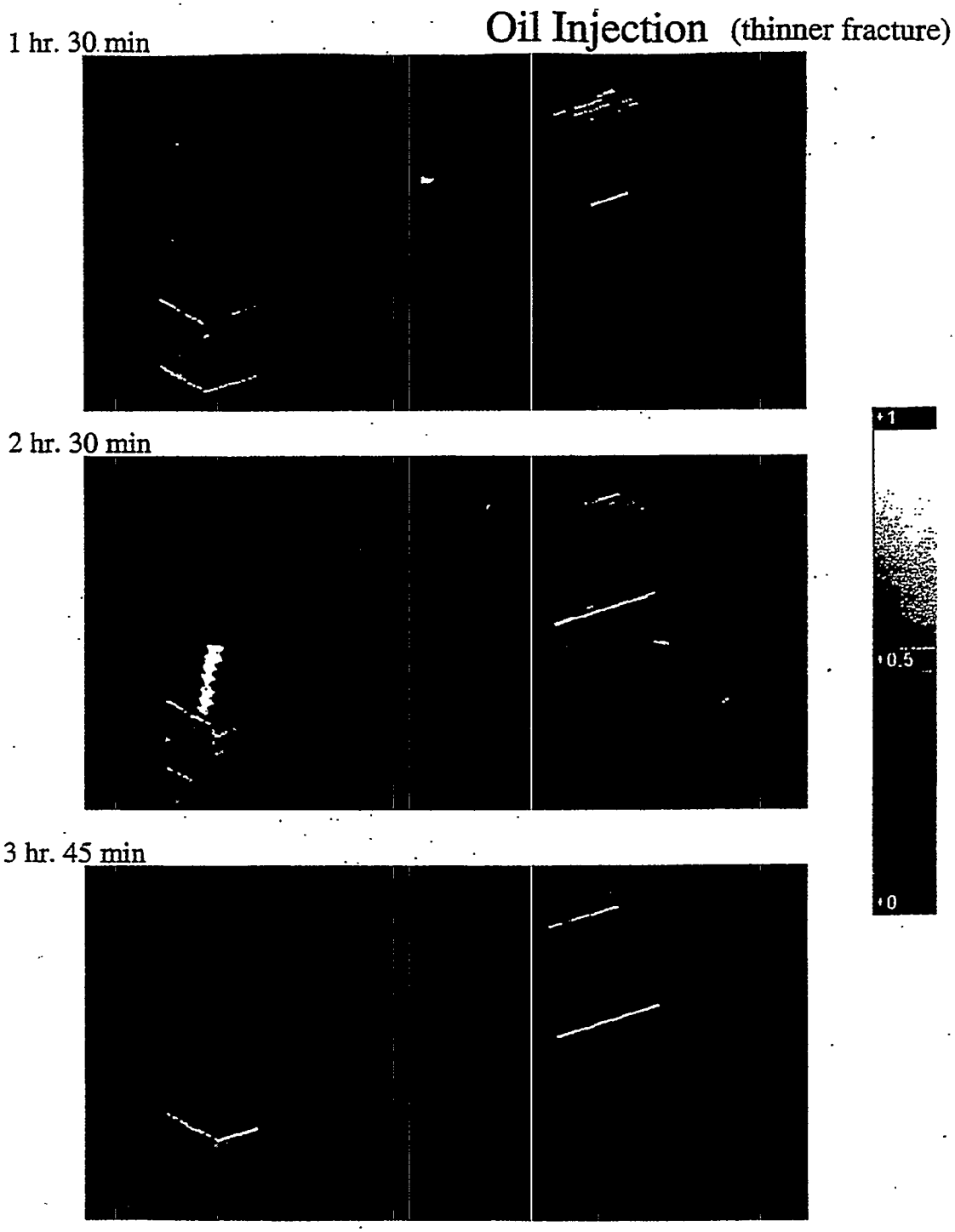

Figure 28. 3-D Reconstructions for the Wide Fracture system

Oil Injection (wider fracture)

1 hr. 30 min

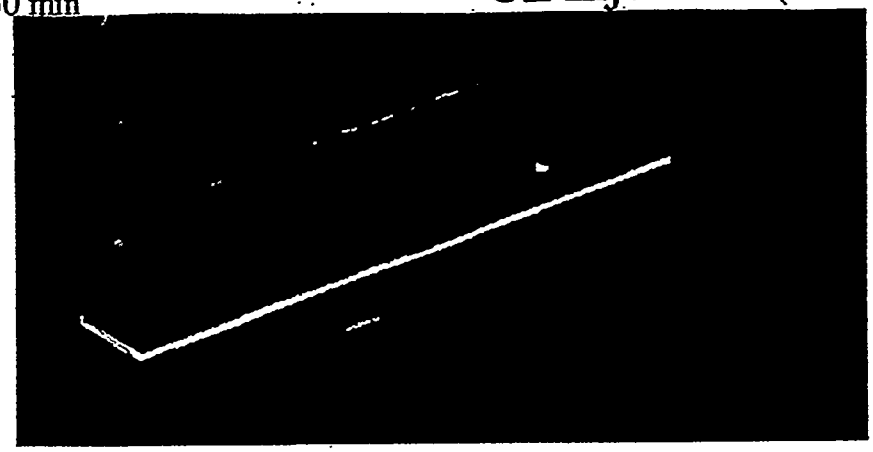

2 hr. 30 min

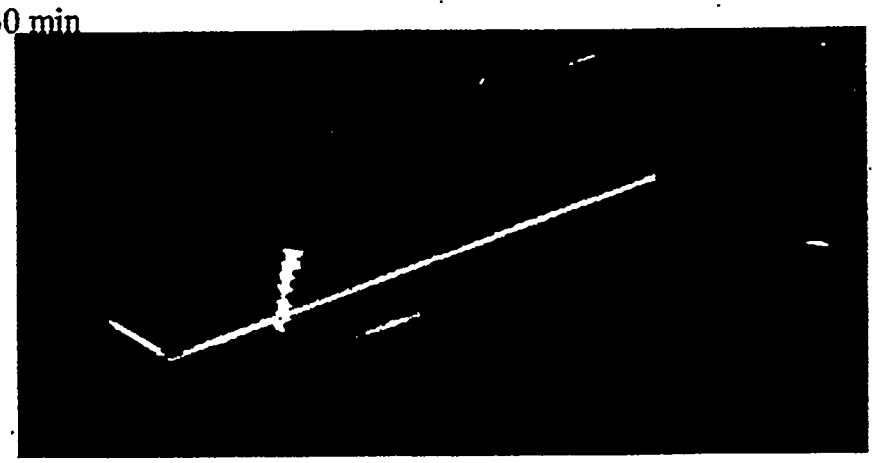

3 hr. 45 min

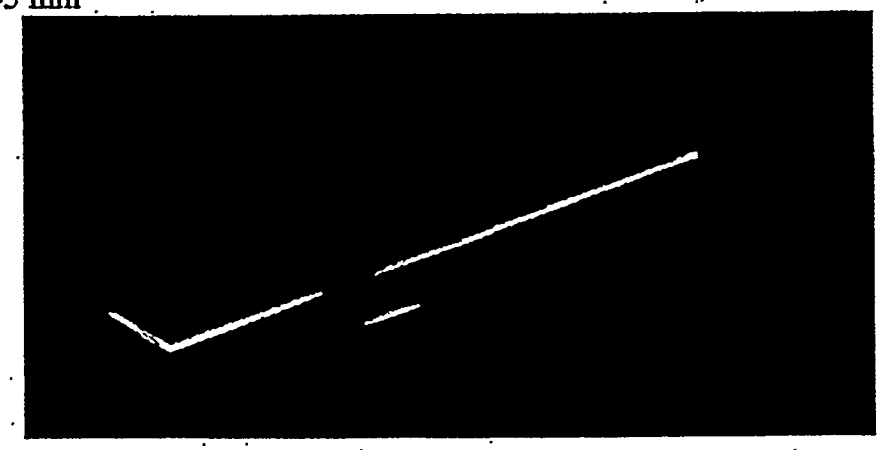

Figure 29. 3-D Reconstructions for the Wide Fracture system

1.3 SPONTANEOUS WATER IMBIBITIÓN INTO DIATOMITE

(J. Schembre, S. Akin, L.M. Castanier, and A.R. Kovscek)

1.3.1 Spontaneous Water Imbibition into Diatomite

(J. Schembre, S. Akin, L.M. Castanier, and A.R. Kovscek)

The paper on the following page was prepared for presentation at the 1998 Western Regional Meeting held in Bakersfield, California, May 10-13, 1998.

SPE 46211

Spontaneous Water Imbibition into Diatomite

J.M. Schembre, S. Akin, L.M. Castanier, and A.R. Kovscek, SPE, Stanford U.

This paper was prepared for presentation at the 1998 SPE/DOE Improved Oil Recovery Symposium held in Tulsa, Oklahoma, 19–22 April 1998.

Abstract

A systematic experimental investigation of capillary pressure characteristics and fluid flow in diatomite has begun. Using an X-ray CT scanner and a specially constructed imbibition cell, we study spontaneous water imbibition processes in diatomite and for reference Berea sandstone and chalk. The mass of water imbibed as a function of time is also measured. Imbibition is restricted to cocurrent flow. Despite a marked difference in rock properties including permeability and porosity, we find similar trends in saturation profiles and weight gain versus time functions. Imbibition in diatomite is relatively rapid when initial water saturation is low due to large capillary forces.

Introduction

Water imbibition is fundamental to both waterflood and steamdrive performance in low permeability reservoir rocks such as diatomite and chalk. Imbibition is an immiscible displacement process, whereby a non-wetting fluid within a porous medium is spontaneously expelled by wetting fluid that surrounds the medium and is drawn into the medium by capillary suction. This phenomenon is caused by the differential attraction forces between the pore walls and fluids. The rate of imbibition is primarily dependent on the rock permeability, pore structure, wettability, and the interfacial tension between the resident phase and the imbibing phase. On the macroscopic scale, capillary imbibition forces determine, in part, how rapidly and easily a hydraulically fractured water injector injects water into a low permeability formation and at what rate the injected water propagates. In naturally fractured systems with a high degree of interconnectedness, imbibition forces must be strong for a waterflood to be successful. If they are not, water will propagate through the fracture network from injector to producer and the waterflood will fail.

Capillary phenomena are equally important during steam injection into diatomite or lower permeability sandstones. Steam injection, especially at short times, is accompanied by condensation and flow of the resulting hot water away from the injector. Likewise, for live steam to enter the matrix of a low permeability rock, a substantial capillary entry pressure must be overcome. Producers might also suffer from capillary effects as the formation attempts to maintain capillary equilibrium with fluids in the production hydraulic fracture and the well.

Because of the importance of imbibition on oil recovery, it has been studied widely. However, our knowledge of hydrocarbon recovery and fluid displacement in porous media is less than complete. To date, much of the focus on imbibition has centered on carbonaceous rocks. This is a result of the importance of the North Sea Chalks, the West Texas Carbonates, and the Middle Eastern Limestones. An important class of low permeability rock that remains relatively unstudied is diatomite. Diatomite is a hydrous form of silica or opal composed of the remains of microscopic shells of diatoms, which are single-celled aquatic plankton [1]. Diatomites are very porous (frequently exceeding 50%) with high internal surface area, but exceptionally impermeable [2]. Permeabilities range from 0.1 to 10 mD. Diatomite is commercially important [3]: estimates of the original oil in place for the California Diatomites (Kern Co., CA) range from 10 to 15 billion barrels [4]. Reservoir rock is assumed to be strongly to moderately water wet. Because the formations are very porous and the initial oil saturation is large (35 to 70%), the target for potential production is high.

Multiphase flow in diatomite is dominated by capillary forces. Yet, a detailed scan of the literature shows few reported capillary pressure curves and little information on the extent and rate of imbibition. Likewise, the mechanisms of oil displacement and trapping are unclear, but presumed to be similar to those in sandstone. However, rock morphology is very different [5].

Thus, it seems helpful to undertake a systematic study of fluid transport in diatomite; it appears that capillary driven

flow is relevant to reservoir flow processes. In this work, our main focus is the study of one-dimensional spontaneous imbibition of water into air-filled diatomite. This simpler system provides some understanding of the behavior of water-oil-rock systems [6]. For contrast, we conduct experiments with a typical sandstone and chalk. Thus, we illustrate the effects of pore structure, permeability, and porosity on imbibition. We also present preliminary work on water imbibition into core samples containing oil. The progress and effectiveness of imbibition fronts is monitored using an X-ray CT scanner and a specially constructed imbibition cell.

Before describing the experimental apparatus, procedures, and results, we briefly review some theory regarding imbibition. This review helps to put experimental results into context and will simplify the discussion to follow.

Imbibition. Handy[6] provides a classic analysis and experimental investigation of the dynamics of imbibition in sandstone. He examines imbibition in the limit that capillary forces dominate over buoyancy and viscous forces, and displacement occurs vertically upward. Mainly, air-water systems are examined. It is noted that imbibition could be described by either a diffusion-like equation or a frontal-advance equation, depending on assumptions. In the former, the diffusion coefficient is proportional to the partial derivative of capillary pressure with respect to water saturation and computed displacement fronts are significantly diffuse. Whereas in the latter, the velocity of the imbibed phase is proportional to the gradient of capillary pressure with respect to distance, and fronts are assumed to be sharp. The main difference between the two descriptions is that the diffusion equation predicts that the smallest pores fill first and the larger pores fill later. The frontal advance equation assumes that pores of all sizes fill simultaneously because large pores are connected to small pores, and *vice versa*. Thus, it is hard to fill the small pores selectively.

Both developments predict that the mass of water imbibed is a linear function of the square root of time and experiments agree with this dependence. However, the end of imbibition is quite abrupt which is contrary to the expected result for a diffusive-type process. This observation lead Handy to assert that the frontal advance equation more nearly described the true process. Indeed, recent experiments where the position and shape of a water imbibition front in a homogeneous Berea sandstone were accurately tracked indicate relatively sharp and steep fronts [7]. These experiments were also modeled numerically with a diffusion equation incorporating buoyancy driven advection. The authors note that the computed saturation profiles are not sufficiently sharp at the displacement front to match the experimentally determined profiles. Also, water breakthrough occurs too early in the calculations.

Hence, we follow Handy and recognize that the rate of imbibition in porous media, especially air-water systems, is in many respects similar to capillary rise in small diameter tubes. Upon assuming that water imbibes in a piston-like manner, gas viscosity is negligible, capillary forces outweigh gravity forces, and the spatial gradient of capillary pressure is linear, the mass of imbibed water is given by

$$m = \rho_w A \left(\frac{2 P_c k \phi S_w}{\mu_w} \right)^{1/2} t^{1/2} \quad (1)$$

In Eq. (1), m is the mass of water imbibed, ρ_w is the density of water, A is the cross-sectional area, P_c is the capillary pressure, k is the permeability to water, ϕ is the porosity, S_w the aqueous phase saturation, μ_w is the viscosity, and t is the time. The linear relation between the mass imbibed and the square root of time is apparent and the slope is proportional to the square root of the product of $P_c k S_w$. In most situations, the mass, time, and cross-sectional area are easily measured; the density and viscosity of water are known constants under isothermal conditions; and the porosity is measurable volumetrically. Thus, the only unknown quantities remaining in Eq. (1) are $P_c k S_w$. Dimensional analysis teaches that this quantity has units of force and it is a measure of the likelihood of imbibition. Intuitively, it is expected that the larger is $P_c k S_w$, the more rapidly a porous medium imbibes. For simplicity, we refer to $P_c k S_w$ as the imbibition potential.

Preparation of Samples

The rock samples used in this study were Berea sandstone, diatomite and chalk. Their description is given in Table 1. The Berea cores were both cylindrical and square shaped, (core 1 and core 2 respectively). The diatomite (core 3), an outcrop from Lompoc, California, and chalk (core 4), an outcrop from Kansas (core 4) are cylindrical shaped. The objective of using differently shaped, but similar cross-sectional area, Berea sandstone cores was to confirm that cross-sectional shape did not influence results.

The Berea and chalk were cored using conventional drilling and cutting methods. In the case of the diatomite, the core could not be formed by the same method due to its fragile structure. Thus, a piece of the rock is cut by bandsaw to approximate dimensions and it is shaped manually by fixing two circular 1 inch-diameter patterns, held at both ends of the rock. These pieces are used as guides in the shaping process with a file. Final shaping is achieved with sandpaper.

The sandstone samples are fired at 450 °C for 12 hours to remove the effect of clay swelling and migration during the imbibition process. Diatomite and chalk are not fired. The cores are then sealed with epoxy on the sides parallel to the flow direction to obtain one-dimensional imbibition (See Fig. 1). It is important to mention that, in the case of the diatomite, the coating is a very critical process since the epoxy does not adhere securely to the surface. Without care, delamination of the epoxy coat occurs after some use of the

sample.

Experimental Method

Our objective is to obtain the change of average water saturation with time, the time rate of imbibition, and to calculate the imbibition potential term from the slope of the average water saturation versus the square root of time. Thus far, we have concentrated on water imbibition into air-filled cores. A limited number of water-oil experiments have been conducted also.

The weight gain of the core was measured by two methods. Initially, the sample core was suspended by means of an acrylic and steel frame directly from a weighing balance in an acrylic container filled with water. Although this method gives good results, we found some disadvantages in the handling of the core when CT-imaging was performed. Mainly, asymmetry in the scanning plane leads to numerous uncorrectable X-shaped beam hardening artifacts. The design of an imbibition cell which permitted CT-scanning of the core during the imbibition process and minimized artifacts was necessary.

Description of Experimental Cell. The experimental cell, shown schematically in Fig. 2, is constructed from acrylic tubes, and it consists of two separate chambers. The main chamber is the core holder and it is surrounded by the second chamber that is filled with water to reduce possible beam hardening. Beam hardening refers to the differential adsorption of longer wavelength X-rays and leads to shadows around the periphery of CT images. There is no fluid exchange between containers and the outer water-filled chamber allows for some measure of temperature control. The core holder has two end caps for fluids to flow in and out of the core holder. The inlet cap at the bottom of the core holder is connected to a fluid tank through a rubber tube. The weight of imbibed fluid is measured directly by means of a balance as shown in Fig. 3. Displaced fluids exit from the top.

The CT-Scanner used is a Picker™ 1200 SX X-ray scanner with 1200 fixed detectors. The voxel dimension is (0.5 mm by 0.5 mm by 5 mm), the tube current is 65 mA, and the energy level of the radiation is 140 keV. The porosity and aqueous-phase saturation fields are measured on a single vertical volume section in the center of the core as a function of time. The acquisition time of one image is 3 seconds while the processing time is around 40 seconds. The total time of measurement is short enough to capture accurately the position of the front and construct the saturation profiles along the core.

Experimental Procedure. After preparation and coating, the core is exposed to house vacuum and a temperature of 50 °C, for 10 hours. This ensures a "dry" core at the beginning of the experiment. The procedure is as follows:

1. The dry core is placed in the core holder (main chamber).
2. A paper filter is placed at the bottom of the core. The objective is to obtain a uniform distribution of water at the bottom rock face.
3. Since the core holder is surrounded by water during the CT-experiments, a leak test is performed by applying a slight gas pressure and checking that the pressure in the core holder is maintained for a period of time.
4. The core holder is placed in the second chamber and leveled.

In the cases where CT scanning is performed, the second chamber is filled with water. Water is introduced to the open bottom face of the core and the progress of the imbibition front monitored with frequent CT-scans.

Since imbibition is spontaneous, care was taken to maintain the water level in the core holder so that it just contacts the rock base. The data acquisition system for the balance is started. Once the imbibition begins, the weight of the water reservoir is recorded every 10 seconds. The gain of weight in the core is computed directly by the change of weight measured in the tank containing the water. The reference weight corresponds to time equal to zero in which tubing is filled with water and the water-air interface is just below the bottom face of the core.

In the case where CT-Scanning is performed, dry images of the core are taken to obtain the reference dry core CT-values. Scanning is performed every 50 seconds for the first 5 minutes. Afterwards the intervals between the images are longer since the change of saturation in the core becomes slower with time.

The data acquisition process is stopped when changes in the weight are no longer observed. Also, constant water saturation is verified by measuring the average CT-number and standard deviation in the image of the core and verifying that it is the same from one scan to another. In order to have a reference wet image of the core, a final scan is conducted at least 12 hours later. After spontaneous imbibition is complete, water is sometimes pumped through the core to ensure 100% water saturation.

Data Processing. Once the weight-gain data is collected during the spontaneous imbibition process, it is converted into weight imbibed into the core and a linear regression is performed to obtain the slope of the resulting straight line. This correlates the weight gain of the core to the square root of time.

Regarding the CT-number related calculations, the map of porosity and the saturation profiles are obtained using the method of subtraction of images of raw CT data (*c.f.* [8]). Thus, in the case of the porosity

$$\phi = \frac{CT_{wet} - CT_{dry}}{CT_{water} - CT_{air}} \qquad (2)$$

where,

CT_{wet}: CT value for a fully water saturated core, obtained

from a last scan performed after 12 hours or more of water imbibition.
CT_{dry}: CT value for the dry core, obtained from the scanning of the core before the imbibition process starts
CT_{water}: CT value of water
CT_{air} : CT value of air

To construct saturation profiles we have

$$S_w = \frac{CT_{obj} - CT_{dry}}{CT_{wet} - CT_{dry}} \qquad (3)$$

where CT_{obj} is the CT value of the image being processed.

It is important to note that CT_{wet} corresponds to 100% water saturation. This is verified by comparing the porosity fields computed from the dry and water-filled images. When the core is completely saturated, they are the same.

Results

First, we present and summarize weight gain as a function of time and then the corresponding CT-images of the imbibition process are given.

Weight Gain vs Square Root of Time. Data obtained from the imbibition experiments for the different cores were converted into the weight of water imbibed as a function of time in order to measure the rate of change of water saturation in the core. The results are summarized in Figures 4 to 7 and in Table 2.

Figure 4 plots the weight gain versus the square root of time for the Berea sandstone. The three different sets of symbols indicate three different experiments. In this case, the weight gain was measured directly by hanging the core from a balance and bringing a beaker of water up until it just touched the bottom of the core, as described in the experimental section. Deviation from linearity in the early time response is explained by the level of the free water surface in contact with the bottom of the core. Because the core is slightly submerged, imbibition is forced and the response is faster than expected. Once the water front passes the free water level, a straight line results. Note that all experimental runs show a straight line with the same slope indicating good reproducibility. Spontaneous imbibition ceases when the water front reaches the end of the core. This time is practically the same for all three cases.

Next, a series of experiments were performed in Berea sandstone cores to confirm that the cross-sectional shape of the cores did not bias our results. Cores with both circular and square cross-sectional areas, as shown in Fig. 5, were used. The straight-line portion in both cases has the same slope. The cross sectional areas were approximately the same, hence the slopes are the same. The difference in the total weight gain and the time for completion of spontaneous imbibition is due to differences in the length of the cores, as shown in Table 1. The core with square cross-sectional area did not imbibe immediately because, initially, the end of the core was not fully submerged in water.

These initial experiments with Berea sandstone confirmed that our experimental approach was adequate to collect the data required. Imbibition in diatomite was considered next. Figure 6 shows weight gain obtained for the diatomite during two different experiments. All diatomite experiments were conducted in the imbibition cell. Again, there is some deviation from linearity in the initial stages of imbibition. For later times, the response is linear with respect to the square root of time and the slopes are identical. This deviation can be explained by reasons related to the experimental method. Experiments conducted in the imbibition cell also have the possibility that the water level of the tank is not exactly equal to that of the bottom of the core. Forced imbibition could exist for a short time. The second explanation is the filter paper at the bottom of the imbibition cell, which might not saturate uniformly at the beginning of the imbibition process. Thus, imbibition is retarded. Interestingly, the water imbibition process is quite rapid despite the low permeability of diatomite. These diatomite samples imbibe water at rates rivaling sandstone.

For comparison, experiments on a low permeability chalk sample were also conducted. Figure 7 shows the results. The trend of weight gain is not as smooth as either the sandstone or diatomite case. But, we do observe, overall, a relatively linear response versus the square root of time. Heterogeneities observed during CT-scanning account for the jaggedness of the linear weight gain. These heterogeneities will be discussed further in the next section. Spontaneous imbibition in the chalk is much slower than in either the Berea sandstone or diatomite, as indicated by the length of time necessary to complete imbibition.

A linear regression was performed on the straight line portions of Figs. 4 to 7 to obtain the slope. Table 2 shows (a) the slope, (b) the porosity of the samples obtained by Eq. (2), (c) the imbibition potential calculated by Eq. (1) and, (d) the slope divided by the cross-sectional area for each experiment. In the case of Berea Sandstone with circular cross-sectional area, the three different experiments show similar slope, confirming the repeatability of the method. Also, a similar slope is found for the experiment on square cross-sectional area cores.

The diatomite shows the highest values for slope and imbibition potential. The average imbibition potential for diatomite is 0.0060 dyne, whereas it is only 0.0045 dyne for the sandstone and 0.0038 dyne for the chalk. We find that capillary forces during the spontaneous imbibition process make a contribution to flow that offsets the low permeability of the diatomite.

CT-Scanning Results. Porosity maps and the saturation profiles obtained during the imbibition for the Berea sandstone, diatomite and chalk are shown in Figures 8, 9 and

10, respectively. Both water saturation and porosity are indicated by gray-scale shading. In the case of saturation, black indicates 0 % water and white indicates fully water saturated. Porosity maps are located in the right-hand corner. The shading scale for the porosity images is compressed to highlight heterogeneity, but again dark is small and white is large.

Sandstone porosity ranges from 0.08 to 0.23. The Berea sandstone images in Fig. 8 show some surprising results. The weight gain data agree with a piston-like assumption, but images of the water displacement front are not truly piston like. Initially, water enters at the center of the core. Intuitively, we expect capillary forces to spread the saturation front laterally as well as upward. However, the front is rounded and centered in the middle of the core (refer to Fig. 8 at 200 s). The leading edge of the water front moves through the core maintaining its rounded shape until reaching the core outlet. At about 120 s, the water saturation front does span the cross-section of the core at the inlet. This rear portion of the water front appears to move through the core displacing any remaining gas. Interestingly, the time taken for the rounded water saturation front to span the core (120 s) corresponds roughly with the onset of linear weight gain in Fig. 8 (10 $s^{1/2}$).

The porosity map for diatomite shown in Fig. 9 indicates that this sample is relatively homogeneous and average porosity is about 65%. Strong capillary forces are evident in the CT images for imbibition in diatomite. Water again enters the core in the center, but it spreads laterally quite rapidly. The water front is sharp and the displacement is clearly piston like. As the front progresses down the core it diffuses somewhat. The water front reaches the end of the core in about 3600 s. The CT images correspond to the lower curve in Fig. 6 that deviated from linearity at short time. Figure 9 shows that the saturation front was not piston like until roughly 90 s. Hence, the deviation from linearity results from the nonuniform displacement front.

In contrast to the sandstone and diatomite samples, the chalk core contains some heterogeneities. These are evident in the porosity map as illustrated in Fig. 10. For instance, there is a dark portion, indicating low porosity, on the left hand side about a quarter of the way up the chalk core. Chalk porosity ranges from 0.15 to 0.25. Like the diatomite, the chalk shows a practically uniform and sharp front at the beginning that becomes less sharp at later times. It is interesting to note that the heterogeneities fill with water at somewhat different rates. The slow filling of the above mentioned heterogeneity is evident in the saturation images at 300, 540, and 600 s.

A comparison of the time necessary for the spontaneous imbibition to be completed in each type of rock, confirms the weight gain results. Diatomite takes about three times longer than Berea Sandstone, while the chalk takes ten to eleven times. It is important to recall that the pore volume of the diatomite is about five times the pore volume of the Berea sandstone.

Water-Oil Imbibition. Upon construction of an imbibition cell that permits high resolution scanning with minimal CT artifacts, the successful capture of saturation images for water imbibing into an air-filled core, and the excellent repeatability of these experiments, we have turned to water imbibition into diatomite containing oil. First the core is dried as explained above and then it is completely saturated with n-decane via vacuum saturation. Oil is purged from the supply lines and replaced with water. The experiment is then conducted in the same manner as the water/air cases. Produced oil exits the top of the core. Some preliminary CT images are shown in Fig. 11. From the times associated with each CT image in Fig. 11, it is apparent that water imbibition is much slower in the water/oil case than in the water/air case. At 17,460 s in Fig. 11 the water/oil front is roughly half of the way up the core, while in Fig. 9, imbibition in the water/air system is complete in less than 6900 s. This is expected because the water/oil interfacial tension is lower as are the buoyancy forces. Also, the oil is much more viscous than air and hard to displace. Nevertheless, a strong, sharp displacement front is witnessed and strong capillary effects are evident. Displacement is not as effective in the water/air case. The gray scale shading indicates that the water saturation upstream of the displacement front is about 80%.

Although the experimental setup was designed to promote one-dimensional cocurrent imbibition, there is anecdotal evidence that countercurrent imbibition may have resulted at times due to the strong capillary forces. Periodically, imbibition, as judged from the decrease in weight of the water supply, would cease. In order to restart imbibition, the water reservoir was raised a few centimeters via a laboratory jack until imbibition resumed and then lowered again. Countercurrent imbibition allows oil to exit at the bottom face of the core and this oil could impede water flow. Applying a slight amount of hydraulic head might be sufficient to disturb the system and reinitiate water flow.

Our work on water/oil systems continues, and includes cases of initial water saturations greater than zero.

Discussion

The simple water displacing air experiments provide some insight into the capillary pressure characteristics of diatomite. Denote the imbibition potential by *IP* and take the ratio of diatomite *IP* to sandstone:

$$\frac{IP_d}{IP_s} = \frac{(P_c k S_w)_d}{(P_c k S_w)_s} \quad (4)$$

where the subscripts *d* and *s* refer to diatomite and sandstone, respectively. Using average values from Table 2, this quantity is 2.4 indicating the strong tendency of diatomite to imbibe water. From Figs. 8 and 9, we judge that the water saturation upstream of the saturation front is about 1. So, the ratio of saturations in Eq. (4) is about 1. Next, we replace P_c with the appropriate Leverett J-function:

$$P_c = \sigma\left(\frac{\phi}{k}\right)^{1/2} J(S_w) \qquad (5)$$

for water wet rocks. In Eq. (5), σ is the air-water interfacial tension and $J(S_w)$ is the Leverett J-function[9]. Upon some rearrangement

$$\frac{IP_d}{IP_s} = \left(\frac{k_d}{k_s}\right)^{1/2}\left(\frac{\phi_d}{\phi_s}\right)^{1/2}\left(\frac{J_d(S_w)}{J_s(S_w)}\right) > 1 \qquad (6)$$

Equation (6) teaches us about the magnitude of the J-function for diatomite. The first term in parentheses on the right is clearly less than 1 because diatomite is less permeable than sandstone. With typical sandstone (100 to 1000 md) and diatomite (0.1 to 10 md) permeabilities, k_d/k_s might range from 0.1 to 1E-4. Table 2 shows that the diatomite samples are roughly 4 times as porous as the sandstone. For Eq. (6) to be greater than 1, J_d/J_s must be greater than 1. This explains, in part, why the relatively impermeable diatomite imbibes strongly when the rock is initially filled with air.

Another interesting aspect of these experiments is the very low trapped gas saturation. For instance, Fig. 9 at 4800 s shows water saturation in excess of 95% shortly after breakthrough. The strong capillary forces and the small pore throat to body aspect ratio of diatomite suggests much snap-off and trapped gas. However, for snap-off to occur, pore corners and crevices must fill with wetting liquid and sufficient liquid for snap-off must accumulate at pore throats before the pore is filled completely by the advancing imbibition front. We speculate that trapped gas saturation is low because the advancing front fills pores with water at least as rapidly as pore corners fill with water. Indeed, recent pore-level network modeling of imbibition shows that in the absence of flow in pore corners the displacement pattern is a flat front with little or no trapping of the nonwetting phase[10].

Conclusions

An experimental apparatus and method to permit the collection of data and CT images during spontaneous imbibition into an air or oil-filled core was designed. The samples examined were Berea sandstone, diatomite and chalk, which allowed the study and comparison of the contribution of porosity, permeability, and capillary forces during imbibition. Several tests were performed and they confirmed the repeatability of the method. The water/air system was examined extensively. It was confirmed that different core cross-sectional areas did not bias results.

CT imaging of the imbibition process permitted not only the observation of the advance of the water front into the cores but explains the observed trends in weight gain as a function of time. Images obtained for diatomites and chalk show a homogeneous and piston-like water front during the process. Results for sandstone showed good agreement with previous work [6,7,11] and permitted the comparison of imbibition potential for different types of rocks. In impermeable diatomite, capillary forces result in a strong imbibition potential for water. However, the rate of imbibition in oil-filled systems appears to be slow. This work is a stepping stone to a more complete study of spontaneous imbibition in water/oil systems.

Nomenclature

A = *cross-sectional area,* L^2
k = *permeability,* L^2
m = *mass of water imbibed, M*
ρ_w = *water density,* mL^{-3}
S_w = *water saturation, dimensionless*
μ_w = *water viscosity,* $ML^{-1}T^{-1}$
P_c = *capillary pressure,* $ML^{-1}T^{-2}$
ϕ = *porosity, dimensionless*
σ = *interfacial tension,* MT^{-2}
t = *time, T*
IP = *Imbibition potential,* LMT^{-2}
$J(S_w)$ = *Leverett's J-function, dimensionless*
CT_{wet} = *CT value for a fully water saturated core*
CT_{dry} = *CT value for the dry core*
CT_{water} = *CT value of water*
CT_{air} = *CT value of air*
CT_{obj} = *CT value of the image being processed*

Subscripts

d = *diatomite*
s = *sandstone*

Acknowledgments

This work was supported by the Assistant Secretary for Fossil Energy, Office of Oil, Gas and Shale Technologies of the U.S. Department of Energy, under contract No. DE-FG22-96BC14994 to Stanford University. The support of the SUPRI-A Industrial Affiliates is likewise gratefully acknowledged.

References

1. Stosur, J.J. and A. David: "Petrophysical Evaluation of the Diatomite Formation of the Lost Hills Field, California," *Jour. of Petroleum Tech.*, 28(October) (1971) 1138-1144.
2. Schwartz, D.E.: "Characterizing the Lithology, Petrophysical Properties, and Depositional Setting of the Belridge Diatomite, South Belridge Field, Kern County, California", in *Studies of the Geology of the San Joaquin Basin*, S.A.Graham and H.C. Olson, Editors, Society of Economic Paleontologists and Mineralogists, Los Angeles, (1988) p. 281-302.
3. "Shell Expanding Bellridge Diatomite Program," *Oil and Gas Journal*, 92(April 11) (1994) 40-42.
4. Ilderton, D.C., T.W. Patzek, J.W. Rector, and H.J. Vinegar: "Passive Imaging of Hydrofractures in the South Belridge Diatomite," *SPE Formation Evaluation*, **March**(1996) 46-54.
5. Bhat, S.K., L.M. Castanier, and A.R. Kovscek: "Unpublished results: scanning electron microscopy and mercury porosimetry

of diatomite," (1997).
6. Handy, L.L.: "Determination of Effective Capillary Pressures for Porous Media from Imbibition Data," *Petroleum Transactions, AIME*, 219(1960) 75-80.
7. Garg, A., E. Zwahlen, and T.W. Patzek: "Experimental and Numerical Studies of One-Dimensional Imbibition in Berea Sandstone," Proceedings of the The Sixteenth Annual American Geophysical Union Hydrology Days, Fort Collins, CO (April 15-18, 1996).
8. Garg, A., A.R. Kovscek, M. Nikrakvesh, L.M. Castanier, and T.W. Patzek: "CT Scan and Neural Network Technology for Construction of Detailed Distribution of Residual Oil Saturation During Waterflooding," SPE 35737, in Proceedings of the Western Regional Meeting, Anchorage, Alaska (May 22-24, 1996).
9. Leverett, M.C.: "Capillary Behavior in Porous Solids," *Trans., AIME*, 142(1941) 152-169.
10. Blunt, M.J. and H. Scher: "Pore-Level Modeling of Wetting," *Physical Review E: Statistical Physics, Plasmas, Fluids, and Related Interdisciplinary Topics*, 52(6) (1995) 6387-6403.
11. Babadagli, T. and I. Ershaghi: "Imbibition Assisted Two-Phase Flow in Natural Fractures," SPE 24044, in Proceedings of the Western Regional Meeting of the Society of Petroleum Engineers, Bakersfield, CA (March 30 - April 1, 1992).

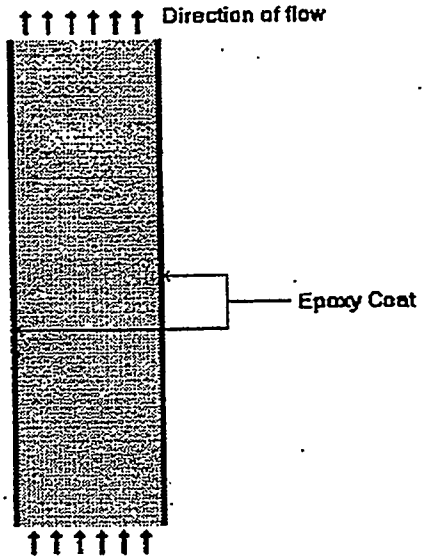

Fig. 1 Schematic representation of flow path through the core (One dimensional flow)

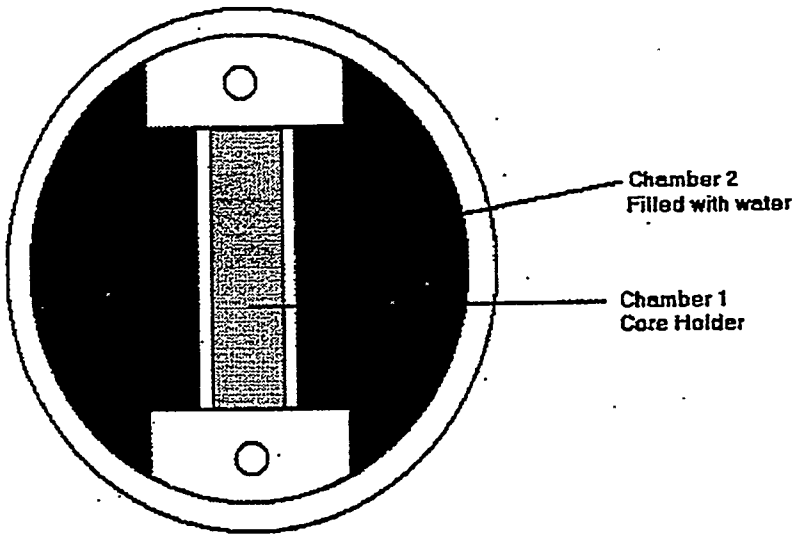

Fig. 2 Outline of the cell showing the two chambers

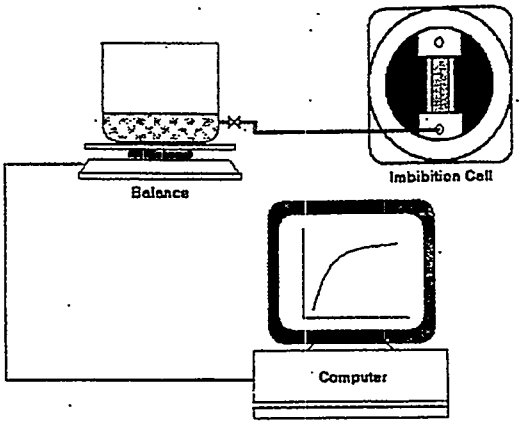

Fig. 3 Schematic representation of experimental design for CT scanning and recording of the change in the weight of the core

Table 1: Rock sample characteristics

Core	Rock Type	Shape	Length cm	Diameter cm	Side cm	Porosity %
1	Berea	Cylindrical	11.0	2	----	15
2	Berea	Square	9.0	---	1.7	15
3	Diatomite	Cylindrical	8.43	2.5	----	65
4	Chalk	Cylindrical	10.0	2.5	----	21

Table 2: Results obtained for spontaneous imbibition in different experiments

Core	Rock Type	Slope [1E01gr/sec$^{0.5}$]	Porosity %	Imbibition Potential [1E3 dyne]	Slope / A [1E2gr/sec$^{0.5}$/cm^2]
1	Berea	1.4226	15	3.9953	3.4621
1	Berea	1.4883	15	4.4479	3.6652
1	Berea	1.4990	15	5.1705	3.9384
2	Berea	1.4723	15	4.3357	3.6065
3	Diatomite	4.4803	65	5.9118	8.7709
3	Diatomite	4.3310	65	6.1461	8.9386
4	Chalk	0.6051	21	0.3845	1.2708

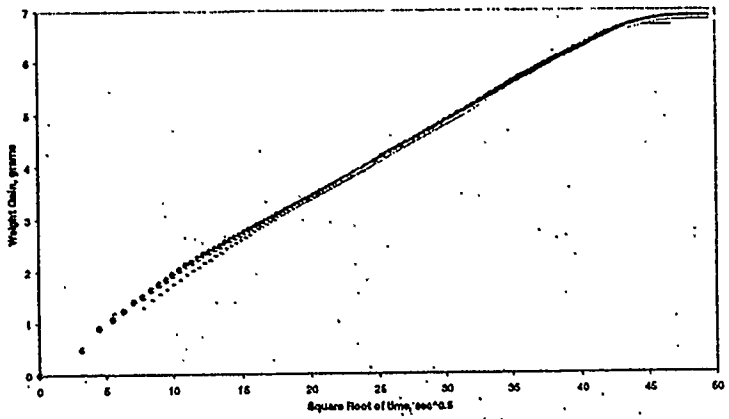

Fig. 4 Spontaneous imbibition in Berea sandstone
Repeatability tests

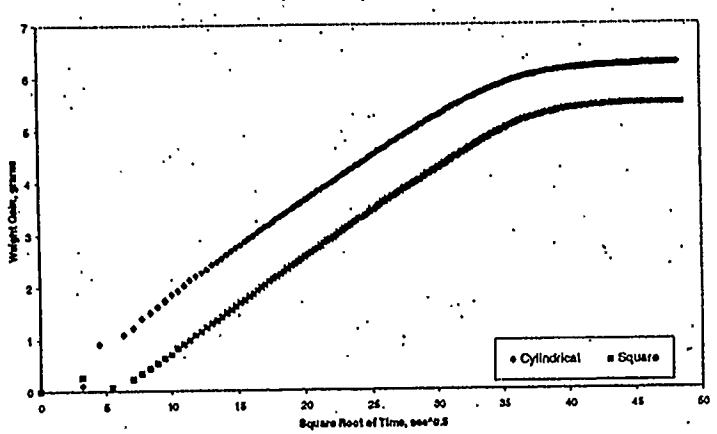

Fig. 5 Spontaneous imbibition in cylindrical and squared core
(Berea Sandstone)

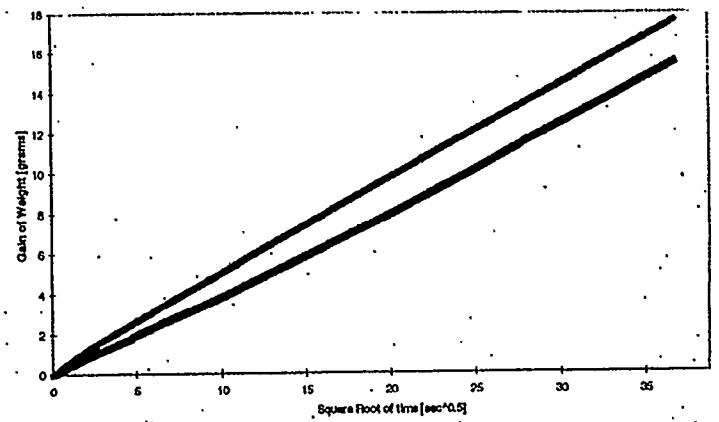

Fig. 6 Spontaneous imbibition in diatomite
repeatability Tests

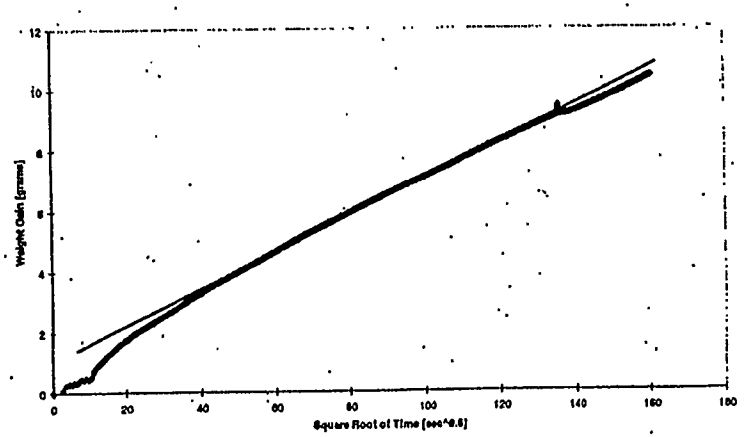

Fig. 7 Spontaneous imbibition in chalk

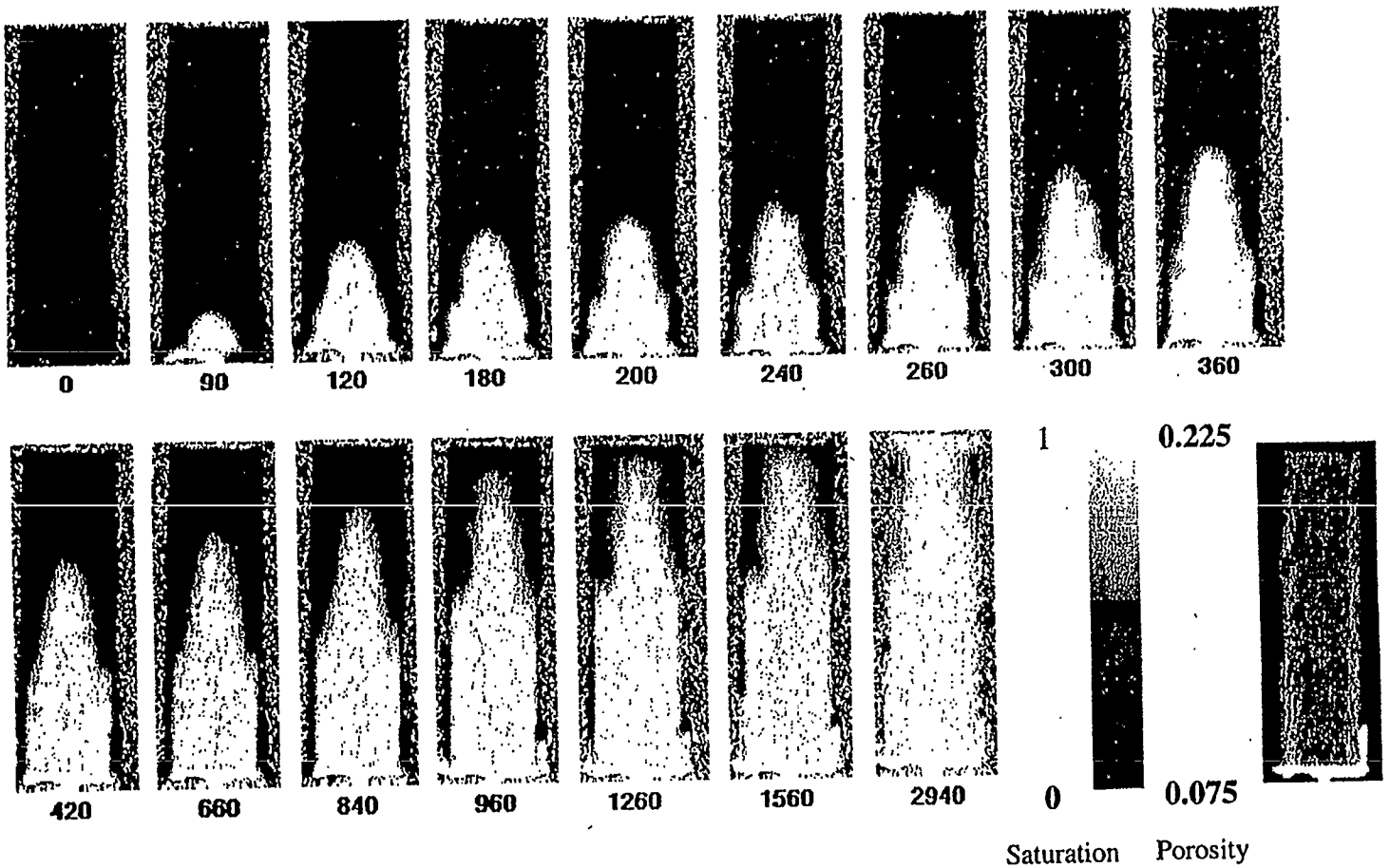

Fig. 8 : Images of Spontaneous Imbibition on Berea Sandstone at different times (sec)

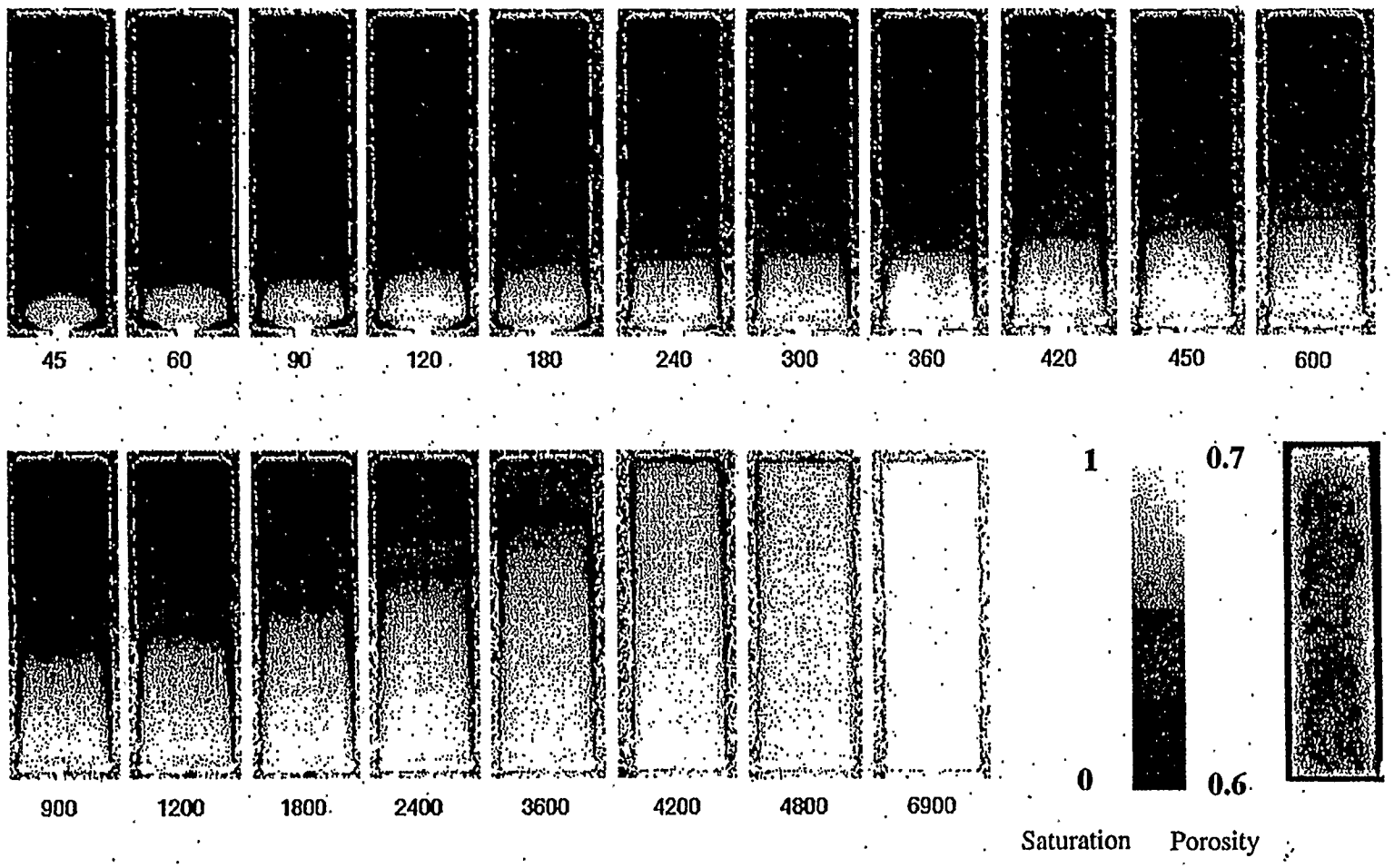

Fig. 9 : Images of Spontaneous Imbibition on Diatomite at different times (sec)

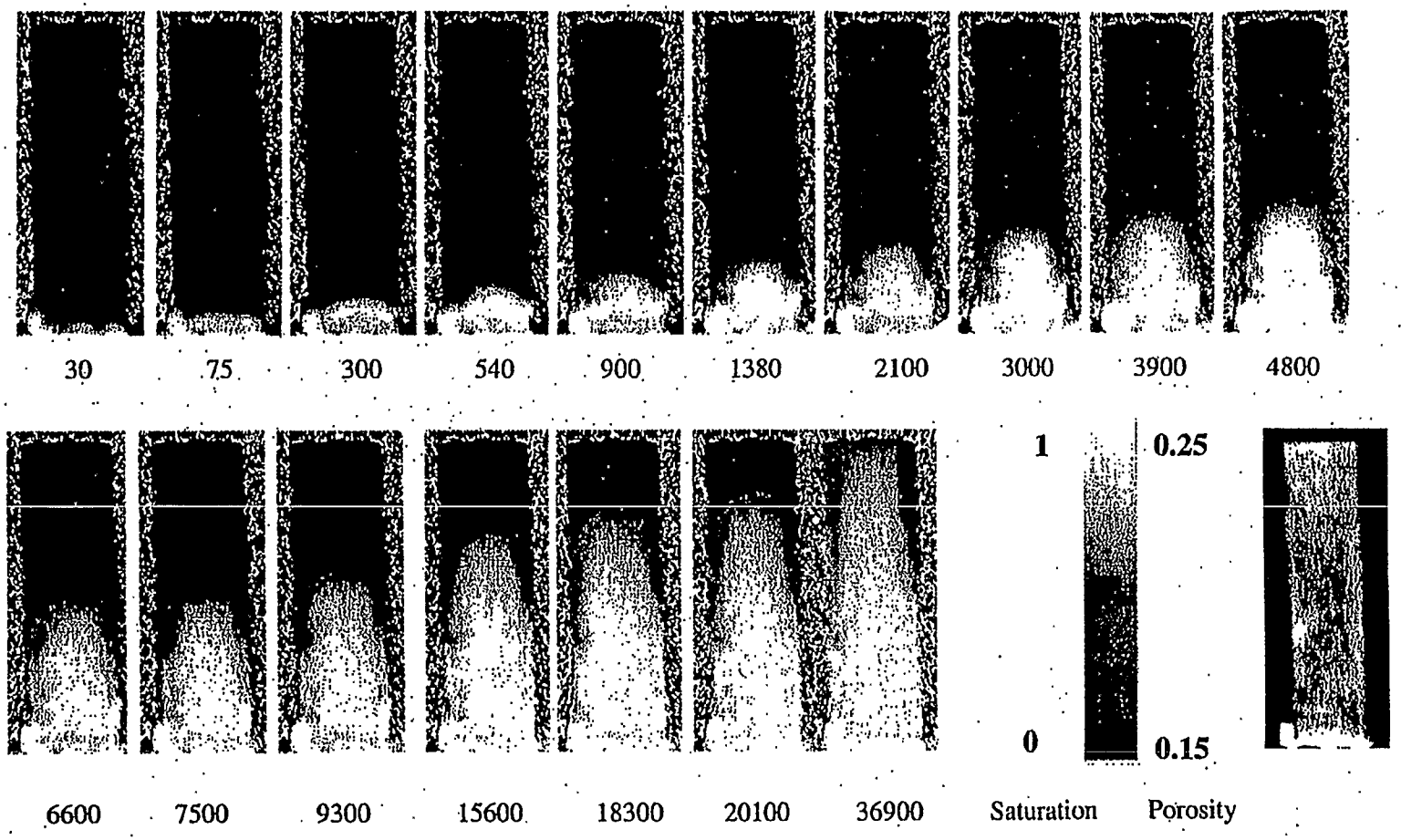

Fig. 10 : Images of Spontaneous Imbibition on Chalk at different times (sec)

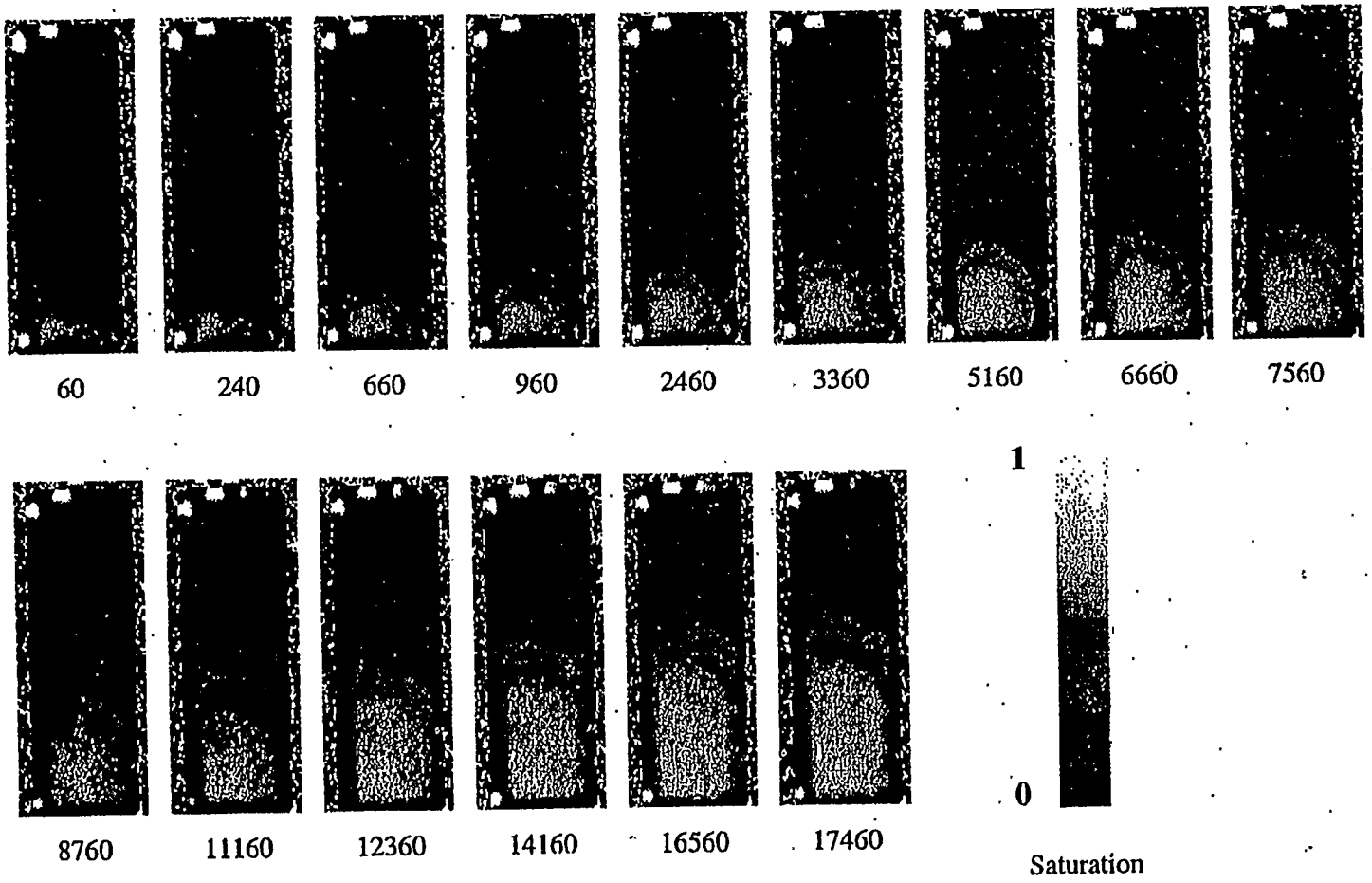

Fig. 11 : Images of spontaneous imbibition in diatomite at different times (sec).
Water-oil system

PROJECT 2: IN-SITU COMBUSTION

To evaluate the effect of different reservoir parameters on the in-situ combustion process. This project includes the study of the kinetics of the reactions.

2.1 IN-SITU COMBUSTION USING WATER SOLUBLE METALLIC ADDITIVES

(U. Diwan)

2.1.1 INTRODUCTION

Crude oils are often grouped into three categories based on specific gravity range:

1. Heavy Oil (10°-20°API)
2. Intermediate Oil (20°-30°API)
3. Light Oil (greater than 30°API)

Heavy oils consist mainly of high density naphthenes, aromatics and heteroatoms that are poor in alkanes, while light oils consist mainly of alkanes (Boduszynski, 1987; Boduszynski, 1988). Bitumen or tar are extremely dense hydrocarbons (about 10°API or less), and are non-volatile liquids, semi-solids or solids.The deposits are often referred to as oil sands or tar sands.

2.1.2 IN-SITU COMBUSTION

In-situ combustion is a thermal recovery technique in which a part of the heavy oil in place is burned to generate heat. This heat brings about a reduction in viscosity of the crude oil to get improved mobility and hence oil production rate and recovery. In a laboratory the process of ignition is initiated by using electric heaters while a stream of air is injected into a combustion tube to initiate and sustain combustion. Pure oxygen may also be used, but for economy sake air is popular. The fuel that is burned is the unrecoverable carbon rich residue of that is left on the reservoir matrix behind the steam front as a result of steam distillation, thermal cracking and some catalytic cracking. The heat that is generated partially distills the crude oil. The lighter ends are distilled off, and they condense in the cooler regions ahead of the combustion front along with the vaporized connate water and

water produced as a combustion byproduct. The region ahead of the combustion front is heated by conduction, by convection of combustion gases, and by the condensation of volatiles (light ends) and steam. The oil ahead of the combustion front is displaced toward the production well by gas drive provided by the combustion gases, by hot water and steam steam drive, and by miscible drive provided by the condensed light hydrocarbons (Alexander *et al.*, 1962; Holt, 1992).

A typical combustion front moves through the reservoir matrix by consuming the fuel as it moves ahead, thereby leaving no oil behind the burning front. Figure 1 (Shallcross, 1989) shows the typical combustion zones and a temperature profile of the in-situ combustion process. As the combustion front approaches the volume element, the temperature of the element rises and water and light ends are vaporized. These vapors are carried in the gas stream and condense in the cooler regions ahead of the combustion front. The water vapors condense to form a water bank (E), following a bank of light hydrocarbons (F). A steam plateau (D) comprises of the steam-liquid, two-phase region. As the temperature in the volume element exceeds $350^{\circ}C$ the oil undergoes thermal cracking to form a volatile fraction and a low volatility heavy residue (represented by C). The volatile fraction gets carried in the gas stream and the heavy residue constitutes the fuel which gets burned in the combustion zone (B). The heat generated in the combustion zone gets transported ahead of the front by conduction and convection by the vapors and liquids. The combustion zone is often only a few inches in thickness and has a temperature in the range 350° - $650^{\circ}C$. As the combustion front moves past this volume element it leaves behind a zone of clean sand (A) which serves as a preheater for the incoming air.

2.1.2.1 Applicability, Merits and Demerits of In-situ Combustion

In-situ combustion is applicable to a wide range of reservoir fluid characteristics. The absence of well bore heat losses in the injection well allows in-situ combustion to be carried out in deeper reservoirs having thinner, tighter sand sections which are not amenable to steam injection. The oil that is produced is also lighter than the oil in place as a result of cracking and distillation.

This technique is amongst the most energy efficient of improved oil recovery methods available today for heavy oils. However, one major constraint that limits its practical application is the amount of fuel formation in the matrix. If a sufficient amount of fuel is not deposited, as is often the case for light oils, the combustion front will not sustain itself. Conversely, if the quantity of fuel deposited is large, as is often the case with very heavy oils, the rate of advance of the front tends to be slower, with an uneconomically high demand for compressed air to sustain combustion (Alexander *et al.*, 1962).

As a result it would be desirable to find substances that alter the reaction kinetics of oil oxidation during in-situ combustion. There are a number of factors affecting the rates of these reactions, among which are the composition and concentration of the catalyst, surface of the catalyst available for reaction temperature. Combustion tube studies with metallic additives (Baena *et al.*, 1990; Castanier *et al.*, 1992; Holt, 1992) have shown that the addition of water soluble metallic salts can change the reaction kinetics of combustion. These indicate an increased fuel deposition in runs which carried salts of iron or tin. It has not been established for certain how the presence of theses substances affect the fuel deposition mechanism, but it may be due to the reduction in the temperature required for cracking reactions.

Kinetic tube studies with metallic additives (de los Rios *et al.*, 1988; Shallcross, 1989) indicate that aqueous solutions of certain metallic salts like zinc, iron and tin increased the fuel concentrations. All these studies indicate that the overall oxidation mechanism of crude oils in porous media is the result of an overlap of several reactions that occur at different ranges of temperature. These have been classified as low temperature, medium temperature and high temperature reactions.

In a properly designed combustion process there should be minimal amount of low temperature oxidation (Agrawal and Sidqi, 1996). Therefore, the presence of metallic additives, which affect reaction kinetics, would affect the overall performance of the combustion process. It is believed that low temperature oxidation reactions affect fuel formation, therefore the alteration of this reaction would affect fuel deposition characteristics.

Earlier work done by De Los Rios (1987), has shown, on a quantitative basis, that the use of metallic additives affects the nature of the fuel formed; this, in turn, will affect

the heat of combustion, the air-oil ratio, the air requirements, the front velocity and the oil recovery rate.

2.1.2.2 Metallic Additives in In-situ Combustion

Studies on the effect of metallic additives (salts) on in-situ combustion date back to the early nineteen seventies. It was observed that reservoirs having mineral contents with high metallic content in the rock matrix had increased fuel deposition (Burger and Sahuquet, 1972).

Early attempts at understanding the mechanics of oil oxidation reactions was done through kinetic tube experiments in the presence of metallic additives.

A brief description to explain how the oxidation reactions take place is given on the following page.

2.1.2.3 Kinetic Studies with Metals and Metallic Additives

Several studies have been performed to determine the influence of metals and metallic additives on the oxidation characteristics of crude oils. The work performed and observations made during these experiments are described below.

1. Of particular importance to the current study are the kinetic studies performed by De Los Rios (1988) and Shallcross (1989) at Stanford University. De Los Rios performed kinetic experiments on Huntington Beach Oil and various metallic additives. Shallcross performed kinetic experiments on Huntington Beach and Venezuelan oils with various metallic additives. Both studies analyzed oxygen consumption data by decoupling the total oxygen consumption data into three parts. This was done to represent the oxygen consumed by the three competing groups of reactions. The found that metallic additives iron and tin increased oxygen consumption. They also reported that iron and tin increased the reaction rates for the oxidation reactions. They found that zinc did not produce the effects reported for iron and tin. From the results of these studies it was

expected that iron and tin may be useful agents in catalyzing combustion reactions (Mamora, 1993).

2. Burger and Sahuquet (1981) report on two kinetic runs using 2000 ppm copper performed on a 27°API oil. The activation energy for the LTO was found to be lowered due to the copper additive (Holt, 1992).
3. Fassihi *et al.* (1981) report on kinetic experiments with 2000 ppm copper says that the activation energy of the LTO was unaffected, but itís reaction rate was increased. Fassihi also reported that the activation energy for the high temperature portion of the reaction was reduced (Baena *et al.*, 1990; Mamora, 1993).

Reactions taking place:

1. Low temperature oxidation (LTO)	Result in formation of peroxides, hydroperoxides, aldehydes, ketones, carboxylic acids and alcohols (Burger and Sahuquet, 1972). Alexander *et al.*(1962) and Al-Saadon (1970) showed that fuel availability was increased when LTO of crude oil took place. Dabbous and Fulton (1974) corroborated this and also found that LTO causes a substantial decline in recoverable oil from the distillation and cracking zones, an increase in the fuel deposition and marked changes in the fuel characteristics and coked sand properties. Weijdema (1968) and Fassihi (1981) found that the order for the LTO reaction, in terms of the partial pressure of oxygen, was close to unity.

2. Medium temperature oxidation (MTO)	Involve distillation, visbreaking and coking of the fuel along with partial oxidation of the products formed (Bardon and Gadelle, 1977; Fassihi, 1981; Sidqi *et al.*, 1985). The amount of coking and atomic H/C ratio of the fuel were found to decrease with increasing coking temperature (Bousaid, 1967). Increasing pressure was found to increase the amount of hydrocarbon residue formed; but the fuel deposited has a lesser hydrogen content (Sidqi *et al.*, 1985).
3. High temperature oxidation (HTO)	Involve oxidation of the cracked hydrocarbon residue. HTO takes place according to the following equation:
$CH_n + \left(\frac{2m+1}{2m+2} + \frac{n}{4}\right) O_2 \rightarrow \left(\frac{m}{m+1}\right) CO_2 + \left(\frac{1}{m+1}\right) CO + \left(\frac{n}{2}\right) H_2O$ m: ratio of carbon dioxide to carbon monoxide formed upon oxidation of the fuel n: atomic hydrogen to carbon ratio of fuel burned The reaction rate has been found to be first order with respect to the fuel concentration and was found to have an order of 0.5 to 1.0 with respect to the oxygen partial pressure (Dabbous and Fulton, 1974).	

To recap:

- It has been found by previous researchers that the presence of certain metals can affect the kinetic parameters used to model combustion reactions.
- These kinetic experiments can give estimates of activation energies and reaction rates for combustion reactions.

2.1.2.4 Tube Studies with Metallic Additives

Observations that the physical and chemical properties of the core material can affect the combustion performance in tube runs was made by several researchers. Some of them are mentioned below.

1. Vossoughi *et al.*, 1982, Hardy *et al.*, 1972, Alexander *et al.*, 1962 observed that, for a particular oil, more fuel can be expected from a native core than from a clean sand pack. This is believed to result from both physical and chemical processes. Fine grained material in native cores provides more surface area for combustion reactions while metals in natural minerals act as catalysts (Baena *et al.*, 1990; Bardon and Gadelle, 1977).
2. Baena *et al.*, 1990 report on experiments with 22°API Huntington Beach Oil. They observed that tin and iron additives increased oxygen utilization efficiency, burning front velocity, and fuel concentration. The zinc additive showed lesser effect (Baena *et al.*, 1990).
3. Castanier *et al.*, 1992 report on thirteen metallic additive combustion tube runs. The runs made with 10°API Hamaca oil show that tin and iron increased the fuel deposition, oxygen utilization efficiency, and front velocity while zinc was less effective (Bardon and Gadelle, 1977).

2.1.3 PRESENT STUDY

The present study shall involve a series of combustion tube experiments performed with the Wilmington Oil (~15°API) and a couple of aqueous metallic additives.

2.1.4 WORK COMPLETED

- Thermocouple testing
- Calibration of mass flow meter
- Calibration of mass flow controller
- Calibration of carbon monoxide gas analyzer
- Calibration of carbon dioxide gas analyzer

2.1.5 FUTURE WORK

- Calibration of oxygen analyzer
- Checking apparatus for leakages
- Checking data logger
- Transducer calibration to measure pressure drop along tube
- Conduct a trial run using no packing, just air
- Observe temperature profiles
- Pack the combustion tube with the crude oil
- Perform runs

2.1.6 REFERENCES

1. Agrawal, V.K. and Sidqi, A.: "A Study of In-situ Combustion on Saudi Tar," Stanford University Petroleum Research Institute, SUPRI-TR-105 [DE-FG22-93BC14899], Stanford University, Stanford (April 1996).
2. Alexander, J.D., Martin, W.L., and Dew, J.N.: "Factors Affecting Fuel Availability and Composition During In-Situ Combustion," *J. Pet. Tech.* (October 1962) 1154-1162.

3. Baena, C.J., Brigham, W.E., and Castanier, L. M.: "Effect of Metallic Additives on In-Situ Combustion of Huntington Beach Crude Experiments," Stanford University Petroleum Research Institute, SUPRI-TR-78 [DE-FG19-87BC14126], Stanford University, Stanford (August 1990).
4. Boduszynski, M. M.,: "Composition of Heavy Petroleums. 1. Molecular Weight, Hydrogfen Deficiency, and Heteroatom Concentration as a Function of Atmospheric Equivalent Boiling Point upto 1400°F (760°C)," *Energy & Fuels* (1987) **1.**
5. Boduszynski, M. M.: "Composition of Heavy Petroleums. 2.Molecular Characterization," *Energy & Fuels* (1988) **2.**
6. Bardon, C. And Gadelle, C.: ìEssai de Laboratoire Pour LíEtude de la Combustion In-Situ,î Institute Francais du Petrole, Paris (May 1977).
7. Bousaid, I.S. and Ramey, H.J. Jr.: "Oxidation of Crude Oil in Porous Media," *Soc. Of Pet. Eng. J.* (June 1968) 137-148.
8. "Combustion Kinetics," *Soc. Pet. Eng. J.* (October 1972) 410-420.
9. Castanier, L. M., Baena, C.J., Tavares, C., Holt, R. J., and Brigham, W.E.: "In-Situ Combustion with Metallic additives," No. SPE 23708, paper presented at the SPE-AIME Latin American Petroleum Engineering Conference, Caracas (March 1992).
10. Dabbous M.K. and Fulton, P.F.: "Low-Temperature Oxidation Reaction Kinetics and Effects on the In-Situ Combustion Process," *Soc. of Pet. Eng. J.* (June 1974) 253-262.
11. De Los Rios, C. F., Brigham, W. E., and Castanier, L. M.: "The Effect of Metallic Additives on the kinetics of Oil Oxidation Reactions in In-Situ Combustion," Stanford University Petroelum Research Institute, SUPRI-TR-63 [DE-FG19-87BC14126] Stanford University, Stanford, (November 1988).
12. Fassihi, M. R.: "Analysis of Fuel Oxidation in In-Situ Combustion Oil Recovery," PhD disertation, Stanford University, Stanford (May 1981).
13. Gureyev, A. A., and Sablena, Z. A.: "The Role of Metals in Oxidation of Hydrocarbon Fuels in the Liquid Phase," Scientific Research Institute of Fuel and Lubricating Materials, Pergamon Press (1965).
14. Holt, R. J.: "In-Situ Combustion with Metallic Additives," Stanford University Petroleum Research Institute, SUPRI-TR-87 [DE-FG22-90BC14600], Stanford University, Stanford (July 1992).

15. Mamora, D. D.: "Kinetics of In-Situ Combustion," PhD dissertation, Stanford University, Stanford, California (May 1993).

16. Shallcross, D. C.: "Modifying In-Situ Combustion Performance by the use of Water-Soluble Metallic Additives," No. SPE 19485, paper presented at the SPE-AIME Aia-Pacific Conference, Sydney, Australia (September 1989).

17. Sidqi, A., Ramey, H. J. Jr.,Pettit, P., and Brigham, W. E.: "The Reaction Kinetics of Fuel Formation for In-Situ Combustion," Stanford University Petroleum Research Institute, Stanford, CA, SUPRI-TR-46 [DE-AC03-81SF 11564] (May 1985).

18. Weijdema, J.: "Determination of the Oxidation Kinetics of the in-Situ Combustion Process," Report from Koninklijke/Shell Exploratie En Producktie Laboratorium, Rijswijk, The Netherlands (1968).

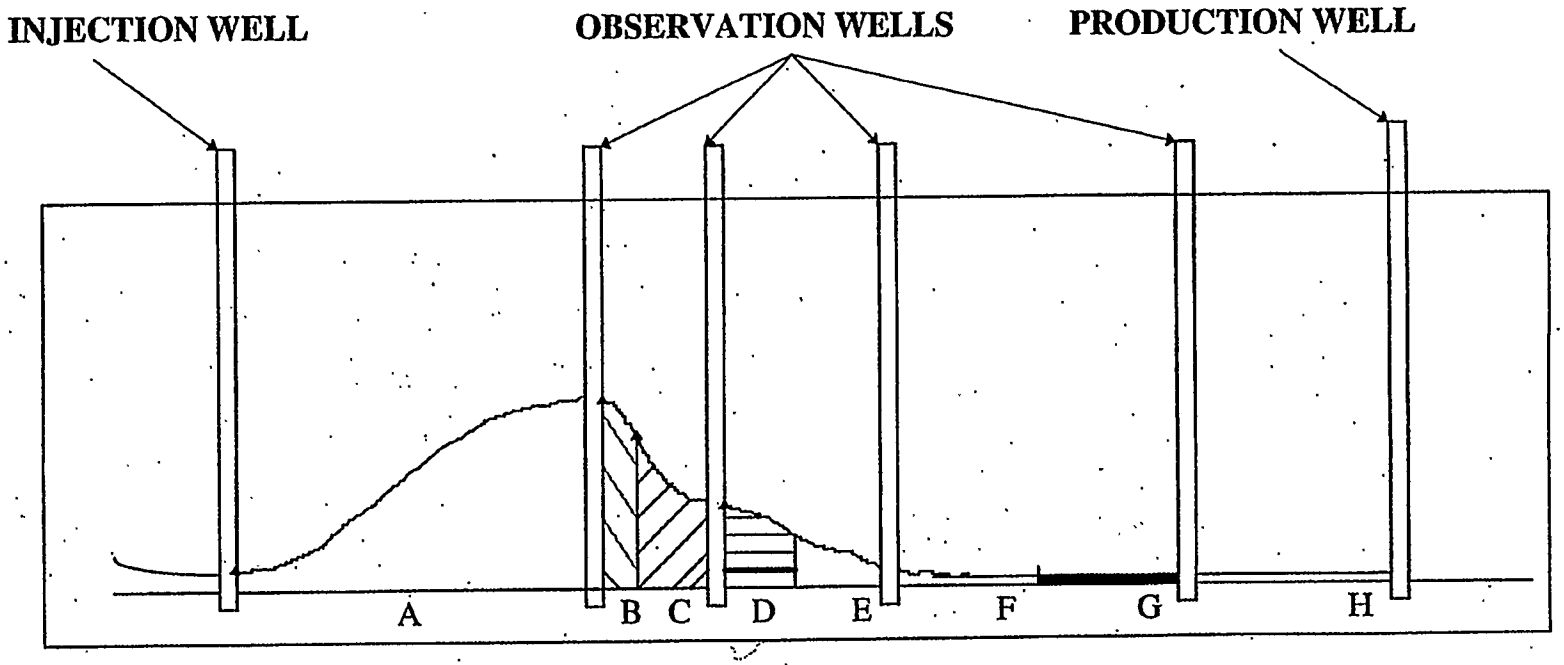

A : BURNED ZONE
B : COMBUSTION ZONE
C : CRACKING ZONE
D : STEAM PLATEAU
E : WATER BANK
F : LIGHT HYDROCARBONS
G : OIL BANK
H : INITIAL ZONE

Fig 1 : TEMPERATURE PROFILES AND CORRESPONDING COMBUSTION ZONES

PROJECT 3: STEAM WITH ADDITIVES

To develop and understand the mechanisms of the process using commercially available surfactants for reduction of gravity override and channeling of steam.

3.1 SIMULATION OF OIL RECOVERY WITH SINGLE WELL SAGD

(K.T. Elliott)

3.1.1 INTRODUCTION

Steam-assisted gravity drainage (SAGD) is an effective method of producing heavy oil. SAGD is essentially a special form of steamflooding. The primary objective in steamflooding, and thermal recovery in general, is to mobilize the oil by increasing temperature and decreasing viscosity. Thermal recovery is effective because slight increases in temperature cause drastic decreases in viscosity.

In comparison to traditional steamflooding, SAGD is advantageous because it uses gravity as the chief driving force to affect oil movement, and it avoids viscous fingering which occurs when heavy oils are pushed by lighter fluids. Conventional SAGD involves drilling a horizontal injection well above a horizontal production well. During the process, a steam chamber forms and rises to the top of the reservoir, while warmed oil and condensed steam fall to the production well.

A new and similar technique which involves drilling only one horizontal well to create the same gravity drainage mechanism has been tested with favorable results by ELAN Energy in Canada[1]. The success of this project has prompted us to look into single-well steam assisted gravity drainage (SW-SAGD). We are primarily interested in using computer simulation to gain a better understanding of the SW-SAGD process. Likewise, we will assess the suitability of current thermal simulators for evaluating SW-SAGD.

3.1.2 PROJECT PLANS

We plan to evaluate three different scenarios which are displayed in Fig. 1 and described on the following page.

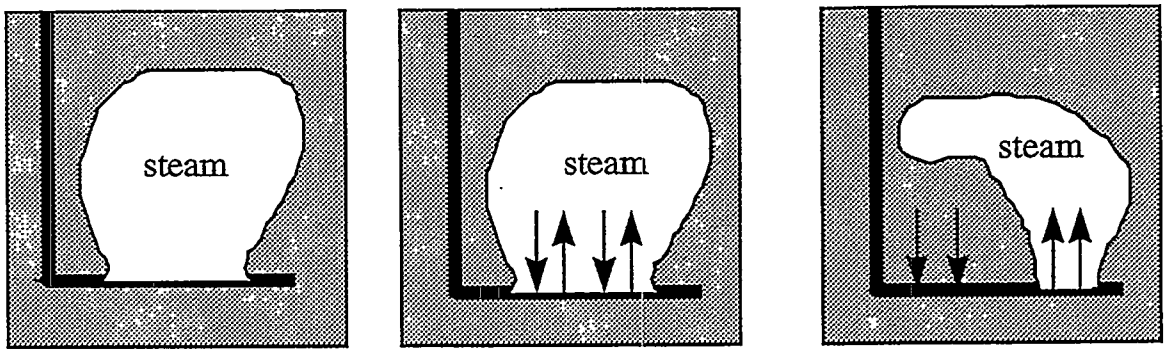

1. Cyclic Injection/Production

2. Counter-Current Injection/ Production

3. Co-Current Injection/ Production

Fig. 1 - Proposed Single-Well SAGD Test Cases

1. *Cyclic Injection/Production.* In this process the well will alternate as a horizontal steam injection well, then revert to production in a cyclic pattern. The length of steam soak on recovery efficiency will also be investigated.
2. *Counter-Current Injection and Production.* Under this idealized process, steam injection and concurrent oil/water/steam production occurs along the entire length of the wellbore.
3. *Co-Current Injection at the Toe and Production from the Heal.* In this process steam injection at the toe of the well occurs simultaneously with production from the heal.

Reviewing these three strategies will help us understand the reservoir characteristics that will best allow for SW-SAGD, and will help us understand how to optimally apply the process.

A significant challenge in the project will be representing the well in a simulator. We suspect that development of the well model is difficult under the circumstances of SW-SAGD. Nonetheless, we will assess the suitability of current thermal simulators for evaluating SW-SAGD.

3.1.3 LITERATURE SURVEY

There is currently very little literature available on the topic of SW-SAGD. In fact, we encountered only one paper that deals specifically with the topic. The available paper, by Oballa and Buchanan (1996), discusses results from a simulation study of SW-SAGD. The authors simulated drainage and cyclic processes for both mobile and viscous oil. Their major conclusions follow:

1. SW-SAGD may be difficult to operate because it is dominated by varying conditions in the wellbore.
2. SW-SAGD may be a feasible method of producing mobile oil if a proper operating strategy is applied.
3. In viscous oil reservoirs, energy efficiency is very poor and cycling may be more advantageous.
4. The cyclic process with a single horizontal well is promising and should be studied in more detail.

A discussion directed by Nzekwu at the CIM 1996 Annual Technical Meeting also reviewed the topic. Nzekwu is an engineer closely tied to the SW-SAGD attempt by ELAN Energy Inc. Unfortunately, he never published a corresponding paper. Townson (1997) discusses recent developments in the technology of heavy oil production. Along with other techniques, he briefly discusses SW-SAGD and notes the companies that have experimented with it. Duerksen (1990) describes his work in simulating concurrent production and steam injection in vertical wells.

While there are few papers that discuss SW-SAGD, numerous papers exist which describe the development of analytical, experimental, and simulation models for conventional SAGD. In our attempt to gain an understanding of SW-SAGD, it will certainly be instructive to review these papers. Butlerís Thermal Recovery of Oil and Bitumen, is a comprehensive text which describes in detail the concepts and theory behind SAGD. Other relevant references are also listed below.

3.1.4 SW-SAGD References

1. Towson, D.E.: "Canadaís Heavy Oil Industry: A Technological Revolution," paper SPE 37972 presented at the 1997 SPE International Thermal Operations and Heavy Oil Symposium, Bakersfield, CA (February 10-1, 1997).
2. Oballa, V., and Buchanan, W.L.: "Single Horizontal Well in Thermal Recovery Processes," paper SPE 37115, presented at the 1996 International Conference on Horizontal Well Technology, Calgary, Canada (November 18-20, 1996).
3. Duerksen: "Simulation of a Single-Well Injection/Production Steamflood (SWIPS) Process in an Athabasca Tar Sand," paper SPE 20017, presented at the 1990 Californai Regional Meeting , Ventura, CA (April 4-6, 1990).
4. Ben Nzekwu, SAGD Technologies, Inc., ELAN Energy Inc. "Can Single-Well Based EOR Processes Inject New Life into Mature Reservoirs?" discussion at the 1996 CIM Annual Technical Meeting, Calgary (June 10-12, 1996).

3.1.5 Bibliography

5. Butler, R.M.: Thermal Recovery of Oil and Bitumen, Englewood Cliffs, N.J., Prentice Hall, 1991.
6. Card, C., Oballa, V., Kisman, K., Fu., M., and Wang, X.: "Three-Dimensional SAGD Simulation of Dipping Oil Sand Reservoir," paper CIM 96-56, presented at the 1996 Annual Technical Meeting, Calgary (June 1996).
7. Chow, L. and Butler, R.M.: "Numerical Simulation of the Steam-assisted Gravity Drainage Process (SAGD)," J. Cdn. Pet. Tech. (June. 1996) 55-62
8. Farouq-Ali, S.M.: "Is There Life After SAGD?" *J. Can. Pet Tech.* (June 1997) 20-23.
9. Ito, Y. and Suzuki, S.: "Numerical Simulation of the SAGD Process in the Hangingstone Oil Sands Reservoir," paper CIM 96-57, presented at the 1996 Annual Technical Meeting, Calgary (June 10-12).

10. Kamath, V.A. and Hatzignatiou, D.B.: "Simulation Study of Stealm-Assisted Gravity Drainage Process in Ugnu Tar Sand Reservoir," paper SPE 26075, presented at the Western Regional Meeting, Anchorage (May 26-28, 1993).
11. Kisman, K.E., and Yeung, K.C.: "Numerical Study of the SAGD Process in the Burnt Lake Oil Sands Lease," paper SPE 30276, presented at the Inbternational Heavy Oil Symposium, Calgary (June 19-21, 1995).
12. Nasr, R.N., Golbeck, H., and Lorimer, S.: "Analysis of the Steam Assisted Gravity Drainage (SAGD) Process Using Experimental/Numerical Tools," paper SPE 37116 presented at the 1996 International Conference on Horizontal Well Technology, Calgary (November 18-20, 1996).
13. Sasaki, K., Akibayashi, S., Kosukegawa, H., and Kato, M.: "Experimental Study on Initial Stage of SAGD Process Using 2-Dimensional Scaled Model for Heavy Oil Recovery," paper SPE 37089, presented at the 1996 International Conference on Horizontal Well Technology, Calgary (November 18-20, 1996).
14. Singhal, A.K., Das, S.K., Leggit, S.M., Kasraie, M., and Ito, Y.: "Screening of Reservoirs for Exploitation by Application of Steam Assisted Gravity Drainage/Vapex Processes," paper SPE 37144 presented at the 1996 International Conference on Horizontal Well Technology, Calgary (November 18-20, 1996).
15. Zhou, G., Zhang, R., Shen, D., and Pu, H.: "Horizontal Well Application in a High Viscous Oil Reservoir," paper SPE 30281 presented at the International Heavy Oil Symposium, Calgary (June 19-21, 1995).

3.2 PERMEABILITY MODIFICATION OF DIATOMITE DURING HOT FLUID INJECTION

(S.K. Bhat and A.R. Kovscek)

3.2.1 Permeability Modification of Diatomite During Hot Fluid Injection

(S.K. Bhat and A.R. Kovscek)

The paper on the following page was prepared for presentation at the 1998 Western Regional Meeting held in Bakersfield, California, May 10-13, 1998.

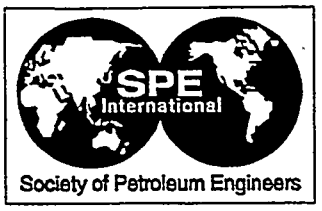

SPE 46210

Permeability Modification of Diatomite During Hot Fluid Injection

S. K. Bhat and A. R. Kovscek, Stanford U.

This paper was prepared for presentation at the 1998 Western Regional Meeting held in Bakersfield, California, 10-13 May 1998.

Abstract

One area of concern that has accompanied steam injection into diatomite for oil recovery is the evolution of permeability and porosity as silica dissolves in hot steam condensate and is redistributed on rock surfaces as condensate cools. Since grain size is quite fine and typical pore throat dimensions in diatomite range from roughly 1 to 6 μm, dissolution of silica near pore throats should increase permeability drastically. Likewise, a small amount of deposition at pore throats will cause clogging.

Our goals are to improve understanding of the effects of mineral dissolution/reprecipitation in diatomite and to formulate permeability versus porosity relationships necessary for reservoir simulation. We employ a network model to gauge how evolving pore topology affects permeability and porosity. Hence, we calculate macroscopic trends by incorporating pore-level physics. The model is anchored to real rock through actual pore-throat and pore-body size distributions. Results indicate that plugging of the network and a corresponding decrease in permeability occur when moderate amounts of silica precipitate. Plugging is most severe for small values of network connectivity and large values of the pore-body to pore-throat aspect ratio.

When porosity change from 0 to 10 % is examined closely, it is found that permeability decrease correlates with porosity decrease according to a power-law expression with power-law exponents in the range of 8 to 9. Such a power-law dependence has been measured previously by experiment[1]. These values confirm the strong dependence of permeability on deposited silica. The dissolution process displays an equally strong dependence on porosity change and again permeability increases most dramatically for dissolution in networks with small values of connectivity and large values of the pore-throat to pore-body aspect ratio. Again, power-law expressions adequately describe permeability increase as a function of porosity for a moderate range of dissolution.

Introduction:

Experience is beginning to show that steam drive with careful control of injection pressure can be an efficient technique for oil recovery from siliceous reservoirs that are relatively shallow, low permeability, thick, and highly layered. In the case of steam drive, recovery occurs by direct displacement of oil by steam and condensate and also by volumetric expansion of oil due to thermal conduction of heat through the formation. In contrast, water flood recovery relies on direct physical contact of water with the oil in the reservoir.

Steam injection has been used successfully to recover heavy and light oil from the South Belridge and Cymric diatomite (Kern Co, CA) [2-7]. The California diatomites are highly layered, thick, have permeability ranging from 0.01 mD to 10 mD [8,9], and porosity that ranges from 38 % to 65 % [10]. The low permeability results from extremely small-sized pore throats usually 1 to 6 μm in diameter. Steam injection into diatomite is not without complications. One factor is the solubility of diatomite in hot water. Diatomite is a hydrous form of silica or opal composed of microscopic shells of diatoms which are the remains of single-celled microscopic aquatic plankton. During steam injection, diatomite, which is principally silica (SiO_2) can dissolve in hot aqueous condensate and this dissolved silica is carried forward by the moving condensate. As the condensate travels away from the injector, it cools and the dissolved silica precipitates. Experiments [1] with injection of silica laden hot water suggest that silica deposition in diatomite leads to plugging. Later, the deposited silica may dissolve again if the local temperature increases. This process causes permeability redistribution within the reservoir, which is already relatively impermeable. Similarly, silica dissolution might increase permeability around the injection wells, thereby improving injectivity.

Silica deposition could also be a concern for waterflood operations. In the San Joaquin Valley, diatomaceous

reservoirs underly permeable sands containing heavy oil[8]. This heavy oil is recovered by steam injection. Produced hot condensate from the heavy oil recovery operations is sometimes reinjected in the diatomites. These waters are frequently laden with silica that might precipitate when contacting the cooler diatomaceous reservoirs.

To quantify changes in permeability and porosity of porous media undergoing diagenesis, we develop a network model and incorporate evolving pore shapes. The porous medium is represented by a Bethe lattice of known properties, and percolation theory used to predict the effects of dissolution and deposition on permeability and porosity of the porous medium. We consider only the flow of liquid water. Changes in permeability are correlated with changes in conductivity of the lattice, and the amount of silica deposited is related to available porosity of the lattice at any stage of deposition or dissolution. To model the diagenetic process, various dissolution and deposition patterns are considered. Based on these dissolution and deposition patterns, the network is updated to generate network conductivity and porosity. Our networks are anchored to real porous media through pore-throat and pore-body distributions as well as pore body to throat aspect ratios garnered from outcrop diatomite samples.

The following sections describe our network approximation of porous media, the rationale for our choice, and how pore throats and bodies are represented. Next, incorporation of silica dissolution and precipitation into first a single-pore model and then the network is discussed. The network is used to generate absolute permeability versus porosity relationships for silica redistribution in diatomite.

Network Approximation

Porous media can be approximated by lattices as illustrated in Fig. 1. Examples shown in the figure are a Bethe lattice (Fig. 1A), a hexagonal lattice (Fig. 1B), and a 2D-square lattice (Fig. 1C). A lattice is a connected network of flow paths between various points in space (2D or 3D). An advantage of the Bethe lattice is that analytical solutions are available for network conductivity.

Lattices are used to represent porous media, because they can capture at least two important properties of porous media. Firstly, porous media are a collection of pore bodies connected by pore throats. Secondly, porous media have connectivity between pore throats normally given as the coordination number Z. This number is used to quantify the connectivity of the lattice. These two properties of lattices coupled with the fact that flow properties like flow resistance can be randomly associated with the various bodies or throats or both make lattices a good choice for approximating flow in porous media.

We use a Bethe lattice, as illustrated in Fig. 1A, to approximate the matrix of diatomite pores. It is an endlessly branching network characterized by the coordination number and distribution of pore sizes. Because the problem of Bethe lattice conductivity has been solved analytically[11], these networks are especially attractive for our work. Moreover, Bethe lattices have been used to reproduce two and three-phase relative permeabilities in porous media [12-14]. Although networks more complicated than Bethe lattices are certainly possible, our ignorance in regard to pore-size, pore-shape, the distribution of connectivity, and pore topology of diatomite makes implementation difficult. Thus, the porous medium is represented by a Bethe lattice, with each flow connection having some conductivity governed by a conductivity distribution $G(g)$ where g is the conductivity of a single pore. The effective conductivity G_{eff} for such a network is given by the first derivative of a generating function $C(x)$ at the origin ,

$$G_{eff} = -ZC'(0) \tag{1}$$

where Z is the coordination number of the Bethe lattice [11] and the prime on C indicates differentiation with respect to the variable x which parameterizes the network

The Laplace transform of the generating function satisfies the following recursive integral equation,

$$\int_0^\infty e^{-tx} C(x)dx = \tag{2}$$

$$\frac{1-f}{t} + f\int_0^\infty G(g)\left\{\frac{1+t}{g} + \frac{g^2}{(t+g)^2}\int_0^\infty \exp\left(\frac{x-g}{g+t}\right)C(x)^{Z-1}dx\right\}dg$$

subject to the boundary condition, $C(0)=1$. In Eq.(2), f is the fraction of throats of the Bethe lattice that are available for flow. In the case of single phase flow and in the absence of silica diagenesis, all the throats of the network are available to flow and f equals 1.0. This remains true for dissolution as well. But in the case of deposition, some throats will clog, and hence, all of the throats will not contribute to flow. As deposition proceeds, the value of f decreases as pores fill with silica. Equation (2) can not be solved analytically as it is implicit in $C(x)$, but various series approximations have been developed. For our model, we use the series approximation of Heiba *et al.*[14,15].

The effective volume of a network at any stage in the diagenetic process is found from the volume distribution of the various throats, $V(v)$. The effective pore volume of the network is,

$$V = \int_0^\infty V(v)dv \tag{3}$$

where v is the volume of an individual pore. Evaluating effective network conductivity and available network pore volume using Eq.(2) and Eq.(3) requires functional forms for the distribution functions $G(g)$ and $V(v)$ which correctly represent the porous medium under investigation. We consider a porous medium to have pores characterized by a dimensionless throat radius r and a frequency of occurrence

$\alpha(r)$. Since f is the fraction of pores that are open, the distribution functions can be represented[16] as,

$$G(g) = (1-f)\delta(g) + fX^A\alpha(r)g(r) \quad (4)$$

$$V(v) = (1-f)\delta(v) + fv(r) \quad (5)$$

where $g(r)$ and $v(r)$ are the functions that relate the size, r, of a pore to its individual conductivity and volume, respectively. The Dirac delta function, δ, indicates that the clogged pores do not contribute to conductivity and pore volume. The factor X^A, called accessibility of the network, accounts for the random distribution of throats in the network that causes some non clogged pores to be unavailable for flow because they are cut off from the main mass of open pores by clogged pores. The value of X^A depends on the fraction of throats that are clogged and the connectivity, Z, of the network.

For a Bethe lattice, the accessibility function of the network has been found analytically[17]. It is related to the fraction of open throats by,

$$X^A(f) = \begin{cases} f\left(1-(f^*/f)^{\frac{2Z-2}{Z-2}}\right) & ;f \geq f_c \\ 0 & ;f < f_c \end{cases} \quad (6)$$

where f_c is the percolation threshold, *i.e.* the minimum value of the allowable fraction of throats below which no flow across the lattice occurs and f^* is the root of the following equation,

$$f^*(1-f^*)^{Z-2} - f(1-f)^{Z-2} = 0 \quad (7)$$

such that the root $f^* \to 0$ as $f \to 0$ and $f \to 1$. In our calculations to follow, we use the series approximation to Eq.(7) provided by Larson and Davis[18] as illustrated by Heiba[15].

The network model equations, Eqs.(1) to (7), are anchored to a real porous medium by a two step process: (i) The functional forms of $g(r)$ and $v(r)$ are developed analytically, using a single-pore model suggestive of observed pore structure. (ii) The form of $\alpha(r)$ is based on measured pore-size distributions for diatomite. Likewise, actual body-size distribution information is included. These steps are described in detail in the following sections.

Single-Pore Model

Every pore in a porous medium has at least two distinct parameters, throat size and body size. We use sinusoidal pores as shown in Fig. 2. The pore is periodically constricted according to the following dimensionless equation

$$\lambda(z) = 1 - \left(\frac{1-\lambda_t}{2}\right)\left(1+\cos\frac{2\pi z}{\xi R_b}\right) \quad (8)$$

where z is the distance along the axis, $\lambda = R(z)/R_b$, R_b is a characteristic pore-body dimension, $\lambda_t = R_t/R_b$ is the dimensionless throat radius sometime referred to as an aspect ratio, R_t is pore-throat radius, $\xi = L/R_b$, and L is the pore wavelength. Based on this representation of shape for a single pore and restricting the cross section to be circular, we find the single-phase conductivity and volume of a single pore analytically. Neglecting the influence of pore corners does not have a major effect on single-phase conductivity calculations.

Single-pore conductivity. We solve for single-phase Hagen-Poisuelle flow in a constricted pore analytically and relate pressure drop to flow by the following equation,

$$\frac{\Delta p \pi R_b^4}{8qL\mu} = \frac{\left(9\lambda_t^2 - 6\lambda_t + 5\right)}{\sqrt{\lambda_t^7}} \quad (9)$$

where Δp is the pressure drop, μ is the viscosity, and q is the volumetric flow rate through the pore. In spite of periodic constrictions we suppose that flow is creeping because flow rates are very low and the Reynolds number is thereby small. We define a dimensionless hydraulic conductivity g for a single pore related to the pressure drop through it by,

$$g = \frac{qL\mu}{\Delta p}\frac{8}{\pi R_c^4} \quad (10)$$

where R_c is a characteristic radius. These two equations are combined to give the dimensionless single-phase conductivity of a single pore as,

$$g(r_t, \lambda_t) = \frac{8r_t^4}{\sqrt{\lambda_t}\left(9\lambda_t^2 - 6\lambda_t + 5\right)} \quad (11)$$

where $r_t = R_t/R_c$.

Single-pore volume: Assuming circular cross section, we find the volume of a single pore per unit wavelength to be ,

$$V(R_b, R_t) = \frac{\pi}{8}R_b^2\left(3\lambda_t^2 + 2\lambda_t + 3\right) \quad (12)$$

Based on this equation, we define dimensionless volume per unit wavelength as follows,

$$V(\lambda_t, r_b) = \frac{\pi}{8}r_b^2\left(3\lambda_t^2 + 2\lambda_t + 3\right) \quad (13)$$

where $r_b = R_b/R_c$.

The single pore model, Eqs. (11) and0 (13), take into account both body and throat sizes characterizing a pore. But the expressions generating conductivity and volume distributions require that the single-pore equations be in terms of a single characteristic dimension. We select the dimensionless throat radius to be this characteristic dimension. The choice is made because the Bethe lattice effective conductivity Eq.(1) is for the throat percolation problem, and bonds are analogous to throats in a porous

medium. Thus Eq.(13) and Eq.(15) are modified to yield a form containing throat size only while still retaining embedded body size information.

Incorporation of body size information. Equations (11) and (13) are made single variable equations without losing body-size information by averaging the equations over all possible body sizes associated with a given throat size. If $\alpha_b(r_t, r_b)$ is the frequency distribution of the dimensionless body radius, r_b, associated with a given dimensionless throat radius, r_t, then the effective conductivity and available volume associated with a throat size is given by,

$$\langle g(r_t)\rangle = \int_r^\infty \alpha_b(r_t, r_b) g(r_t, \lambda_b) dr_b \tag{14}$$

$$\langle V(r_t)\rangle = \int_r^\infty \alpha_b(r_t, r_b) V(\lambda_t, r_b) dr_b \tag{15}$$

Porous Medium Characterization

A real porous medium is composed of pores of varying sizes with each pore characterized by a large main body and a narrow throat. The porous medium is characterized by the sizes of bodies and throats and their distributions. The body and throat size distributions can be accurately represented with bivariate gamma distribution functions,

$$\alpha = \frac{r^{a-1} e^{-br} b^a}{\Gamma(a)} \tag{16}$$

where a and b are parameters that characterize the distribution. The use of this function for diatomite body and throat distributions is supported by experimental results and scanning electron microscope (SEM) images[10] Based on Eq.(16), we generate body and throat-size distributions; examples are shown in Fig.3 for diatomite. While developing our single-pore model, we also use the distribution $\alpha_b(r_t, r_b)$ to average over all possible body sizes that can be associated with a given throat size. This is the constrained pore distribution, also shown in Fig. 3 as a dashed line marked with solid circles. Physically, a throat must be connected to a body that is greater than or equal to throat size,

$$\alpha_b(r_t, r_b) = \begin{cases} 0 & ; r_b < r_t \\ \alpha_b(r_b) / \int_{r_t}^\infty \alpha_b(r_b).dr_b & ; r_b \geq r_t \end{cases} \tag{17}$$

Porous Medium Properties

The properties we calculate from the network model are effective hydraulic conductivity and available network volume. These properties are related to permeability and porosity. Permeability can be related to effective conductivity by invoking Darcy's law and the definition of hydraulic conductivity, respectively,

$$\frac{q}{A} = -\frac{k}{\mu}\frac{\Delta p}{L} \tag{18}$$

$$k \propto \frac{\phi R_c^4 G_{eff}}{A_c} \tag{19}$$

where A_c ($=\phi A$)is the cross sectional area available to flow of fluid, k is permeability, and ϕ is porosity. We assume that this area depends on the average throat size $\langle R_t\rangle$ squared and that porosity is proportional to available network volume. Thus, the permeability change at any stage based on these equations is related to original permeability and pore volume, k_0 and $V_{eff,0}$, by the following relation,

$$\frac{k}{k_0} = \frac{V_{eff}}{V_{eff,0}} \frac{\langle R_t\rangle^2}{\langle R_{t,0}\rangle^2} \left(\frac{R_c}{R_{c,0}}\right)^4 \frac{G_{eff}}{G_{eff,0}} \tag{20}$$

Similarly, porosity at any stage of diagenesis can be related to original porosity and network parameters as,

$$\frac{\phi}{\phi_0} = \frac{V_{eff}}{V_{eff,0}} \tag{21}$$

Equations (20) and (21) relate network parameters to the porous medium at any stage in the diagenetic process. Thus, given the mass of silica dissolved or precipitated we obtain k and ϕ.

Pore Evolution Models

There are two distinct pore evolution mechanisms that occur in diatomite during steam drive. One is dissolution of the rock matrix and the other is precipitation of rock minerals. The following subsections describe the models that we choose for representing these aspects of diagenesis.

Dissolution. Silica dissolution has been studied widely in regard to alkaline waterflooding. For instance, dissolution kinetics have been examined[19,20] as well as the migration of alkali[21]. The evolution of grain sizes and shapes during dissolution has also been studied via glass beadpacks[22]. On the basis of observation of grain shapes and from assessing surface chemical potentials, it was suggested that silica dissolution was most likely to occur uniformly along pore walls[22]. In our pore network, we follow these results and dissolve pore walls uniformly. Each pore in the network suffers the same amount of dissolution as shown schematically in Fig. 2b.

We denote the dissolved thickness by t in dimensionless form. It has been non dimensionalized by the characteristic radius R_c. Based on this thickness, the dimensions of a pore after dissolution can be related to its original dimensions by,

$$r_{t,new} = r_{t,old} + t \tag{22}$$

$$r_{b,new} = r_{b,old} + t \tag{23}$$

These single pore equations are used to model the effect of dissolution at the network level. The body and throat size distributions are still given by the gamma distributions of Eq. (16). The distribution parameter a is related to average size by,

$$\langle r \rangle = a - 1 \tag{24}$$

The new average radius can be related to the old average radius and the thickness by,

$$\langle r \rangle_{new} = \langle r \rangle_{old} + t \tag{25}$$

Based on Eqs. (24) and (25), the parameters for generating the body or throat size distributions can be updated in the case of dissolution by,

$$a_{new} = a_{old} + t \tag{26}$$

Thus, body and throat size distributions during dissolution can be generated by parameters in Eq. (26). Since dissolution of the network does not block any pore, the pores at any stage of dissolution are always accessible to flow and X^A for dissolution will always be 1.0.

Based on this approach, different stages of dissolution of the rock matrix are denoted by different values of dimensionless thickness t. Then, the pore size distributions are updated and effective network conductivity and pore volume recalculated. Finally, the permeability and porosity change associated with a particular t is found.

Deposition. We use two different deposition models as given in Fig. 4. to explore clogging of pores. The first model, Fig. 4a, considers deposition to be a pore lining process and the second considers deposition to occur only at throats. Deposition at pore throats is indicated on Fig. 4b by dark gray shading. In both models, deposition takes place in a series of steps. Each step in the deposition sequence depends on the network condition in the previous step. At any stage of deposition, the condition of the network is determined by the condition of the throats constituting the network. Even though the radii change as deposition proceeds, we characterize all throats of the network at any stage of deposition by their original radii, *i.e.*, before the process of deposition starts. The extent of deposition is given by the largest blocked throat with original size r_i. The current size of this throat is zero. This implies that the frequency of a throat with current radius r is given by $\alpha_t(r+r_i)$ when r_i has been clogged. We also define X_i as,

$$X_i = \int_0^{r_i} \alpha_t(r)dr \tag{27}$$

This X_i defines the fraction of the original throats that are not allowed to the main flow due to deposition. The fraction of throats that are allowed to flow is, 1-X_i. All of these allowed pores are not accessible to flow due to random connectivity of the network. Based on the current value of 1-X_i we estimate the current accessible fraction of allowable pores of the network by using Eq.(6). The fraction of completely blocked pores X_b is found by a population balance [16],

$$X_b = \int_0^{X_i} \frac{X_A}{1-X_i} dX_i \tag{28}$$

Determination of these parameters at any stage of deposition thus tells us the condition of our network. A deposition step implies that pores with original throat size between r_i and $r_i+\Delta r_i$ block. First, we completely block accessible throats with current radius between 0 and Δr_i,. That is, for pores with the original radius between r_i and $r_i+\Delta r_i$. We call this amount of precipitate deposited volume V_1. Second, we deposit a layer of thickness Δr_i in all currently accessible throats with current radius between Δr_i and infinity. We call this deposited volume V_2.

Volume determination. To find the available pore volume at the stage $r_i+\Delta r_i$ of deposition we calculate V_1 and V_2 and subtract their total from network volume at start of the deposition step. Thus,

$$V_{eff}(r_i + \Delta r_i) = V_{eff}(r_i) - (V_1 + V_2) \tag{29}$$

The deposition calculations start at r_i=0, and we go on successively subtracting volume from the base volume as calculated in Eq.(3). Formulas for V_1 and V_2 depend on where silica deposition occurs.

Deposition at throats only. In calculating the volumes V_1 and V_2 for deposition occurring only at pore throats, we hold the body size distribution constant and change only the throat-size distribution. Thus, the current body sizes are the same as the original body sizes. The volumes are calculated as,

$$V_1 = \frac{X^A}{1-X^A} \int_0^{\Delta r_i} \alpha_t(r + r_i)\langle V(r)\rangle dr \tag{30}$$

$$V_2 = \frac{X^A}{1-X^A}\left[\int_{\Delta r_i}^{\infty} \alpha_t(r+r_i)\langle V(r)\rangle dr - \int_0^{\infty} \alpha_t(r+r_i+\Delta r_i)\langle V(r)\rangle dr\right] \tag{31}$$

Uniform deposition model. To find the volume change associated with a uniform deposition, we consider a single-pore model and calculate the volume that is deposited by a uniform layer of thickness t :

$$V_{dep}(r_b, r_t, t) = \pi t(r_b + r_t - t) \tag{32}$$

We then average V_{dep} over all possible body sizes to get volume change associated with a throat for a given thickness. The expression is,

$$\langle V_{dep}(r,t)\rangle = \int_r^\infty \alpha_b(r_b,r_t)V_{dep}(r_b,r_t,t)dr_b \qquad (33)$$

We use this equation to calculate the deposition occurring in all throats with current radii ranging from 0 to ∞. Thus, for the uniform deposition case, the volume deposited is given by,

$$V_1 + V_2 = \frac{X^A}{1-X^A}\int_0^\infty \alpha_t(r+r_i)\langle V_{dep}(r,t)\rangle dr \qquad (34)$$

Conductivity calculation. The effective conductivity of the network is found by considering the three kinds of throats in the network at any deposition stage r_i:

- Throats that had original size less than r_i and are currently blocked completely and so do not contribute towards network conductivity.
- Throats that had original size greater than r_i and are accessible to flow and, hence, contribute towards network conductivity.
- Throats that had original size between 0 to ∞ but are not accessible to flow due to random connectivity of the network and, thus, do not contribute to flow.

The conductivity distribution function of the network is generated by,

$$G(g) = \left(X_b + X^{NA}\right)\delta(r) + \frac{X^A}{1-X^A}\alpha_t(r+r_i)\langle g(r)\rangle \qquad (35)$$

Once the conductivity distribution is known, we calculate the effective network conductivity using Eq.(2)

Results:

The models for deposition and dissolution were translated into the following algorithm to gauge the effect of dissolution and precipitation on permeability. A base case with given network connectivity, Z, average aspect ratio, λ_t, pore-body distribution, and pore-throat distribution is constructed. Next, we calculate the effective conductivity and available network volume of the base case. We then update the pore-body and pore-throat distributions according to the rules given above for a specified amount of silica precipitated or dissolved. The effective conductivity and available volume of the network are recalculated. Finally, Eqs.(20) and (21) are used to relate the conductivity and available volume changes to permeability and porosity changes. Connectivity and aspect ratio are varied independently for new base cases and the process repeated.

In the case of uniform dissolution, Fig. 5 represents the permeability versus porosity relationship for an aspect ratio of 20/3 and different values of coordination number Z. The plot has two distinct trends. First, the permeability increases rather dramatically for all values of Z. An order of magnitude increase in permeability is predicted if the porosity increases by 50%. Second, for a fixed value of porosity change, permeability increases most for small Z. For Z equal to 3, the permeability has increased 40 times when ϕ/ϕ_o reaches 1.5. As Z becomes larger the effect is less. It is reasonable that permeability increases most sharply and more severely for rocks with low connectivity as compared to rocks with high connectivity. The role of an individual pore throat on permeability is accentuated in networks with small connectivity.

Figure 6 displays similar dissolution calculations for the case of Z equal to 5 and variable pore aspect ratio. The most dramatic increases in permeability occur for the most constricted pores. When pore throats are small relative to pore bodies, a small amount of dissolution dramatically increases permeability. Note that the least constricted pores display the smallest amount of permeability increase relative to the base case.

Deposition results are similar to dissolution, except that the trends are reversed. Permeability decreases with porosity. Figure 7 shows the permeability versus porosity relationship for an R_b/R_t of 20/3 and various connectivities. Deposition occurs at throats only. For all values of Z, the decrease in permeability is very marked near ϕ/ϕ_o equal to 1 and becomes less steep as the network approaches blockage. Again, the most dramatic effects are seen in the networks with the least connectivity. Figure 8 displays the permeability versus porosity relationship for a Z of 5 and various pore throat to body size ratios. A small amount of silica deposited in a narrow throat in a poorly connected network, can substantially decrease network conductivity, and hence permeability.

For completeness, Figs. 9 and 10 present results for uniform deposition. Figure 9 applies to a fixed aspect ratio of 20/3 with variable Z, whereas Fig. 10 shows results for fixed connectivity and various R_b/R_t. Trends are similar to Figs. 7 and 8, but the trend of decreasing permeability with silica deposition is not as strong. Because deposition is pore lining rather than throat blocking, it takes a greater change in porosity to affect the same change in permeability. As expected, the most dramatic decreases in permeability are found for small Z and large λ_t.

The porosity changes shown in Figs. 5 to 10 are extreme and not expected in the field far away from the well bore. Changes up to about 10% are likely the maximum[1]. If we limit the porosity changes to 10% and examine permeability versus porosity on a log-log plot, a straight line relationship is found for dissolution and both modes of deposition. That is, the ratio of permeabilities varies with ϕ/ϕ_o raised to some power.

This point is illustrated graphically in Fig. 11 for the case of deposition at pore throats. The pore throat to body aspect ratio is fixed at 20/3, the network connectivity varies between 3 and 13, and deposition is limited to 10%. The power-law exponent increases with decreasing Z as indicated by the slopes of the lines. For a Z of 3 the exponent is about 16.5 while for Z = 13 it is about 6.6. The power-law trends

exhibited in Fig 11 can be compared with the experimental results of Koh *et.al*[1]. They measured permeability of diatomite plugs that were flushed with hot, saturated silica laden water (204 °C). The diatomite plug was maintained at 49 °C to induce silica deposition. Experimentally, they found that permeability reduction correlated with porosity decrease according to a power-law relationship. Their best-fit power-law exponent was 9. We find this power-law exponent for Z between roughly 5 and 7 on Fig. 11. In the case of pore-lining silica deposition, this model exhibits an exponent of 9 when Z is between 3 and 4 and R_t/R_t is 20/3. Hence, for reasonable network parameters, we reproduce the experimentally observed trend.

The power-law form exhibited in Fig. 11 suggests that the network results can be expressed according to

$$\frac{k}{k_0} = \left(\frac{\phi}{\phi_0}\right)^{\gamma} \tag{36}$$

where the power-law exponent γ is correlated with the network parameters Z and $\lambda_t = R_t/R_t$. We choose the following form for γ

$$\gamma = B(\lambda_t) + \frac{D(\lambda_t)}{Z - E(\lambda_t)} \tag{37}$$

The coefficients B, D, and E are functions of λ_t. We obtain them by fitting polynomial expressions to network results. Table 1 details the exact functional forms for each of these coefficients.

To verify the data reduction approach and Eqs. (36) and (37), we plot network predicted changes in permeability ($\log k/k_0$), such as those displayed in Figs. 5 to 10, versus the product of the power law exponent and logarithm of porosity change ($\gamma \log \phi/\phi_0$). Deposition or dissolution is limited to a maximum of 10%. Figure 12 gives the results of this procedure for deposition at pore throats. Network results are given as individual data points and lie quite close to the straight line representing Eq. (36). Different symbols indicate differing values for network parameters Z and λ_t. Deviations from the straight-line behavior likely result from small errors in the polynomial representation of coefficients B, D, and E. Figures 13 and 14 show that the data reduction is successful for the pore-lining deposition and uniform dissolution cases as well. Hence, we obtain from our network calculations useful correlations of macroscopic porous medium properties. The power-law exponent is parameterized in terms of measurable rock quantities.

Future Work

Results from this initial study are promising and several extensions are suggested. First, all results obtained here were for a pristine network. That is, silica deposition followed by subsequent redissolution was not examined. This is the expected trend in the field and the network model needs to be developed further to simulate this cycle. Second, agreement between network suggested trends and those found experimentally for the case of deposition appear to be quite good. In order to perform a similar check for the dissolution case, experiments should be conducted. Lastly, the model and calculations presented here are for single-phase flow of water. To be applicable to the simultaneous flow of water and oil in diatomite, the model should be extended to multiple phases.

Conclusions

Beginning with a simple network representation of diatomite, we are able to model permeability evolution as a function of porosity change. For moderate increases or decreases in porosity, we find a power-law relationship describing permeability alteration. Such a trend for silica deposition has been determined experimentally elsewhere. The power-law feature holds promise that permeability change during steam drive, or water flood, in diatomite can be incorporated into reservoir simulators.

Specifically, we find that the porosity-permeability relationship can modeled as a simple power-law relation only for moderate ranges of deposition and dissolution. At low ranges of deposition, it is difficult to distinguish between deposition only at pore throats and pore-lining deposition of silica for expected pore body to throat aspect ratios and connectivity. Also, it is found that permeability change is most dramatic for networks with low connectivity or very small pore throats connected to relatively large bodies. For connectivities of 12 and greater at a fixed value of the throat to body aspect ratio, little variation in results is found as Z is increased.

Nomenclature

$a, b=$	parameters in gamma distribution
$A=$	area
$B, D, E=$	coefficients for data reduction
$C(x)=$	network generating function
$f=$	fraction of pore throats available for flow
$g=$	conductivity of a pore segment
$G=$	network conductivity distribution
$k=$	permeability
$L=$	pore length
$p=$	pressure
$r=$	dimensionless pore radius
$R=$	radius
$t=$	thickness of deposited layer
$v=$	volume of a pore segment
$V=$	network volume distribution
$X=^{A}$	network accessibility
$X=$	fraction of throats not allowed to flow
$z=$	distance in axial direction
$Z=$	coordination number

Greek Symbols

α= pore-size distribution function
δ= Dirac delta function
Δ= difference operator
ϕ= porosity
γ= power-law exponent
Γ= gamma function
λ= radius nondimensionalized by body size
μ= viscosity
ξ= pore length nondimensionalized by body size

Subscripts

b= body
b= completely blocked pores
c= characteristic pore dimension
c= cross-sectional area for flow
eff= effective for flow
i= fraction of original throats now blocked
t= throat
0= denotes properties before dissolution or precipitation
$1, 2$= volumes deposited in precipitation model

Acknowledgments

This work was supported by the Assistant Secretary for Fossil Energy, Office of Oil, Gas and Shale Technologies of the U.S. Department of Energy, under contract No. DE-FG22-96BC14994 to Stanford University. Partial support was also provided by Lawrence Livermore National Laboratory under contract No. DE-AC03-76SF00098 to the University of California.

References

1.Koh, C.J., P.C. Dagenais, D.C. Larson, and A.S. Murer: "Permeability Damage in Diatomite Due to In-situ Silica Dissolution/Precipitation," SPE 35394, in Proceedings of the SPE/DOE Tenth Symposium on Improved Oil Recovery, Tulsa, OK (April 21-24, 1996).

2.Kovscek, A.R., R.M. Johnston, and T.W. Patzek: "Evaluation of Rock/Fracture Interactions During Steam Injection Through Vertical Hydraulic Fractures," *SPE Production and Facilities*, (May) (1997) 100-105.

3.Kumar, M. and F.D. Beatty: "Cyclic Steaming in Heavy Oil Diatomite," SPE 29623, in Proceedings of the SPE 65th Western Regional Meeting, Bakersfield, CA (March 8-10, 1995).

4.Johnston, R.M. and G.T. Shahin: "Interpretation of Steam Drive Pilots in the Belridge Diatomite," SPE 29621, in Proceedings of the SPE 65th Western Regional Meeting, Bakersfield, CA (March 8-10, 1995).

5.Murer, A.S., K.L. McClennen, T.K. Ellison, R.S. Timmer, D.C. Larson, K.D. Wolcott, T.M. Walker, and M.A. Thomsen: "Steam Injection Project in Heavy Oil Diatomite," SPE 38302, in Proceedings of the SPE 67th Annual Western Regional Meeting, Long Beach, CA (June 25-27, 1997).

6.Kovscek, A.R., R.M. Johnston, and T.W. Patzek: "Interpretation of Hydrofracture Geometry During Steam Injection Using Temperature Transients I. Model Formulation and Verification," *In Situ*, **20**(3) (1996) 251-288.

7.Kovscek, A.R., R.M. Johnston, and T.W. Patzek: "Interpretation of Hydrofracture Geometry During Steam Injection Using Temperature Transients II. Asymmetric Hydrofractures," *In Situ*, **20**(3) (1996) 289-309.

8.Schwartz, D.E.: "Characterizing the Lithology, Petrophysical Properties, and Depositional Setting of the Belridge Diatomite, South Belridge Field, Kern County, California", in *Studies of the Geology of the San Joaquin Basin*, S.A. Graham, and Olson, H.C., Editor. , The Pacific Section, Society of Economic Paleontologists and Mineralogists, Los Angeles, (1988) p. 281-301.

9.Stosur, J.J. and A. David: "Petrophysical Evaluation of the Diatomite Formation of the Lost Hills Field, California," *Jour. Pet. Tech.*, **28**(1971) 1138-1144.

10.Bhat, S.K., L.M. Castanier, and A.R. Kovscek: "Unpublished results: scanning electron microscopy and mercury porosimetry of diatomite," (1997)

11.Stinchcombe, R.B.: "Conductivity and Spin-Wave Stiffness in Disordered Systems--An Exactly Soluble Model," *J. Phys. C.: Solid State Physics*, **7**(1974) 179-203.

12.Heiba, A.A., H.T. Davis, and L.E. Scriven: "Effect of Wettability on Two-Phase Relative Permeabilities and Capillary Pressures," SPE 12172, in Proceedings of the SPE 58th Annual Technical Conference and Exhibition, San Francisco, CA (October 5-8, 1983).

13.Heiba, A.A., H.T. Davis, and L.E. Scriven: "Statistical Network Theory of Three-Phase Relative Permeabilities," SPE 12690, in Proceedings of the SPE/DOE Fourth Symposium on Enhanced Oil Recovery, Tulsa, OK (April, 1984).

14.Heiba, A.A., M. Sahimi, L.E. Scriven, and H.T. Davis: "Percolation Theory of Two-Phase Relative Permeability," *SPE Reservoir Engineering*, (Feb. 1992) 123-132.

15.Heiba, A.E.-A.: "Porous Media: Fluid Distributions and Transport with Applications to Petroleum Recovery," PhD Thesis, University of Minnesota (1985) p. 565.

16.Yortsos, Y.C. and M. Sharma: "Application of Percolation Theory to Noncatalytic Gas-Solid Reactions," *AIChE Journal*, **32**(1) (1986) 46-55.

17.Fisher, M.E. and J.W. Essam: "Some Cluster Size and Percolation Problems," *Jour. of Mathematical Physics*, **2**(4) (1961) 609-619.

18.Larson, R.G. and H.T. Davis: "Conducting Backbone in Percolating Bethe Lattices," *J. Phys. C.: Solid State Phys.*, **15**(1982) 2327-2331.

19.Thornton, S.D. and C.J. Radke: "Dissolution and Condensation Kinetics of Silica in Alkaline Solution," *Soc. Pet. Eng. Res. Eng.*, **3**(2) (1988) 743-752.

20.Saneie, S. and Y.C. Yortsos: "Kinetics of Silica Dissolution and Hydroxyl Ion Consumption in Alkaline Flooding," SPE 17409, in Proceedings of the California Regional Meeting(March, 1985).

21.Bunge, A.L. and C.J. Radke: "Migration of Alkaline Pulses in Reservoir Sands," *Soc. Pet. Eng. J.*, **22**(6) (1982) 998-1012.

22.Udell, K.S. and J.D. Lofy: "Permeability Reduction of Unconsolidated Media Caused by Stress-Induced Silica Dissolution," *SPE Formation Evaluation*, (Mar. 1989) 56-62.

Table 1: Coefficients in expression for power-law exponent.

Parameters	Dissolution	Uniform Deposition	Deposition at Throats
$B(\lambda_t)$	$0.0201\lambda_t^2 + 0.645\lambda_t + 1.8633$	$0.0003\lambda_t^2 + 0.147\lambda_t + 2.827$	$-0.0311\lambda_t^2 + 0.5699\lambda_t + 2.8841$
$D(\lambda_t)$	$-0.0168\lambda_t^3 + 0.3126\lambda_t^2 + 0.0525\lambda_t + 2.7042$	$-0.0059\lambda_t^3 + 0.08\lambda_t^2 + 0.614\lambda_t + 5.2683$	$0.0128\lambda_t^3 - 0.3715\lambda_t^2 - 3.876\lambda_t + 2.9961$
$E(\lambda_t)$	$-0.0279\lambda_t + 0.5886$	$-0.0299\lambda_t + 1.7014$	$-0.0185\lambda_t + 1.6878$

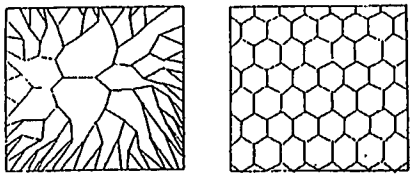

Figure 1 Different types of lattices

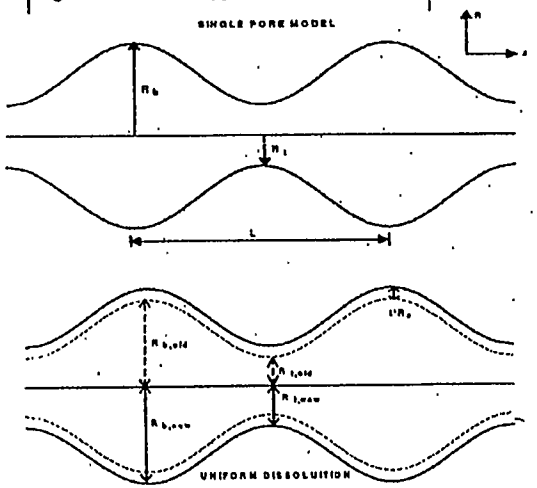

Figure 2 a) Single pore model
2 b) Uniform dissolution model

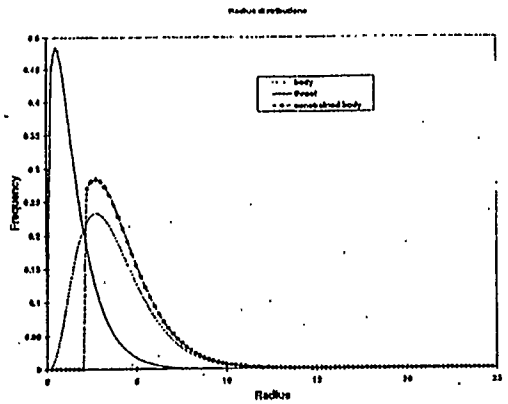

Figure 3 Body size, throat size and constrained body size distributions

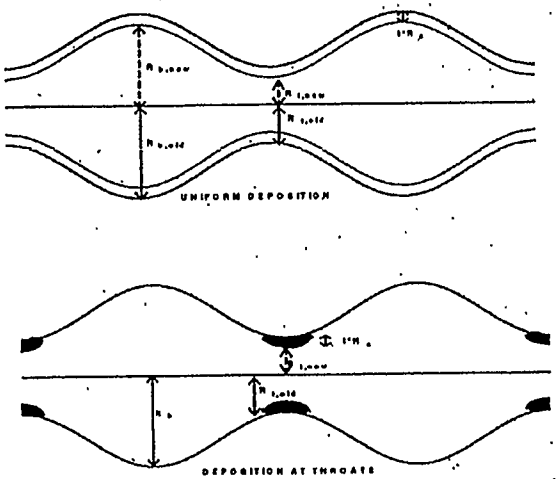

Figure 4 a) Uniform deposition model
b) Deposition at throats only

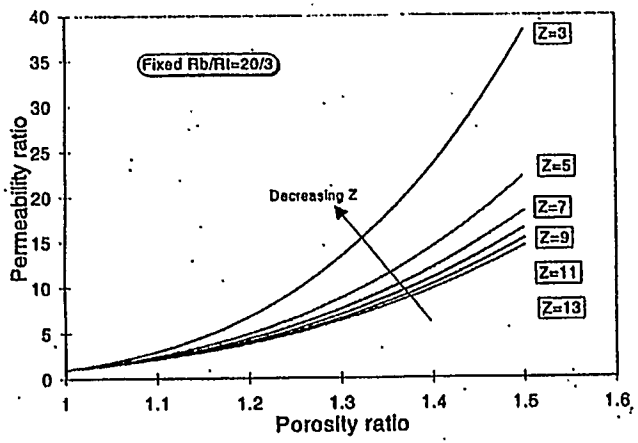

Figure 5 Dissolution case, permeability-porosity relation for different coordination numbers

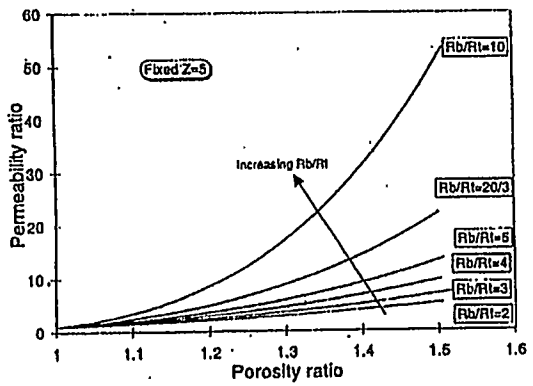

Figure 6 Dissolution case, permeability-porosity relation for different aspect ratios

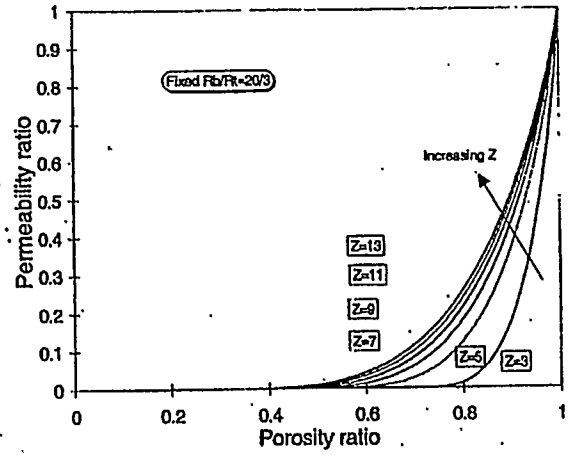

Figure 7 Throat deposition case, permeability-porosity relation for different coordination numbers

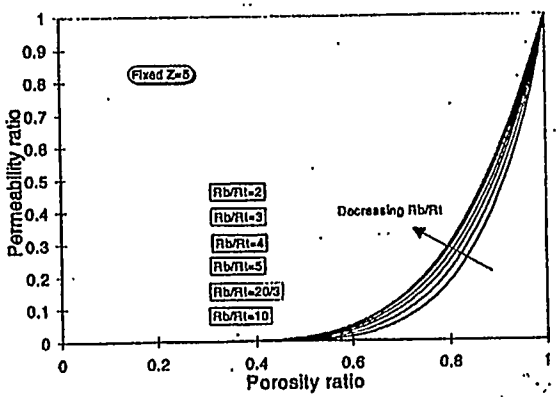

Figure8 Throat deposition case, permeability-porosity relation for different aspect ratios

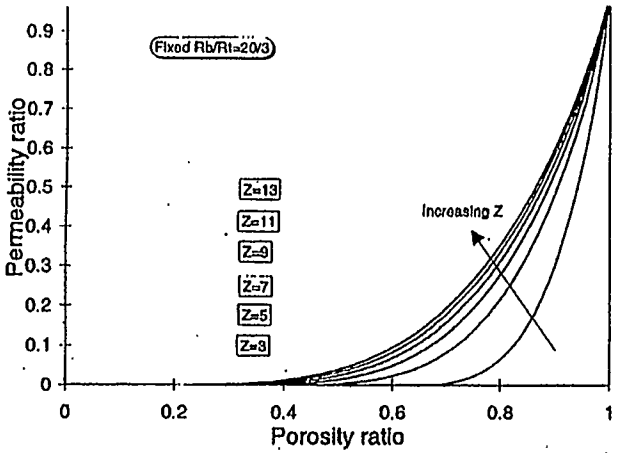

Figure 9 Uniform deposition case permeability-porosity relation for various coordination numbers

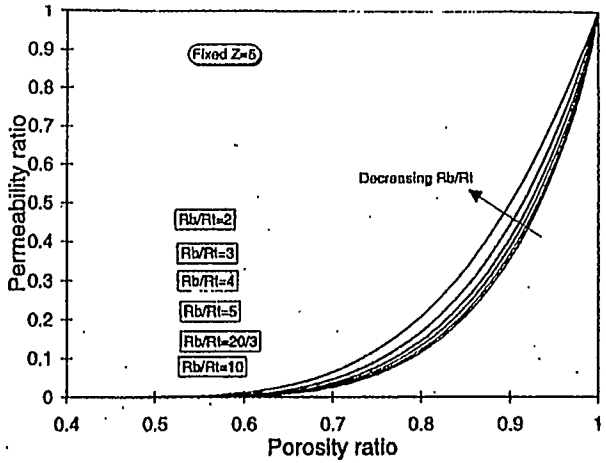

Figure 10. Uniform deposition case permeability-porosity relation for various aspect ratios

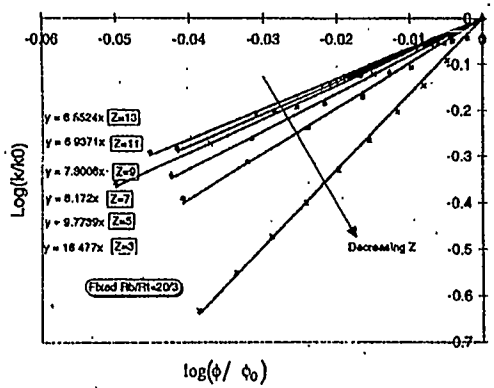

Figure 11. Straight line fits for permeability-porosity relations on log-log scale

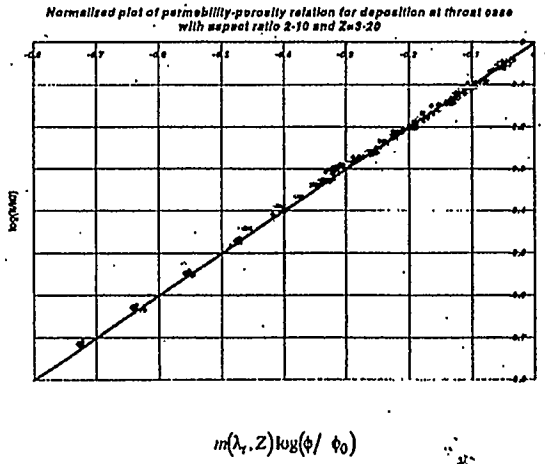

Figure 12. Normalized plot for deposition occurring at at throats

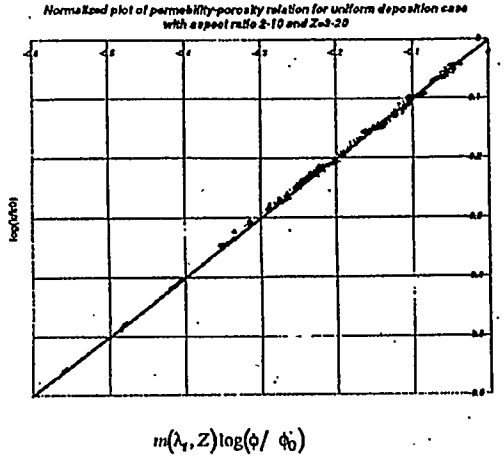

Figure 13. Normalized plot for uniform deposition

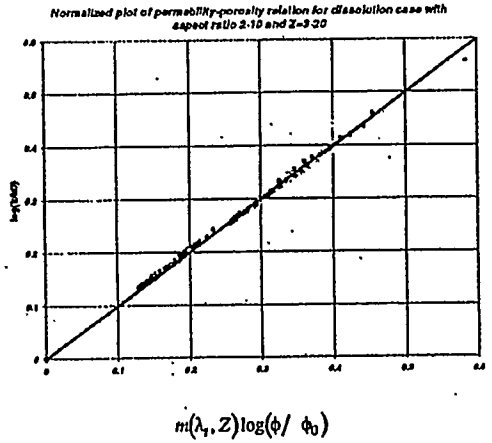

Figure 14. Normalized plot for dissolution case

3.3 VISUALIZATION OF MULTIPHASE FLOW THROUGH POROUS MEDIA AT HIGH PRESSURE

(D. George)

3.3.1 INTRODUCTION

Much research has been performed using micromodels to study foam flow through porous media (Chambers and Radke, 1989). Observations of oil-foam interactions in micromodels have also been made (Sagar, 1997). Because micromodels are not typically constructed to contain fluids at high pressure or elevated temperature, little research has been performed in which multiphase flow through porous media at high pressure conditions has been observed.

The goal of this project is to observe foam flow and oil-foam interactions in a micromodel at high pressures (greater than 100 psi). In order to achieve this goal, a pressure vessel is being constructed in which a micromodel will be housed. A confining liquid in the vessel will allow pressure within the micromodel to be increased without developing a pressure differential between the inside and the outside of the micromodel great enough to cause mechanical failure of the micromodel. A window in the pressure vessel will permit direct observation of the micromodel.

3.3.2 MICROMODELS

Micromodels are produced with the objective of directly observing fluid flow through porous media. Micromodels contain an etched flow pattern that can be viewed with a microscope. The flow pattern can be a lattice of straight or constricted channels, or the pore network can be modeled after the pores found in naturally occurring rock. Fluid enters a micromodel, flows through the porous medium, and exits the micromodel. Several studies

have been performed using etched glass micromodels. Attempts were made to replicate naturally occurring pore patterns with etched glass micromodels, but the necessary etching and annealing processes resulted in a loss of surface roughness and an enlargement of pore size.

The micromodels developed by Hornbrook, *et. al.* (1992), are superior to etched glass micromodels. An almost exact replica of a thin section of Berea sandstone is reproduced on a silicon wafer. The silicon wafer is oxidized to reproduce a water-wet porous medium, and then the silicon wafer is bonded to a glass plate. These micromodels possess roughness and wettability characteristics that are approximately equal to those of the original sandstone. Futhermore, when the micromodels are produced the depth of the pore and channel network can be controlled with great accuracy.

3.3.3 PRESSURE VESSEL

An assessment of the typical conditions for an experiment was made. This led to the selection of expected operating parameters, design guidelines, and concerns about safety.

3.3.3.1 Operating Parameters

The pressure vessel should be able to operate at pressures up to 1000 psi. The temperature of the vessel should be controlled, ranging from 15°C to 50°C. Because the surface of the silicon micromodel is oxidized, higher operating temperatures demand some reconsideration of the use of silicon micromodels. Silicon dioxide (SiO_2) is appreciably soluble in water.

3.3.3.2 Design

A pressure vessel will be constructed to accommodate the micromodels. The micromodel sits inside of the body of the pressure vessel. Holes to serve as fluid inlet/outlet ports are drilled in the bottom of the micromodel. These holes rest directly above tubes that carry fluid to and from the micromodel. O-rings are used to create a seal where the tubes meet the inlet/outlet ports of the micromodel. Figure 1 details the inlet and outlet ports through which fluid will enter and exit the micromodel. Confining liquid circulates through the interior of the pressure vessel, entering and exiting through tubes that are located on opposite sides of the vessel. The confining liquid is used to control the temperature of the micromodel and provide pressure support. A 4.7 mm thick sapphire window is located directly above the micromodel. Sapphire was selected because of its superior mechanical and optical qualities. The window will be held between the micromodel and the pressure vessel lid in a manner such that its edges are considered to be fixed. This leads to maximum mechanical strength. An O-ring between the lid and the window seals the space. The pressure vessel lid is shaped like an annular ring. The lid fits over both the body of the pressure vessel and the window, such that the window, and thus the micromodel, is viewed in the center of the annular ring, as shown in Figure 2. The lid will be held to the pressure vessel by six 1/2 inch bolts, and a seal will be provided by an o-ring located between the lid and the pressure vessel. Figure 2 displays the cross-section of each of the components of the pressure vessel and indicates the proper assembly of these components.

3.3.3.3 Safety Features

In order to prevent failure of the pressure vessel and to protect users, several safety features are designed into the pressure system. A confining liquid will be used. Liquid will not expand nearly as much as gas in the event of failure. A pressure release valve will be located in the pressure system, and set to release pressure at 1100 psi. A burst disk that will break at 1200 psi will be incorporated into the design of the pressure vessel. The pressure system will be designed for 1500 psi, even though the maximum operating pressure of the

system will be 1000 psi, a factor of safety of 1.5. A shield made of Lexan (a highly impact resistant material) may surround the pressure vessel to provide an additional measure of safety to the users.

3.3.4 PROGRESS TO DATE AND A PLAN FOR CONTINUED PROGRESS

I am currently working on a literature review for the project. Marsden (1986) exhaustively describes literature relative to the topic that was generated before 1986. Sagar (1997) gives a thorough review of literature generated after 1986, and particularly literature pertaining to the observation of oil-foam interactions in micromodels. What remains to be reviewed is the most current literature and literature related to micromodel studies performed at high pressure conditions.

The design of the pressure vessel is almost complete. A final design will be produced by late January, and parts will be ordered at that time. All parts should be received by the beginning of February. The optical system that will be used to observe the micromodel from outside of the sapphire window must be selected. To have this done by the time the parts for the pressure vessel arrive is a goal. The construction of the pressure vessel, along with the construction of the rest of the experimental apparatus (including pipes, valves, pumps, vacuums, etc.) should be completed by the end of February or the beginning of March. At this time, the system will be tested. As soon as the system is operable, safe, and effective, data collection will begin.

3.3.5 REFERENCES

1. Chambers, K.T. and C.J. Radke: "Capillary Phenomena in Foam Flow Through Porous Media in Interfacial Phenomena in Petroleum Recovery," N.R. Morrow, Editor. Surfactant Science Series. Marcel Dekker, Inc. New York, pp 191-255, 1991.

2. Hornbrook, J.W., L.M. Castanier, and P.A. Pettit: "Visualization of Foam/Oil in a New High Resolution Sandstone Replica Micromodel," Report SUPRI TR-86, Stanford University, 1992.
3. Marsden, S.S. : "Foams in Porous Media," SUPRI TR-37, Stanford University, 1986.
4. Sagar, N. : "Oil-Foam Interactions in a Micromodel," Stanford University, 1997.

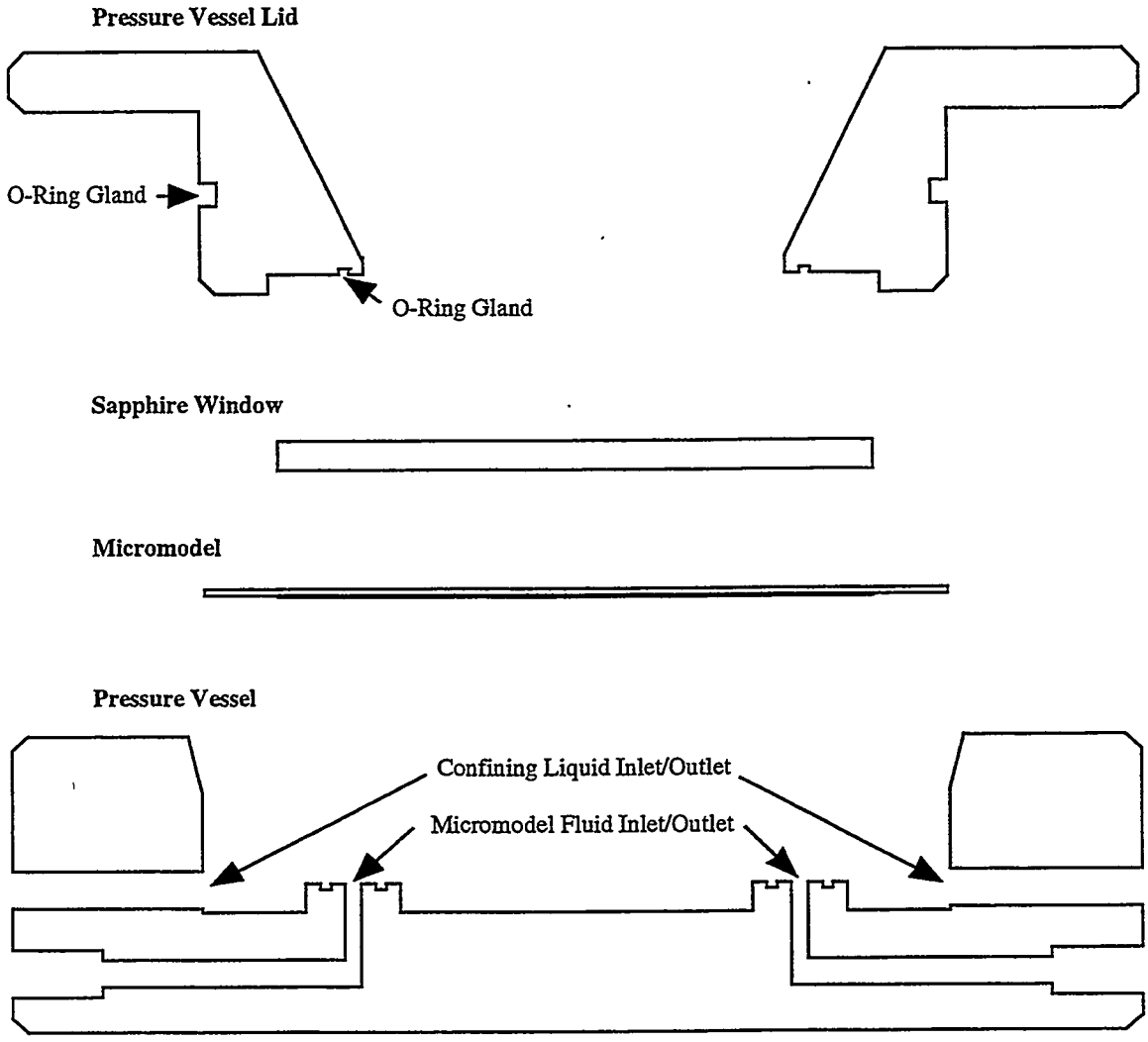

Figure 1: Exploded Cross-Sectional Diagram of the Pressure Vessel

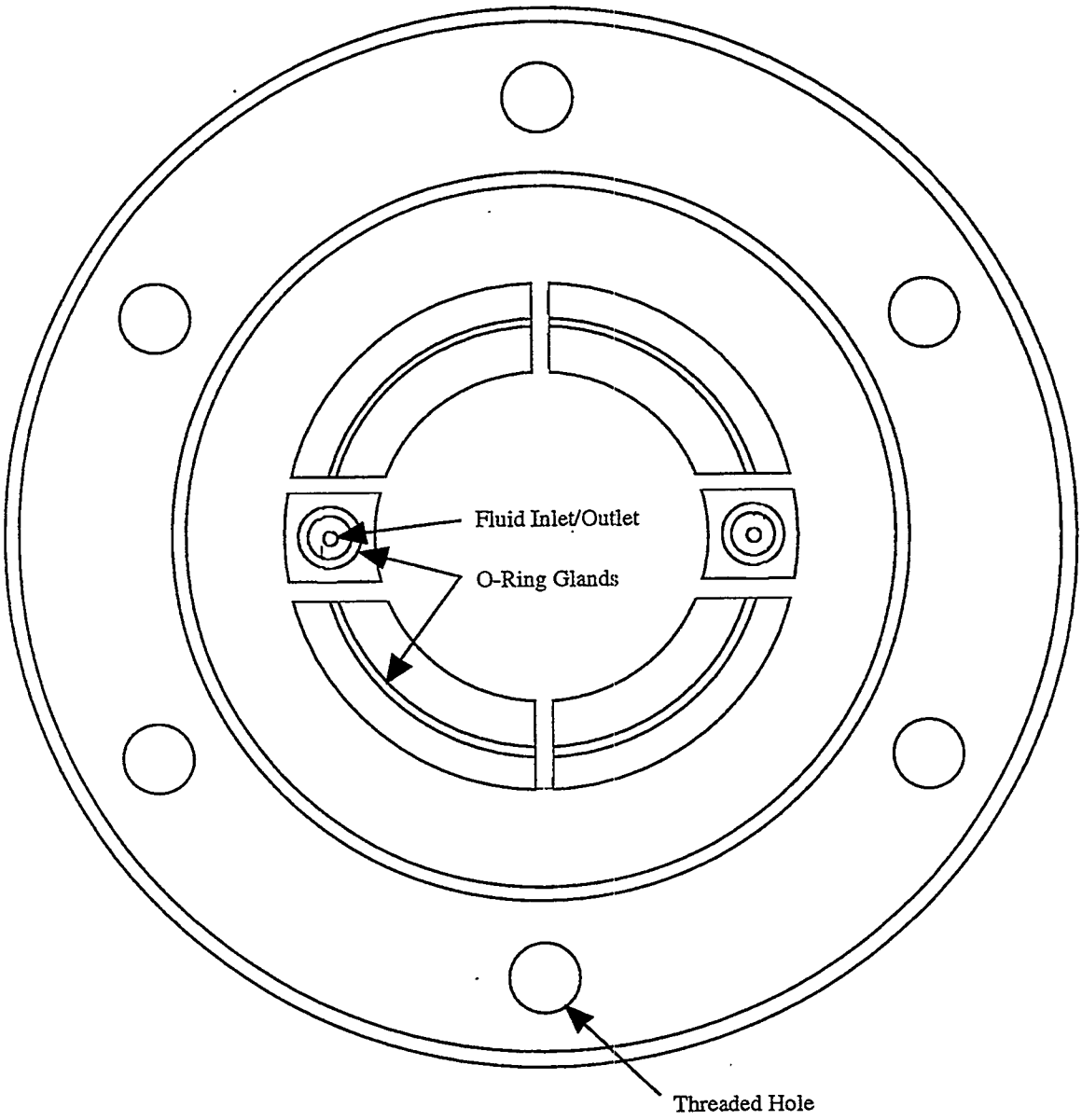

Figure 2: Top View of the Interior of the Pressure Vessel

3.4 FOAM FLOW IN HETEROGENEOUS POROUS MEDIA: EFFECT OF CROSSFLOW

(H.J. Bertin, O.G. Apaydin, L.M. Castanier, and A.R. Kovscek))

3.4.1 Foam Flow in Heterogeneous Porous Media: Effect of Crossflow

(H.J. Bertin, O.G. Apaydin, L.M. Castanier, and A.R. Kovscek)

The paper on the following page was prepared for presentation at the 1998 SPE/DOE Improved Oil Recovery Symposium held in Tulsa, Oklahoma, April 19-22, 1998.

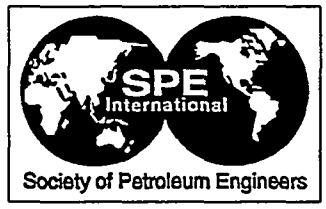

SPE 39678

Foam Flow in Heterogeneous Porous Media: Effect of Crossflow

H. J. Bertin, LEPT -ENSAM, O. G. Apaydin, L. M. Castanier, and A. R. Kovscek, Stanford U.

This paper was prepared for presentation at the 1998 SPE/DOE Improved Oil Recovery Symposium held in Tulsa, Oklahoma, 19–22 April 1998.

Abstract

Previous studies of foam generation and transport were conducted, mainly, in one-dimensional and homogeneous porous media. However, the field situation is primarily heterogeneous and multidimensional. To begin to bridge this gap, we have studied foam formation and propagation in an annularly heterogeneous porous medium. The experimental system was constructed by centering a 5.0 cm diameter cylindrical Fontainebleau sandstone core inside an 8.9 cm acrylic tube and packing clean Ottawa sand in the annular region. The sandstone permeability is roughly 0.1 d while the unconsolidated sand permeability is about 7 d. Experiments with and without crossflow between the two porous media were conducted. To prevent crossflow, the cylindrical face of the sandstone was encased in a heat-shrink Teflon sleeve and the annular region packed with sand as before. Nitrogen is the gas phase and an alpha olefin sulfonate (AOS 1416) in brine is the foamer. The aqueous phase saturation distribution is garnered using X-ray computed tomography.

Results from this study are striking. When the heterogeneous layers are in capillary communication and cross flow is allowed, foam fronts move at identical rates in each porous medium as quantified by the CT-scan images. Desaturation by foam is efficient and typically complete in about 1 PV of gas injection. When cross flow is prohibited, foam partially plugs the high permeability sand and diverts flow into the low permeability sandstone. The foam front moves through the low permeability region faster than in the high permeability region.

Introduction

Foam is applied broadly as a mobility-control and profile modification agent for flow in porous media. Foams are usually formed by nonwetting gases such as steam, carbon dioxide (CO_2), or nitrogen (N_2) dispersed within a continuous surfactant-laden liquid phase. Typical applications include aqueous foams for improving steam-drive [1-3] and CO_2-flood performance[4], gelled-foams for plugging high permeability channels[5], foams for prevention or delay of gas or water coning[6], and surfactant-alternating-gas processes for clean up of ground-water aquifers[7,8]. All of these methods have been tested in both the laboratory and the field.

An unfoamed gas displays low viscosity relative to water or crude oil and is thereby very mobile in porous media. However, dispersing the gas phase within a surfactant solution where the surfactant stabilizes the gas/liquid interface can substantially reduce gas mobility in porous media. Mobility is reduced because pore-spanning liquid films (foam lamellae) and lenses block some of the flow channels. Additionally, flowing lamellae encounter significant drag because of the presence of pore walls and constrictions. One aspect of foams that makes them attractive is that a relatively small amount of surfactant chemical can affect the flow properties of a very large volume of gas. The volume fraction of gas in a foam frequently exceeds 80 percent and stable foams up to 99 percent volume fraction are not uncommon. Recent reviews of foam flow phenomena and mechanisms are given in refs. [9-11].

Laboratory studies on foam generation and transport have aided greatly in formulating and improving both our microscopic and macroscopic understanding of foam flow in porous media. They have focused, for the most part, on one-dimensional and homogeneous porous media. These studies, however, leave gaps in our knowledge of foam behavior because the field situation is primarily heterogeneous and multidimensional.

While much work has been conducted in homogeneous systems, the literature on flow in stratified systems is sparse. Notable experiments in stratified systems include Casteel and Djabbarah who performed steam and CO_2 displacements with foaming agents in two parallel porous media[12]. Robin studied foam generation and transport in layered beadpacks that simulated reservoir strata [13]. In these experiments he

surmised that foam blocked the high permeability layer. Llave et al observed that foam can divert gas flow from high permeability layers to low permeability layers when the layers are isolated[14]. More recently, Hirasaki et al performed foam displacements in layered porous media to study the removal of organic liquids from groundwater aquifers[15]. Gas was injected at a fixed pressure gradient rather than a specified rate. By dyeing the various fluids, they observed displacement patterns directly. They found that injection of gas slugs into a porous medium containing surfactant resulted in foam generation and selective mobility reduction in the high permeability layers. In turn, recovery of the organic liquid was greatly enhanced.

For the most part, the effect of flow among parallel layers in capillary communication has not been investigated. We denote this as cross flow. To bridge this gap, we perform foam flow experiments in an axially symmetric, cylindrical, heterogeneous porous medium. The central portion of the porous medium is a Fontainebleau sandstone core and a uniform sand is packed in the annular region between the core and the pressure vessel wall to complete the porous medium. By the use or absence of a heat-shrink Teflon jacket around the sandstone, fluid communication, or cross-flow, is prohibited or allowed. The sandstone is about two orders of magnitude less permeable than the sand to provide a strong permeability and capilllary pressure contrast. We interpret the experiments in terms of the evolution of in-situ water saturation as a function of time.

In the following sections we first discuss the construction and characterization of the porous medium, characterization of our foamer solution, and then experimental determination of water saturation via X-ray CT scanning. CT provides accurate resolution of the progress of displacement fronts as well as the in-situ displacement efficiency. Next, we outline the experimental program and give results. A discussion and conclusions complete the paper.

Experimental Apparatus and Procedures

The centerpiece of the experimental program is a heterogeneous porous medium. It is constructed by centering a 0.050 m diameter and 0.368 m long Fontainebleau sandstone core inside a long, cylindrical, acrylic core holder. The inner diameter of the acrylic tube is 0.089 m and total length is 0.65 m. The annular space between the sandstone and the coreholder wall is packed with Ottawa sand. Similarly, the remaining 0.282 m of coreholder is packed with sand. Hence, the tube contains a heterogeneous portion consisting of sandstone and sand, and a homogeneous portion filled with sand. For experiments where we seek to prevent exchange of fluid between the sandstone and the sand, a heat-shrink Teflon tube is fit around the sandstone. In this case, only the circular faces at the beginning and end of the Fontainebleau core are left open to flow. When cross-flow is not prevented, we make no special preparation of the sandstone core.

Figure 1 is a reconstructed image of the porosity field measured using the CT scanner. Further details on the scanner and imaging methods will be given later, but the sandstone and sand portions of the porous medium are labeled and apparent in Fig. 1. Average porosity values obtained with CT along both the sand and sandstone portions of the core are displayed in Fig. 2. Each component of the heterogeneous porous medium is relatively homogeneous with an average sandstone porosity of 0.14 and an average sand porosity of 0.32. The Ottawa sand permeability was measured at 6.7 μm2 and the Fontainebleau sandstone permeability is 0.1 μm2. Both values are permeability to brine. The contrast in permeability between the sand and sandstone is 67 to 1.

The coreholder is designed so that fluids can be injected from either end. Machined endcaps distribute injected fluids across the cross-sectional area of the coreholder. When gas is injected into the sand-filled region, foam can generate before reaching the heterogeneous zone. On the other hand, when gas is injected directly into the heterogeneous end, foam generation in an initially liquid-filled heterogeneous porous medium can be observed. Unfortunately, coreholder design precluded the installation of pressure taps to measure the in-situ pressure profile.

Nitrogen (N_2) is injected into the porous medium saturated with foamer solution at a rate of 3 SCCM (standard cubic centimeters per minute) using a Matheson (Montgomeryville, PA) Model 8141 0-10 SCCM mass flow controller. Nominally, the superficial gas velocity is 0.67 m/day (8.04 E-6 m/s) relative to the outlet pressure of 101325 PA. Foamer solution was not injected simultaneously with the gas because such experiments in one-dimensional, homogeneous sandstones can lead to pressure drops on the order of 2000 kPa/m (100 psi/ft) (c.f. [16]), and we did not wish to over-pressurize the experimental system. Previous one-dimensional experiments using gas only injection and a similar surfactant and sand resulted in moderate pressure drops[17].

Through the combination of communicating and noncommunicating heterogeneities and injection into homogeneous or heterogeneous portions of the core, 4 different experiments are possible:

1. Injection across the heterogeneous side, noncommunicating sand and sandstone
2. Injection across the heterogeneous side, communicating sand and sandstone
3. Injection across the homogenous sand, noncommunicating sand and sandstone
4. Injection across the homogenous sand, communicating sand and sandstone

Figure 3 shows schematically each of these cases and indicates where gas is injected. A dark, solid line indicates the heat-shrink jacket if present.

The surfactant is an alpha olefin sulfonate (AOS C14-C16) supplied by Shell Chemical (Houston, TX). A concentration

of 0.1% by weight active surfactant in a 0.5 wt% NaCl brine was chosen as the optimal foamer solution. The screening procedure was two pronged. First, the pressure drop across a small (0.01 m diameter and 0.25 m long) chromatography column packed with the Ottawa sand was measured for increasing surfactant concentrations for a variety of brines. Nitrogen was injected at a rate of 10 SCCM while the surfactant solution injection rate was 0.34 cm3/min. A backpressure of 696 kPa (100 psi) was maintained at the sandpack outlet. Next, the interfacial tension between air and surfactant solution was measured for increasing concentration of surfactant using the pendant drop method. A broad range of surfactant concentrations was used in order to identify the critical micelle concentration (CMC). Figure 4 presents both the pressure drop and surface tension data collected. For the 0.5 wt% brine, strong foaming action, as witnessed by pressure drop, is found once the CMC is exceeded. Further, no benefit is found when surfactant concentration is increased above 0.1 wt% in either the pressure-drop or surface-tension data. Hence, this 0.1 wt% surfactant concentration was chosen.

An experiment begins by flushing the porous medium with gas (CO_2 or N_2) until it is free of liquid. A dry scan is made. If needed, the core is refilled with CO_2, and saturated with brine to 100% water saturation, because the CO_2 is soluble in the brine. At the minimum, 10 pore volumes of surfactant solution are injected to saturate the solid and aqueous phases with surfactant. A wet scan of the porous medium is then obtained. Once the porosity field has been determined, CT is used to confirm that 100 % liquid saturation is obtained. If it has not, more foamer solution is injected to dissolve the CO_2. Once an S_w of 100% is obtained, N_2 is injected at a constant rate. The progress of foam generation is seen directly in the CT data collected. Gas is injected until foam breakthrough at the outlet occurs and is continued for an additional 0.5 to 1. PV.

Porosity and aqueous-phase saturation fields are measured on 18 volume sections equally distributed along the core using a fourth generation (1200 fixed detectors) Picker™ 1200 SX X-ray scanner. Typically, the voxel dimension is (0.25mm by 0.25mm by 4mm). The acquisition time of one image is 7 seconds while the processing time is around 40 seconds. The total time of measurement is short enough to capture accurately the position of the front and construct saturation profiles along the core. Porosity and saturation measurements require so-called "dry" and "wet" scans to obtain CT numbers for the medium free of liquid and then fully saturated with liquid. Porosity is computed by a ratio between the dry and wet counting (CT numbers) from the known air attenuation. Saturation is determined in the same way after garnering CT numbers during the displacement. The measurement accuracy depends on the different parameters chosen for the X-ray emitter such as voltage and intensity, filters, and reproducibility of the positioning system moving the coreholder apparatus into and out of the gantry. A theoretical computation of the measurement accuracy, assuming no error in the positioning system, provides an error of 6% [18].

Results

To provide a baseline, gas was injected at 3 SCCM into surfactant-free cores. Figure 5 illustrates gas flow in the absence of foam when heterogeneities communicate. Saturation values are obtained by averaging the saturation for each voxel in a cross section for the sandstone and sand regions, respectively. Time is reported nondimensionally in pore volumes of injected gas and distance is measured from the inlet. Figure 5a shows the saturation profiles for the sandstone, while Fig. 5b the profiles for the sand. Straight lines connect the individual data points. Gas displacement of water is poor. Strong displacement fronts are not witnessed and even after 4 PV of gas injection, water saturation remains high. In this case, gas breakthrough occurs at 0.05 PV and the total production at 4.5 PV is about 0.1 PV. In the case of noncommunicating heterogeneities, gas breakthrough occurs at 0.11 PV and total water production at 3 PV is only 0.17 PV.

Next, foam displacements in all four of the configurations detailed in Fig. 3 were completed. First injection through the heterogeneous face of the core is discussed and then injection through the homogeneous face. The extent of foam generation and reduction in gas mobility is quantified through the saturation profiles determined by CT and the length of time to gas breakthrough. A breakthrough time approaching 1 PV indicates efficient desaturation of the core and by implication strong foam generation.

Noncommunicating layers, heterogeneous face injection. In this experiment, the heat-shrink wrapped Fontainebleau sandstone core cannot exchange fluid with the sand except through the inflow and outflow ends. N_2 is injected from the heterogeneous region and across both sand and sandstone. Figure 6 displays typical saturation fields across the cross section of the core holder at various locations. The elapsed time is 0.23 PV of gas injection. In the figure, a shading of black represents a water saturation, S_w, of 1 while white indicates S_w equal to 0. In the last section, taken at 16 cm ($x/L = 0.25$) from the inlet, it is evident that gas is present in the low permeability sandstone, but has not yet reached this location in the sand. The dark shading of Fig. 6 indicates that an effective displacement is occuring.

Figure 7 presents the averaged aqueous-phase saturation profiles measured at various times. Figure 7a shows the saturation profiles for the sandstone, while Fig. 7b the profiles for the sand. The 18 data points for the sand region correspond to the number of volume sections analyzed.

The first point to note is that desaturation of both the sand and sandstone by foamed gas is efficient. Saturation fronts are relatively steep and sharp in both porous media. The entire porous medium is saturated with foamer solution initially and S_w, downstream of the front is everywhere 1. In the case of the sandstone, S_w immediately following the passage of the foam front is about 0.3 whereas in the sand it is roughly 0.15. That is, following desaturation by foam, each layer is within a

few saturation units of its irreducible saturation. Foam has effectively diverted a portion of the injected gas into the sandstone.

Secondly, the position of the saturation fronts as a function of time tells an interesting story. When t equals 0.12 PV the leading edge of the foam front in both the high and low permeability media is at a dimensionless position of 0.14. At the succeeding time of 0.23 PV the front in the sandstone is at x/L equal to 0.3, while in the sand it is slightly behind at x/L equal to 0.26. At a t of 0.35 PV, it appears that the foam front has just exited the sandstone. The leading edge of the foam front in the sand at this same time significantly lags behind at a position of 0.35. Examination of the saturation profiles at 0.46 PV confirms this trend. The saturation at x/L equal to 0.45 in the sandstone clearly shows that foam has pushed its way through the sandstone core and exited into the sand. On the other hand, the foam front pushing through the annular sand region is only positioned at x/L equal to 0.4. It is apparent that the foam front in the low permeability layer moves more quickly than in the high permeability layer. This fact is also evidenced in the raw saturation data in Fig. 6. In the discussion, we will rationalize this behavior in terms of the effect of capillary pressure on foam texture.

At times of 0.46, 0.54, and 0.70 PV the effect of the foam fronts moving at different speeds in each media can still be seen in the saturation profiles. The foamed gas exiting the sandstone results in fronts positioned in the neighborhood of x/L from roughly 0.75 to 0.85. A second trailing front is also apparent. For instance, at 0.70 PV this trailing front is positioned at roughly 0.45. This second front results from the foamed gas and water exiting the annular region packed with sand as well as water that was not displaced in the completely sand-filled region by the first foam front. By 1.3 PV, the average aqueous-phase saturation in the sand is about 0.10 and desaturation is complete.

Communicating layers, heterogeneous face injection. The configuration is similar to the first case, except that the heat-shrink Teflon is absent from the sandstone. The sandstone and the sand are thereby in capillary communication and free to exchange fluid along the length of the sandstone.

Figure 8 presents the results of the displacement in a fashion similar to that in Fig. 7. Sandstone saturation profiles are given in Fig. 8a and sand profiles in Fig. 8b. Again, strong and steep displacement fronts in both the sandstone and sand are witnessed. Foam effectively desaturates each layer. In contrast to Fig. 7, the displacement fronts in each porous medium move at the same rate. At times of 0.25, 0.33, and 0.41 PV front position is 0.3, 0.4, and 0.45, respectively. At the shortest time of 0.08 PV, displacement fronts do not coincide exactly. This is likely an inlet artifact.

Displacement fronts that move with identical velocity in communicating heterogeneous zones is also the expected result for the propagation of unfoamed gas[19] if the effect of gravity is minimal. The striking result is the degree of displacement in the low permeability sandstone.

Noncommunicating layers, homogeneous face injection. In this, the third case, gas is injected into the saturated porous medium from the side completely filled with sand. Flow across the cylindrical face of the sandstone is again prohibited by the Teflon jacket barrier.

Figure 9 shows the saturation profiles. In the initial homogeneous section, gas enters the sand, a foam is generated, and displacement of foamer solution from the sand is quite efficient. Foam generation is rapid as a strong displacement front is seen even at 0.15 PV. At roughly 0.54 PV, the foamed gas first enters the sandstone. Again, the foamed gas moves more quickly through the low permeability sandstone than it does through the more permeable sand. The leading edge of the displacement front is at x/L equal to 0.7 in the sandstone and at 0.6 in the sand after 0.7 PV of total gas injection. At 0.85 PV of injection, front positions are roughly 0.85 and 0.75 in the sandstone and sand, respectively. Consistent with this observation, gas breakthrough occurs from the sandstone first.

Initially, foam displacement in the sandstone is not as efficient as in the earlier two cases. Examining the saturation profiles at 0.7, 0.85, and 1.1 PV, we find that the height of the displacement front grows from 0.3 to over 0.6 saturation units.

Communicating layers, homogeneous face injection. Figure 10 reports the saturation profiles obtained during gas injection into the homogeneous sand-filled side with capillary communication between the sandstone and sand. Displacement from both the sand and the sandstone is excellent at all time levels. As in the second case where crossflow occurs, saturation fronts move at the same speed in each layer. It is seen by comparing Figs. 10a and 10b that front positions at times of 0.63, 0.74, and 0.88 PV are equal and correspond to x/L equal to 0.65, 0.75, 0.85, respectively.

Discussion

The foam flow behavior discovered in each of these cases can be rationalized by considering foam texture (i.e., bubble size) and the effect that porous medium capillary pressure plays in setting foam texture. It is well established that finely textured foams, that is foams with small average bubble size, present a larger resistance to flow than do coarsely textured foams [20,21]. In turn, bubble size is dictated by pore-level foam generation and coalescence events[11]. Foam generation is largely a mechanical process and independent of surfactant formulation and concentration. On the other hand, foam collapse depends strongly on the foamer solution. Foam lamellae are stable provided that surfactant can stabilize the gas-liquid interface against suction capillary pressure that seeks to thin foam films. Hence, it is expected that the rate of

foam coalescence increases with porous medium capillary pressure. In turn, the foam becomes more coarse. The characteristic value of capillary pressure that a porous medium approaches during strong foam flow is referred to as the limiting capillary pressure, and it is set principally by surfactant type and concentration[22].

In the first case reported in Fig. 7, each porous medium accepts whatever portion of the injected gas it desires. Because the sand and sandstone are isolated in the sense that crossflow is not allowed, foam is generated and assumes a texture that is independent of events occurring in the adjacent layers. We surmise that in the low permeability sandstone the foam is not as finely textured as in the sand. Sandstone capillary pressure is larger for a given saturation due to lower medium permeability. Hence, a greater suction pressure is exerted on foam lamellae inducing foam coalescence. This in turn leads to a more coarsely textured foam that is more mobile than its finely textured counterpart in the sand. Hence, foamed gas progresses more rapidly through the low permeability porous media. Nevertheless, gas mobility has been lowered substantially and water displacement is efficient.

In the situation summarized in Fig. 8, the porous media communicate with each other across the long cylindrical interface of the sandstone. Since the porous media communicate, gas at the foam front minimizes its flow resistance via foam bubble texture. When the flow resistance in the sandstone increases, foamed gas diverts into the sand, and vice versa. Thus, foam propagates at an equal rate in each layer because the saturation fronts are bound together by the necessity to maintain the minimum flow resistance. Bubble textures in sand and sandstone are not expected to be identical, but to yield identical gas mobility[19]. In this case, the mobility is low and promotes effective desaturation. In the cases where the heterogeneous section is at the end of the core, similar explanations follow.

When crossflow is prohibited between the sand and the sandstone, each porous medium sets foam texture and, hence, gas mobility independently. Capillary pressure in the low permeability sandstone is higher than in the sand, coalescence ensues, and foam in the sandstone is more mobile than in the sections filled with sand. If crossflow occurs, gas mobility is balanced because low flow resistance forces gas to divert into the adjacent layer. Foam propagates at equal rates in each layer.

Interestingly, the transient experimental results shown here bear striking qualitative similarity to previous simulation of foam behavior in heterogeneous porous media reported elsewhere[19]. We note that the preceding qualitative arguments bear strong resemblance to the quantitative results reported in that study.

Conclusions

An experimental study of foam generation and propagation in heterogeneous porous media using Fontainebleau sandstone and Ottawa sand was performed. The contrast in permeability between high and low permeability homogeneous zones was 67 to 1. Despite this drastic permeability contrast and despite the fact that high permeability zones typically lead to gas channeling, foamed gas is diverted to low permeability channels in these experiments. In this regard, the foam generated in these experiments can be regarded as strong. Foam effectively desaturates both the high permeability and low permeability portions of the experimental setup and desaturation is complete following roughly 1 PV of gas injection. This result is found for both systems that permit and prohibit cross flow.

Foam in heterogeneous systems appears to be self regulating in that gas mobilities in each porous medium equalize when layers communicate and nearly equalize in noncommunicating systems. Similar efficient diversion and desaturation is likely in heterogeneous, layered field situations where the permeability contrast is not as large provided that foam is tolerant of the presence of oil. Also, the capillary pressure of each layer must be less than the critical capillary pressure for foam coalescence.

In general, and in agreement with a previous theoretical study, it is observed that when permeability heterogeneities communicate and there is fluid crossflow that foam displacement fronts move at equal velocity in each zone. When crossflow is prohibited by an impermeable barrier, rapid foam propagation and desaturation of the low permeability zone is witnessed.

Acknowledgement

This work was supported by the Assistant Secretary for Fossil Energy, Office of Oil, Gas, and Shale Technologies of the U.S. Department of Energy under Contract No. DE-FG22-96BC14994 to Stanford University. Likewise, the support of the SUPRI-A Industrial Affiliates is acknowledged.

H. J. Bertin acknowledges NATO and Institut Francais du Petrole for supporting his sabbatical at Stanford.

References

1. Patzek, T.W. and M.T. Koinis: "Kern River Steam-Foam Pilots," *Journal of Petroleum Technology*, 42(4) (1990) 496-503.
2. Djabbarah, N.F., S.L. Weber, D.C. Freeman, J.A. Muscatello, J.P. Ashbaugh, and T.E. Covington: "Laboratory Design and Field Demonstration of Steam Diversion with Foam," SPE 20067, in Proceedings of the 60th California Regional Meeting, Ventura (Apr. 1990).
3. Mohammadi, S.S., D.C. Van Slyke, and B.L. Ganong: "Steam-Foam Pilot Project in Dome-Tumbador, Midway-Sunset Field," *SPE Reservoir Engineering*, 4(1) (1989) 7-16.
4. Hoefner, M.L., E.M. Evans, J.J. Buckles, and T.A. Jones: "CO2 Foam: Results from Four Developmental Field Trials," SPE/DOE 27787, in Proceedings of the SPE/DOE Ninth Symposium on Improved Oil Recovery, Tulsa, Oklahoma (Apr. 1994).
5. Friedmann, F., T.L. Hughes, M.E. Smith, G.P. Hild, A. Wilson, and S.N. Davies: "Development and Testing of a New Foam-Gel Technology to Improve Conformance of the Rangely-CO2 Flood," SPE 38837, in Proceedings of the SPE Ann. Tech. Conf. and Exhibition, San Antonio, TX (Oct. 1998).
6. Aarra, M.G., A. Skauge, S. Sognesand, and M. Stenhaug: "A

Foam Pilot Test Aimed at Reducing Gas Inflow in a Production Well at the Oseberg Field," *Petroleum Geoscience*, 2(1996) 125-132.
7. Hirasaki, G.J., C.A. Miller, R. Szafranski, J.B. Lawson, D. Tanzil, R.E. Jackson, J. Londergan, and H. Meinardus: "Field Demonstration of the Surfactant/Foam Process for Aquifer Remediation," SPE 39393, in Proceedings of the SPE Ann. Tech. Conf. and Exhibition, San Antonio, TX (Oct. 1997).
8. Hirasaki, G.J., C.A. Miller, R. Szafranski, D. Tanzil, J.B. Lawson, R.E. Jackson, H. Meinardus, J. Avvakoumides, M. Jin, L. Kennedy, P. Mariner, G.A. Pope, and T. Oolman: "AATDF Surfactant/Foam Process for Aquifer Remediation," Report , Intera, Austin, Texas (1997)
9. Kovscek, A.R. and C.J. Radke: "Fundamentals of Foam Transport in Porous Media", in *Foams in the Petroleum Industry*, L.L. Schramm, Editor., American Chemical Society, Washington, D.C., (1994) p. 115-163.
10. Rossen, W.R.: "Foams in Enhanced Oil Recovery", in *Foams: Theory, Measurmeents and Applications*, R.K.Prudhomme and .S. Khan, Editors, (1995.
11. Chambers, K.T. and C.J. Radke: *Capillary Phenomena in Foam Flow Through Porous Media.* Interfacial Phenomena in Petroleum Recovery, ed. N.R. Morrow. Vol. Ch. 6. , Marcel Dekker Inc., New York, (1991) 191-255.
12. Casteel, J.F. and N.F. Djabbarah: "Sweep Improvement in CO2 Flooding by Use of Foaming Agents," *SPE Reservoir Engineering*, 3 (1988) 1186-1192.
13. Robin, M.: "Laboratory Evaluation of Foaming Additives Used to Improve Steam Efficiency," SPE 16729, in Proceedings of the 62nd Annual Technical Conference and Exhibition of the Society of Petroleum Engineers, Dallas (Sep. 1987).
14. Llave, F.M., F.T.-H. Chung, R.W. Louvier, and D.A. Hudgins: "Foams as Mobility Control Agents for Oil Recovery by Gas Displacement," SPE/DOE 20245, in Proceedings of the SPE/DOE Seventh Symposium on Enhanced Oil Recovery, Tulsa, Oklahoma (Apr. 1990).
15. Hirasaki, G.J., C.A. Miller, R. Szafranski, J.B. Lawson, and N. Akiya: "Surfactant/Foam Process for Aquifer Remediation," SPE 37257, in Proceedings of the SPE International Symposium on Oilfield Chemistry, Houston, TX (Feb. 1997).
16. Kovscek, A.R., T.W. Patzek, and C.J. Radke: "A Mechanistic Population Balance Model for Transient and Steady-State Foam Flow in Boise Sandstone," *Chemical Engineering Science*, 50(23) (1995) 3783-3799.
17. Fergui, O., M. Quintard, H. Bertin, and D. Defives: "Transient Foam Flow in Porous Media: Experiments and Simulations," Proceedings of the 8th European IOR-Symposium, Vienna, Austria (1995).
18. Burger, J.: Personal Communication, Stanford University, Stanford (1996)
19. Kovscek, A.R., T.W. Patzek, and C.J. Radke: "Mechanistic Foam Flow Simulation in Heterogeneous Multidimensional Porous Media," *SPEJ*, 2(4) (1997) 511-526.
20. Hirasaki, G.J. and J.B. Lawson: "Mechanisms of Foam Flow in Porous Media: Apparent Viscosity in Smooth Capillaries," *Soc. Pet. Eng. J.*, 25(2) (1985) 176-190.
21. Falls, A.H., J.J. Musters, and J. Ratulowski: "The Apparent Viscosity of Foams in Homogeneous Beadpacks," *Soc. Pet. Eng. Res. Eng.*, 4(2) (1989) 155-164.
22. Khatib, Z.I., G.J. Hirasaki, and A.H. Falls: "Effects of Capillary Pressure on Coalescence and Phase Mobilities in Foams Flowing Through Porous Media," *Soc. Pet. Eng. Res. Eng.*, 3(3) (1988) 919-926.

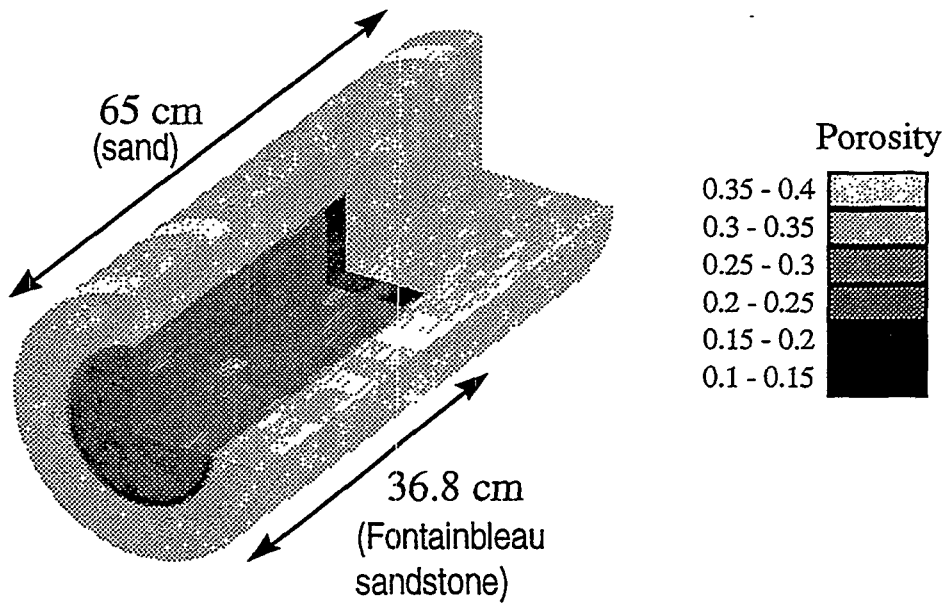

Figure 1: Reconstruction of porosity distribution in heterogeneous porous medium.

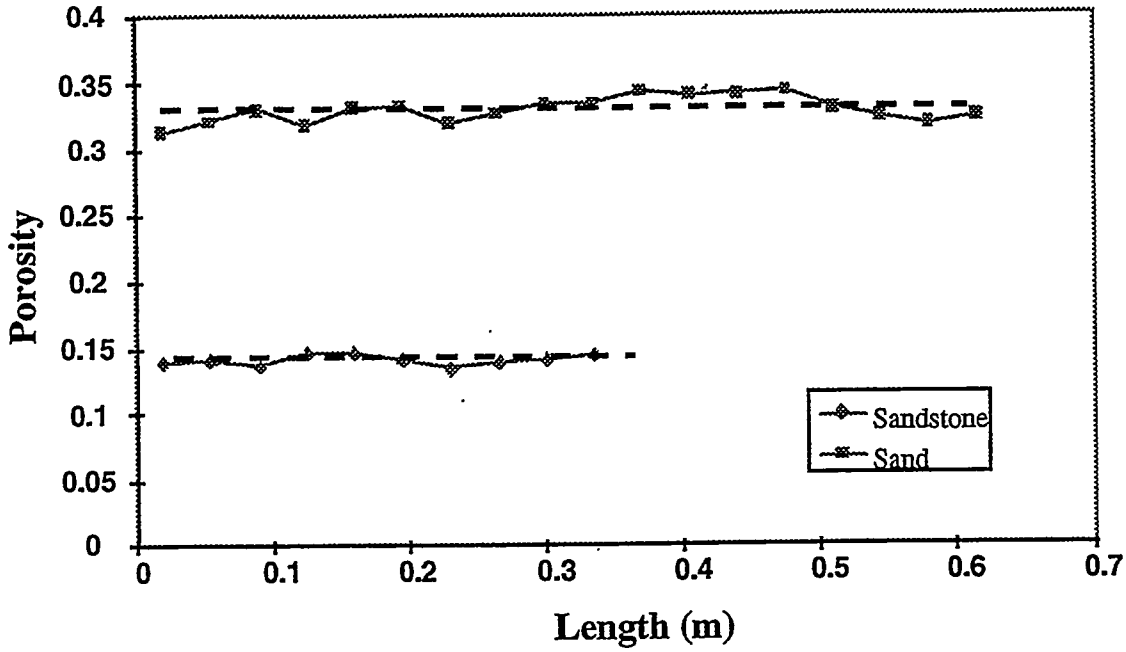

Figure 2: Average sand and sandstone porosity along the length of the heterogeneous core.

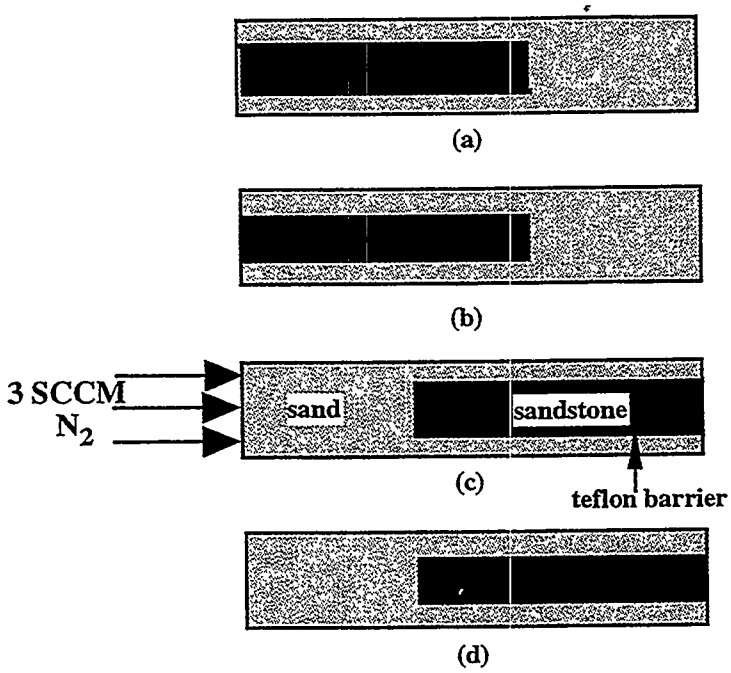

Figure 3: Configuration of heterogeneous porous medium during experiments. Gas is injected at the left face.

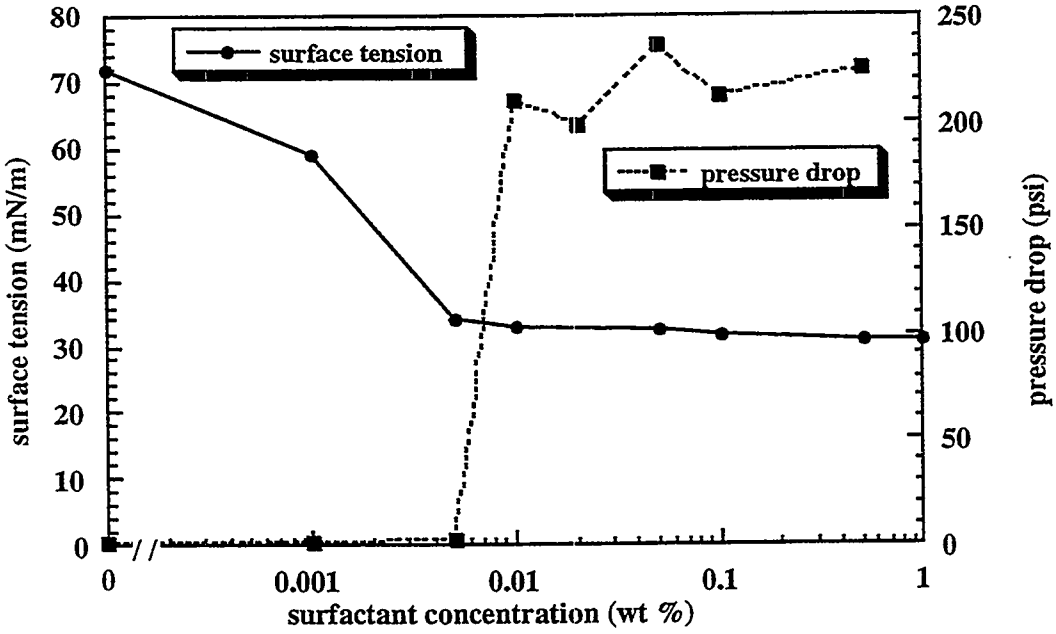

Figure 4: Pressure drop and surface tension for foamer solution as a function of surfactant concentration. Brine concentration is 0.5 wt%.

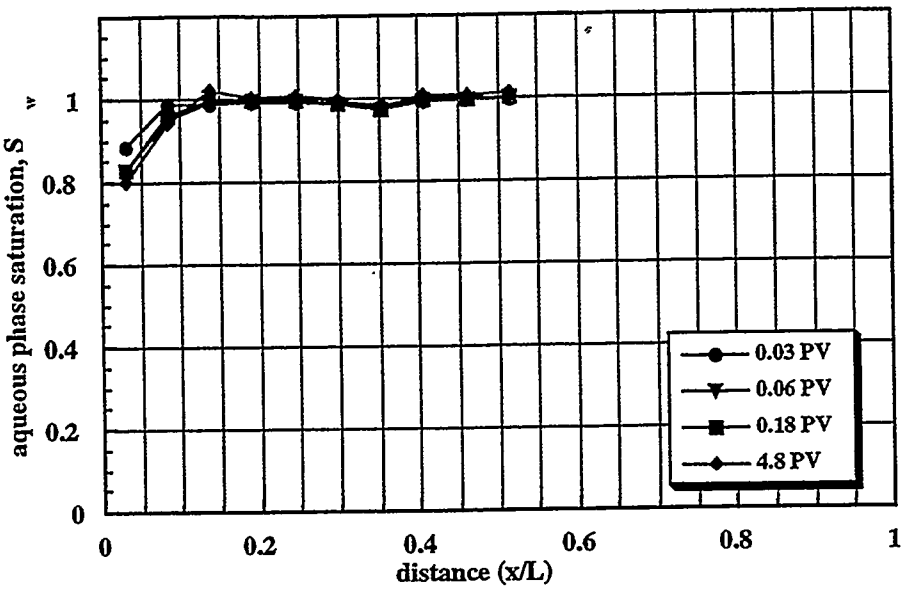

(a)

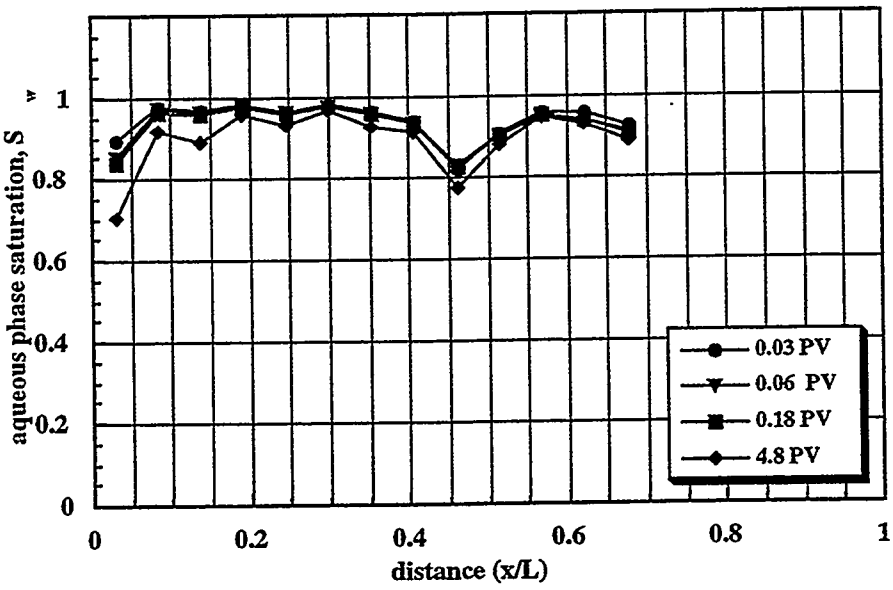

(b)

Figure 5: Transient aqueous phase saturation profiles for gas-only displacement with crossflow: (a) sandstone and (b) sand regions.

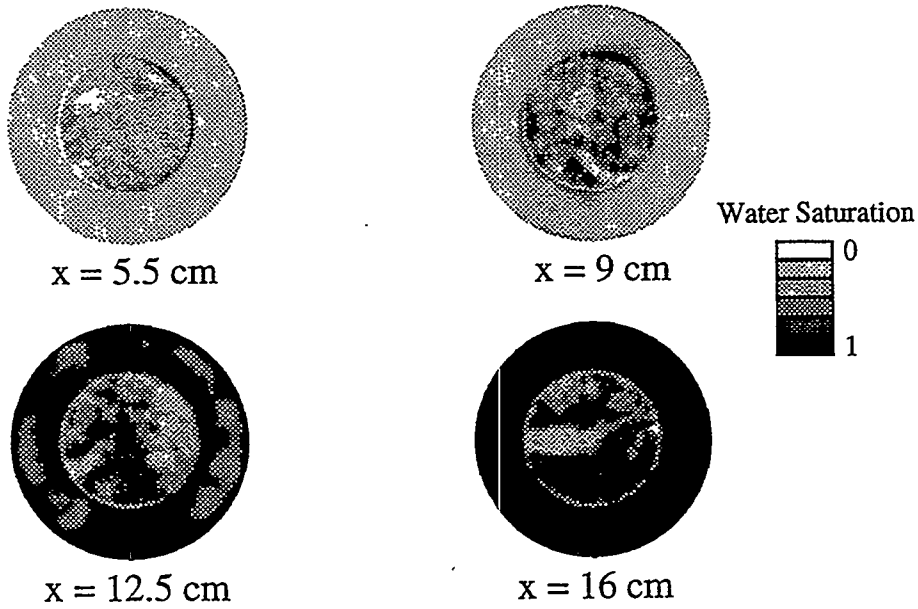

Figure 6: Water saturation profiles in the heterogeneous core section, t = 0.23 PV. Cross flow is not permitted.

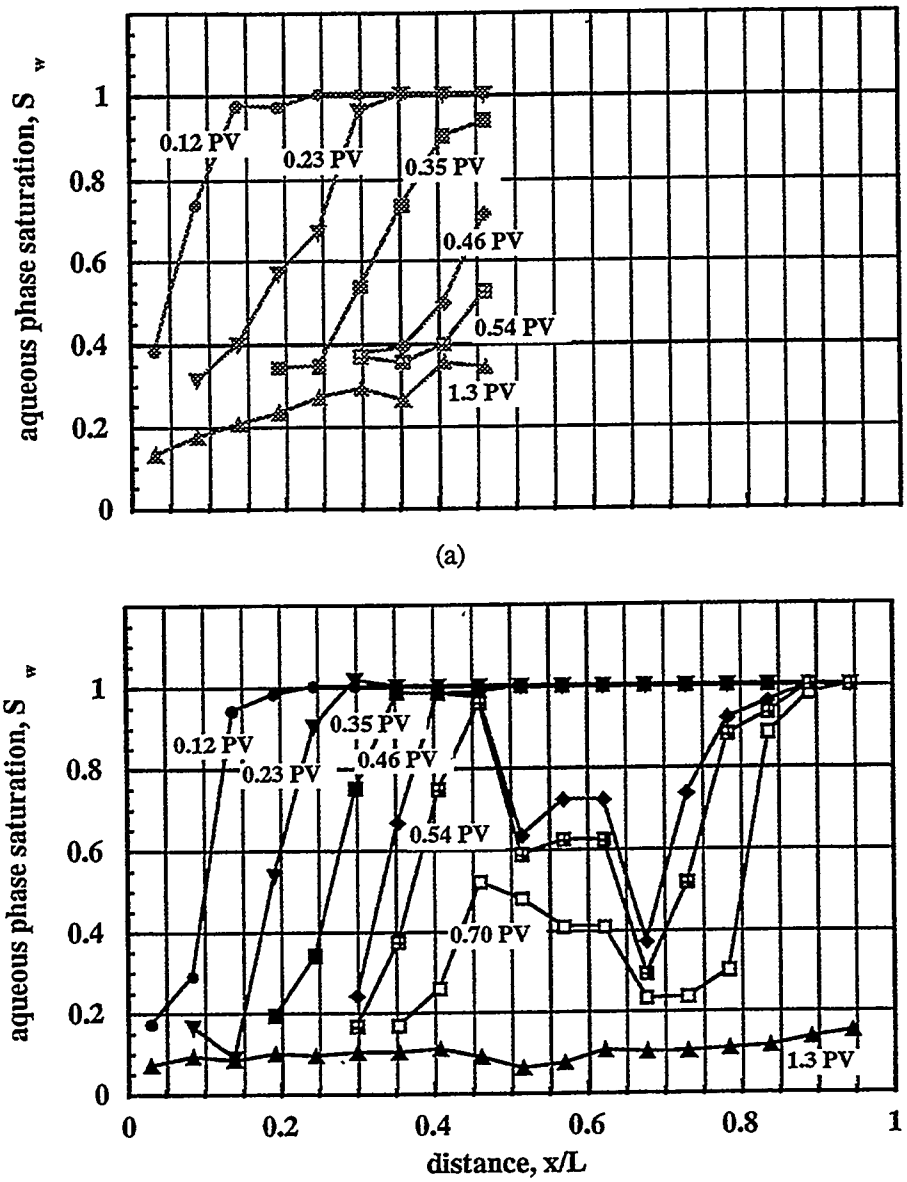

Figure 7: Transient aqueous phase saturation profiles for displacement without crossflow: (a) sandstone and (b) sand regions.

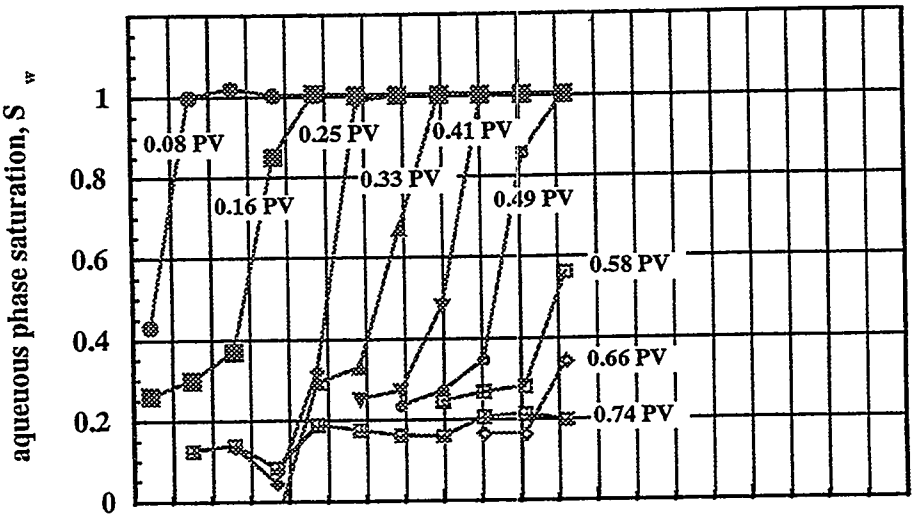

(a)

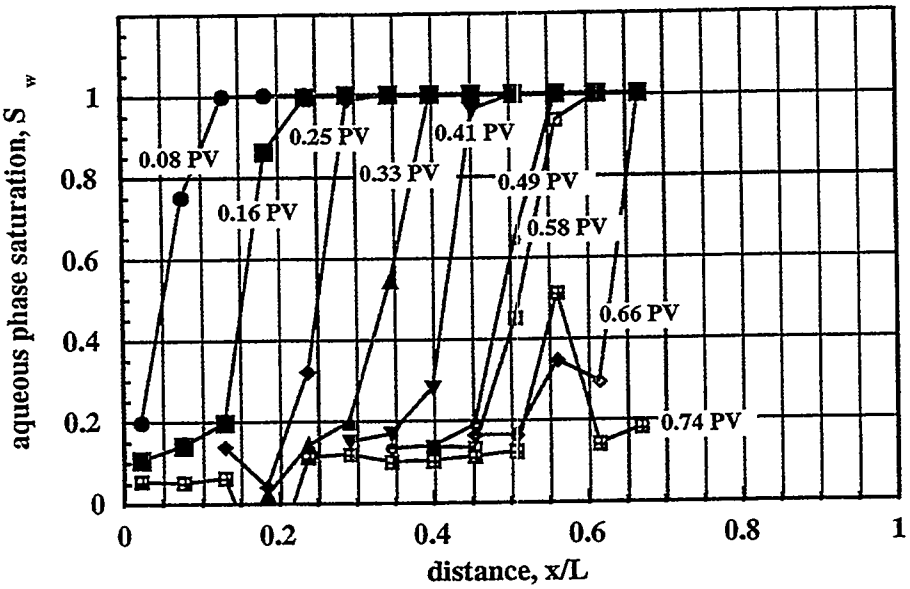

(b)

Figure 8: Transient aqueous phase saturation profiles for displacement with crossflow: (a) sandstone and (b) sand regions.

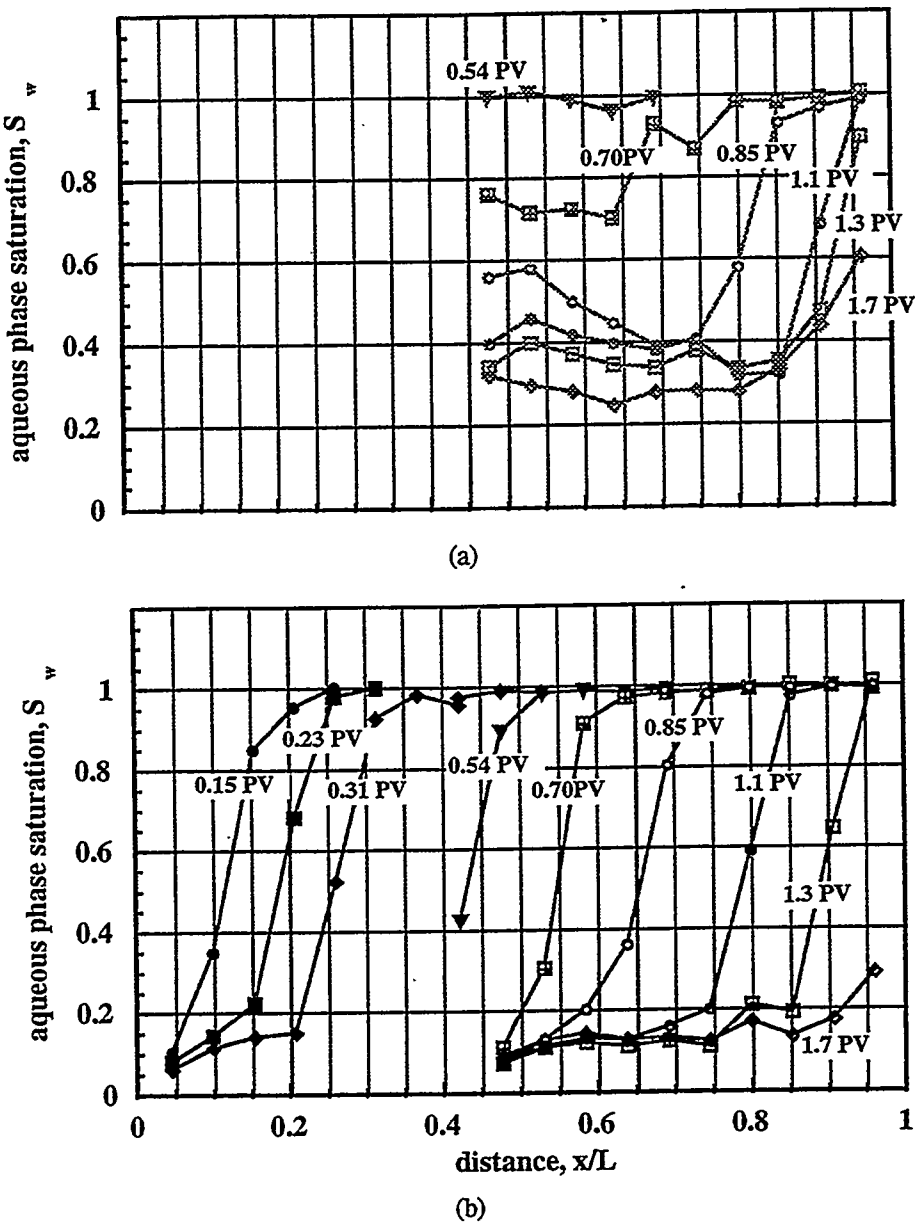

Figure 9: Transient aqueous phase saturation profiles for displacement without crossflow: (a) sandstone and (b) sand regions.

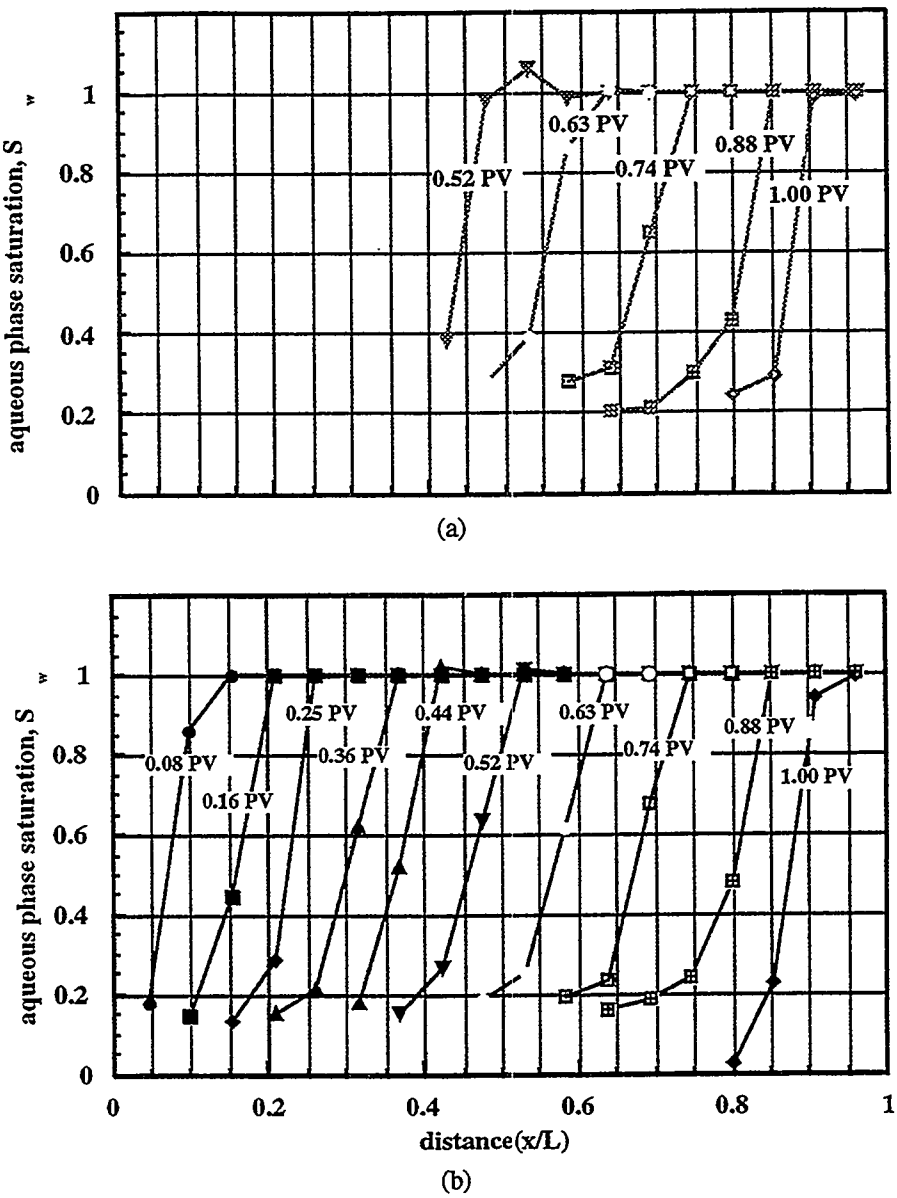

Figure 10: Transient aqueous phase saturation profiles for displacement with crossflow: (a) sandstone and (b) sand regions.

3.5 PORE-LEVEL VISUALIZATION OF OIL/FOAM INTERACTIONS IN A SILICON MICROMODEL

(N. Sagar, L. Castanier, and W. Brigham)

3.5.1 SUMMARY

The paper on the following page was presented at the SPE India Oil and Gas Conference and Exhibition, New Delhi, India (February 17-19, 1998).

SPE 39512

Pore-Level Visualization of Oil/Foam Interactions in a Silicon Micromodel

N. Sagar, Schlumberger, L.M. Castanier, SPE, Stanford U., and W.E. Brigham, SPE, Stanford U.

This paper was prepared for presentation at the 1998 SPE/DOE Improved Oil Recovery Symposium held in Tulsa, Oklahoma, 19–22 April 1998.

Abstract

This paper presents some cases of pore-level visualization of foam with oil. Many laboratory investigations have been carried out in the absence of oil, but comparatively few have been carried out with oil present. For field application, where the residual oil saturation may vary depending on the recovery method applied, any effect of the oil on foam stability becomes a crucial matter.

Silicon micromodels were used in this study. The micromodels are two-dimensional replicas of the flow path of Berea sandstone etched on a silicon wafer to a prescribed depth, using fabrication techniques from the computer industry. After flooding the models to connate water and residual oil saturations, a surfactant flood was followed by gas injection to generate foam. Starting with low concentrations of surfactant the concentrations were gradually increased. Visual observations were recorded on videotape.

Two different surfactants were used, a fluoro-surfactant (for generating a non-aqueous oil foam) and an alpha-olefin sulfonate. Oseberg (Norway) crude was the oleic phase in the first set of experiments, and kerosene in the next two sets. While the fluoro-surfactant created a strong static gas-blocking foam in the presence of oil, the alpha-olefin sulfonate (AOS) foamer did not.

The fluoro-surfactant foam gave the oil-tolerant behavior expected from its non-entering, non-spreading characteristics. The AOS on the other hand, did not behave in accordance with its bulk observations, and its behavior was seen to be controlled by formation of emulsions. Generation sites for both foam and the emulsions were controlled by pore geometry and local saturations. For the foam, no obvious link could be found between the number of films observed and the strength of gas blockage. Many other observations were made; including snap-off, emulsion formation and breakdown sequences, foam lamella formation and breakdown sequences, and static emulsion and foam in different configurations within the model.

Introduction

Primary and secondary production of an oil field often recovers less than half of the original oil in place. To recover additional oil, it is necessary to apply enhanced oil recovery (EOR) techniques such as miscible or imiscible gas displacement (CO_2, hydrocarbon gases, etc.). However, major problems occur in these EOR methods because the displacing agent has high mobility and low density compared with that of reservoir fluids. Fingering (channeling) and gravity override reduce the sweep efficiency, contribute to early breakthrough of injected fluid, and thus reduce the amount of oil recovered. The use of surfactant stabilized foams to counteract these problems was suggested decades ago. Foam is advantageous compared with a simple fluid of the same nominal mobility because the foam, which has an apparent viscosity greater than its components, lowers the gas mobility in the swept or higher permeability parts of the formation. This diverts at least some of the displacing gas to other parts of the formation that were previously unswept, thus recovering additional oil. Because foam mobility is reduced more in the higher permeability zones, improvement in both vertical and areal sweep efficiency is achieved.

This work focuses on stability of foams in porous media when oil is present. For field applications, any effect of the oil on foam stability becomes a crucial matter. Two differing approaches have been used in an attempt to scale up foam properties to the reservoir. They represent differing descriptions of the physics of foam. One approach is purely empirical and relies on calibrating a flexible simulator, based on laboratory data in conventional cores, to represent the most critical foam effects. The empirical foam model implemented in STARS™, a pseudo-compositional reservoir simulator, is probably the best example of this

approach (Coombe and Mohammedi[1] and Surguchev *et al.*[2]). The other approach attempts to extract information about the physical flow mechanisms observed at the pore level, and constructs mathematical relationships between experimental parameters. One such model was developed at the University of California at Berkeley. The physical mechanisms in this model rely on observations of foam flow in etched-glass micromodels, especially from a comprehensive study by Radke and Chambers.[3]

Currently accepted theories on foam flow are largely built on the basis of pore model observations by Mast,[4] Owete *et al.*,[5] Huh *et al.*,[6] and Schramm and Novosad.[7] Most micromodels were made by etching a flow pattern into a glass plate and are two-dimensional representations of the pore structure. With glass micromodels, the reaction kinetics of acid etching makes it necessary to enlarge the pore sizes of typical sandstone pores, usually by a factor of 5 to 50 compared to their natural size. Obviously, this is a serious limitation for their use in studying processes that depend critically on capillary forces, and involve thin films as seen in foam flow.

The silicon micromodel on the other hand, replicates a pore structure of any design on a silicon wafer, adapting fabrication techniques from the computer industry. The pore cavities are created photochemically, a process which is not rate-limited. The micromodels used in this study offer 1:1 scaling of typical sandstone pores in two dimensions.

Literature Survey

Many laboratory investigations of foam flooding have been carried out in the absence of oil, and comparatively few have been carried out with oil present. When research began to include oil, it was seen that the effect of oil on foam stability was indeed complicated. Oil saturation could alter foam stability and its propagation mechanisms to a great extent. The nature of the foam, foam injection procedures, reservoir wettabilities and pore geometry were seen to affect the oil-foam interactions.

A foam is a dispersion of gas in liquid, usually with a surface active agent present. Foams are not thermodynamically stable and ultimately decay into their constituent phases, but can be mechanically stable for long periods of time. When a foam exists inside a confining medium, the dimensions of this confining medium relative to the average bubble size, determine the texture and properties of the foam. Holm[8] found liquid to flow as a continuous phase, but gas flow to occur by a sometimes very slow process of continually breaking and reforming of liquid films. This explains why gas flow may be essentially blocked by foam in pores, while the permeability to liquid is merely a function of its saturation. The ability of foam to reduce gas mobility has led to its application in a number of processes, including gas injection, steam flooding, and well treatment techniques.

The use of surfactant stabilized foams to counteract problems such as fingering and gravity override was suggested several decades ago. Marsden[9] reviewed previous findings, surmising that apparent gas viscosity was a function of the gas flow rate, flow history and surfactant concentration, and that 'breaking and reforming' processes are a dominant mode of foam propagation in micromodels. Sanchez and Schechter[10] suggested that gas permeability was a function of the wetting phase film thickness.

Owete *et al.*[11] suggested that air was propagated by displacement of lamellae in long bubbles flowing and extending across several pore lengths while the liquid flowed through the network of films. They also observed snap-off occurring at pore constrictions and the resultant bubble 'break and reform' process. Radke and Ransohoff[12] categorized the various mechanisms of foam generation within glass bead packs as 'snap-off', 'lamella leave behind', and 'lamella division', with snap-off being the primary mechanism for strong foam generation.

Roof[13] studied the specific pore geometry necessary for snap-off mechanisms. Roof noted that the front is always at least seven pore radii from the throat of the constriction before snap-off can occur. Falls *et al.* [14] and Kovscek *et al.*[15] proposed that at steady state conditions, the rates of generation and collapse of lamellae must be equal.

Castanier and Hanssen[16] noticed in silicon micromodels the sliding of lamellae (bubble train flow) over liquid films covering the grains.

Oils are among the earliest chemicals to be used for foam inhibition and foam breaking, as discussed in the literature by Harkins,[17] Robinson,[18] and Ross and McBain.[19] Some theories for the mechanisms of anti-foaming action have emerged from this work. In general matters are not simple. Apparently oils can destabilize foams by several mechanisms, and more than one mechanism may be operating in a given case.

Some possibilities for the mechanisms of foam destabilization by a given oil phase include: (1) surfactant partition in the oil, (2) surfactant adsorption by the foam lamellae, (3) alteration of the wettability of the solid phase, (4) oil spreading on foam lamellae. and (5) oil emulsification.

Nikolov *et al.*,[20] studying bulk oil-foam interactions, reported three distinct films during three phase foam thinning: 'foam films', or water films between air bubbles; 'emulsion films', or water films between oil droplets; and 'pseudo-emulsion films' where water film resides between air and oil droplets. Pseudo-emulsion films, droplet sizes and numbers may all contribute to foam destabilization.

Kuhlman[21] and Manlowe,[22] and Radke[3] observed in micromodels that oils were destroying foams. Work done by Novosad and Ionescu[23] Jensen and Friedmann,[24] Kristiansen and Holt,[25] and Hutchinson *et al.*[26] suggested that foam

sensitivity to oil is also manifested as an increased difficulty of forming and propagating foams through porous media containing oil. Novosad and Ionescu[23] found lower mobility reduction factors in foam floods in cores containing residual oil, compared to the same floods in oil free. The lower mobility reduction factors are due to some kind of foam destruction by the oil.

Lau and O'Brien[27] through the use of sand packs and both spreading and non-spreading oils, showed an increase in foam generation time, a reduction in foam propagation rate, and an increased foam destruction rate with spreading oils. This finding is contrary to Manlowe[22] and Kovscek *et al.*,[15] who argue that there is no correlation between oil spreading and foam stability. Instead, they state that pseudo-emulsion film collapse is the general destabilization mechanism.

Hanssen and Dalland,[28] in a model system (glass bead pack) of a gas blocking foam in an oil reservoir, observed clear trends in mobility reduction with varying concentrations of oil and surfactant. They concluded that the change in interfacial tension between gas and the aqueous phase, upon equilibration with oil, appeared to be a good predictor of gas blockage efficiency for the systems studied.

Oil interactions with foam have been studied by Dalland and Hanssen.[29] Conducting experiments with flowing and gas blocking foams, using a set of conventional and fluorinated surfactants and various oils, they found varying oil tolerance and sensitivities. In all cases the combination of non-spreading and non-entering oil created a strong gas-blocking foam, or a low mobility flowing foam. The 'Lamella Number', L, calculated from interfacial tensions was found to be of no predictive power. The results indicated that the mechanisms of oil-foam interactions are the same for gas blocking and for flowing foams in porous media0

Castanier and Hanssen[16] worked on oil-foam interactions using a fluorosurfactant foam and an AOS foam. The fluorosurfactant foam gives the oil tolerant behavior expected from its non-entering, non-tolerant characteristics. AOS foam by contrast, is controlled by formation of oil-water emulsions which appear to prevent the formation of strong foam until a large excess of foaming agent is present.

Because petroleum reservoirs are often of intermediate, mixed or oil wettability, some researchers have included reservoir wettabilities in their studies. Huh *et al.*[6] found that micromodel wettability was altered to intermediate or oil wet as a result of crude oil saturation. The effects of various phase affinities to grain surfaces was studied by Sanchez and Hazlett[30] as well. An indication of surface reaction, from hydrophobic to hydrophilic, was detected after the addition of surfactant. This suggests wettability alteration. Kuhlman[21] obtained similar results, and said that the deleterious effect of oil on foam was due to the high concentration of light hydrocarbons in the oil, and the oil wetness of the medium itself.

Castanier and Hornbrook[31] noted that wettability alteration was due to the surfactant injection procedure. They found that with surfactant slug injection, oil appeared to be the wetting phase, and with foam injection, surfactant appeared to wet the medium.

Schramm and Novosod[7] conducted oleophilic microvisual cell experiments with several foams. They found that the foams were significantly less stable in the presence of crude oil and oleophilic solid surfaces, compared with some crude oils and hydrophilic surfaces. Kristiansen and Holt[32] studied foams flowing in cores under North Sea reservoir conditions that were either partially or completely oil wetted. Any degree of oil-wetness reduced the effectiveness of the flowing foam.

The surfactants may adsorb onto the solid surfaces and alter the wettability. In the microvisual experiments of Schramm and Novosod,[7] some of the foaming systems changed the wettability to water wet, in which case the foam sensitivities to oil reverted back to the water wet cases. This result is consistent with the coreflood tests of Sanchez and Hazlett[33] in which foaming surfactants caused wettability reversal in oil wet porous media. This reversal was the reason that stable foams could be generated and propagated in their oil wet cases.

Experimental Apparatus

All the experiments were done at constant pressure. A basic line diagram of the apparatus is shown in Fig. 1.

Surface tensions were measured using a ring tensiometer and interfacial tensions were determined by a spinning drop tensiometer. More details on the equipment can be found in Sagar *et al.*[34] The micromodels used in our experiments replicate the pore structure of Berea sandstone on a silicon wafer. The fabrication technique is a direct adaptation of the etching techniques used by the computer industry. The pore cavities are created photochemically, a process which is not rate-limited, such as acid etching. These high resolution silicon micromodels offer 1:1 scaling of the Berea sandstone pores and throats. A detailed description of the fabrication and construction process of the models used can be found in Castanier and Hornbrook.,[31] Woody *et al.*[35] and Lolomari.[36]

A description of the pore structure of the model along with permeability calculations can be found in Woody *et al.*[35] Scanning electron microscopy (SEM) photographs of the model can be seen in Fig. 2. The characteristics of the models are outlined below:

1. 500 micron patterns repeated 10,000 times on a 5 cm square silicon wafer
2. Etch depth 15 microns.
3. Porosity 35%
4. Permeability: 1 millidarcy
5. Pore Sizes : 1-150 mm
6. Throats : 0.5-10 mm

Experimental Procedure and Experiments Performed

Before beginning the experiments, the model was first

cleaned with water followed by methanol to remove traces of foam or solvent. All the experiments were performed at ambient temperatures using the following generic procedure:

1. CO_2 flood
2. Water/brine flood to displace all CO_2.
3. Oil flood to connate water saturation.
4. Water/brine flood to residual oil saturation.
5. Surfactant flood.
6. Gas injection to generate foam
7. Surfactant flood (higher concentration)
8. Gas injection to generate foam

Steps 5 and 6 were repeated (as shown in 7 and 8) for higher concentrations of surfactant. The outlet was at atmospheric pressure and the inlet pressure was measured. All fluids entering the micromodel were filtered to 0.22mm. A dye (benzene-azo-2-napthol) was used to color the surfactant for better viewing. Note that interfacial properties were not affected by the dye. All the experiments were recorded on videotape and can be made available for viewing on request. Table 1 shows the experiments conducted.

For Experiments 2 and 3, brine was used as the aqueous phase instead of water. The brine formulation is based on North Sea water.

Results

The results of the three sets of experiments conducted are described in this section. Each set of experiments is discussed separately, and is accompanied by images captured during the course of the experiment.

Experiment 1

Experiment 1 was the only experiment in which crude oil (Oseberg, a Norwegian crude) was used. The surfactant was an alpha olefin sulfonate, AOS 1618, and the gas used for foam generation was carbon dioxide. The aqueous (wetting) phase was water.

The pressure difference applied to the micromodel was usually 35 psig. Only two concentrations of the AOS surfactant were used in this experiment. The experiment had to be discontinued due to excessive clogging and asphaltene deposition.

The flow through the micromodel was extremely slow as compared to the flow mentioned by Hornbrook *et al.*[33] and Woody *et al.*,[37] even though the etch depth for the new models was greater then those used by Hornbrook[33] and Woody.[37] This slow flow was caused by overheating the glass during the bonding process which reduced the model permeability. This defect has since been corrected, in more recent micromodels.

After injection of the surfactant and more often during gas injection, stable crude oil emulsions were observed in the model (Fig. 3). These emulsions were seen at concentrations of 0.01% by weight and over and were observed to be stable in the micro- model. This emulsion formation occurred extremely rapidly when gas was injected.

An emulsion forming sequence with the crude oil was observed where crude oil coated water bubbles started forming in a narrow throat and were seen being pushed into a pore where these bubbles conjoined to form an emulsion (Fig. 4).

A bubble coalescence sequence was also observed where carbon dioxide bubbles coated with crude oil were generated from a very narrow throat and were pushed into a pore where they coalesced to form a larger carbon dioxide bubble (Fig. 5).

Emulsion breakdown sequences were also seen to occur in the pores. A very visible crude oil emulsion broke down in a matter of seconds and was captured in the stills shown (Fig. 6).

Emulsions sizes with crude oil varied from 10μm to 60μm in size. The emulsions were usually composed of water surrounded by oil films. The color of the water seemed to be darker (brownish) after contact with the crude oil. This shows some, still unexplained, mass transfer mechanism between the oil and water.

As can be seen from the above observations, the Oseberg crude oil clearly formed emulsions in the presence of the AOS surfactant, indicating the non-tolerant behavior of the Oseberg crude to this surfactant. No foam lamella were observed during the experiment. The displacements were according to the theory of imiscible displacement: Displacement of water by gas caused viscous fingering, and displacement of water by oil was a stable front propagation.

Experiment 2

In Experiment 2, the surfactant used was the same alpha olefin sulfonate (AOS 1618). The wetting phase was brine and the non-wetting phase (oil) was kerosene. Kerosene emulsions were observed at as low as 0.001% concentration of surfactant (Fig. 7). During carbon dioxide flooding the gas phase was discontinuous and did not fill the model completely. The emulsions were very mobile at low concentrations of surfactant (< 1%) .

The diameters of the emulsions were smallest at lower concentrations and were seen to increase with higher concentrations. The stability of the emulsions also increased at higher concentrations. Certain areas in the model which had less oil were seen to have thinner emulsions (Fig. 8). At increased surfactant concentrations the oil saturations in the model had decreased, and the emulsions were still widely present and more stable.

The emulsion bubble size also was seen to depend on the pore geometry (Fig. 8). Different sizes of emulsions seem to co-exist but varied in size with the size being the smallest in

the throats and the smaller pores.

Emulsions started at 0.001% surfactant concentration. The emulsions at this stage flowed very rapidly through the narrow throats until they clogged the flow path after gathering in large pores. Emulsion sizes, as mentioned earlier, increased with surfactant concentration. Although the pore geometry had some effect, emulsion sizes after 0.1% surfactant flood varied from a few microns to about 60μm. Emulsion composition after the 1% surfactant flood was very similar to that seen at 0.1%. The emulsion were hardly seen to move, while at lower concentrations, most of the narrow throats had been blocked by the smaller emulsions. Two emulsion forming and breaking sequences were also observed. No foam was observed during the experiment.

Experiment 3

In Experiment 3, we formed an oil-foam. The surfactant was a fluorocarbon diluted in kerosene. The wetting phase was brine and the non-wetting phase was kerosene. Carbon dioxide was used to generate the foam in-situ. The exploitation of the gas blocking properties of foam, by using it as a gas coning barrier, is an old idea. An attractive means of achieving a favorable barrier geometry is by using low density non-aqueous foams. This is the primary reason for our focus on the oil foam studied in this experiment.

Flow through this model was extremely fast as compared to Experiments 1 and 2. After the water flood and the oil flood, water was seen residing in the narrow throats indicating that the model was water wet. Before foam was generated in the system, the carbon dioxide was discontinuous . Stable foam lamellae were seen by 0.01% surfactant concentration. A snap off sequence of a carbon dioxide bubble coated with surfactant was seen (Segar[36]).

In certain areas, at 0.1% concentration of the fluoro-surfactant, a lamella formation and breakdown sequence was captured in a five frame sequence.

Foam was observed as lamellae throughout the model at the differing concentrations of the surfactant (Fig. 9). Certain pore geometries were seen to be more conducive to forming stable lamellae then others. Many different lamellae configurations were seen. Stable lenses were also observed to co-exist with the lamellae.

In one configuration, a water droplet in a foam lamella did not seem to affect the lamella stability (Fig. 10). Also, in a certain pore geometry, thin stable lamellae were seen as well as thicker lamellae.

No significant increase in the number of foam lamellae were seen from 0.1% to 1.0% surfactant concentration, in spite of a noticeably higher gas blockage as seen from the flow rate reduction at higher concentration.

Interfacial Tension Measurements

Interfacial tensions between the surfactant solutions and the oil (kerosene) were measured for Experiments 2 and 3 and and listed below. No significant difference in the interfacial tension was observed because of the presence of an ethyl-oil soluble dye, benzene-azo-2-napthol used as dye.

Conclusions

The silicon micromodels used in these experiments give us a realistic feel for the pore level mechanisms which would occur in reality. The three sets of experiments conducted in this study, which included different oils and foamers, lead us to the conclusions outlined below.

The AOS Surfactant

With the AOS surfactant, with differing oils present, no foam formation was seen at the pore level. However emulsions were observed which varied in size and stability with surfactant concentration. The pore and throat sizes also seemed to influence the emulsion size.

Most of the emulsions seen were composed of water covered with oil films. With the crude oil the water became discolored to brown. Very little oil was required to form these emulsions as could be seen at higher concentrations of surfactant after the model had been flooded with surfactant a few times resulting in low oil saturation. It can be concluded that the emulsion formation with the AOS surfactant could be the reason for the delayed foam forming observed by Kristiansen and Holt.[25,32] These have, in the past, often been ascribed to so-called "aging" or "incubation" effects. According to a mechanism suggested by Lau and O'Brien,[27] the emulsion scavenges all surfactant and makes it impossible to generate foam initially. Only when excess surfactant solution becomes available, through reinjection or rearrangement, can foam generation take place. This concept, however, does not apply to our case, where excess surfactant is always present.

The ability to form water-in-oil emulsions is governed by the balance of forces between those tending to keep the oil in large drops (or continuous oil areas) and those favoring formation of small emulsified oil droplets. It is well known, from anti-foam theory, that small emulsion droplets make better anti-foam agents. An attempt to develop a theory for foam destabilization by emulsified oil droplets has been published by Schramm and Novosad.[7] However, their lamella number fails to correlate oil tolerance data for fluorosurfactant foams; likewise the lack of emulsions formed with the fluorosurfactant. The presence of oil in the system resulted in emulsions for the AOS surfactant, and no foam was observed. Whether foam would actually form on continuous surfactant and gas flooding is yet to be seen in the micromodel and would be an interesting area for further research. Currently no theory explains this phenomenon of emulsion with foamers which seems different from the conventional "aging" of cores, which is essentially a liquid/solid adsorption process.

The Fluorosurfactant

For the oil-foam with the fluorosurfactant, a strong foam was generated both in the oil saturated and the oil free zones. Lamellae were observed both in oil saturated and oil free areas, indicating oil tolerant behavior, as expected, from the negative entering coefficient and the bulk behavior. Generation sites for the foam lamellae were seen to be controlled by pore geometry and local saturation. The foam lamellae were stabilized by the surfactant and therefore an increase in foamer concentration increased the lifetime of the lamellae, and thereby the strength of the foam.

No obvious link could be found with the number of films observed and strength of gas blockage. Although lenses were observed to be present in the system, no lens-lamella transition was observed. We can conclude from these observations that this oil-foam can be used for achieving a favorable barrier geometry for gas coning problems.

Further Research

Further research suggestions include studying the behavior of emulsions and how they effect foam properties in porous media with an emphasis on foam destabilization by emulsified foam droplets.

Using different thin sections (other than Berea) would help in studying flow behavior in other pore geometries. The effect of "aging" as the reason for the delayed foam forming (if any) with the AOS surfactant also deserves more investigation. As mentioned before, whether foam would form under continuous surfactant and gas injection would be an interesting area to be looked into to supplement this work. The new micromodels are currently under construction at the 'Center for Integrated Systems' at Stanford.

Acknowledgments

The authors are very obliged to Hilde Carlsen Jonsbraten of Rogaland Research Inst., Stavanger, Norway for help with all the experiments during her stay at Stanford. Mariann Dalland also from Rogaland Research, provided valuable insight and comments as well as the fluids and surfactants used in this work.

Financial aid for this work was provided by the Department of Energy under contract DE-FG22-96BC14994 and the SUPRI-A industrial affiliates.

References

1. Coombe, D.A.; Mohammadi, S.S.: "Characteristics of Steam-Foam Drive Process in Massive Multi-Zone and Single-Zone Reservoirs," SPE 24030, paper presented at SPE California Regional Meeting, Bakersfield (1992).
2. Surguchev, L. M., Coombe, D., Hanssen, J.E. and Svorstøl, I.: "Simulation of WAG and Gas Injection with Potential Sweep Improvement by Application of Foam", paper presented at 8 European Symposium on Improved Oil Recovery, Vienna (1995).
3. Radke, C J. and Chambers, K.T.: "Capillary Phenomenon in Foam Flow Through Porous Media, " Interfacial Phenomenon in Petroleum Recovery, N.R. Morrow, Editor, Surfactant Science Series. Marcel Dekker, Inc., New York, pp 191-255 (1991).
4. Mast, R.F.: "Microscopic Behavior of Foam in Porous Media," SPE 3997, paper presented at the 47 SPE Annual meeting, San Antonio (1972).
5. Owete O. S., Castanier, L.M., and Brigham, W.E.: "Flow of Foam Through Porous Media, " SPE Reservoir Engineering, 2, 315-323 (August 1987).
6. Huh, D.G., Cochrane, T.D. and Kovarik, F.S.: "The Effect of Microscopic Heterogeneity on CO_2 Foam Mobility: Part 1- Mechanistic Study," Jour. of Pet. Tech. *41*, 872-879 (August 1989).
7. Schramm, L. L. and Novosad, J. J.: "Micro-visualization of Foam Interactions with a Crude Oil." Colloids and Surfaces, 46, 21-43 (1990).
8. Holm, L.W.; "The Mechanisms of Gas and Liquid Flow Through Porous Media in the Presence of Foam," SPEJ, 359-369 (December 1968).
9. Marsden, S. S.: "Foams in Porous Media", SUPRI TR-37, Stanford University, (1986).
10. Sanchez, J.M. and Schechter, R.S.: "The Effect of Trace Quantities of Surfactant on Nitrogen/Water Relative Permeabilitie," SPE 15446, paper presented at the 61 Annual Technical Conference, New Orleans (1986).
11. Owete, O.S., Castanier, L.M., and Brigham, W.E.: "Flow Behavior of Foam: A Porous Micromodel Study," SPE Reservoir Engineering 2, 315-323 (August 1987).
12. Kovscek A.R. and Radke C.J.: "Fundamentals of Foam Transport in Porous Media in Foams," Fundamentals and Applications in the Petroleum Industry, L. L. Schramm, Editor. Advances in Chemistry Series, 242. American Chemical Society, Washington, DC (1994).
13. Roof, J.G.: "Snap-Off of Oil Droplets in Water-Wet Pores," Society of Petroleum Engineers Jour. *10*, 85-90 (March 1970).
14. Falls, A.H., Hirasaki, G.J., and Patzek, P.W.: "Development of a Mechanistic Foam Simulator: The Population Balance and Generation by Snap-Off," SPE Reservoir Engineering, *3*, 884-892 (August 1988).
15. Kovscek, A.R. Patzek, T.W. and Radke, C.J.: "Mechanistic Prediction of Foam Displacement in Multi-Dimensions: A Population Balance Approach" SPE/DOE 27789, paper presented at the 9 Symposium on Improved Oil Recovery, Tulsa (April 1994).

16. Castanier L.M. and Hanssen J.E. "Micromodel Observations of Foam in Realistic Size Micromodels," Proceedings, Final RUTH Seminar, Stavanger, Norway (1994).
17. Harkins, W.D.: Journal of Chem. Phys. 9, 552-568 (1941).
18. Robinson, J.W.: Woods, W.W.: J. Soc. Che. Ind. *67*, 361-365 (1948).
19 Ross, S. and McBain, J.W.: Ind. Eng. Chem. 36(6), 570-573 (1944).
20. Nikolov, A.D., Wasan, D.T., Huang, D.W., and Edwards, D.A.: "The Effect of Oil on Foam Stability, Mechanisms and Implications for Oil Displacement by Foam in Porous Media" SPE 15443, paper presented at the 61 Annual Technical Conference and Exhibition, New Orleans (1986).
21. Kuhlman, M.I.: SPE/DOE 17356, Proceedings of the SPE/DOE Enhanced Oil Recovery Symposium, Richardson (1988).
22. Manlowe, J.D. and Radke, C.J.: "A Pore-Level Investigation of Foam/Oil Interactions in Porous Media." SPE Reservoir Engineering (November 1990).
23. Novosad, J.J. and Ionescu, E.F.: CIM 87-38-80, paper presented at the Proceedings of the 38 Annual Technical Meeting of CIM, Canadian Institute of Mining, Mettalurgy, and Petroleum, Calgary, Canada (1987).
24. Jensen, J.A. and Friedmann, F.: paper SPE/DOE 16375, Proceedings of the California Regional Meeting of SPE; Richardson, (1987).
25. Kristiansen, T.S. and Holt, T.: "Proceedings of the 12 International Workshop and Symposium of the IEA Collaborative Project on Enhanced Oil Recovery"; AEA Technology: Winfrith, United Kingdom (1991).
26. Hutchinson, David A., Demiral, Birol, and Castanier, Louis M.: "Steam Foam Studies in the Presence of Residual Oil," SUPRI-A TR 84, Stanford University (May 1992)
27. Lau, H. C. and O'Brien, S. M.: "Effects of Spreading and Non-Spreading Oils on Foam Propagation Through Porous Media." SPE Reservoir Engr. *3*, 893-896 (August 1988).
28. Hanssen, J.E. and Dalland, M.: Proceedings of the SPE/DOE 7th Enhanced Oil Recovery Symposium, paper CIM 86-27-01, Richardson (1990).
29. Dalland, M. and Hanssen, J.E.: Oil Interaction with Foams at Static and Flowing Conditions in Porous Media. Paper at the 13th EOR Workshop and Symposium, Banff (1992).
30. Sanchez, J.M. and Hazlett, R.D.: "Foam Flow Through Oil-Wet Porous Medium: A Laboratory Study", SPE 19687, paper presented at the SPE Annual Technical Conference and Exhibition, San Antonio (1989).
31. Castanier, L.M. and Hornbrook, J.W.: "Observation of Foam/Oil Interactions in a New, High Resolution Micromodel," SPE 22631, paper presented at the 66 Annual Technical Conference and Exhibition, Dallas (1991).
32. Kristiansen, T S. and Holt, T.: "Properties of Flowing Foam in Porous Media Containing Oil," SPE 24182, paper presented at the 8 SPE Symposium on Enhanced Oil Recovery, Tulsa (1992).
33. Sanchez, J. M.; Hazlett, R. D.: SPE Res. Eng. *7(1)*, 91-97 (1992).
34. Sagar, Neeraj S. and L.M. Castanier: "Oil-Foam Interactions in a Micromodel," SUPRI TR 110, (June 1997) [DOE/BC/14994].
35. Woody, F., Blunt, M. and Castanier, L.M.: "Pore level Visualization of Foam Flow in a Silicon Micromodel" SUPRI TR-100, Stanford University, 1995
36. Lolomari, T.O. and Blunt, M.J.: "Micromodel Studies of Three Phase Flow in Porous Media", M.S. Thesis, Stanford University, 1996.

Table 1. Experiments Conducted.

Experiment	Surfactant	Concentration	Oil
1.	AOS 1618	0.001% 0.01%	Oseberg Crude
2.	AOS 1618	0.001% 0.01% 0.1% 1%	Kerosene
3.	Fluorosurfactant Kerosene	0.01% 0.1% 1%	Kerosene

Table 2. Interfacial Tension Measurement.

Surfactant	Concentration	Interfacial Tension (dynes/cm)
(AOS 1618)	1%	1.4
	0.1%	0.71
	0.01%	1.63
	0.001%	7.9
(Fluorosurfactant in Kerosene)	1%	14.928
	0.1%	8.868
	0.01%	19.686

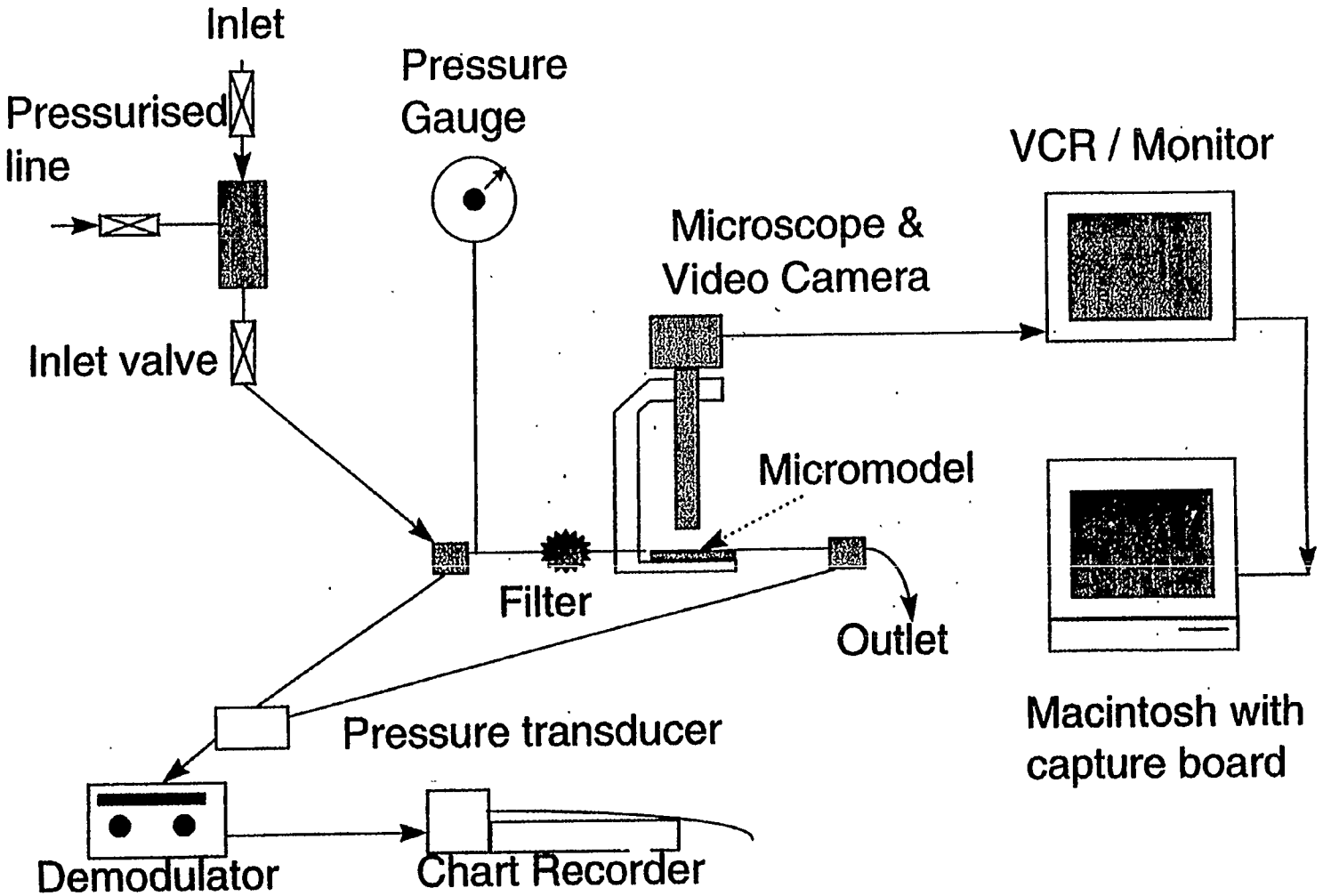

Figure 1. Line diagram of the Experimental Apparatus.

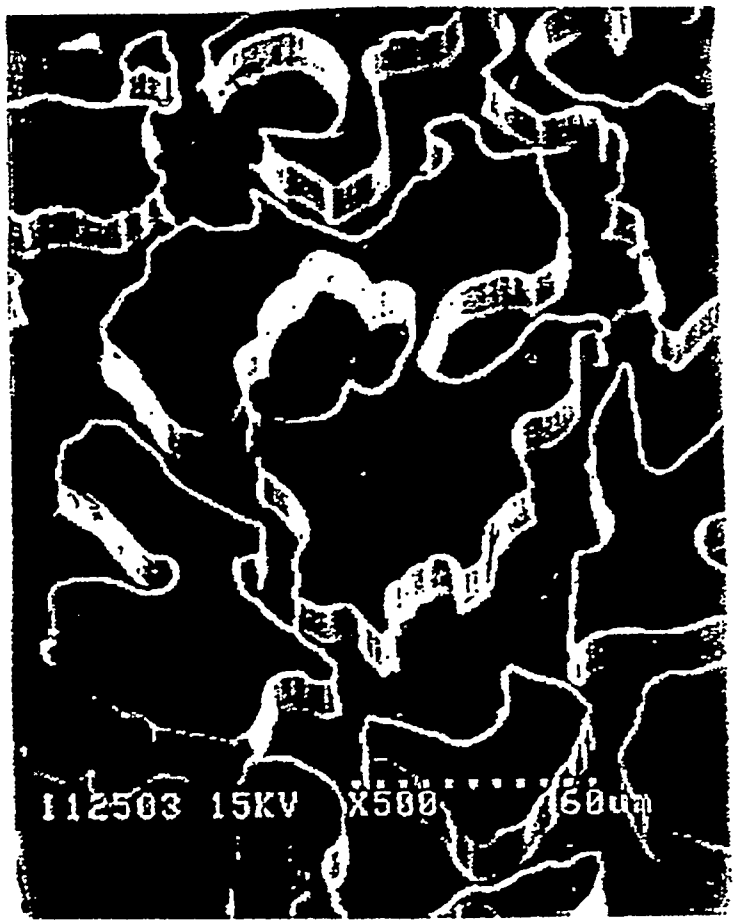

Figure 2(a). SEM of Model A (old).

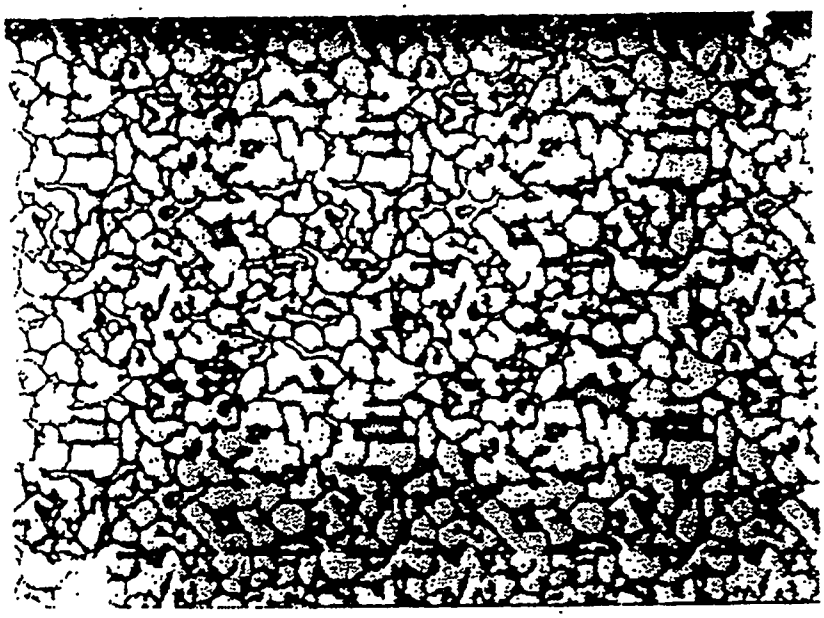

Figure 2(b). SEM of Model A (old).

EXPERIMENT 1

Figure 3 **Crude oil emulsions seen in the large pores in the model after 0.01% surfactant flood.**

EXPERIMENT 1

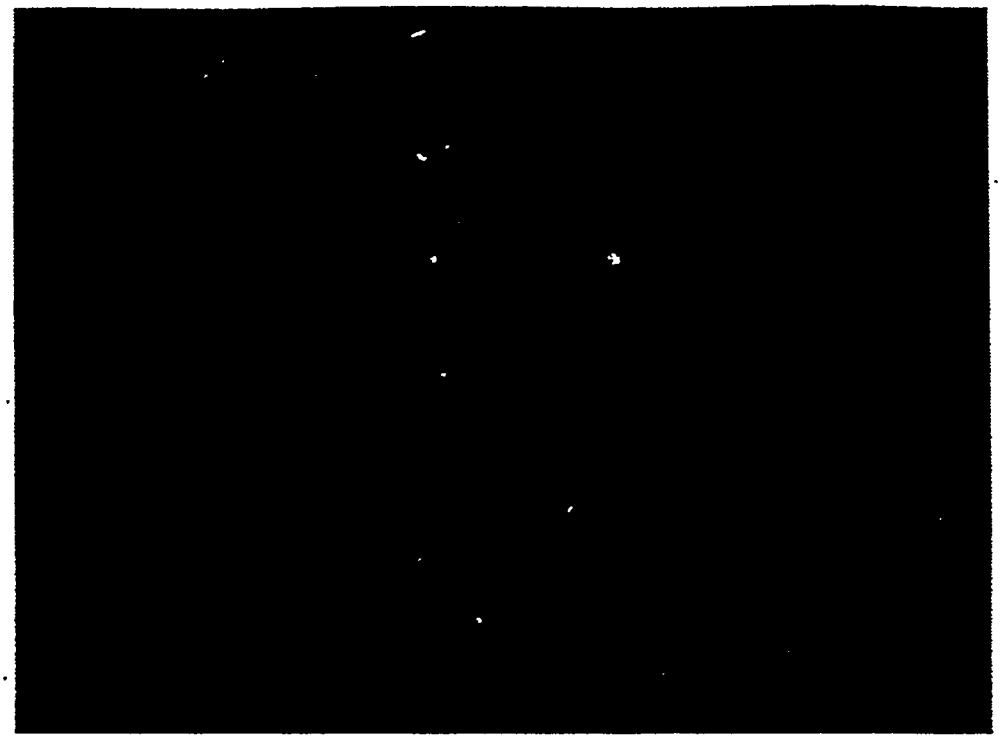

Figure 4(a)

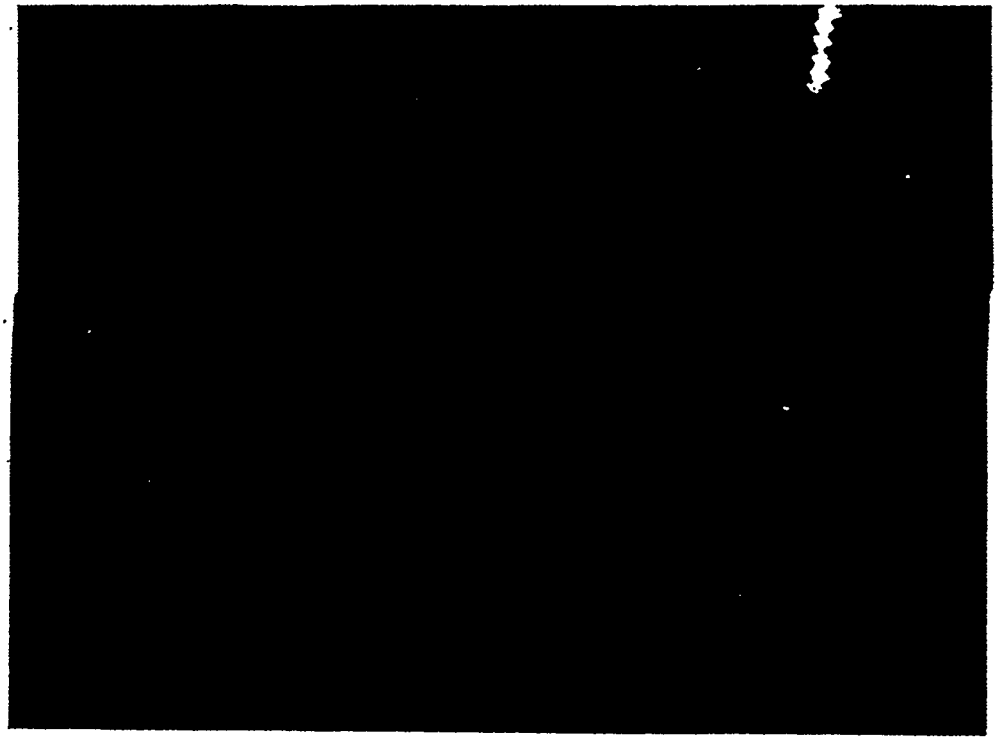

Figure 4(b)

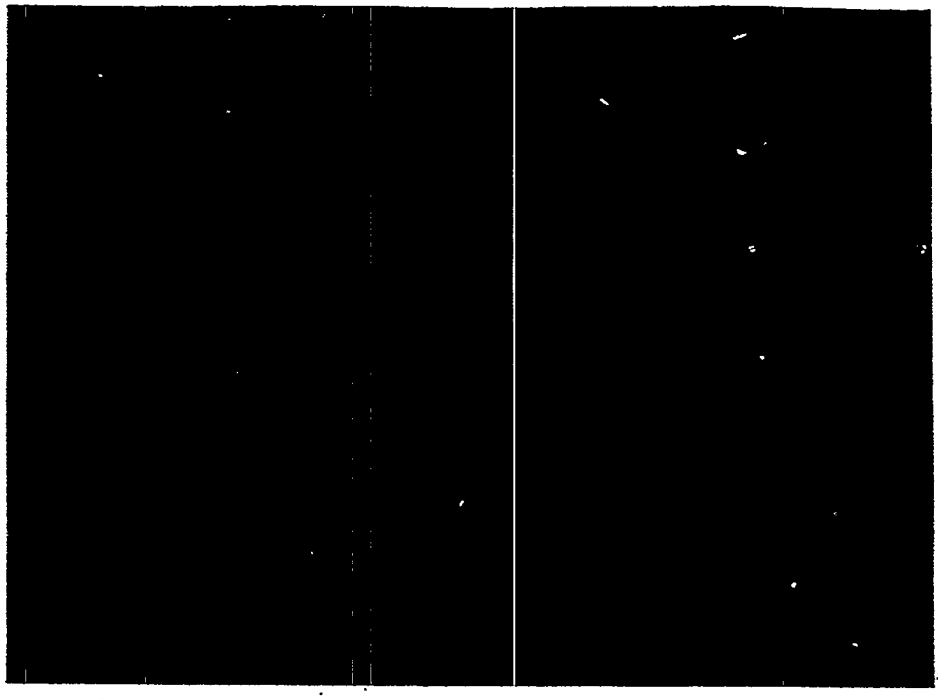

Figure 4((c)

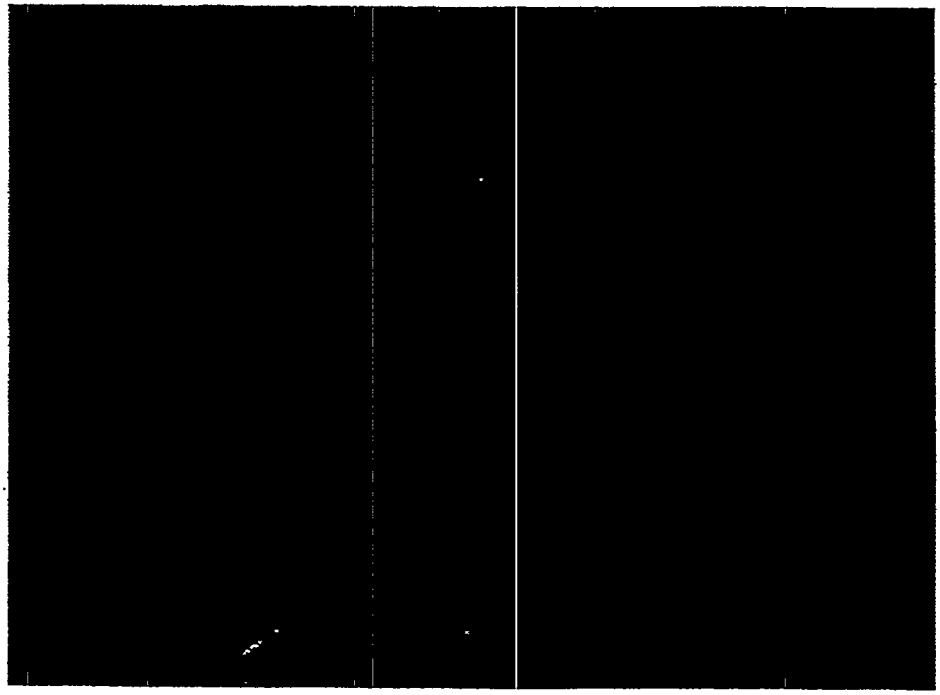

Figure 4(d) **Emulsion formation sequence.**

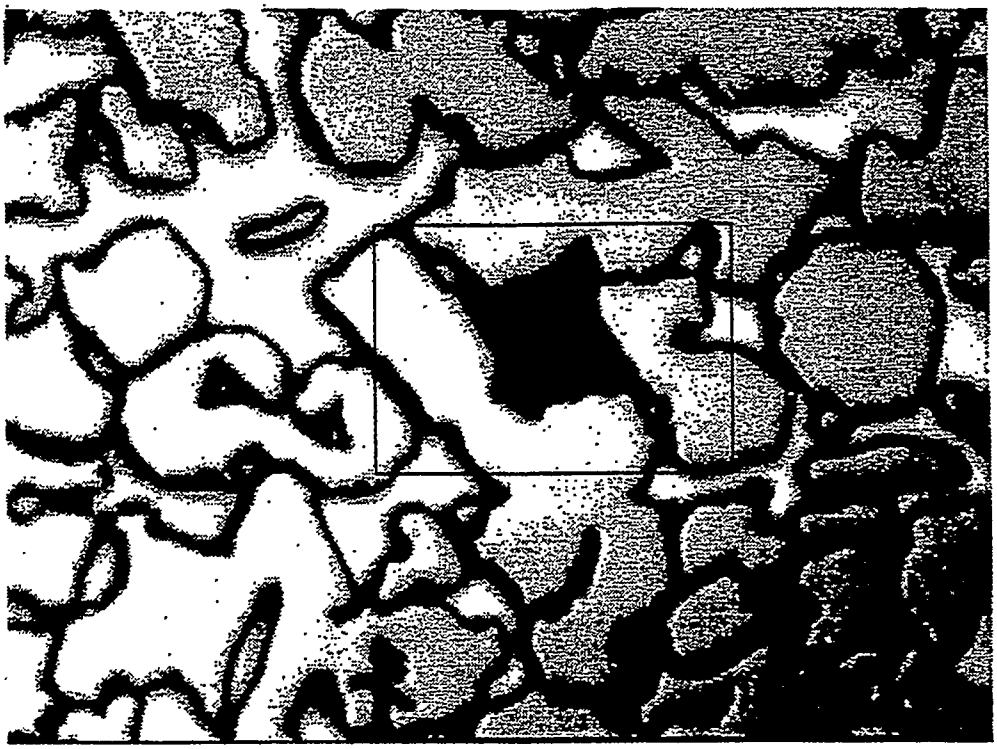

Figure 5(a)

Figure 5(b) Bubble coalescence.

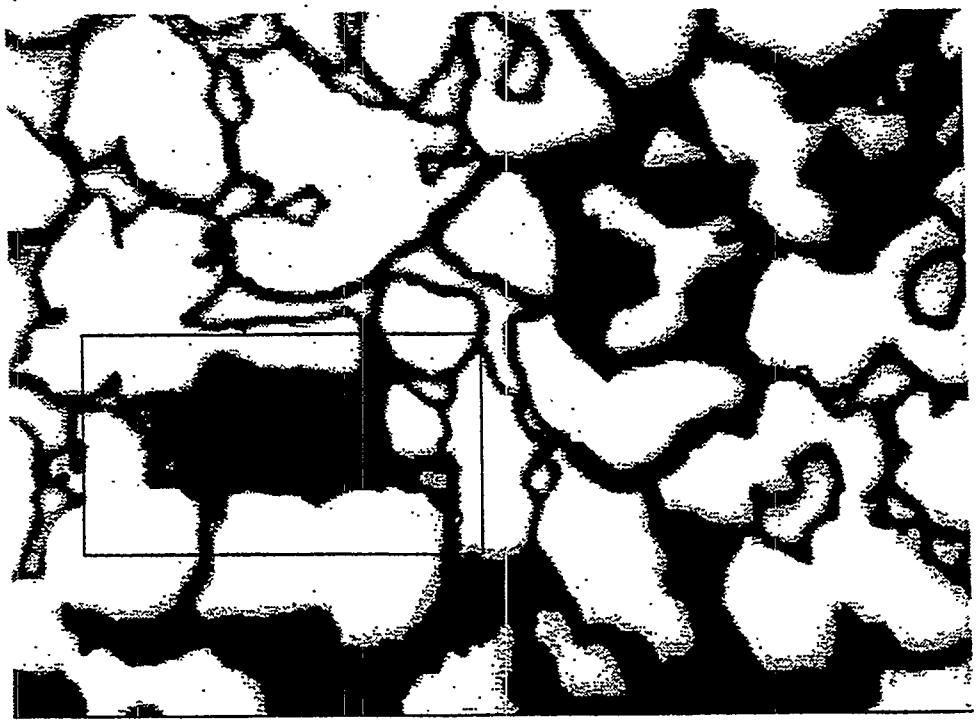

Figure 6(a)

Figure 6(b)

EXPERIMENT 1

Figure 6(c) Emulsion breaking sequence.

EXPERIMENT 2

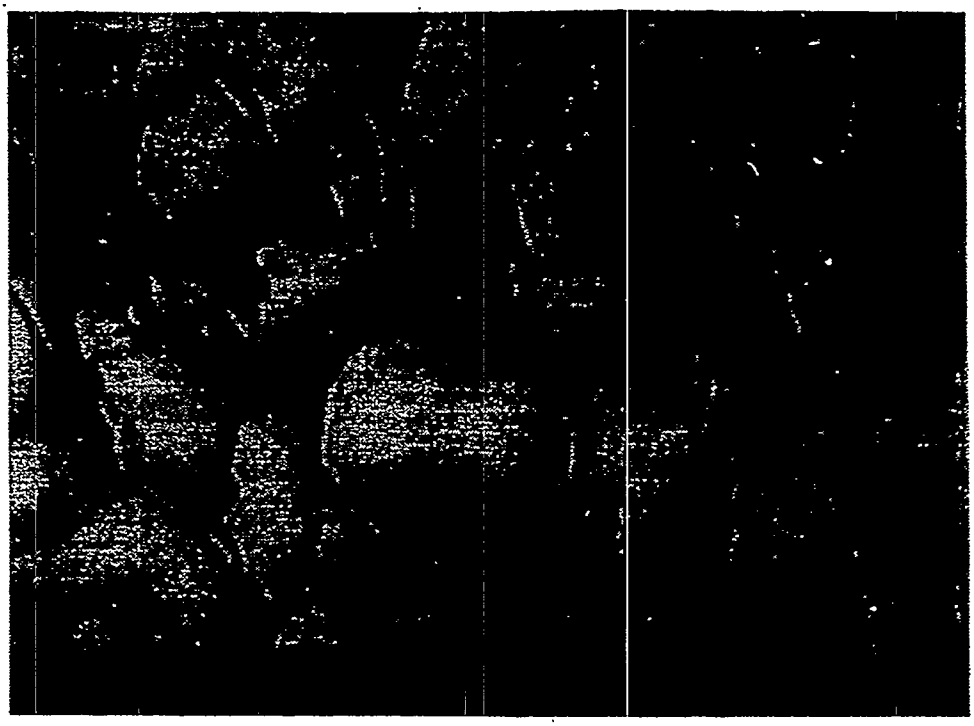

Figure 7 Emulsions as seen after 0.01% surfactant flood.

Figure 8 Very stable emulsions seen at the end of the experiment (after 1% surfactant flood).

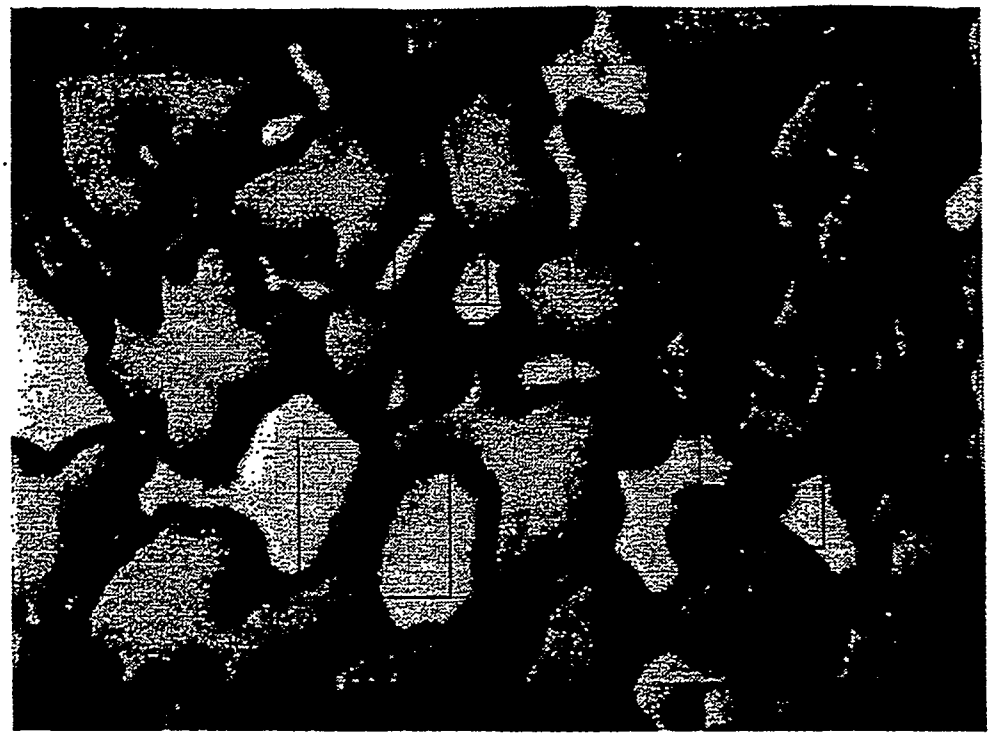

Figure 9 Four stable lamellae seen after 0.1% FC740 surfactant flood.

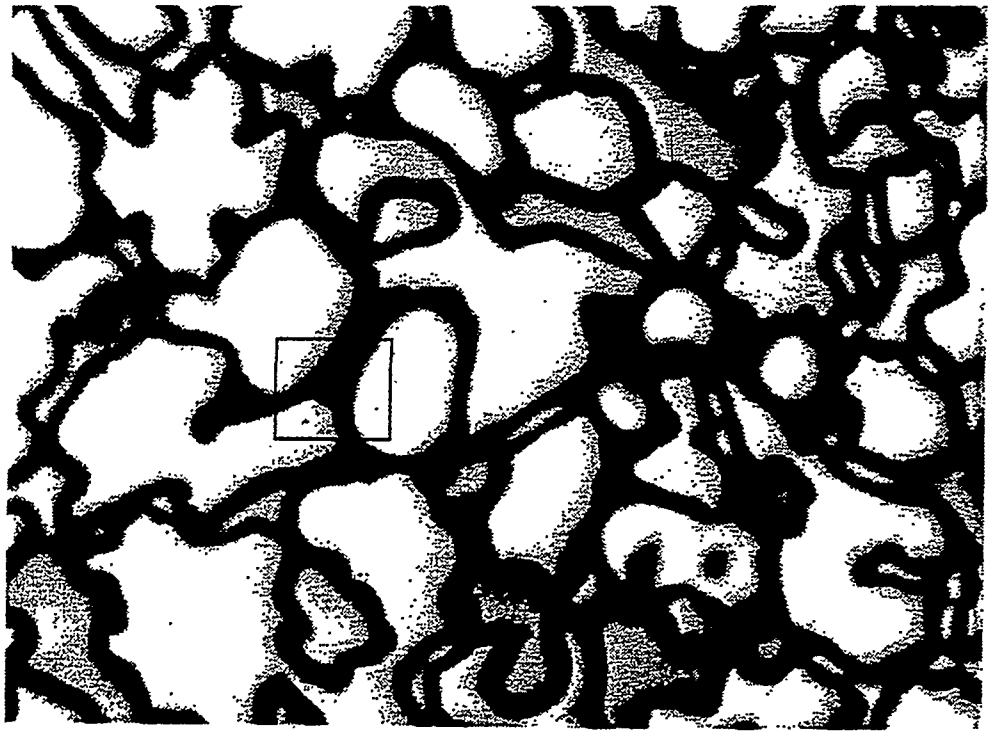

Figure 10 A drop of water in a lamella. It doesn't seem to affect the lamella stabilty.

PROJECT 4: RESERVOIR DEFINITION

To develop and improve techniques of formation evaluation such as tracer tests and pressure transient tests.

4.1 RECURSIVE LEAST SQUARE METHODS FOR ESTIMATION OF RESERVOIR PARAMETERS

(F. Murad)

4.1.1 INTRODUCTION

This is a history matching project for identifying reservoir parameters. The data is from the South Belridge Diatomite (Kern County, CA) (Kovscek *et al.,* 1996; Kovscek *et al.,* 1996). In a pilot project, steam was injected into low permeability diatomite through two vertical hydrofractures. Pressure and temperature responses were observed at different well locations. Additionally, steam injection pressure and rate were measured as well as oil production.

The idea is to match the temperature and pressure profiles in order to identify reservoir parameters such as permeability and thermal conductivity.

4.1.2 BACKGROUND

Having a systems engineering background, the problem was approached as a system identification exercise. A recursive least squares identification method was selected (Landau, 1990; Lyung and S^derstr^m, 1983). They are extensively used for the identification of discrete-time model parameters. A typical discrete time model can be written as

$$\underline{y}(t+1) = \theta^T \underline{y}(t) + \theta^T \underline{y}(t-1)..... \quad (1)$$

where q is the parameter vector to be estimated and the output, y, depends upon

observations at times, t, prior to the current time instant. This is an example of an autoregressive process, that is, no exogenous inputs are present.

The idea is to discretize the partial differential pressure diffusion and temperature conduction equations describing steam and heat transport in porous media (Kovscek *et al.*, 1996). Then model parameters are adjusted to obtain an optimal fit. It should be stressed that most of the identification algorithms have been developed for ordinary differential equations. Processes represented by partial differential equations are called distributed parameter systems.

4.1.3 PROGRESS

Considering the pressure diffusion equation

$$\frac{\partial P}{\partial t} = div\{\alpha(x,t;k(x))\nabla P\} \tag{2}$$

α is the hydraulic diffusivity that maybe a function of location x and time t and is parametrized by permeability k. For the purpose of this study, α is assumed to be either constant or to vary spatially. For a one-dimensional grid, the above PDE is expanded to

$$\frac{\partial P}{\partial t} = \frac{\partial \alpha(x,t;k(x))}{\partial x}\frac{\partial P}{\partial x} + \alpha(x,t;k(x))\frac{\partial^2 P}{\partial x^2} \tag{3}$$

In case α is constant, Eq. 3 simplifies to

$$\frac{\partial P}{\partial t} = \alpha\frac{\partial^2 P}{\partial x^2} \tag{4}$$

Equation 4 was the starting point in the development of a recursive identification technique. This was followed by the development of an algorithm for identification of α with the process modeled by Eq. 3. These will be discussed next.

4.1.4. RECURSIVE IDENTIFICATION ALGORITHM FOR DISTRIBUTED PARAMETER SYSTEMS

The first example considered was Eq. 4 where α is constant. Using finite differences for the partial derivatives (2nd order spatial and explicit Euler in time), the model equation is

$$P_j^{(n+1)} = P_j^n + \alpha \frac{\Delta t}{\Delta x^2}\{P_{j+1}^{(n)} - 2P_j^{(n)} + P_{j-1}^{(n)}\} \tag{5}$$

for a uniform time and space grid. The least square objective function to be minimized is

$$J = \sum_{n=1}^{t}\{P_j^{obs,n} - P_j^{calc,n}\}^2 \tag{6}$$

Using Eq. 5

$$J = \sum_{n=1}^{t}\{P_j^{obs,n} - P_j^{n-1} - \alpha \frac{\Delta t}{\Delta x^2}(P_{j+1}^{(n-1)} - 2P_j^{(n-1)} + P_{j-1}^{(n-1)})\}^2 \tag{7}$$

$$J = \sum_{n=1}^{t}\varepsilon(n) = \varepsilon(t) \tag{8}$$

where ε denotes the difference between the observed and model data. Using the standard calculus result where Eq. 7 is minimized with respect to α

$$\frac{\partial J}{\partial \alpha} = 0 \tag{9}$$

which yields

$$\sum_{n=1}^{t} 2[P_j^{obs,n} - P_j^{(n-1)} - \alpha \frac{\Delta t}{\Delta x^2}\{P_{j+1}^{(n-1)} - 2P_j^{(n-1)} + P_{j-1}^{(n-1)}\}][-\frac{\Delta t}{\Delta x^2}\{P_{j+1}^{(n-1)} - 2P_j^{(n-1)} + P_{j-1}^{(n-1)}\}] = 0 \tag{10}$$

Simplifying,

$$\sum_{n=1}^{t}[P_j^{obs,n} - P_j^{(n-1)}][P_{j+1}^{(n-1)} - 2P_j^{(n-1)} + P_{j-1}^{(n-1)}] - \alpha\frac{\Delta t}{\Delta x^2}\sum_{n=1}^{t}[P_{j+1}^{(n-1)} - 2P_j^{(n-1)} + P_{j-1}^{(n-1)}]^2 = 0 \quad (11)$$

Defining

$$R(t) \equiv \sum_{n=1}^{t}[P_j^{obs,n} - P_j^{(n-1)}][P_{j+1}^{(n-1)} - 2P_j^{(n-1)} + P_{j-1}^{(n-1)}] \quad (12)$$

$$F(t) \equiv \sum_{n=1}^{t}[P_{j+1}^{(n-1)} - 2P_j^{(n-1)} + P_{j-1}^{(n-1)}]^2 \quad (13)$$

Equation 11 can be written as

$$R(t) = \alpha(t)F(t) \quad (14)$$

To develop a recursive algorithm the following can be written

$$R(t+1) = \alpha(t+1)F(t+1) \quad (15a)$$

$$\alpha(t+1)F(t+1) = \sum_{n=1}^{t}[P_j^{obs,n} - P_j^{(n-1)}][P_{j+1}^{(n-1)} - 2P_j^{(n-1)} + P_{j-1}^{(n-1)}] + [P_j^{obs,t+1} - P_j^{(t)}][P_{j+1}^{(t)} - 2P_j^{(t)} + P_{j-1}^{(t)}]$$

(15b)

$$\alpha(t+1)F(t+1) = \alpha(t)F(t) + [P_j^{obs,t+1} - P_j^{(t)}][P_{j+1}^{(t)} - 2P_j^{(t)} + P_{j-1}^{(t)}] \pm \alpha\frac{\Delta t}{\Delta x^2}[P_{j+1}^{(t)} - 2P_j^{(t)} + P_{j-1}^{(t)}]^2$$

(15c)

which can be simplified to

$$\alpha(t+1) = \alpha(t) + F^{-1}(t+1)(P_{j+1}^t - 2P_j^t + P_{j-1}^t)\{(P_j^{obs,t+1} - P_j^t) - \alpha\frac{\Delta t}{\Delta x^2}(P_{j+1}^t - 2P_j^t + P_{j-1}^t)\}$$

(15d)

$$\alpha(t+1) = \alpha(t) + F^{-1}(t+1)(P_{j+1}^t - 2P_j^t + P_{j-1}^t)\varepsilon(t+1) \quad (16)$$

Equations 16 along with Eqs. 17 and 18 form the recursive algorithm

$$F(t+1) \equiv \sum_{n=1}^{t} [P_{j+1}^{(n-1)} - 2P_j^{(n-1)} + P_{j-1}^{(n-1)}]^2 + [P_{j+1}^{(t)} - 2P_j^{(t)} + P_{j-1}^{(t)}]^2 \tag{17}$$

$$\varepsilon(t+1) = (P_j^{obs,(t+1)} - P_j^{(t)}) - \alpha \frac{\Delta t}{\Delta x^2} (P_{j+1}^{(t)} - 2P_j^{(t)} + P_{j-1}^{(t)}) \tag{18}$$

4.1.5 RECURSIVE IDENTIFICATION ALGORITHM FOR DISTRIBUTED PARAMETER SYSTEMS; SPATIALLY DISTRIBUTED

In this case the diffusion process is represented by Eq. 3. Using finite differences for the partial derivatives (2nd order spatial and explicit Euler in time) the model equation is

$$P_j^{(n+1)} = P_j^n + \alpha_j \frac{\Delta t}{\Delta x^2} \{P_{j+1}^{(n)} - 2P_j^{(n)} + P_{j-1}^{(n)}\} + \frac{\Delta t}{4\Delta x^2} \{\alpha_{j+1} - \alpha_{j-1}\} \{P_{j+1}^{(n)} - P_{j-1}^{(n)}\} \tag{19}$$

for a uniform time and space grid. Substituting in the least square objective function, Eq. 6, and minimizing with respect to α_j the following result is obtained.

$$\sum_{n=1}^{t} [P_j^{obs,n} - P_j^{(n-1)}][P_{j+1}^{(n-1)} - 2P_j^{(n-1)} + P_{j-1}^{(n-1)}] - \alpha_j \frac{\Delta t}{\Delta x^2} \sum_{n=1}^{t} [P_{j+1}^{(n-1)} - 2P_j^{(n-1)} + P_{j-1}^{(n-1)}]^2$$

$$- \alpha_{j+1} \frac{\Delta t}{4\Delta x^2} \sum_{n=1}^{t} [P_{j+1}^{(n-1)} - P_{j-1}^{(n-1)}][P_{j+1}^{(n-1)} - 2P_j^{(n-1)} + P_{j-1}^{(n-1)}]$$

$$+ \alpha_{j-1} \frac{\Delta t}{4\Delta x^2} \sum_{n=1}^{t} [P_{j+1}^{(n-1)} - P_{j-1}^{(n-1)}][P_{j+1}^{(n-1)} - 2P_j^{(n-1)} + P_{j-1}^{(n-1)}] = 0 \tag{20}$$

Proceeding similar to the constant hydraulic difusivity case, define

$$R_j(t) \equiv \sum_{n=1}^{t} [P_j^{obs,n} - P_j^{(n-1)}][P_{j+1}^{(n-1)} - 2P_j^{(n-1)} + P_{j-1}^{(n-1)}] \tag{21}$$

$$F_{j,j}(t) \equiv \frac{\Delta t}{\Delta x^2} \sum_{n=1}^{t} [P_{j+1}^{(n-1)} - 2P_j^{(n-1)} + P_{j-1}^{(n-1)}]^2 \tag{22}$$

$$F_{j,j-1}(t) \equiv \frac{\Delta t}{4\Delta x^2} \sum_{n=1}^{t} [P_{j+1}^{(n-1)} - P_{j-1}^{(n-1)}][P_{j+1}^{(n-1)} - 2P_j^{(n-1)} + P_{j-1}^{(n-1)}] \tag{23}$$

$$F_{j,j+1}(t) \equiv \frac{\Delta t}{4\Delta x^2} \sum_{n=1}^{t} [P_{j+1}^{(n-1)} - P_{j-1}^{(n-1)}][P_{j+1}^{(n-1)} - 2P_j^{(n-1)} + P_{j-1}^{(n-1)}] \tag{24}$$

Equation 20 can be written as

$$R_j(t) = -\alpha_{j-1}(t)F_{j,j-1}(t) + \alpha_j(t)F_{j,j}(t) + \alpha_{j+1}(t)F_{j,j+1}(t) \tag{25}$$

For N number of nodes a system of equations is obtained.

$$\begin{bmatrix} R_1(t) \\ R_2(t) \\ R_3(t) \\ \vdots \\ R_N(t) \end{bmatrix} = \begin{bmatrix} F_{11}(t) & F_{12}(t) & 0 & \cdots & 0 \\ F_{21}(t) & F_{22}(t) & F_{23}(t) & \cdots & 0 \\ 0 & F_{32}(t) & F_{33}(t) & \cdots & \vdots \\ & & \ddots & \ddots & F_{N-1,N}(t) \\ 0 & \cdots & 0 & F_{N,N-1}(t) & F_{NN}(t) \end{bmatrix} \begin{bmatrix} \alpha_1(t) \\ \alpha_2(t) \\ \alpha_3(t) \\ \vdots \\ \alpha_N(t) \end{bmatrix} \tag{26}$$

To develop a recursive algorithm the same procedure is repeated as for the previous case. An intermediate result is

$$\begin{aligned} R_j(t+1) = R_j(t) + [P_{j+1}^{(t)} - 2P_j^{(t)} + P_{j-1}^{(t)}][(P_j^{obs,(t+1)} - P_j^{(t)}) - \\ \alpha_j \frac{\Delta t}{\Delta x^2}(P_{j+1}^{(t)} - 2P_j^{(t)} + P_{j-1}^{(t)}) - \frac{\Delta t}{4\Delta x^2}(\alpha_{j+1} - \alpha_{j-1})(P_{j+1}^{(t)} - P_{j-1}^{(t)})] \\ + \alpha_j \frac{\Delta t}{\Delta x^2}[P_{j+1}^{(t)} - 2P_j^{(t)} + P_{j-1}^{(t)}]^2 - \alpha_{j-1}\frac{\Delta t}{4\Delta x^2}[P_{j+1}^{(t)} - P_{j-1}^{(t)}][P_{j+1}^{(t)} - 2P_j^{(t)} + P_{j-1}^{(t)}] \\ + \alpha_{j+1}\frac{\Delta t}{4\Delta x^2}[P_{j+1}^{(t)} - P_{j-1}^{(t)}][P_{j+1}^{(t)} - 2P_j^{(t)} + P_{j-1}^{(t)}] \end{aligned} \tag{27}$$

Defining

$$\varepsilon_j(t+1) \equiv (P_j^{obs,(t+1)} - P_j^{(t)}) - \alpha_j \frac{\Delta t}{\Delta x^2}(P_{j+1}^{(t)} - 2P_j^{(t)} + P_{j-1}^{(t)}) - \frac{\Delta t}{4\Delta x^2}(\alpha_{j+1} - \alpha_{j-1})(P_{j+1}^{(t)} - P_{j-1}^{(t)}) \tag{28}$$

The following system of equations is obtained

$$\underline{R}(t+1) = \underline{R}(t) + \underline{D}(t+1)\underline{\varepsilon}(t+1) + \underline{T}(t+1)\underline{\alpha}(t)$$

From which the following recursion on α is obtained

$$\underline{\alpha}(t+1) = \underline{\alpha}(t) + \underline{F}^{-1}(t+1)\underline{D}(t+1)\underline{\varepsilon}(t+1) \tag{29}$$

where D is a diagonal matrix with elements

$$d_j(t+1) = P_{j+1}^{(t)} - 2P_j^{(t)} + P_{j-1}^{(t)} \tag{30}$$

and T is tridiagonal with elements

$$t_{j,j-1}(t+1) = -\frac{\Delta t}{4\Delta x^2}(P_{j+1}^{(t)} - P_{j-1}^{(t)})(P_{j+1}^{(t)} - 2P_j^{(t)} + P_{j-1}^{(t)})$$

$$t_{j,j}(t+1) = \frac{\Delta t}{\Delta x^2}(P_{j+1}^{(t)} - 2P_j^{(t)} + P_{j-1}^{(t)})^2$$

$$t_{j,j+1}(t+1) = -t_{j,j-1}(t+1) \tag{31}$$

4.1.6 A BETTER FINITE DIFFERENCE SCHEME: MODIFIED DUFORT FRANKEL

It was found that the scheme used above for Eq. 3 is not a numerically stable scheme. So a semi-implicit method, Dufort-Frankel method, was used. However the original DF finite difference is developed for the diffusion Eq. 4. It had to be modified for Eq. 3. This development is briefly discussed below.

Using second order finite differences for space and time, Eq. 3 is written as

$$\frac{P_j^{(n+1)} - P_j^{(n-1)}}{2\Delta t} = \frac{1}{4\Delta x^2}[\alpha_{j+1} - \alpha_{j-1}][P_j^{(n+1)} - P_j^{(n-1)}] + \alpha_j \frac{1}{\Delta x^2}[P_{j+1}^{(n)} - 2P_j^{(n)} + P_{j-1}^{(n)}] \quad (32)$$

and replacing

$$P_j^{(n)} = \frac{P_j^{(n+1)} - P_j^{(n-1)}}{2}$$

Equation 32 becomes

$$(1+2\beta\alpha_j)P_j^{(n+1)} - (1-2\beta\alpha_j)P_j^{(n-1)} = \beta[\frac{\alpha_{j+1} - \alpha_{j-1}}{2} + 2\alpha_j]P_{j+1}^{(n)} + \beta[-\frac{\alpha_{j+1} - \alpha_{j-1}}{2} + 2\alpha_j]P_{j-1}^{(n)} \quad (33)$$

where $\beta = \frac{\Delta t}{\Delta x^2}$.

The modification afforded to Eq. 33 is to substitute

$$\alpha_j = \frac{\alpha_{j+1} + \alpha_{j-1}}{2} \quad (34)$$

The simplified equation is

$$\{1+\beta(\alpha_{j+1} + \alpha_{j-1})\}P_j^{(n+1)} = \{1-\beta(\alpha_{j+1} + \alpha_{j-1})\}P_j^{(n-1)} + \frac{\beta}{2}(\alpha_{j+1} + 3\alpha_{j-1})P_{j-1}^{(n)}$$

$$+\frac{\beta}{2}(3\alpha_{j+1} + \alpha_{j-1})P_{j+1}^{(n)} \quad (35)$$

This scheme is more stable compared to Eq. 33 as regards to time step and spatial grid size. However, two important points are to be noted. The first one is that now P_j no longer depends on a_j. Second, for the estimation of α both Eq. 33 and the modified equation would be nonlinear functions of the parameter to be estimated which implies that a

linear equation solver must be replaced by nonlinear equation solver, such as Newton-Raphson.

So we proceed to develop a recursive algorithm. The objective function as before is

$$J = \sum_{n=1}^{t} \sum_{j=1}^{N} (P_j^{obs,n+1} - P_j^{calc,n+1})^2 \tag{36}$$

Substituting Eq. 35 in Eq. 36,

$$J = \sum_{n=1}^{t} \sum_{j=1}^{N} [P_j^{obs,n+1} - \frac{B_j}{A_j} P_j^{(n-1)} - \frac{C_j}{A_j} P_{j-1}^{(n)} - \frac{D_j}{A_j} P_{j+1}^{(n)}]^2 \tag{37}$$

where

$$A_j = 1 + \beta(\alpha_{j+1} + \alpha_{j-1})$$

Rewriting Eq. 37, for one particular node position

$$J_j(t) = \sum_{n=1}^{t} [P_j^{obs,n} - \frac{1-\beta\alpha_{j+1}}{A_j} P_j^{(n-2)} + \frac{\beta\alpha_{j+1}}{2A_j} P_{j-1}^{(n-1)} - \frac{3\beta\alpha_{j+1}}{2A_j} P_{j+1}^{(n-1)}$$

$$+ \frac{\beta\alpha_{j-1}}{A_j} \{-P_j^{(n-2)} + \frac{3}{2} P_{j-1}^{(n-1)} + \frac{1}{2} P_{j+1}^{(n-1)}\}]^2 \tag{38}$$

Differentiating Eq. 38 with respect to a_{j-1} to find a minimum, it is realized that Eq. 38 is in the form

$$J_j(t) = \sum_{n=1}^{t} \{P_j^{obs,n} - P_j^{calc,n}(\alpha_{j-1})\}^2 \tag{39}$$

The derivative with respect to a_{j-1}. would take the form

$$\frac{dJ_j}{d\alpha_{j-1}} = 0 = 2 \sum_{n=1}^{t} \{P_j^{obs,n} - P_j^{calc,n}(\alpha_{j-1})\} \frac{dP_j^{calc,n}(\alpha_{j-1})}{d\alpha_{j-1}} \tag{40}$$

Let

$$F_j^{calc,n} = \frac{dP_j^{calc,n}(\alpha_{j-1})}{d\alpha_{j-1}} \tag{41}$$

To develop a recursion, at t+1 we have

$$\sum_{n=1}^{t}\{P_j^{obs,n} - P_j^{calc,n}(\alpha_{j-1})\}F_j^{calc,n} + \{P_j^{obs,t+1} - P_j^{calc,t+1}(\alpha_{j-1})\}F_j^{calc,t+1} = 0 \tag{42}$$

This is a nonlinear equation in a_{j-1} which needs to be solved at each time step for a_{j-1}. After simplification we have

$$F_j^{calc,n} = \frac{1}{A_j^{2(n)}}[-2\beta\alpha_{j+1}^{(n-1)}P_j^{(n-2)} + (1.5+\beta\alpha_{j+1}^{(n-1)})P_{j-1}^{(n-1)} + (0.5-\beta\alpha_{j+1}^{(n-1)})P_{j+1}^{(n-1)}] \tag{43}$$

For NR iterations Eq. 42 needs to be solved as,

$$\alpha_{j-1}^{(k)} = \alpha_{j-1}^{(k-1)} - \frac{H_j(\alpha_{j-1}^{(k-1)})}{H_j'(\alpha_{j-1}^{(k-1)})} \tag{44}$$

where

$$H_j^{(t+1)} = \sum_{n=1}^{t}\{P_j^{obs,n} - P_j^{calc,n}(\alpha_{j-1}^{(n)})\}F_j^{calc,n} + \{P_j^{obs,t+1} - P_j^{calc,t+1}(\alpha_{j-1}^{(t+1)})\}F_j^{calc,t+1} \tag{45}$$

In Eq. 45, it is to be noted that the summation term is constant and has been summed over the previous time steps. This is parallel to the estimate of a_{j-1} at the new time from the past estimates, that is,

$$H_j^{(t+1)} = C + M_j^{(t+1)} \tag{46}$$

So when Eq. 46 is differentiated with respect to a_{j-1} the summation term C goes to zero and we are left with

$$\frac{dH_j^{(t+1)}}{d\alpha_{j-1}} = \frac{dM_j^{(t+1)}}{d\alpha_{j-1}} \tag{47}$$

Defining

$$M_j^{(t+1)} = uvw \tag{48}$$

where

$$u = \frac{1}{A_j^2} = \frac{1}{[1+\beta(\alpha_{j+1}+\alpha_{j-1})]} \tag{49}$$

$$v = P_j^{obs,(t+1)} - \frac{1-\beta\alpha_{j+1}}{A_j^{(t)}} P_j^{(t-1)} + \frac{\beta\alpha_{j+1}}{2A_j^{(t)}} P_{j-1}^{(t)} - \frac{3\beta\alpha_{j+1}}{2A_j^{(t)}} P_{j+1}^{(t)} + \frac{\beta\alpha_{j-1}}{2A_j^{(t)}} \{-P_j^{(t-1)} + 1.5P_{j-1}^{(t)} + 0.5P_{j+1}^{(t)}\} \tag{50}$$

$$w = [-2\beta\alpha_{j+1}P_j^{(t-1)} + (1.5+\beta\alpha_{j+1})P_{j-1}^{(t)} + (0.5-\beta\alpha_{j+1})P_{j+1}^{(t)}] \tag{51}$$

Realizing that w is not a function of a_{j-1} we have

$$\frac{dM_j^{(t+1)}}{d\alpha_{j-1}} = uv'w + u'vw \tag{52}$$

such that

$$u' = -\frac{2\beta}{[1+\beta(\alpha_{j+1}+\alpha_{j-1})]^3} \tag{53}$$

$$v' = \frac{\beta}{A_j^{(t)2}}[(1-\beta\alpha_{j+1})P_j^{(t-1)} - \frac{\beta\alpha_{j+1}}{2} P_{j-1}^{(t)} + \frac{3\alpha_{j+1}}{2} P_{j+1}^{(t)}$$

$$+ A_j^{(t)}(-P_j^{(t-1)} + 1.5P_{j-1}^{(t)} + 0.5P_{j+1}^{(t)}) - \beta\alpha_{j-1}(-P_j^{(t-1)} + 1.5P_{j-1}^{(t)} + 0.5P_{j+1}^{(t)})] \tag{54}$$

Thus at each time step we iterate over Eqs. 44 to 54 for each node.

4.1.7 RESULTS

Simulations were carried out for all three algorithms that have been presented in the previous sections. The results for the algorithm given by Eqs. 16-18 are given in Figs. 1-6. The data was generated by the difference Eq. 5. This was merely to check if recursive identification methods could be used for distributed parameter models.

Figures 7-10 show results of the algorithm given by Eqs. 29-31. The data was created using Eq. 19 with three nodes in the space grid. Different cases were studied and the discussion is given in the next section.

Finally Eqs. 44-54 were also implemented but no results are given because the method was found to diverge.

4.1.8 DISCUSSION

Figures 1-6 show that convergence is extremely rapid and in about two to three time steps the unknown parameter is estimated to an accuracy of 10^{-6}. Obviously the data is created from the model equation, hence the results, but this is encouraging since the implication is that once the model is correctly identified estimation is good.

The results shown in Figs. 7-10 are far more interesting and need additional discussion. This method was implemented directly to a single layer, 85 node problem of the actual field, but owing to unstable results it was deemed better to apply to a known data set. Initially 10 nodes on the space grid were considered but still no conclusive results could be reached so the problem was further reduced to 3 nodes only. Several interesting observations were made. Firstly, the finite difference scheme's stability depends strongly on the choice of the time step Δt and distance step Δx as well as on the unknown parameters being estimated, which severely limited the applicability of the method.

However, to generate a stable data set these various values were selected accordingly and simulation carried out. It was observed that the estimated values of the two end

parameters were always grossly in error whereas that at the middle node depended on the initial guess. Hence for a good initial guess the estimate was reasonable. This is shown in Figs. 7-10.

The most curious case was observed when simulations were carried out for an unstable data set. That is, Δt, Δx and the unknown parameters were selected to generate a pressure profile that increased monotonically or in an oscillatory manner with time. For such cases irrespective of the initial guess, the estimated values of the parameters were found to be

accurate to the tenth decimal place. Further, the convergence was quite rapid, in six or seven time steps. These results are illustrated in Fig. 10. However the correction term to the parameter being estimated da was immensely large (to the order of 10^{200}).

4.1.9 SUMMARY

Recursive identification methods were tried for the estimation of an unknown diffusion parameter. Two cases were considered; a constant hydraulic diffusivity α and spatially varying α. The results show that the method is far too dependent upon the finite difference scheme the accuracy of which in turn depends upon the unknown parameter being estimated. Implicit methods were not found to give stable results.

A modification would be tried by discretizing equation 1 instead of using finite differences for Eqs. 3 or 4. Further variational methods based on finite element approximations are being looked into for the solution of this problem.

4.1.10 REFERENCES

1. Kovscek, A. R., Johnston, R. M., and Patzek, T. W.: "Interpretation of Hydrofracture Geometry During Steam Injection Using Temperature Transients. I. Model Formulation and Verification"; *Insitu* 20 (3) (1996) 251-288.
2. Kovscek, A. R., Johnston, R. M., and Patzek, T. W.: "Interpretation of Hydrofracture Geometry During Steam Injection Using Temperature Transients. II. Asymmetric Hydrofractures," *Insitu* 20 (3), (1996) 289-309.
3. Landau, I. D.: System Identification and Control Design, Prentice Hall, 1990.
4. Ljung, L. and Söderström T.: Theory and Practice of Recursive Identification, MIT Press, 1983.

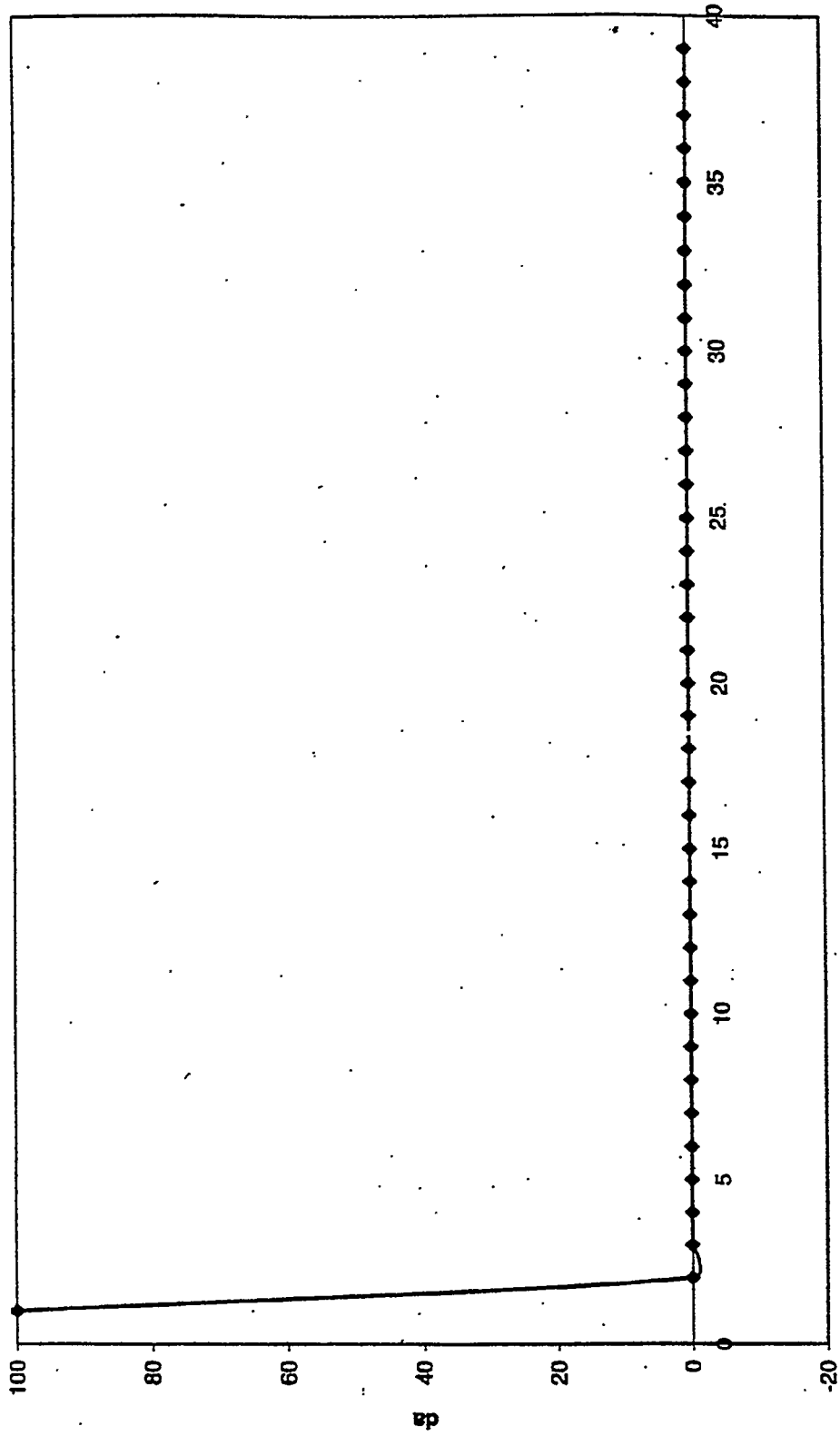

Fig 1: Correction at each time step when alpha=-5e-6

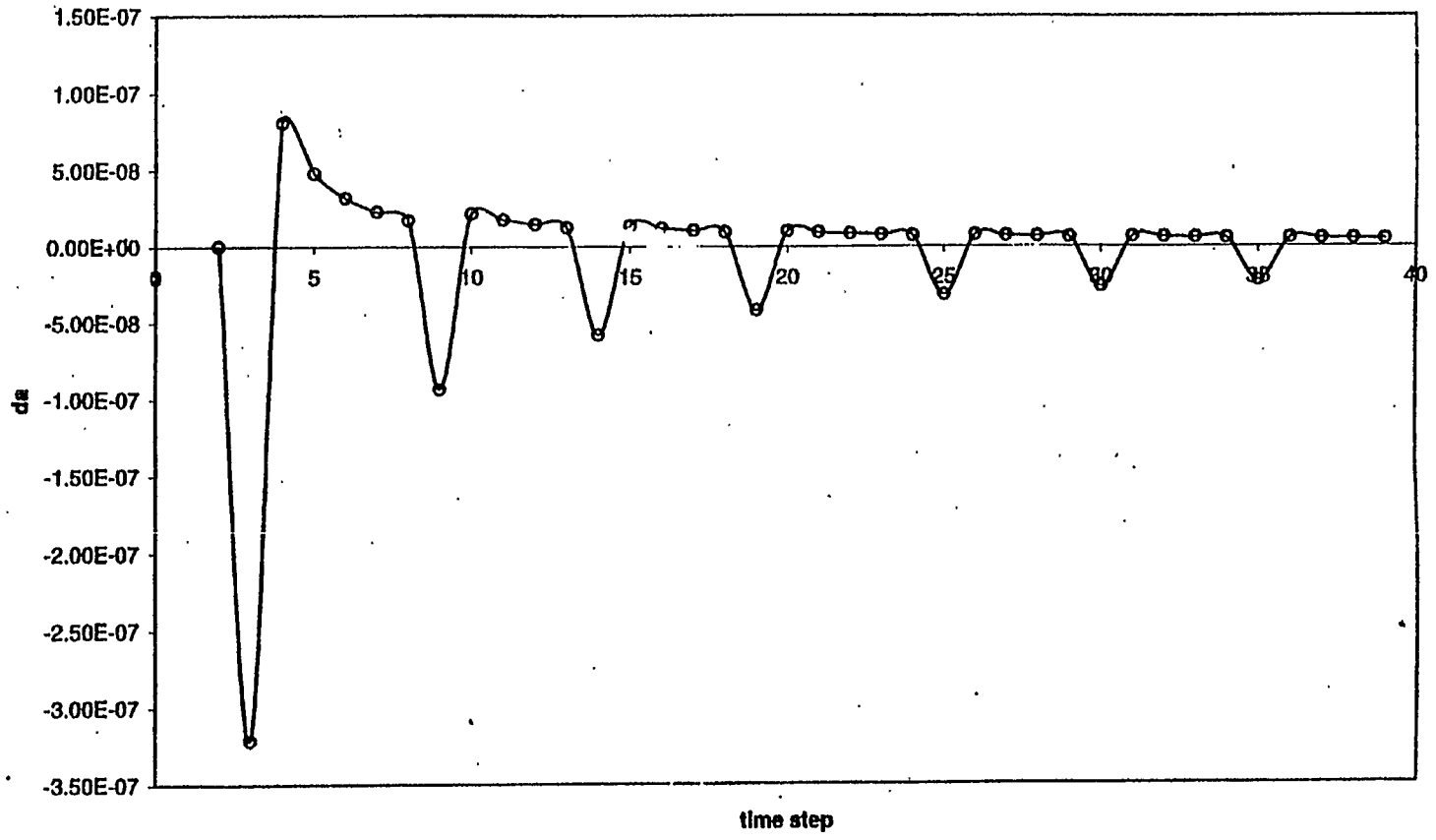

Fig 2: Correction when alpha=-5e-6. A blow up excluding the first time step. It is interesting that pressure variation is negligible but still correct alpha is identified

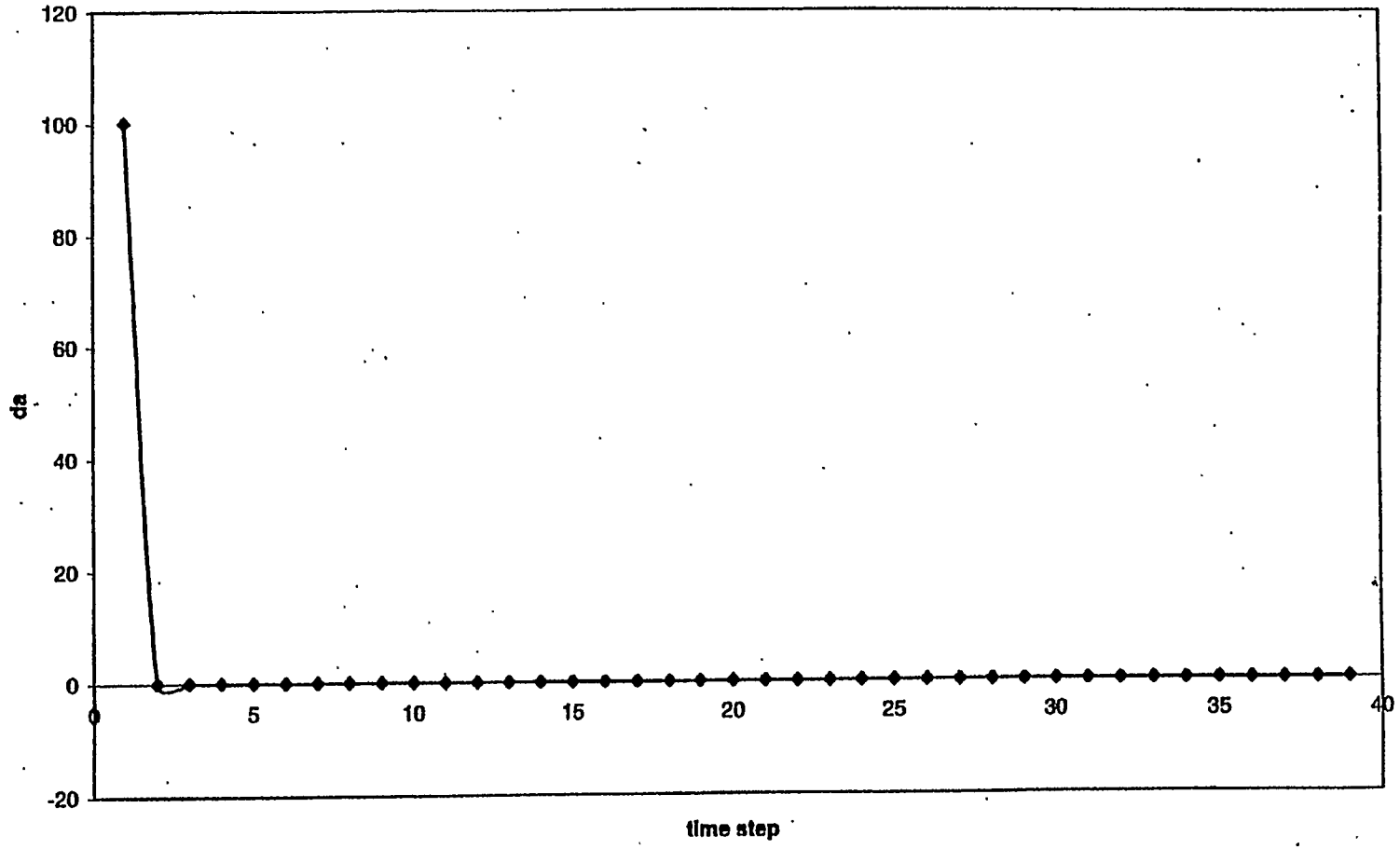

Fig 3: Correction at each time step for alpha =0.1

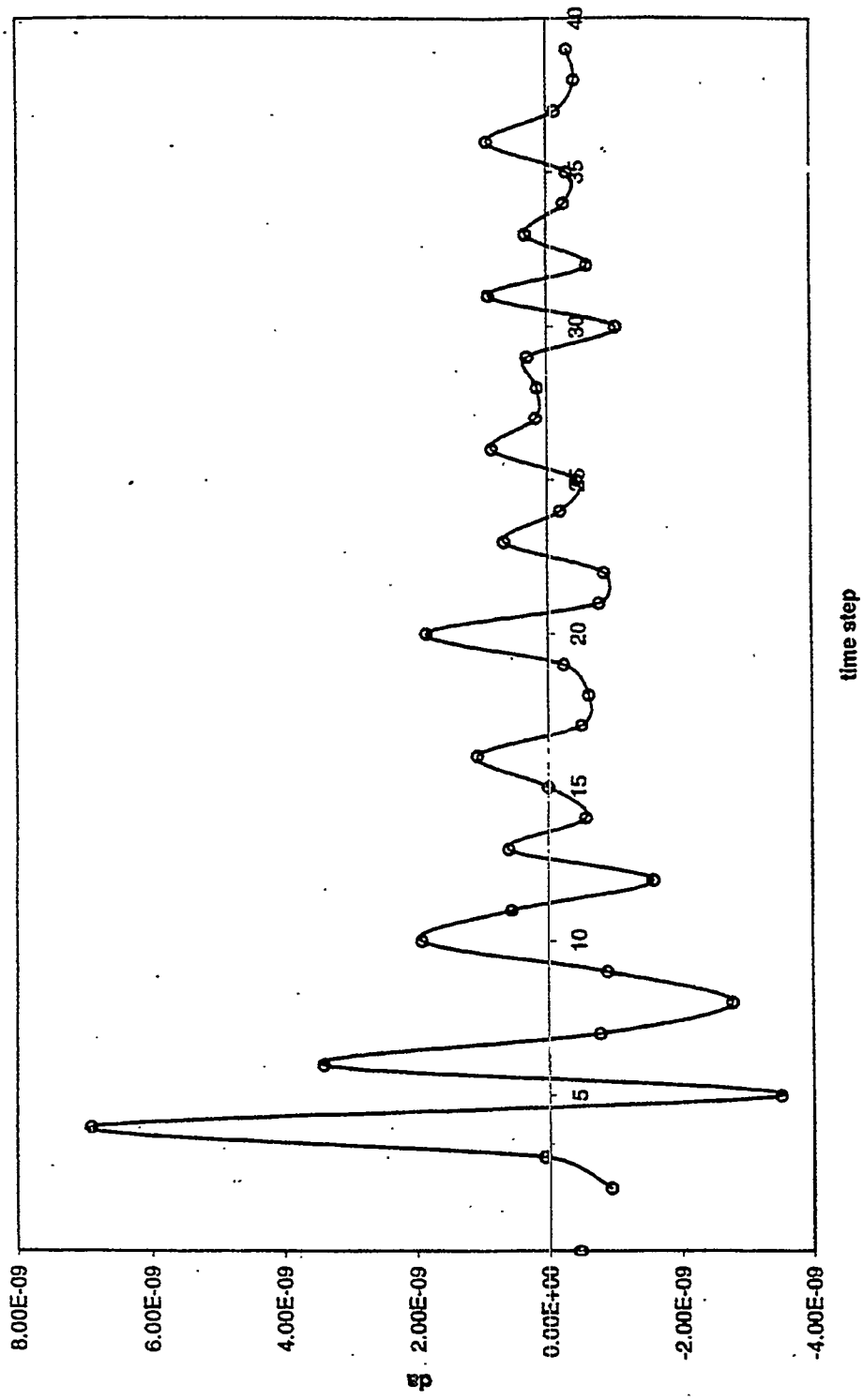

Fig 4: Correction for alpha=0.1. A blow up excluding the first data point

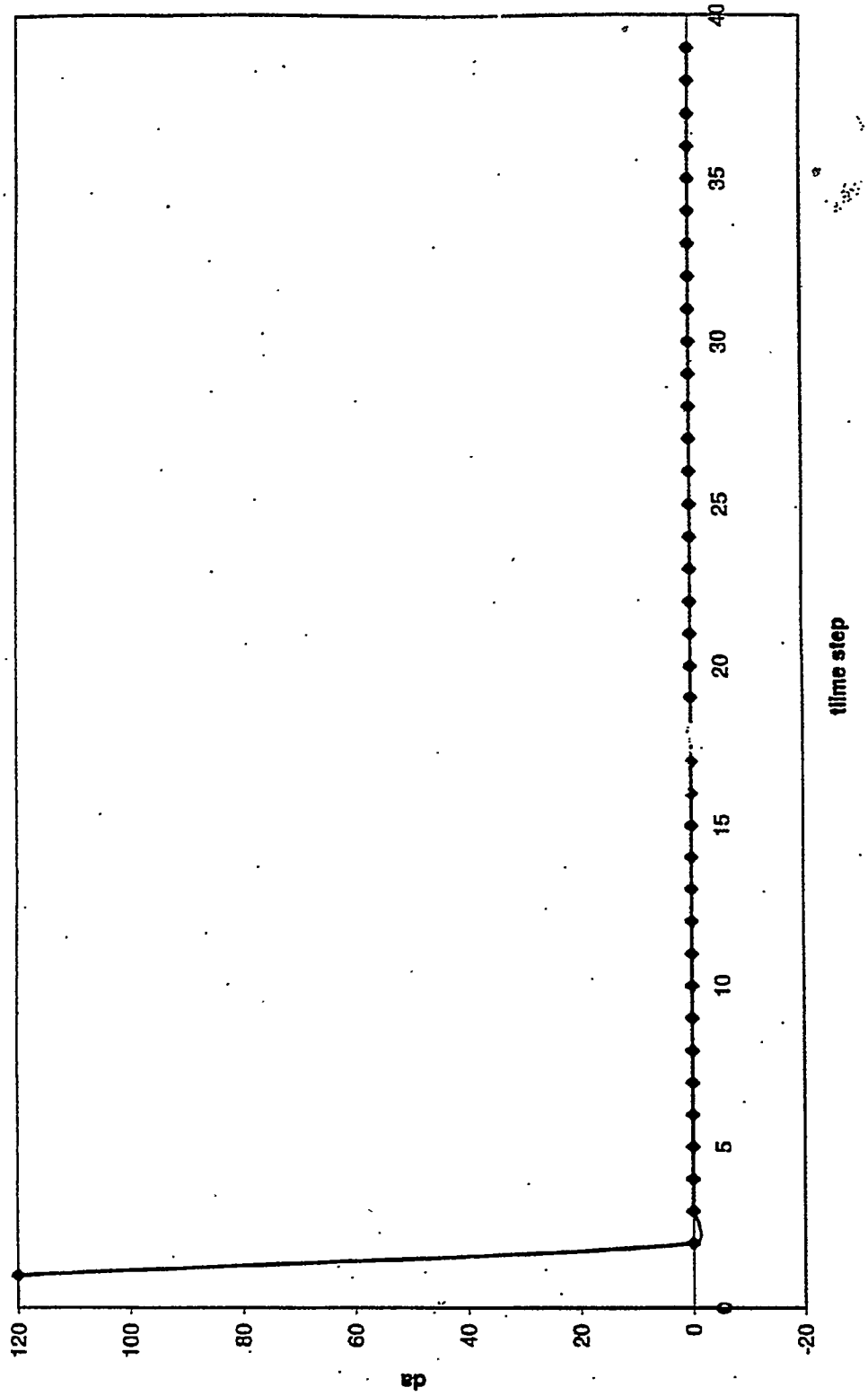

Fig 5: Correction for alpha=20.

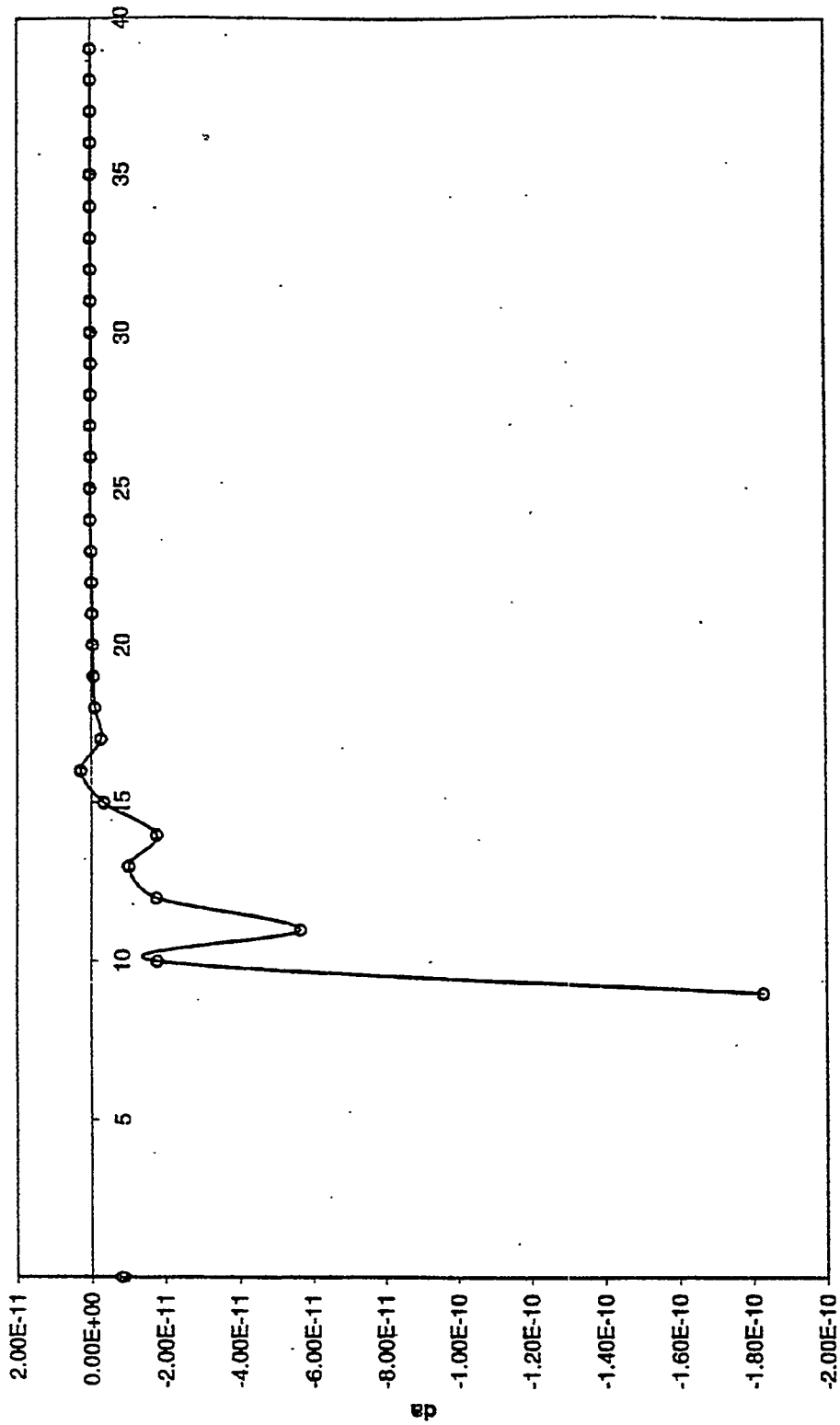

Fig 6: Correction for alpha=20. A blow-up showing correction trend ate later time steps

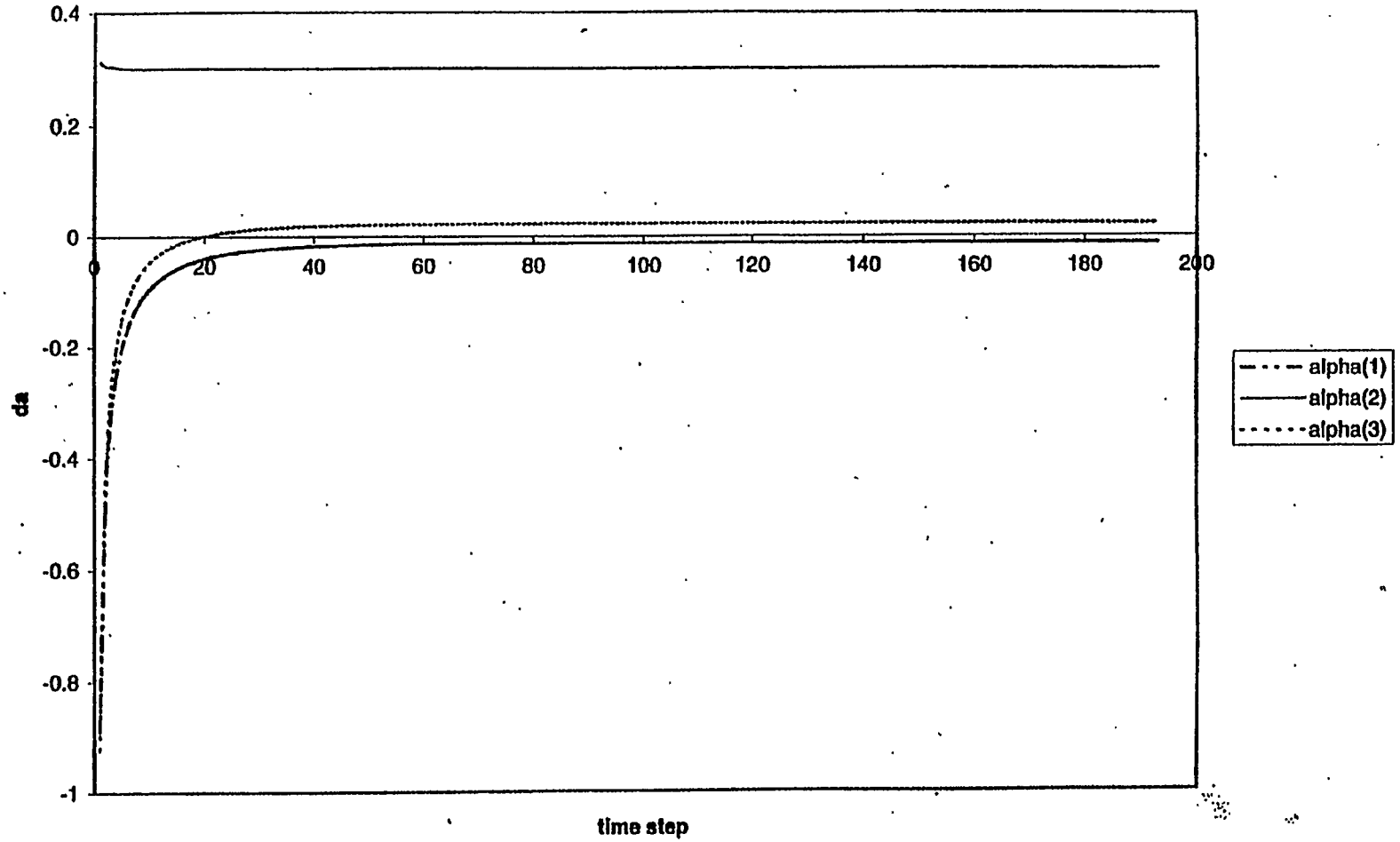

Fig 7: Estimation of alpha for a three node problem using 2nd order finite difference

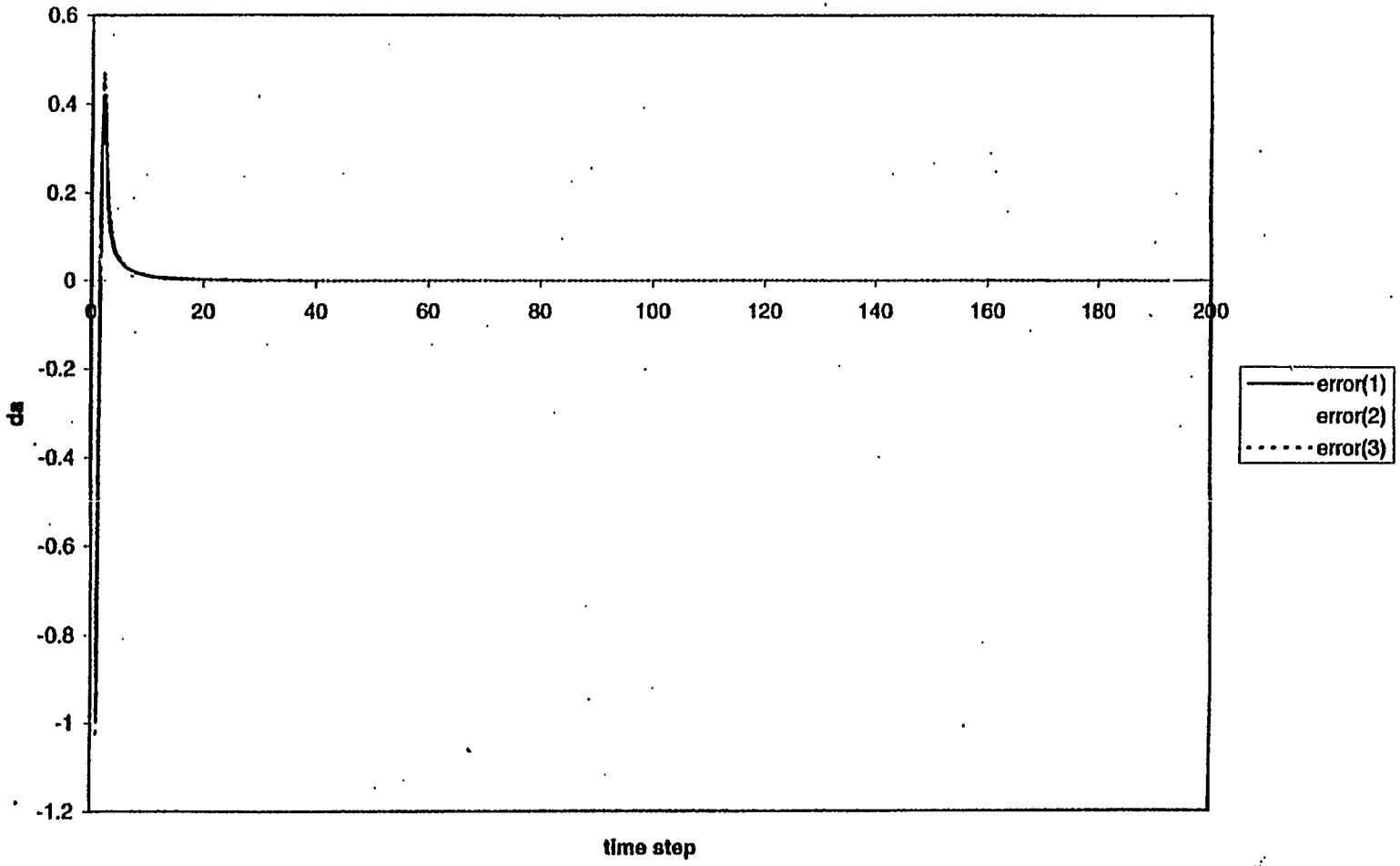

Fig 8: Correction to alpha at each time step for the case in Fig 7

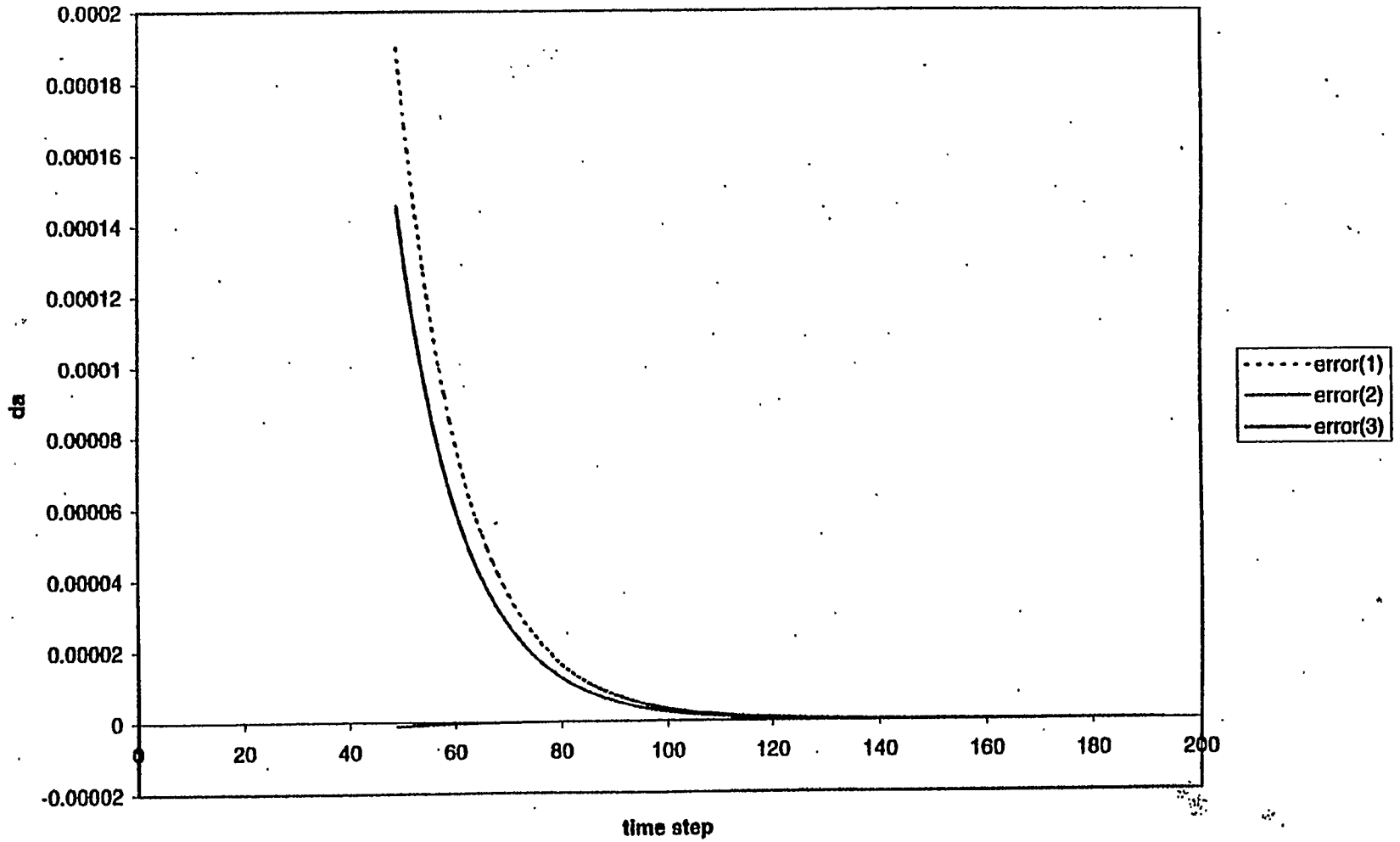

Fig 9: Blow up of corrections for the case in figure 8.

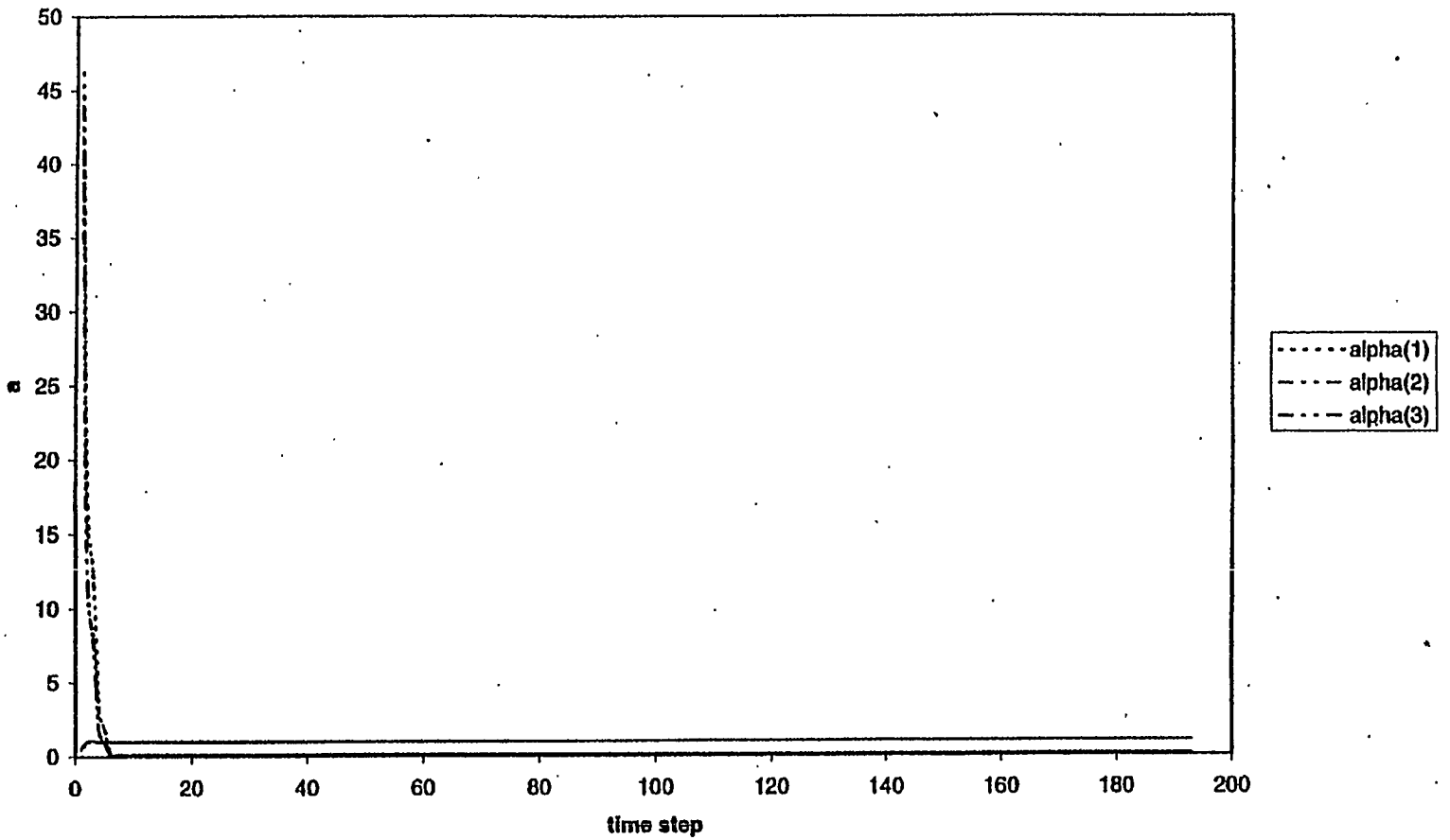

Fig 10: Estimation of alpha. An interesting case because apparently the finite difference scheme is unstable but the estimation is excellent

4.2 EFFECT OF MOBILITY RATIO ON PATTERN BEHAVIOR OF A HOMOGENEOUS POROUS MEDIUM

(Y. Wang)

4.2.1 ABSTRACT

It is well known, for unit mobility ratio, that the areal sweep efficiency of a staggered line drive pattern is always better than a five spot pattern. However, this observation does not hold for very favorable mobility ratios. We present simulation results and, with the help of streamline and saturation distributions, explain the differences between unit and favorable mobility ratios. Simulations compare well with experiments conducted elsewhere. Accurate definition of breakthrough time is also discussed for multiphase, streamline, simulation results. The exact definition of breakthrough is difficult due to physical dispersion in experiments and numerical dispersion in simulations.

4.2.2 INTRODUCTION

Pattern geometry plays a major role in determining oil recovery during secondary and enhanced oil recovery operations. Although simulation is an important tool for design and evaluation, the first step often involves rough calculations based upon areal sweep efficiencies of displacements in homogeneous, two-dimensional, scaled, physical models (c.f., Dyes *et al* , 1954; Craig, 1971; Lake, 1989). These results are available as a function of the displacement pattern and the mobility ratio, M. The mobility ratio is simply the mobility of the displacing phase over that of the displaced, or resident, phase. Because it is possible to compute sweep efficiency when the displacing and displaced phase have the same mobility (Morel-Seytoux, 1966), scaled physical model results have been verified for unit mobility ratios.

Convincing verification of the non-unit mobility ratio cases does not appear in the literature. Typical finite difference solution of the reservoir flow equations suffers from numerical dispersion, the effects of which are hard to evaluate. Furthermore, the scaled physical model results at low mobility ratios ($M << 1$) are provocative. For instance, Fig. 1a shows that recovery from a five spot pattern at breakthrough for 1/M greater than about 6 is virtually 100%, whereas recovery at breakthrough in Fig. 1b for a staggered line drive pattern at an 1/M of 6 is only 88%. This contradicts the common notion that areal sweep efficiency from a staggered line drive pattern is always better than that from a five spot pattern.

We use a 3D streamline simulator (Batycky *et al*, 1997) to analyze displacements in five spot and staggered line drive patterns for stable displacements, that is M less than 1. In the following sections, we present streamline distributions, saturation distributions, and fractional flow versus dimensionless time, t_D, at the producer. The dimensionless time is the pore volumes of displacing fluid injected. With the streamline and saturation distributions at different times, we explain why and at what mobility ratio the five spot pattern can recover more oil than a staggered line drive pattern.

The streamline calculation method is advantageous in that the results suffer from much less numerical dispersion than typical finite difference approximations, but some dispersion in simulation results is evident. Therefore, we discuss how to treat the numerical dispersion to obtain accurate estimates of breakthrough time. We discuss the proper way to calculate fractional flow based on the flow rates at the producer. In comparing the simulation results with the experimental results of Dyes *et al*, physical dispersion in the experiments is found even though a piston-like displacement was assumed.

4.2.3 SWEEP EFFICIENCY

Before proceeding, it is useful to recall the representation of experimental data in Fig. 1 and the meaning of sweep efficiency. Dyes *et al.* (1954) used various oils as both the injected and displaced phases. These hydrocarbons were miscible and they assumed piston-like displacement. An X-ray shadowgraph technique was used to observe the position of the

displacing front. Areal sweep efficiencies are plotted versus displacable pore volumes injected for different mobility ratios. In the figure, the x axis is the reciprocal of mobility ratio. Each curve in the graphs corresponds to a specific $t_D / \Delta S$. That is, displacable pore volume injected. The bottom curves show sweep efficiency at breakthrough. It is assumed that the displacement has a piston-like front and there is no physical dispersion. Likewise, the porous medium is assumed to be perfectly homogeneous.

For piston-like displacement, the areal sweep efficiency is

$$E_A = A_S / A_T \tag{1}$$

where A_s is the swept area and A_T is the total area. Before and at breakthrough, the amount of displacing fluid injected is equal to the displaced fluid produced, disregarding compressibility. Assuming piston-like displacement, injected volume is related to area swept

$$V_I = A_S h \phi \Delta S \tag{2}$$

where V_I is the volume of displacing fluid injected, h is the thickness of the formation, and ϕ is porosity. Hence,

$$E_A = A_S / A_T = V_I / (A_T h \phi \Delta S) = t_D / \Delta S \tag{3}$$

where $t_D = V_I / (A_T h \phi)$ is the pore volume of fluid injected, also commonly called dimensionless time. For $\Delta S = 1$, $E_A = t_D$ before and at breakthrough.

After breakthrough,

$$E_A = (V_I - V_P) / (A_T h \phi \Delta S) \tag{4}$$

where V_P is volume of displacing fluid produced.

4.2.4 SIMULATION RESULTS

We use a three-dimensional streamline simulator, called 3DSL, written by Batycky *et al* (1996-7) to simulate the displacement for the five spot and staggered line drive patterns. In the simulations, we set the conditions identical to those in the experiments and choose relative permeability curves that ensure a piston-like displacement. The conditions:

1. Homogeneous permeability field, *i.e.*, k is constant.
2. Straight line relative permeability curves with end point relative permeability of 1, i.e.,

$$k_{rw} = S_w, \qquad k_{ro} = S_w \tag{5}$$

3. Therefore, $k_{rw} + k_{ro} = 1$ for any S_w.
4. Mobility is altered by changing viscosity, and the mobility ratio is the reciprocal of viscosity ratio.
5. We set $\Delta S = 1$ which means that ahead of the displacing front, the displacing phase saturation is zero, and behind the front, the saturation is unity.

3DSL is very fast compared to conventional finite difference simulators and exhibits much less numerical dispersion (Batycky *et al*, 1996, Thiele *et al*, 1996). For our problem, it offers us the streamline distribution which facilitates explanation of displacement behavior.

We use many pressure solves (time steps) and very fine grids (100 by 100 cells for five-spot and 140 by 70 cells for the staggered line drive) to ensure converged simulation results. A grid refinement study showed these grids to be optimal in that further refinement of the grid did not yield noticeable changes in breakthrough time, the oil production curve, or displacement patterns. For unit mobility ratio (M = 1), we actually only need one pressure solve. But for mobility ratios far from 1, we need many pressure solves. For 1/M = 20, we used up to 1000 pressure solves to ensure that the results were converged. In the

streamline approach, a pressure solve is accompanied by a re-determination of streamline paths; hence, the flow field.

Figure 2 displays areal sweep efficiencies as a function of pore volume injected for differing mobility ratios, and compares simulation and experimental results (Dyes *et al.*, 1954). The solid circles are experimental results, solid lines simulation results, and the experimental breakthrough curve is connected by dashed lines for ease of viewing. In this figure, we concentrate on only the favorable mobility ratios, M < 1. We noticed more numerical dispersion for unfavorable mobility ratio cases, not reported here.

Figure 3 shows the displacing fluid fractional flow as a function of dimensionless time at the producer for several mobility ratios. To compute fractional flow from the numerical data, we use a central finite difference formula rather than backward differences. The shapes of the fractional flow curves at breakthrough (t_D from roughly 0.7 to 1) indicate some numerical dispersion. We expect the fractional flow to increase sharply rather than gradually at water breakthrough. As expected, the numerical dispersion decreases as M becomes more favorable. The most numerical dispersion occurs for unit mobility ratio, as shown in Fig. 3. We modify the breakthrough time by trimming the numerical dispersion as will be described next.

4.2.5 BREAKTHROUGH DETERMINATION

Due to numerical dispersion, injected fluid breaks through earlier at the producer than it should. However the numerical dispersion does not have much effect on the late-time displacing fluid production. The fractional flow versus t_D plots (Fig. 3) show the earlier breakthrough caused by numerical dispersion.

To correct for numerical dispersion in breakthrough times and approximate the breakthrough time more accurately, we use fractional flow data after breakthrough and extrapolate back to breakthrough time. A least squares method with second order polynomials is used:

$$t_D = a + bf_w + cf_w^2 \tag{6}$$

The data are points between $0.1 < f_w < 0.5$. The dashed lines in Fig. 3 illustrate this procedure. All the breakthrough times in Fig.2 are modified using this method.

Numerical dispersion is also related to the number of time steps (*i.e.,* pressure solves). In the streamline approach applied here, dispersion can be introduced through the process of mapping the streamline saturation distribution onto the underlying Cartesian grid used to compute the pressure field (Batycky *et al*, 1996). Hence, for a unit mobility ratio where the pressure field does not change, the most accurate results are obtained when a single time step is used. By performing various single time step simulations, we determine a breakthrough time of 0.7178 for the five spot with M equal to 1. This is in good agreement with the analytical solution of t_D equal to 0.7177. Likewise, analytically (Morel-Seytoux, 1966) and numerically determined breakthrough times for a staggered line drive pattern are both equal to 0.785. With multiple time steps (50) and the quadratic curve-fitting method above, we obtain the same values for the breakthrough times, at $M = 1$.

4.2.6 DISCUSSION OF THE EXPERIMENTAL AND SIMULATION RESULTS

Comparing simulation results and experimental results in Fig. 2, we notice that breakthrough occurs earlier in the experiments than predicted by the simulations. For the staggered line drive pattern in Fig 2(b), experimental data indicates that E_A at breakthrough is roughly 0.75 for M equal to 1. In the experiments, there is physical dispersion even though a piston-like displacement front is assumed.

After breakthrough, the differences in areal sweep efficiencies between the experiments and simulations become much smaller (Fig. 2). After breakthrough, the numerical dispersion consists of only a portion of the displacing fluid produced. As time increases, this portion decreases and the dispersion has less effect on areal sweep efficiency. However, the differences between the experimental results and the simulation results are consistent, i.e. the areal sweep efficiencies of the simulations are generally higher than those

of the experiments. As shown in Fig. 2(a), the simulated breakthrough curve levels off at large $1/M$ with zero slope and does not exceed 1. However, the experimental curve shows E_A equal to 1 at $1/M$ equal to 7. We note that in the plot drawn by Dyes *et al*, the point where the breakthrough curve hits the E_A equal to 1 line is only an extrapolation from other data points.

4.2.7 MOBILITY RATIO VS. PATTERN ON AREAL SWEEP EFFICIENCY

Figure 4 plots computed breakthrough, t_D, versus the conventional shape factor d/a for various mobility ratios. The analytical solution for the unit mobility ratio (Morel-Seytoux, 1966) is also plotted on the same figure for comparison. We find a good match of the sweep efficiency at breakthrough between the analytical solution and simulation results.

For unit mobility ratio, Fig. 4 teaches that a staggered line drive pattern always has better areal sweep efficiency than a five-spot pattern. As the staggered line drive pattern becomes longer relative to its width, the displacement pattern approaches linear flow. High sweep efficiency results.

As the mobility ratio becomes more favorable, the advantage of staggered line drive on sweep efficiency diminishes. When the mobility ratio decreases to 0.2, the five spot pattern becomes better than the staggered line drive pattern with $d/a=1$. However, if d/a is increased, the staggered line drive recovery is better than the five spot pattern for this mobility ratio.

When the mobility ratio decreases to 0.1 or lower (very favorable), the areal sweep efficiency for the five spot pattern is essentially 1 at breakthrough. That is, sweep out is complete at breakthrough. At this mobility ratio, the five spot pattern is as good as a very long staggered line drive ($d/a=25$, almost linear flow), and much better than the common staggered line drive ($d/a=1$). The transition point for five spot sweep efficiency exceeding that from a staggered line drive is around a mobility ratio of 0.3. That is to say, if the mobility ratio is higher than 0.3, a staggered line drive is always better than a five spot. If mobility ratio is lower than 0.3, then the five spot can be higher in sweep efficiency

than a staggered line drive. The excellent displacement from a five spot pattern is discussed below.

4.2.8 DISCUSSION OF PATTERN BEHAVIOR

In this section, we explain, with the help of streamline distributions, how a five spot pattern can exhibit higher areal sweep efficiency than a staggered line drive pattern for very favorable mobility ratios.

4.2.8.1 Unit Mobility Ratio

For the unit mobility ratio, the pressure field remains unchanged throughout the displacement, and so do the streamlines. The streamline distributions at $M = 1$ for the five spot and staggered line drive $(d/a = 1)$ patterns are shown in Fig. 5. Every pair of streamlines forms a stream tube, and the volumetric flow rate is the same in all the stream tubes. All of the stream tubes connect with the same injector and producer, and the pressure drop for all the streamtubes is the same. With the same pressure drop and the same volumetric flow rate, the flow resistance is the same for all the streamtubes.

For our straight-line relative permeability assumption $(k_{rw} + k_{ro} = 1)$, we have

$$R_i = -\Delta p / q = \int_0^{L_i} \frac{\mu}{kA} dl \tag{7}$$

where R_i and L_i are the resistance and length of streamtube i, respectively; k is the permeability, for our study, k is uniform throughout the field; A is the cross sectional area of the streamtube along the streamtube.

$$A = hw$$

where h is the thickness of the layer and is the same for all streamtubes, and w is the width of the streamtube.

Resistance in streamtube i is the same as that in streamtube j, which leads to

$$\int_0^{L_i} \frac{\mu}{kA} dl = C \tag{8}$$

for all the streamtubes at a given time, where C is constant. Move the constant parameters k and h to the right hand side and we have

$$\int_0^{L_i} \frac{\mu}{w} dl = C \tag{9}$$

For a piston-like displacing front, we have

$$\mu_1 \int_0^{l_{fi}} \frac{1}{w} dl + \mu_2 \int_{l_{fi}}^{L_i} \frac{1}{w} dl = C \tag{10}$$

where μ_1 and μ_2 are the viscosity of the displacing and displaced fluids, respectively, and l_f is the distance from the injector to the displacing front.

For unit mobility ratio,

$$\int_0^{L_i} \frac{1}{w} dl = C \tag{11}$$

From Eq. 11, we know that, if the ith streamtube is longer than the jth streamtube, then the average width of the ith streamtube w_i is greater to keep the same resistance or flow rate. Therefore, the volume of the ith streamtube is larger than the jth streamtube. The greater the difference in streamtube length, the bigger the difference in streamtube width, and, when

breakthrough happens in the jth streamtube, the front has not progressed as far in the ith streamtube.

For a five spot pattern, the longest streamline is that along the boundary, which is 2a. The shortest streamline is the one along the diagonal, at a length of $\sqrt{2}\,a$. The ratio of the longest streamtube length over the shortest is $\sqrt{2}$. Since the width of the longest streamtube is also $\sqrt{2}$ times as great as the shortest streamtube, the volume of the longest streamtube is twice that of the shortest.

However, for a staggered line drive pattern, the ratio of the length along the boundary $(d+a=3a)$ over the diagonal $(\sqrt{d^2+a^2}=\sqrt{5}a)$ is $3/\sqrt{5}\approx 1.34$. From the streamline distribution in Fig. 5, we know that the shortest streamline is longer than diagonal, and therefore the ratio of the longest streamline over the shortest is less than 1.34. This ratio is about 1.3 and, therefore, less than that ratio for a five spot pattern which is 1.41. That is to say, the streamlines are more evenly distributed in the staggered line drive than in the five spot pattern. Therefore, when the shortest streamtube breaks through, a larger portion of the other streamtubes have been swept in a staggered line drive than in a five spot pattern. When d/a increases, the streamtube length ratio (longest to shortest) decreases. When breakthrough happens in the shortest streamtube, a greater portion is swept in the longest streamtube, and therefore results in higher sweep efficiency at breakthrough.

4.2.8.2 Five-spot Pattern, Very Favorable Mobility Ratio

For a favorable mobility ratio ($M<1$), the displacement is stable. For equal volumetric flow rate streamtubes, Eq. 10 holds

$$\mu_1 \int_0^{l_{fi}} \frac{1}{w}\,dl + \mu_2 \int_{l_{fi}}^{L_i} \frac{1}{w}\,dl = C$$

Here, we consider the case of very favorable mobility ratio, i.e., the displacing fluid viscosity is much higher than that of the displaced fluid. When the front moves a portion of

the way down the streamtube, the pressure drop is mainly in the displacing phase. That is to say, after a short time(compared to breakthrough) of injecting displacing phase, the pressure drop in the displaced phase is negligible. Therefore, Eqn. 10 can be simplified to the following form

$$\int_0^{l_{fi}} \frac{1}{w} dl = C \tag{12}$$

In this extreme case, the displacing phase does not feel the producer until it is very close to it because the pressure drop between the front and the well plays a negligible role in displacement. Initially, flow around the injector is radial, because the pattern appears to be infinite at short times. For example, examine Fig. 6b for $t_D = 0.204$ and 0.408.

However, after the front passes the corner of a pattern without a well, the no-flow boundary condition along pattern borders alters the radial flow pattern. Pressure isobars must intersect the no-flow boundaries at 90°. This constrains the streamlines in the region adjacent to a boundary to be parallel to it. Because the fluids are incompressible, streamlines cannot terminate. The flow field in the region near the front transitions from radial to quasi-radial. From the figure, we also see that streamtubes ahead of the front are narrower along the boundary than those in the center, which makes the front in the boundary streamtubes move faster than in the central streamtubes. Before the front reaches the no-flow corners of the pattern, the flow is radial around the producer, as we can see in Fig. 6b. Little area is unswept and the sweep efficiency at breakthrough approaches unity.

Similar to before, if the path of displacing fluid in the ith streamtube is longer than that in the jth streamtube, then the ith streamtube should be wider in displacing fluid to keep the same resistance(same flow rate and pressure). Therefore, the streamtubes along the boundary become wider near the corner where the streamtube changes direction. Streamlines remain smooth. This streamline distribution trend is apparent in Fig. 6.

In summary, the very favorable mobility ratio conspires with boundary conditions to determine the way that streamlines evolve, and makes the sweep efficiency at breakthrough

near unity. If the mobility ratio is very favorable, the pressure drop is mainly in the displacing phase, and it does not feel the well, but is affected by the boundary.

4.2.8.3 Staggered Line Drive, Very Favorable Mobility Ratio

For the staggered line drive pattern, the displacement at the beginning is similar to that in the five spot pattern. That is, the displacement pattern is radial around the injector before the front reaches the no-flow corner. The differences in displacement behavior between the two patterns occur after the front reaches the corner. For a five spot, because of the symmetry, the front reaches the two no-flow corners at the same time. However, for a staggered line drive, the front reaches the nearest no-flow corner first.

After the front passes the near corner, the streamlines evolve in a way similar to the five spot. The streamtubes along the boundary are wide near the corner but narrow near the front. This makes the front near the boundary move faster because the streamtubes are narrower than those in the center of the pattern. Therefore, the front near the boundary on the near no-flow corner side catches up, and the displacement approaches linear flow (see the relevant streamline distribution in Fig. 7). If the aspect ratio is large, flow in the center of the pattern must become nearly linear because the pressure isobars are nearly straight and intersect the pattern boundary at 90°.

Similar to the discussion above for a five-spot pattern, for a very favorable mobility ratio, the displacing front is perpendicular to the borders of the pattern both before and after the front passes the no-flow corner. As a result, we see linear displacement for some time until the front on the near-corner side approaches the producer. We see these front shapes in Fig. 7.

When the front approaches the producer, the streamtubes narrow due to the confinement of the pattern boundary and the well. And therefore, with the same flow rate, the displacing fluid will break through relatively quickly in these streamtubes. However, the front on the far no-flow side progresses more slowly. This streamline distribution does not change greatly as the mobility ratio becomes more favorable for staggered line drive

patterns. Sweepout of the pattern is not complete at breakthrough. For instance, a small amount of the resident fluid remains along the right hand boundary as shown in Fig 7a at $t_D = 0.940$.

If the length of staggered line drive is increased (increasing d / a), then the displacement will approach linear flow and the sweep efficiency will approach unity. The proportion of unswept area decreases as d / a increases.

4.2.9 CONCLUSIONS

Pattern performance changes with mobility ratio. For unit mobility ratio, unfavorable mobility ratios and some favorable mobility ratios ($M > 0.3$), a staggered line drive pattern has higher areal sweep efficiency than a five spot pattern. However, for very favorable mobility ratios ($M < 0.3$), a five spot pattern has better sweep efficiency than a staggered line drive.

The reason for this behavior is the change of streamline and pressure distributions with mobility ratios. For very favorable mobility ratios, the displacing front is near an isobar and intersects the pattern boundary at 90°. This causes the fronts at late times near breakthrough to become circles around the producer for a five spot pattern. This displacing front shape is due to the symmetry of the five spot pattern.

For a staggered line drive, the displacing front is also perpendicular to the border of the pattern. However, because the pattern is not symmetric, when the displacing front on one side reaches the producer, it has only moved partially along the other side border.

The simulation results are quite close to the analytical solutions for unit mobility ratio. The results are also very close to the experimental data, Dyes *et al* (1954), after breakthrough at various mobility ratios. We find physical dispersion in the Dyes experimental results that cause earlier breakthrough time.

We observed some numerical dispersion in our simulation results. For very favorable mobility ratios, the dispersion is small. We corrected the simulation results by fitting the fractional flow curve with a second order polynomial to estimate breakthrough time.

4.2.10 NOMENCLATURE

A	area
A_S	area swept
A_T	total area of the pattern
a	distance between like wells (injection or production) in a row
d	distance between adjacent rows of injection and production wells
E_A	areal sweep efficiency
f_w	fractional flow of water
h	bed thickness
k	permeability
k_{ro}	relative permeability of oil
k_{rw}	relative permeability of water
l	length
L_i	length of stream tube i
l_{fi}	distance (length) of the displacing front from the injector in stream tube i
M	mobility ratio
p	pressure
q	flow rate
R_i	flow resistance of stream tube i
S	saturation
S_w	water saturation
t_D	dimensionless time
V_I	volume of displacing phase injected
w	width of a stream tube
ϕ	porosity
μ	viscosity

4.2.11 REFERENCES

1. Abbaszadeh-Dehghani, M. And Brigham, W. E.: "Analysis of Unit Mobility Ratio Well-to-Well Tracer Flow to Determine Reservoir Heterogeneity," SUPRI-TR 36, Stanford University, Stanford (August 1982),.
2. Batycky, R. P., Blunt, M. J., and Thiele, M. R.: "A 3D Field Scale Streamline Simulator with Gravity and Changing Well Conditions," SPE (October 1996).
3. Craig, F. F. Jr.: "The Reservoir Engineering Aspect of Water Flooding," Henry L. Doherty Memorial Fund of AIME, 1971..
4. Dyes, A. B., Caudle, B. H., and Erickson, R. A.: "Oil Production after Breakthroughóas Influenced by Mobility Ratio", Petroleum Transactions, *AIME* (1954) 27-32.
5. Lake, L. W.: Enhanced Oil Recovery, Prentice Hall Inc., New Jersey (1989).
6. Morel-Seytoux, Hubert J.: "Unit Mobility Ratio Displacement Calculations for Pattern Floods in Homogeneous Medium," SPE 1359 (September 1966) 217-226.
7. Thiele, M. R., Batycky, R. P., Blunt, M. J. and Orr Jr, F. M.: "Simulating Flow in Heterogeneous Systems Using Streamtubes and Streamlines," *SPERE* (February 1996), 5-12.

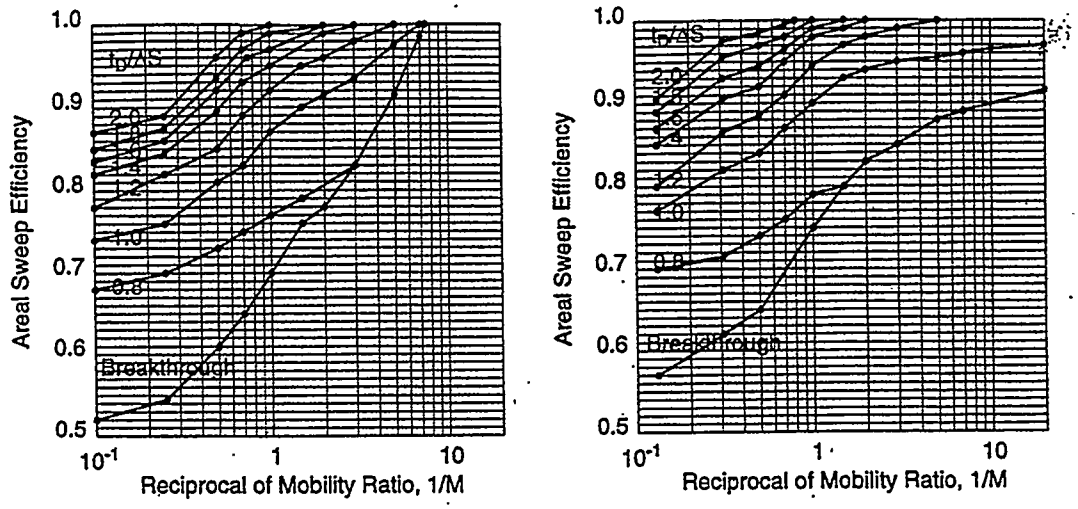

(a) Five Spot Pattern (b) Staggered Line Drive, d/a = 1

Fig.1 Dyes et al(1954) Experimental Results

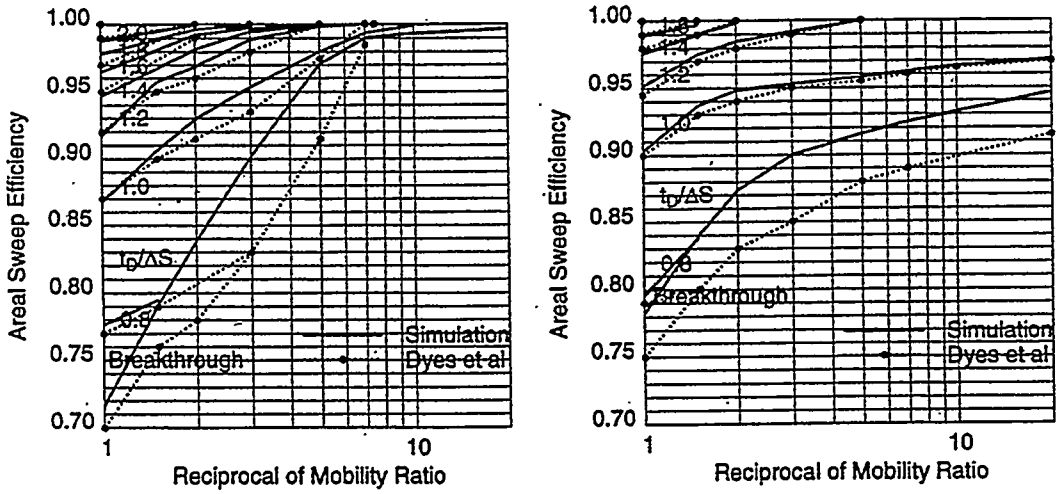

(a) Five Spot Pattern (b) Staggered Line Drive, d/a = 1

Fig 2. Comparison of Simulation and Experimental Results by Dyes et al(1954)

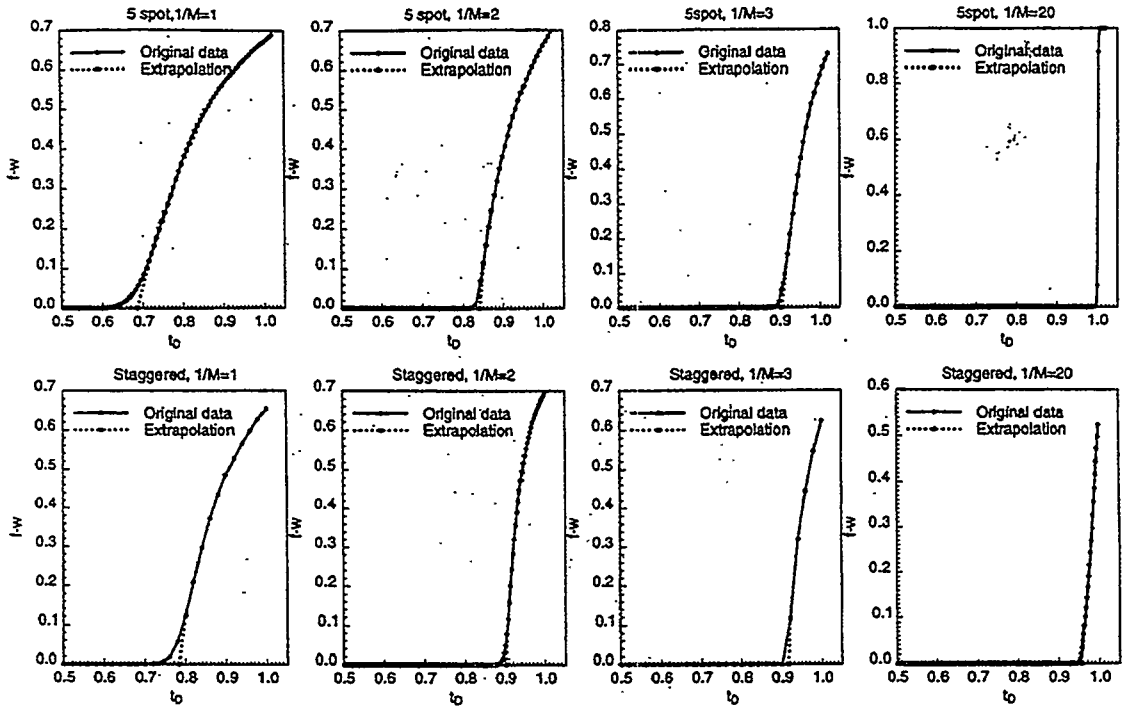

Fig 3 Fractional Flow(f_w) vs t_D at Producer

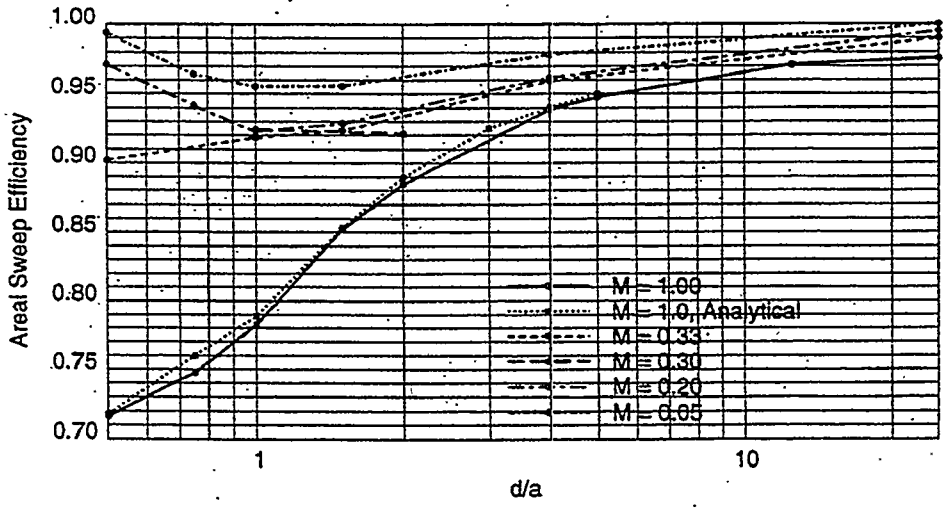

Fig 4 Effect of Mobility Ratios and Patterns
On Areal Sweep Efficiency

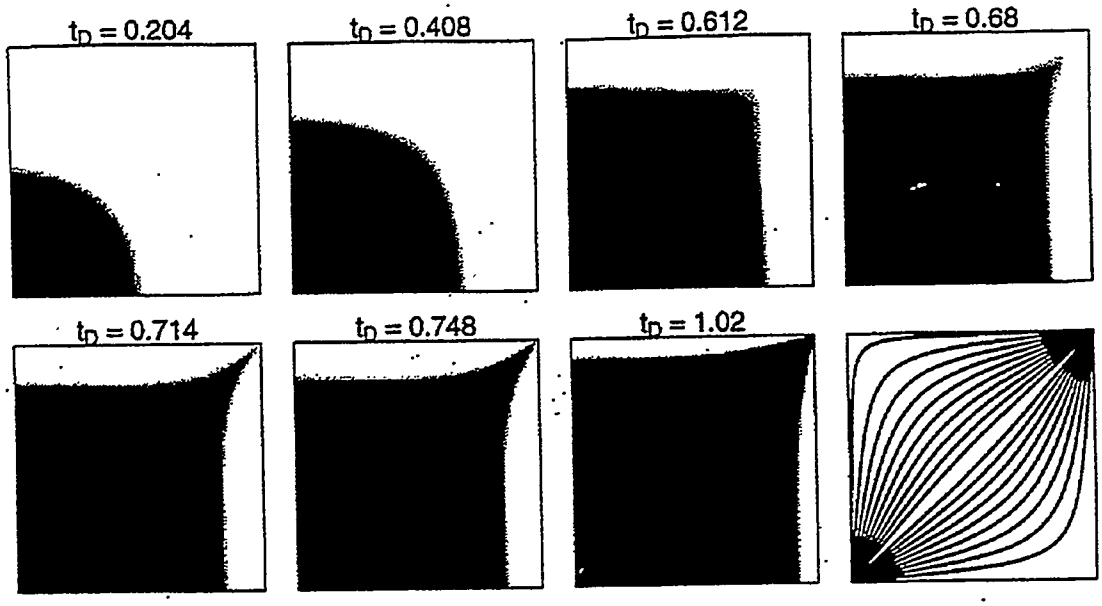

(a) Saturation Distribution

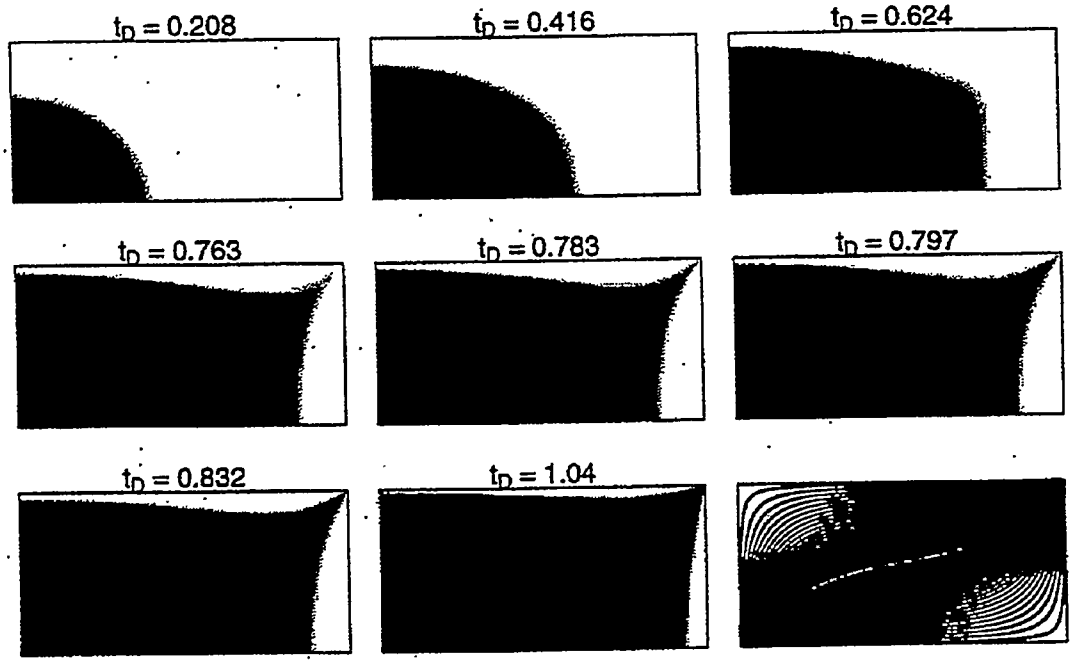

(b) Streamline Distribution

Fig 5 Five Spot and Staggered Line Drive, Unit Mobility Ratio

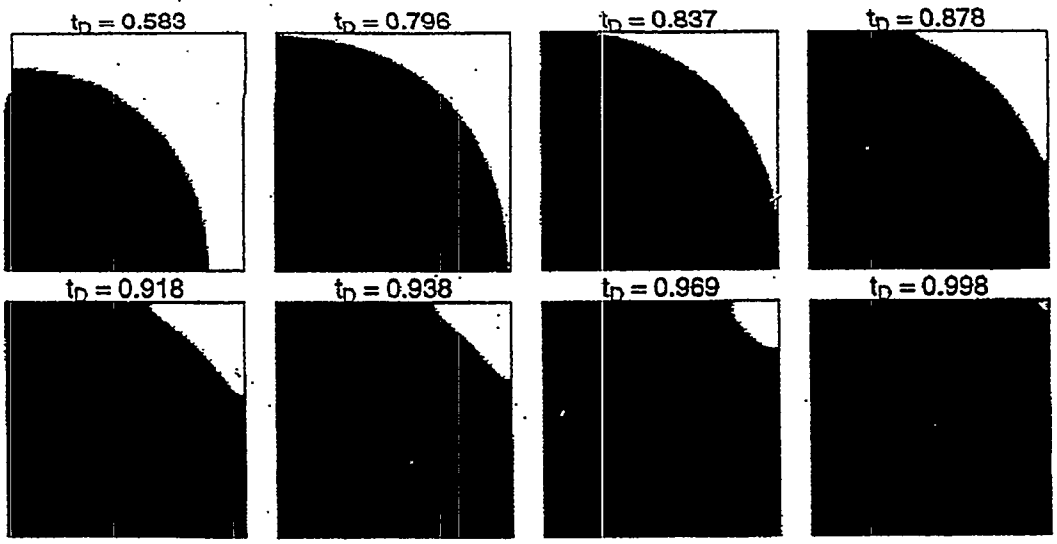

(a) Saturation Distribution

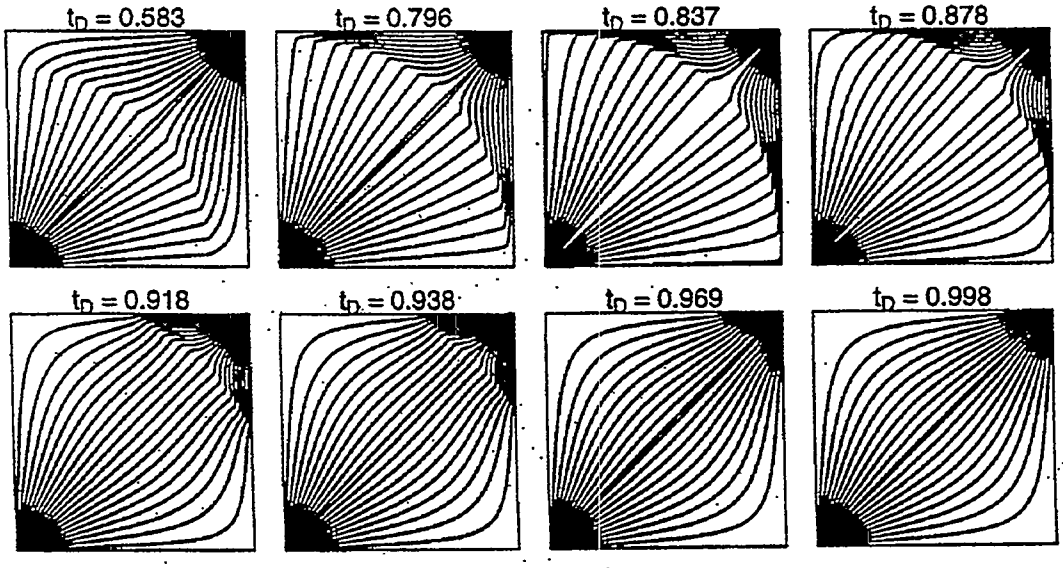

(b) Streamline Distribution

Fig 6 Five Spot Pattern, Very Favorable Mobility Ratio(1/M=20)

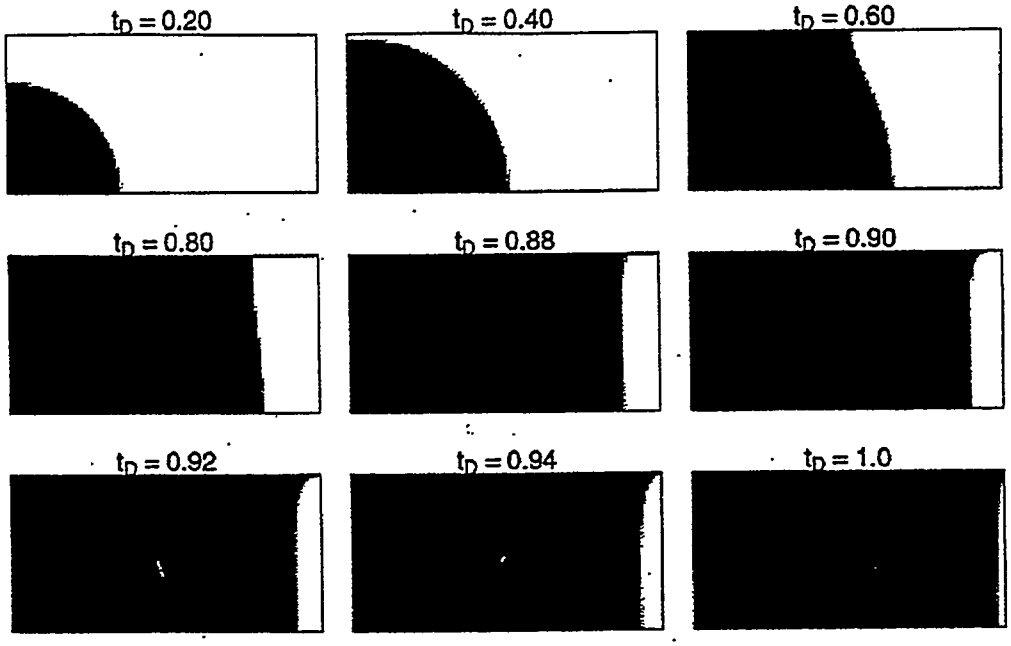

(a) Saturation Distribution

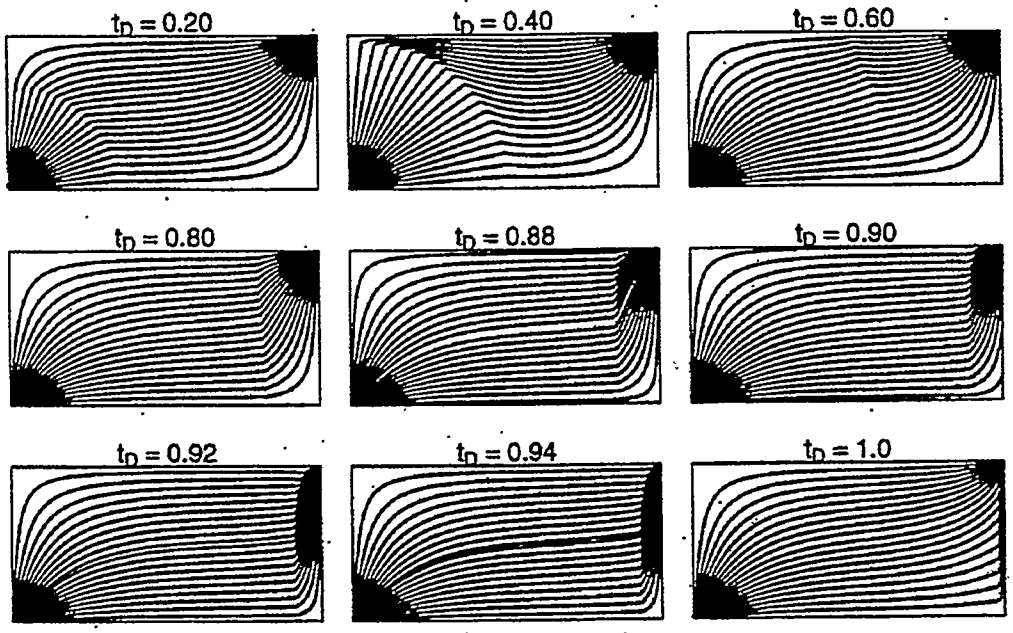

(b) Streamline Distribution

Fig 7 Staggered Line Drive, Very Favorable Mobility Ratio(1/M=20)

PROJECT 5: FIELD SUPPORT SERVICES

To provide technical support for design and monitoring of DOE sponsored or industry initiated field projects.

5.1 PSEUDOSTEADY STATE FLOW

(W. Brigham)

5.1.1 ABSTRACT

Whenever a closed system is being produced at a constant rate, after a period of time the entire system starts to be depleted. This depletion rate is constant everywhere in the system. This state of dynamic equilibrium is usually called pseudosteady state flow, for the forms of the equations look a great deal like their steady state equivalents.

These equation forms follow the diffusivity equation. However, they can be derived without using that equation, but rather, by integrating Darcy's Law and by invoking the overall material balance equation. The forms of these equations can be examined for all three of the geometries commonly used by reservoir engineers; linear, radial and spherical. These solutions are found to be imbedded in the published transient equations for these geometries. However, these transient results are written in such a way that it is not obvious that these concepts have been included in them.

Thus the results seen in these notes are not new. But, in the form presented, they give great insight on the nature of these flow equations, and the concepts leading up to them. It is always useful to clarify concepts of this sort.

5.1.2 INTRODUCTION

I have written a series of notes for steady state flow, and for successions of steady states (Brigham, 1987). I'm going to deviate from that scenario to discuss transient flow in closed bounded systems. This is flow that follows the diffusivity equation; however, in discussing this type of flow behavior, the diffusivity equation will not need to be used.

5.1.3 PSEUDOSTEADY STATE CONCEPTS

If we have a well producing at a constant rate in a closed system, the pressure at the well drops with time; also the effect of flow at the well is to cause the pressure drop to move further into the reservoir with time. After a period of time the effect of the well is seen at the outer boundary. Since it is a closed system, with no flow at the outer boundary, the pressure gradient there must be zero. However, since the well is depleting the reservoir, the pressure must drop there with time just as it does in the remainder of the reservoir.

After a period of time in this closed system, a state of dynamic equilibrium is reached where the well begins to deplete the entire reservoir. From this time onward each part of the system will be depleted at an equal rate, thus the rate at which the pressure declines becomes the same everywhere. For now, I'll have to ask you to take this statement on faith. Later, after we have developed the equations, we will see if we can prove that it is valid.

This type of flow is often called pseudosteady state, for, as we will see later, it has many characteristics and equation forms similar to steady state flow. It has also occasionally been called quasisteady state; however, this phrase never seemed to catch on in the petroleum industry. Dake, in his book (1978) calls it semisteady state. This seems to be commonly used by the worldwide Shell organization. I don't like it because it is bad English; the prefix "semi" means "half," which is a meaningless term in this context. Craft and Hawkins (1959) on pp. 285-289 and others even refer to this type of flow as "steady state." This is clearly wrong. So I will use "pseudosteady state" when discussing constant rate depletion of closed bounded systems. Let us turn now to consideration of the implications of the depletion mechanism discussed earlier.

If we were to look at a given point in a reservoir, we can ask ourselves how much fluid is flowing past that point. It seems clear that the fluid flowing past that point is only that fluid which is being produced from points further out and which is flowing toward the well. At the outside edge the flow is zero, as we move closer to the well the flow increases, and finally, as we get to the well, the flow reaches the constant rate that was stipulated earlier.

These concepts can be put into equations, the forms of which will depend on the geometry of the system. There are three geometries that are convenient to consider; linear, radial and spherical. I'll discuss all three, starting with the cylindrical (radial) system, for that is the one most commonly seen in reservoir flow.

5.1.4 CYLINDRICAL (RADIAL) FLOW

Let us consider a closed cylindrical reservoir with a drainage radius, r_e , and a wellbore radius, r_w . If the flow, $q(r)$, at any distance, r, is proportional to the volume being depleted beyond r , and the flow at the well, q_w , is proportional to the entire drainage volume, we can write the following equation:

$$\frac{q(r)}{q_w} = \frac{r_e^2 - r^2}{r_e^2 - r_w^2} \tag{1}$$

which is merely a mathematical statement of the idea. Note that Eq. 1 tells us that $q(r)$ becomes zero at r_e , and q_w at r_w , as it should.

Let us now write Darcy's Law for flow at any radius, r , and substitute Eq. 1 into it.

$$q(r) = -\frac{2\pi k h r\, dp}{\mu\, dr} = q_w\left(\frac{r_e^2 - r^2}{r_e^2 - r_w^2}\right) \tag{2a}$$

or, upon rearranging:

$$-\frac{2\pi k h}{q_w \mu}\, dp = \left(\frac{r_e^2 - r^2}{r_e^2 - r_w^2}\right)\frac{dr}{r} \tag{2b}$$

Let us integrate Eq. 2b from the wellbore out to a general radius, r , and also out to r_e :

$$-\frac{2\pi k h}{q_w \mu}\int_{p_w}^{p(r)} dp = \frac{r_e^2}{r_e^2 - r_w^2}\int_{r_w}^{r}\frac{dr}{r} - \left(\frac{1}{r_e^2 - r_w^2}\right)\int_{r_w}^{r} r\, dr$$

$$-\frac{2\pi k h[p(r) - p_w]}{q_w \mu} = \frac{r_e^2(\ln r - \ln r_w)}{\left(r_e^2 - r_w^2\right)} - \frac{\left(r^2 - r_w^2\right)}{2\left(r_e^2 - r_w^2\right)} \tag{3}$$

and, out to r_e :

$$-\frac{2\pi kh}{q_w \mu}(p_e - p_w) = \left(\frac{r_e^2}{r_e^2 - r_w^2}\right)\ln\left(\frac{r_e}{r_w}\right) - \frac{1}{2} \tag{4}$$

In general, in reservoirs, $r_e >> r_w$; thus the ratio in front of the log term is nearly equal to 1.0, and Eq. 4 can be simplified to:

$$q_w = -\frac{2\pi kh(p_e - p_w)}{\mu\left[\ln(r_e/r_w) - 1/2\right]}$$

or,

$$= -\frac{2\pi kh(p_e - p_w)}{\mu \ln(0.607\, r_e/r_w)} \tag{5}$$

A glance at either form of Eq. 5 will show why this type of flow is called pseudosteady state. The equation certainly looks a great deal like the equation for steady state radial flow. It differs only by the constant on the log term. Equation 5, however, is not very useful, for it contains the pressure drop from the outer boundary to the well; and we seldom have a convenient way to measure that outer boundary pressure. If we could, it would be much better to relate the equation to the average pressure, $\bar{p}$. This pressure could be measured easily in the field by merely shutting in the well and allowing it to build up to its average pressure. Of course, transient testing pressure buildup techniques could also be used to calculate this pressure.

The average pressure we want is the volumetric average. This means we need to integrate pressure over the entire volume and divide it by the total volume, as follows:

$$\bar{p} = -\frac{\int_{r_w}^{r_e} 2\pi r h \phi\, p(r)\, dr}{\int_{r_w}^{r_e} 2\pi r h \phi\, dr}$$

or,

$$\bar{p} = \frac{\int_{r_w}^{r_e} 2r\, p(r)\, dr}{\left(r_e^2 - r_w^2\right)} \tag{6}$$

Actually, we are interested in the pressure drop terms in the equation; so instead of the average pressure, let us calculate the pressure drop, $\overline{p} - p_w$, and include the flow terms by substituting Eq. 3 into Eq. 6, as follows,

$$-\frac{2\pi kh(\overline{p}-p_w)}{q_w\mu} = -\frac{2\pi kh}{q_w\mu\left(r_e^2-r_w^2\right)}\int_{r_w}^{r_e} 2r\left[p(r)-p_w\right]dr$$

$$= \frac{r_e^2}{\left(r_e^2-r_w^2\right)^2}\int_{r_w}^{r_e}\left(2r\ln r - 2r\ln r_w\right)dr$$

$$-\frac{1}{2\left(r_e^2-r_w^2\right)^2}\int_{r_w}^{r_e}\left(2r^3-2r_w^2 r\right)dr \qquad (7)$$

When integrated, Eq. 7 becomes:

$$-\frac{2\pi kh(\overline{p}-p_w)}{q_w\mu} = \frac{r_e^2}{\left(r_e^2-r_w^2\right)^2}\left(r_e^2\ln r_e - r_e^2/2 - r_w^2\ln r_w + r_w^2/2 - r_e^2\ln r_w + r_w^2\ln r_w\right)$$

$$-\frac{1}{2\left(r_e^2-r_w^2\right)^2}\left[r_e^4/2 - r_w^4/2 - r_w^2\left(r_e^2-r_w^2\right)\right]$$

$$= \frac{r_e^2}{\left(r_e^2-r_w^2\right)^2}\left[r_e^2\ln\left(r_e/r_w\right) - \frac{r_e^2-r_w^2}{2}\right]$$

$$-\frac{1}{2\left(r_e^2-r_w^2\right)^2}\left[\frac{\left(r_e^2-r_w^2\right)\left(r_e^2+r_w^2\right)}{2} - r_w^2\left(r_e^2-r_w^2\right)\right]$$

$$= \frac{r_e^4\ln\left(r_e/r_w\right)}{\left(r_e^2-r_w^2\right)^2} - \left(\frac{1}{r_e^2-r_w^2}\right)\left[\frac{r_e^2}{2} + \frac{r_e^2+r_w^2}{4} - \frac{r_w^2}{2}\right]$$

$$= \frac{r_e^4\ln\left(r_e/r_w\right)}{\left(r_e^2-r_w^2\right)^2} - \left(\frac{1}{r_e^2-r_w^2}\right)\left(\frac{3r_e^2}{4} - \frac{r_w^2}{4}\right) \qquad (8)$$

Again, we can recognize that, $r_e^2 >> r_w^2$, thus Eq. 8 can be simplified and rearranged to:

$$q_w = -\frac{2\pi kh(\bar{p} - p_w)}{\mu\left[\ln(r_e/r_w) - 3/4\right]}$$

$$= -\frac{2\pi kh(\bar{p} - p_w)}{\mu\left[\ln(0.472 r_e/r_w)\right]} \tag{9}$$

This is the same as Eq. 6.27, p. 288 of Craft and Hawkins, and Eq. 6.12, p. 144 of Dake. It is an extremely useful equation for it gives us the flow behavior of a depleting radial system. As you can see, it looks remarkably like the steady state radial flow equation with merely an additional constant.

Considering the constant $(-3/4$ or $0.472)$, we might wish to look at this drainage cylinder in terms of its area rather than its radius. If we were to define the area, A, in acres, and r_e in feet, they are related as follows:

$$A = \frac{\pi r_e^2}{43{,}560}$$

or,

$$r_e = \sqrt{\frac{43{,}560A}{\pi}} = 117.75\sqrt{A} \tag{10}$$

Thus we could change Eq. 9 to:

$$q_w = -\frac{kh(\bar{p} - p_w)}{\mu \ln\left[117.75(0.472)\sqrt{A}/r_w\right]}$$

$$q_w = \frac{kh(\bar{p} - p_w)}{\mu \ln\left(55.6\sqrt{A}/r_w\right)} \tag{11}$$

Equation 11 is for pseudosteady state flow from a cylindrical reservoir. From the earlier description of the flow, however, it should be clear that flow toward a well from any bounded system will eventually reach pseudosteady state. Thus we should expect that other outer boundary shapes might result in an equation similar to Eq. 11. This supposition is correct. In fact, there is a commonly-used areal geometric term in transient flow called the Dietz shape factor, C_A (Dietz, 1965). In a cylindrical system, C_A is equal to 31.62. In general if we call the constant in Eq. 11, ψ, we can write the equation for pseudosteady

flow as,

$$q_w = \frac{kh(\bar{p} - p_w)}{141.2\,B\mu \ln\left(\psi\sqrt{A}\,/r_w\right)} \tag{12}$$

In oilfield units; and from the constants defined above, the equation which relates ψ to the shape factor, C_A, is:

$$\psi = 313/\sqrt{C_A} \tag{13}$$

or,

$$q_w = -\frac{kh(\bar{p} - p_w)}{141.2\,B\mu \ln\left(\frac{313}{r_w}\sqrt{\frac{A}{C_A}}\right)} \tag{14}$$

Equation 14 is extremely useful in many reservoir engineering calculations.

5.1.5 PROOF THAT THE RADIAL PSEUDOSTEADY STATE EQUATION FITS THE DIFFUSIVITY EQUATION

Earlier I stated that the equations developed here can be proved to fit the diffusivity equation. In radial coordinates this equation is:

$$\frac{\partial^2 p}{\partial r^2} + \frac{1}{r}\frac{\partial p}{\partial r} = \frac{\phi\mu c_t}{k}\frac{\partial p}{\partial t} \tag{15}$$

If the equations we have developed fit Eq. 15 and also fit the boundary conditions, they must be solutions to Eq. 15. The boundary conditions are:

$$-\frac{2\pi kh}{\mu}\left(r\frac{\partial p}{\partial r}\right)_{r_w} = q_w \tag{16}$$

and

$$-\frac{2\pi kh}{\mu}\left(r\frac{\partial p}{\partial r}\right)_{r_e} = 0 \tag{17}$$

The partial derivatives on the left-hand side of Eq. 15 can be evaluated by differentiating Eq. 3, as can the boundary conditions. It only remains to evaluate the time derivative on the

right side of Eq. 15, to see if Eq. 3 fits Eq. 15; and also to show that Eq. 3 fits Eqs. 16 and 17.

The time derivative requires a little thought. Earlier I stated that the pressure will drop at a constant rate in all parts of the reservoir during pseudosteady flow. Looking at the equation for average pressure, we see that if the pressures at all points drop at a given rate, so does the average pressure. Thus we can write,

$$\frac{\partial p(r)}{\partial t} = \frac{d\bar{p}}{dt} = \text{Constant} \tag{18}$$

and the constant can be evaluated by performing an overall material balance, through the definition of the compressibility, as follows:

$$c_t = -\frac{1}{V}\left(\frac{\partial V}{\partial \bar{p}}\right)_T$$

or,

$$(dV)_T = -c_t V (d\bar{p})_T \tag{19}$$

Recognizing that the temperature, T, is constant, and by defining the flow rate, q_w, as the time derivative of V, we get:

$$-q_w = \left(\frac{dV}{dt}\right) = -c_t V\left(\frac{d\bar{p}}{dt}\right) = -\pi\left(r_e^2 - r_w^2\right)\phi c_t h\left(\frac{d\bar{p}}{dt}\right)$$

$$= -\pi\left(r_e^2 - r_w^2\right)\phi c_t h\frac{\partial p(r)}{\partial t} \tag{20}$$

Equation 20 allows us to check whether our assumptions and equations are, in fact, a proper solution to the diffusivity equation.

To develop the terms of the diffusivity equation, we begin by rearranging Eq. 3, as follows,

$$p(r) - p_w = -\frac{q_w \mu}{2\pi kh}\left[\frac{r_e^2(\ln r - \ln r_w)}{\left(r_e^2 - r_w^2\right)} - \frac{\left(r^2 - r_w^2\right)}{2\left(r_e^2 - r_w^2\right)}\right] \tag{21}$$

Differentiating Eq. 21 with respect to r, as indicated in Eq. 15 we get,

$$\frac{\partial p(r)}{\partial r} = -\frac{q_w \mu}{2\pi kh}\left[\frac{r_e^2}{\left(r_e^2 - r_w^2\right)r} - \frac{r}{\left(r_e^2 - r_w^2\right)}\right] \tag{22}$$

and dividing by r, as in Eq. 15,

$$\frac{1}{r}\frac{\partial p(r)}{\partial r} = -\frac{q_w \mu}{2\pi kh}\left[\frac{r_e^2}{\left(r_e^2 - r_w^2\right)^2} - \frac{1}{\left(r_e^2 - r_w^2\right)}\right] \tag{23}$$

We can also differentiate Eq. 22 with respect to r, to get the first term in Eq. 15,

$$\frac{\partial}{\partial r}\left[\frac{\partial p(r)}{\partial r}\right] = \frac{\partial^2 p(r)}{\partial r^2} = -\frac{q_w \mu}{2\pi kh}\left[-\frac{r_e^2}{\left(r_e^2 - r_w^2\right)^2} - \frac{1}{\left(r_e^2 - r_w^2\right)}\right] \tag{24}$$

Rearranging Eq. 20 to evaluate the diffusivity term on the right-hand side of Eq. 15, we get,

$$\frac{\phi\mu c_t}{k}\frac{\partial p(r)}{\partial t} = \frac{\phi\mu c_t}{k}\left[\frac{q_w}{\pi\left(r_e^2 - r_w^2\right)\phi c_t h}\right]$$

$$= \frac{q_w \mu}{\pi\left(r_e^2 - r_w^2\right)kh} \tag{25}$$

Now we can substitute Eqs. 23, 24, and 25 into Eq. 15, the radial diffusivity equation. The result is

$$\frac{q_w \mu}{2\pi kh}\left[\frac{r_e^2}{\left(r_e^2 - r_w^2\right)^2} + \frac{1}{\left(r_e^2 - r_w^2\right)}\right] - \frac{q_w \mu}{2\pi kh}\left[\frac{r_e^2}{\left(r_e^2 - r_w^2\right)^2} - \frac{1}{\left(r_e^2 - r_w^2\right)}\right] = \frac{q_w \mu}{\pi\left(r_e^2 - r_w^2\right)kh} \tag{26a}$$

Note in Eq. 26a, the terms $r_e^2/\left(r_e^2 - r_w^2\right)^2$ cancel; while the terms $1/\left(r_e^2 - r_w^2\right)$ are additive, thus Eq. 26a simplifies to

$$\frac{q_w \mu}{2\pi kh}\left[\frac{2}{\left(r_e^2 - r_w^2\right)}\right] = \frac{q_w \mu}{\pi\left(r_e^2 - r_w^2\right)kh} \tag{26b}$$

The terms on both sides of Eq. 26b are identical, thus proving that the diffusivity equation is honored by Eqs. 3 and 20.

It only remains to show that the boundary conditions (Eqs. 16 and 17) are also correctly stipulated by Eq. 3. In Eq. 22, we differentiated Eq. 3 to get,

$$-\frac{2\pi kh}{q_w \mu}\left[\frac{\partial p(r)}{\partial r}\right]=\left[\frac{r_e^2}{\left(r_e^2-r_w^2\right)}-\frac{r}{\left(r_e^2-r_w^2\right)}\right] \tag{22}$$

We multiply this by r, as Eqs. 16 and 17 require, to get,

$$-\frac{2\pi kh}{q_w \mu}\left[r\frac{\partial p(r)}{\partial r}\right]=\frac{r_e^2}{\left(r_e^2-r_w^2\right)}-\frac{r^2}{\left(r_e^2-r_w^2\right)} \tag{27}$$

Setting $r=r_w$, as in Eq. 16, we get,

$$-\frac{2\pi kh}{q_w \mu}\left[r\frac{\partial p(r)}{\partial r}\right]_{r=r_w}=\frac{r_e^2}{\left(r_e^2-r_w^2\right)}-\frac{r_w^2}{\left(r_e^2-r_w^2\right)}=1 \tag{28}$$

which is Eq. 16, as expected. Setting $r=r_e$ as in Eq. 17, we get,

$$-\frac{2\pi kh}{q_w \mu}\left[r\frac{\partial p(r)}{\partial r}\right]_{r=r_e}=\frac{r_e^2}{\left(r_e^2-r_w^2\right)}-\frac{r_e^2}{\left(r_e^2-r_w^2\right)}=0 \tag{29}$$

which is Eq. 17, which again as what we expected. Thus it is clear that Eq. 3 combined with Eq. 20 is a solution to the diffusivity equation during radial pseudosteady state flow.

A thoughtful reader may wonder whether this result can be seen in Van Everdingen and Hurst's (1949) or Chatas' (1953) tables and equations for the solutions to closed systems at constant rate. It turns out that it is in their solutions, but the equations are written in such a way that this fact is hard to see. Chatas shows the long time result for the constant rate case with a closed outer boundary. This result in present day nomenclature is,

$$p_D(t_D)=\frac{1/2+2t_D}{r_D^2-1}-\frac{3r_D^4-4r_D^4\ln r_D-2r_D^2-1}{4\left(r_D^2-1\right)^2} \tag{30a}$$

where $r_D=r_e/r_w$

which, after considerable algebraic manipulation, simplifies to,

$$p_D(t_D) = \frac{2t_D}{r_D^2 - 1} + \frac{r_D^4 \ln r_D}{\left(r_D^2 - 1\right)^2} - \frac{3r_D^2 - 1}{4\left(r_D^2 - 1\right)} \tag{30b}$$

Note that the last two terms on the right side of Eq. 30b are exactly the same as Eq. 8 of these notes. But remember that Eq. 8 defines $\overline{p}_D$ which is based on $\overline{p} - p_w$, while $p_D(t_D)$ is based on $p_i - p_w$. The first term on the right of Eq. 30b, $2t_D/\left(r_D^2 - 1\right)$, defines $(p_i - \overline{p})_D$; it is the material balance term from Eq. 20.

Chatas' way of writing the equation, although correct, really didn't emphasize the physical concepts involved, while Eq. 30b shows them clearly. These same ideas will also hold true for the linear and spherical systems. I'll derive the depletion equations for these systems, but will not bother to prove they fit the diffusivity equations and the boundary conditions, as I have done here for the radial system. It seems clear that these proofs will act similarly to these radial flow results.

5.1.6 LINEAR FLOW

Using concepts similar to those used to derive the radial flow equation, for linear depletion at constant rate, we stipulate that the flow rate at any distance, x , is proportional to the volume beyond that point out to the total distance, L ; and the flow rate at the inner boundary is equal to the total rate, q_w . Thus we can write,

$$\frac{q(x)}{q_w} = \frac{L - x}{L} \tag{31}$$

We can now substitute this concept into Darcy's Law for linear flow, as follows,

$$q(x) = \frac{-kA\,\partial p}{\mu\,\partial x} = q_w\left(\frac{L - x}{L}\right) \tag{32a}$$

We can rearrange and integrate out to x ,

$$-\frac{kA}{q_w\mu}\int_{p_w}^{p(x)} dp = \int_0^x \frac{(L-x)\,dx}{L}$$

$$-\frac{kA}{q_w\mu}[p(x)-p_w] = x-\frac{x^2}{2L} \tag{32b}$$

and also integrate to the outer boundary at L ,

$$-\frac{kA}{q_w\mu}[p(L)-p_w] = \frac{L}{2} \tag{32c}$$

This result looks much like Darcy's Law for linear flow, as we might have expected. The only difference is the constant, 1/2. However, it is not very useful, for it is hard to determine $p(L)$. As we did for the radial system, we will look at the average pressure instead. This is accomplished easily as follows.

$$\bar{p}-p_w = \frac{\int_0^L [p(x)-p_w]dx}{\int_0^L dx} = \frac{1}{L}\int_0^L [p(x)-p_w]dx \tag{33}$$

Substituting Eq. 32b into Eq. 33, and rearranging, we get,

$$-\frac{kA(\bar{p}-p_w)}{q_w\mu} = \frac{1}{L}\int_0^L \left(x-\frac{x^2}{2L}\right)dx \tag{34a}$$

which, when integrated, becomes

$$-\frac{kA(\bar{p}-p_w)}{q_w\mu} = \frac{1}{L}\left|\frac{x^2}{2}-\frac{x^3}{6L}\right|_0^L$$

$$= \frac{L}{3} \tag{34b}$$

Note that this, too, looks a great deal like the steady state equation. The only difference is the constant, 1/3.

We should also be interested in determining $p_i - p_w$, for this term is the one usually listed in transient flow solutions. To do this, we need to define $p_i - \bar{p}$. But this is

accomplished easily by a simple material balance calculation, as we did for the radial system in Eq. 20. Using linear coordinates, the material balance results in,

$$p_i - \overline{p} = -\frac{q_w t}{\phi c_t AL} \tag{35}$$

We can define t_D as follows, for a linear system,

$$t_D = \frac{kt}{\phi \mu c_t L^2} \tag{36}$$

Substituting Eq. 36 into Eq. 35, we get

$$-\frac{kA(p_i - \overline{p})}{q_w \mu L} = t_D \tag{37}$$

We wish to define the term, $p_i - p_w$, rather than $p_i - \overline{p}$. To do this we can write,

$$-\frac{kA(p_i - p_w)}{q_w \mu L} = -\frac{kA(p_i - \overline{p})}{q_w \mu L} - \frac{kA(\overline{p} - p_w)}{q_w \mu L} \tag{38a}$$

But the two terms on the right side of Eq. 38a are defined in Eqs. 34b and 37, so the result is very simple,

$$-\frac{kA(p_i - p_w)}{q_w \mu L} = p_D = t_D + \frac{1}{3} \tag{38b}$$

The interested reader will note that Eq. 38b is exactly the same as seen in Nabor and Barham's (1964) Eq. 17 on linear flow solutions, just as we should have expected.

5.1.7 SPHERICAL FLOW

By now the reader should be able to predict the methods used to derive the equations for spherical pseudosteady state flow. The flow rate at any radius, r, is proportional to the volume beyond r, and the total flow rate is q_w. Thus the resulting flow rate equation is,

$$\frac{q(r)}{q_w} = \frac{r_e^3 - r^3}{r_e^3 - r_w^3} \tag{39}$$

We can now write Darcy's Law for spherical flow at a general radius,

$$q(r) = -\frac{4\pi k r^2 dp}{\mu dr} = \frac{q_w\left(r_e^3 - r^3\right)}{\left(r_e^2 - r_w^3\right)} \tag{40a}$$

and we can rearrange Eq. 40a and integrate out to a general radius, r, as follows,

$$-\frac{4\pi k[p(r) - p_w]}{q_w \mu} = \frac{r_e^3}{\left(r_e^3 - r_w^3\right)} \int_{r_w}^{r} \frac{dr}{r^2} - \frac{1}{\left(r_e^3 - r_w^3\right)} \int_{r_w}^{r} r\, dr$$

$$= \frac{r_e^3}{\left(r_e^3 - r_w^3\right)}\left(\frac{1}{r_w} - \frac{1}{r}\right) - \frac{r^2 - r_w^2}{2\left(r_e^3 - r_w^3\right)} \tag{40b}$$

and also integrate to the outer boundary, r_e,

$$-\frac{4\pi k(p_e - p_w)}{q_w \mu} = \frac{r_e^3}{\left(r_e^3 - r_w^3\right)}\left(\frac{1}{r_w} - \frac{1}{r_e}\right) - \frac{r_e^2 - r_w^2}{2\left(r_e^3 - r_w^3\right)} \tag{40c}$$

We can compare Eq. 40c with the steady state spherical flow equation from r_w to r_e. From my notes (Brigham, 1987), it is,

$$-\frac{4\pi k(p_e - p_w)}{q_w \mu} = \left(\frac{1}{r_w} - \frac{1}{r_e}\right) \tag{41}$$

Notice the similarity in the two equations. The multiplier in front of the $1/r$ terms in Eq. 40c approaches unity when r_e is quite a bit greater than r_w. And, similar to the radial and linear equations, there is an additional term, that is a function of the size of the system,

which is subtracted from the steady state term. So the pressure drop for pseudosteady state is less than for steady state flow.

But, as before, we realize that $\bar{p} - p_w$ is a more useful way to look at the pressure drop terms. To evaluate $\bar{p} - p_w$, we integrate the pressure drop from r_w to r_e and divide that by the volume, as follows,

$$\bar{p} - p_w = \frac{\int_{r_w}^{r_e} [p(r) - p_w] r^2 dr}{\int_{r_w}^{r_e} r^2 \, dr}$$

$$= \frac{3}{\left(r_e^3 - r_w^3\right)} \int_{r_w}^{r_e} [p(r) - p_w] r^2 dr \tag{42}$$

We can now substitute Eq. 40b into Eq. 42, to get,

$$-\frac{4\pi k(\bar{p} - p_w)}{q_w \mu} = \frac{3r_e^3}{\left(r_e^3 - r_w^3\right)^2} \int_{r_w}^{r_e} \left(\frac{1}{r_w} - \frac{1}{r}\right) r^2 \, dr$$

$$-\frac{3}{2\left(r_e^3 - r_w^3\right)^2} \int_{r_w}^{r_e} \left(r^2 - r_w^2\right) r^2 \, dr \tag{43a}$$

$$= \frac{3r_e^3}{\left(r_e^3 - r_w^3\right)^2} \left| \frac{r^3}{3r_w} - \frac{r^2}{2} \right|_{r_w}^{r_e} - \frac{3}{2\left(r_e^3 - r_w^3\right)^2} \left| \frac{r5}{5} - \frac{r_w^2 r^3}{3} \right|_{r_w}^{r_e}$$

$$= \frac{r_e^3}{r_w\left(r_e^3 - r_w^3\right)} - \frac{3r_e^3\left(r_e^2 - r_w^2\right)}{2\left(r_e^3 - r_w^3\right)^2}$$

$$- \frac{3\left(r_e^5 - r_w^5\right)}{10\left(r_e^3 - r_w^3\right)^2} + \frac{r_w^2}{2\left(r_e^3 - r_w^3\right)} \tag{43b}$$

We need to recognize that the dimensionless pressure term in spherical flow contains an r_w multiplier in the numerator on the left hand side of Eq. 43. Also it would be more

convenient if we were to express Eq. 43b in terms of the r_e / r_w ratio, which I will call r_D. The first and fourth terms in Eq. 43b can then be combined into a common denominator; and the second and third can also be combined to get,

$$-\frac{4\pi k r_w(\bar{p}-p_w)}{q_w \mu} = \frac{2r_D^3+1}{2\left(r_D^3-1\right)} - \frac{15\, r_D^3\left(r_D^2-1\right)+3\left(r_D^5-1\right)}{10\left(r_D^3-1\right)^2} \tag{44a}$$

and after come further algebraic manipulation,

$$\begin{aligned} -\frac{4\pi k r_w(\bar{p}-p_w)}{q_w \mu} &= 1+\frac{3}{2\left(r_D^3-1\right)} - \frac{18r_D^5-15r_D^3-3}{10\left(r_D^3-1\right)^2} \\ &= 1+\frac{3}{2\left(r_D^3-1\right)} - \frac{18\left(r_D^5-1\right)}{10\left(r_D^3-1\right)^2} + \frac{15\left(r_D^3-1\right)}{10\left(r_D^3-1\right)^2} \\ &= 1+\frac{3}{\left(r_D^3-1\right)} - \frac{9\left(r_D^5-1\right)}{5\left(r_D^3-1\right)^2} \end{aligned} \tag{44b}$$

As we have done before, we can define $p_i - \bar{p}$ using the depletion material balance based on the total system volume,

$$p_i - \bar{p} = \frac{-3q_w t}{4\pi\phi\, c_t \left(r_e^3 - r_w^3\right)} \tag{45}$$

For spherical flow, t_D is defined the same way it is for radial flow.

$$t_D = \frac{kt}{\phi\mu\, c_t r_w^2} \tag{46}$$

Substituting Eq. 46 into Eq. 45, and again calling the radius ratio r_D, we get,

$$-\frac{4\pi k r_w(p_i-\bar{p})}{q_w \mu} = \frac{3t_D}{\left(r_D^3-1\right)} \tag{47}$$

Now we can combine Eqs. 44b and 47 to define the total pressure drop for pseudosteady state spherical flow.

$$-\frac{4\pi k r_w (p_i - p_w)}{q_w \mu} = p_D = \frac{3t_D}{\left(r_D^3 - 1\right)} + 1 + \frac{3}{\left(r_D^3 - 1\right)} - \frac{9\left(r_D^5 - 1\right)}{5\left(r_D^3 - 1\right)^2} \tag{48}$$

Equation 48 has an interesting property as r_D approaches infinity. Note that it degenerates to 1.00 under this condition. That is, the dimensionless pressure drop is limited to this value. This is correct. The spherical geometry is the only case which exhibits this strange behavior.

As we have done before, it would be well to check whether this result agrees with the published equations. Chatas wrote a paper on transient behavior for spherical systems (Chatas, 1966). His equation which results in pseudosteady state flow is his Eq. 53. His long time result, in my nomenclature, is,

$$p_D = \frac{\left[(r_D - 1)^2 + 3r_D\right]\left[\frac{1}{6}(r_D - 1)^2(2r_D + 1) + t_D\right] - \frac{1}{2}(r_D - 1)^2\left[\frac{1}{5}(r_D - 1)^2 + r_D\right]}{(r_D - 1)\left[\frac{1}{3}(r_D - 1)^4 + 2r_D(r_D - 1)^2 + 3r_D^2\right]} \tag{49}$$

Obviously, to compare Eqs. 48 and 49, I will need to do considerable algebraic manipulation.

First we will look at the denominator of Eq. 49.

$$\begin{aligned}
&(r_D - 1)\left[\frac{1}{3}(r_D - 1)^4 + 2r_D(r_D - 1)^2 + 3r_D^2\right] \\
&\quad = \frac{(r_D - 1)}{3}\left[(r_D - 1)^4 + 6r_D(r_D - 1)^2 + 9r_D^2\right] \\
&\quad = \frac{(r_D - 1)}{3}\left[(r_D - 1)^2 + 3r_D\right]^2 = \frac{(r_D - 1)}{3}\left(r_D^2 + r_D + 1\right)^2 \\
&\quad = \frac{(r_D - 1)}{3}\,\frac{\left(r_D^3 - 1\right)^2}{(r_D - 1)^2} = \frac{\left(r_D^3 - 1\right)^2}{3(r_D - 1)}
\end{aligned} \tag{50}$$

Note how the denominator simplifies to a great extent.

These same ideas can be used on the terms in the numerator. Since it is so long, I'll divide it up. First let's look at the multiplier on t_D . It can be simplified in a manner similar to that used above, as follows,

$$\left[(r_D-1)^2+3r_D\right]t_D=\frac{\left(r_D^3-1\right)}{(r_D-1)}t_D \tag{51}$$

Dividing this numerator term by the denominator we get,

$$\frac{\left(r_D^3-1\right)t_D}{(r_D-1)}\left[\frac{3(r_D-1)}{\left(r_D^3-1\right)^2}\right]=\frac{3t_D}{\left(r_D^3-1\right)} \tag{52}$$

Note that this result is exactly the same as the first term on the right side of Eq. 48. The remainder of the terms are only functions of r_D . The first r_D term in the numerator can be divided by the denominator to get,

$$\left[\frac{3(r_D-1)}{\left(r_D^3-1\right)^2}\right]\left[(r_D-1)^2+3r_D\right]\left[\frac{1}{6}(r_D-1)^2(2r_D+1)\right]$$

$$=\left[\frac{(r_D-1)}{2\left(r_D^3-1\right)^2}\right]\left[\frac{\left(r_D^3-1\right)}{(r_D-1)}\right]\left[(r_D-1)^2(2r_D+1)\right]$$

$$=\frac{(r_D^2-2r_D+1)(2r_D+1)}{2\left(r_D^3-1\right)}=\frac{2r_D^3-3r_D^2+1}{2\left(r_D^3-1\right)}$$

$$=\frac{2\left(r_D^3-1\right)}{2\left(r_D^3-1\right)}-\frac{3\left(r_D^2-1\right)}{2\left(r_D^3-1\right)}=1-\frac{3\left(r_D^2-1\right)}{2\left(r_D^3-1\right)} \tag{53}$$

Note the constant, 1 , in Eq. 53 is seen in Eq. 48. The ratio, $3\left(r_D^2-1\right)/2\left(r_D^3-1\right)$ is not seen. We'll look at the remainder of the numerator in Eq. 49 to find out if everything works out to result in Eq. 48.

To evaluate the remaining numerator term in Eq. 49, we again divide by the denominator (Eq. 50) to get,

$$-\frac{(r_D-1)^2}{2}\left[\frac{3(r_D-1)}{\left(r_D^3-1\right)^2}\right]\left[\frac{(r_D-1)^2}{5}+r_D\right]$$

$$=-\frac{3(r_D-1)^3}{10\left(r_D^3-1\right)^2}\left[(r_D-1)^2+5r_D\right]=-\frac{3(r_D-1)^3}{10\left(r_D^3-1\right)^2}(r_D^2+3r_D+1)$$

$$=-\frac{3\left(r_D^5-5r_D^3+5r_D^2-1\right)}{10\left(r_D^3-1\right)^2}=-\frac{3\left(r_D^5-1\right)}{10\left(r_D^3-1\right)^2}+\frac{15\left(r_D^3-1\right)}{10\left(r_D^3-1\right)^2}-\frac{15\left(r_D^2-1\right)}{10\left(r_D^3-1\right)^2}$$

$$=\frac{3}{2\left(r_D^3-1\right)}-\frac{3\left(r_D^5-1\right)}{10\left(r_D^3-1\right)^2}-\frac{3\left(r_D^2-1\right)}{2\left(r_D^3-1\right)^2} \tag{54}$$

We can now combine Eqs. 53 and 54 to get the total of the r_D type terms.

$$r_D \text{ Function } =1-\frac{3\left(r_D^2-1\right)}{2\left(r_D^3-1\right)}+\frac{3}{2\left(r_D^3-1\right)}-\frac{3\left(r_D^2-1\right)}{2\left(r_D^3-1\right)^2}-\frac{3\left(r_D^5-1\right)}{10\left(r_D^3-1\right)^2}$$

$$=1-\frac{3\left(r_D^2-2\right)}{2\left(r_D^3-1\right)}-\frac{3\left(r_D^2-1\right)}{2\left(r_D^3-1\right)^2}-\frac{3\left(r_D^5-1\right)}{10\left(r_D^3-1\right)^2}$$

$$=1+\frac{3}{\left(r_D^3-1\right)}-\frac{3r_D^2}{2\left(r_D^3-1\right)}-\frac{3\left(r_D^2-1\right)}{2\left(r_D^3-1\right)^2}-\frac{3\left(r_D^5-1\right)}{10\left(r_D^3-1\right)^2} \tag{55}$$

Clearly the first two terms in Eq. 55 are the same as the first two r_D type terms in Eq. 48. It only remains to see if the remaining terms combine to become the same as the last r_D term in Eq. 48.

We can combine the third and fourth terms to get the following result for Eq. 55.

$$
\begin{aligned}
r_D \text{ Function } &= 1+\frac{3}{\left(r_D^3-1\right)}-\frac{3\left[r_D^2\left(r_D^3-1\right)+\left(r_D^2-1\right)\right]}{2\left(r_D^3-1\right)^2}-\frac{3\left(r_D^5-1\right)}{10\left(r_D^3-1\right)^2} \\
&= 1+\frac{3}{\left(r_D^3-1\right)}-\frac{3\left(r_D^5-r_D^2+r_D^2-1\right)}{2\left(r_D^3-1\right)^2}-\frac{3\left(r_D^5-1\right)}{10\left(r_D^3-1\right)^2} \\
&= 1+\frac{3}{\left(r_D^3-1\right)}-\frac{15\left(r_D^5-1\right)}{10\left(r_D^3-1\right)^2}-\frac{3\left(r_D^5-1\right)}{10\left(r_D^3-1\right)^2} \\
&= 1+\frac{3}{\left(r_D^3-1\right)}-\frac{9\left(r_D^5-1\right)}{5\left(r_D^3-1\right)^2}
\end{aligned}
\tag{56}
$$

Note, Eq. 56 is identical to the r_D terms in Eq. 48. So Chatas' equation is the same as the one we developed here, just as we had hoped. Further it is clear that my way of expressing this equation (Eq. 48) is far simpler than Chatas' equation; Eq. 49 of these notes. Thus it gives considerable insight into the nature of the spherical depletion equation behavior.

5.1.8 CONCLUSIONS

It is clear from these equation developments, that the pseudosteady state conditions result in fairly simple equation forms for pressure drop with time. This statement is true for all outer boundary shapes, and for all types of inner boundary flow (linear, radial, or spherical). Further, these equations all follow the diffusivity equation, even though this equation was not used to derive their behavior.